

University of Southampton Research Repository

Copyright © and Moral Rights for this thesis and, where applicable, any accompanying data are retained by the author and/or other copyright owners. A copy can be downloaded for personal non-commercial research or study, without prior permission or charge. This thesis and the accompanying data cannot be reproduced or quoted extensively from without first obtaining permission in writing from the copyright holder/s. The content of the thesis and accompanying research data (where applicable) must not be changed in any way or sold commercially in any format or medium without the formal permission of the copyright holder/s.

When referring to this thesis and any accompanying data, full bibliographic details must be given, e.g.

Thesis: Author (Year of Submission) "Full thesis title", University of Southampton, name of the University Faculty or School or Department, PhD Thesis, pagination.

Data: Author (Year) Title. URI [dataset]

University of Southampton

Faculty of Engineering and Physical Science

Electronics and Computer Science

Single-cell Impedance Analysis and Sorting

by

Xueping Zou

ORCID ID: <u>0009-0000-7946-565X</u>

Thesis for the degree of Doctor of Philosophy

October 2025

University of Southampton Abstract

Faculty of Physical Science and Engineering

Electronics and Computer Science

Doctor of Philosophy

Single-cell Impedance Analysis and Sorting

by

Xueping Zou

Microfluidic impedance cytometry (MIC) is a label-free technique for differentiating cell phenotypes according to their inherent biophysical markers, principally mechanical (deformability) and dielectric (membrane capacitance and cytoplasm conductivity) properties. This thesis describes new approaches for the measurement of both parameters coupled with a novel method for real-time sorting of single cells according to their electro-mechanical phenotype.

Single-cell microfluidic impedance spectroscopy has been limited in frequency range and in the ability to extract the full set of electrical parameters from single cells. In this thesis, the measurement frequency range was extended to 500MHz, enabling full characterisation of single nucleated cells at high throughput. System validation used HL60 cells and THP-1 cells (differentiated into macrophages) exposed to different chemical treatments in order to change their electrical properties. It was shown that suspending the cells in saline of lower conductivity enhanced discrimination between the cell types and treatment. Single cell spectra were fitted to the double-shell model to obtain membrane capacitance and cytoplasm conductivity.

Different single-cell deformability cytometers have been developed, but these are mostly based on processing high-speed optical images of single cells undergoing deformation. This thesis describes a prototype microfluidic deformability cytometer that measures both the electrical and optical deformability. It simultaneously measures the optical and electrical shape change of single cells deformed in a viscoelastic shear flow. Optical deformability is measured using a low-cost CMOS camera with images of single cells generated with a short LED pulse triggered by an impedance signal from a cell. Electrical deformability of the cell is determined by electrode arrays that measure the shape changes along two axes. The system was characterised by measuring the deformability of HL60 cells treated with cytoskeleton disrupting chemicals. Results show an excellent correlation between the optical and electrical methods.

Finally, a single-cell sorting system was developed by integrating membrane pumps into the micro-cytometer. When the membranes are displaced, they generate short pressure pulses that can deflect single cells into different outlets. An algorithm was developed to generate a trigger according to the particle velocity. Proof of principle experiments demonstrate successful sorting of cells and beads based on size with a throughput of 13 particles/s and purity of 97%.

Tabl	e of C	Contents	. 3
Tabl	e of T	ables	. 7
Tabl	e of F	igures	. 9
Res	earch	Thesis: Declaration of Authorship	33
Ackı	nowle	edgements	34
List	of Syı	mbols	35
List	of Ab	breviations	38
Cha	pter 1	Introduction	40
1.1	Bac	kground	40
1.2	Cur	rent Challenges and Motivation	40
1.3	Obj	ective	42
1.4	The	sis outline	43
Cha	pter 2	2 Literature Review	44
2.1	Intr	oduction	44
2.2	Sing	gle-cell Biophysical Properties and Measurements	44
	2.2.1	Mechanical properties and characteristics	45
	2.2.2	Single-cell microfluidic deformability cytometry	47
	2.2.3	Characterisation of cell electrical properties	53
	2.2.4	Single-cell microfluidic impedance cytometry	56
	2.2.5	Discussion	60
2.3	Sing	gle-cell Sorting	60
	2.3.1	Label-based sorting	61
	2.3.2	Label-free sorting	62
	2.3.3	Discussion	69
Cha	pter 3	Theory and Simulation	70
3.1	Intr	oduction	70
		gle-cell Electrical Theory and Model	

3.2.1 C	Complex permittivity	71
3.2.2 C	Clausius-Mossotti factor and Maxwell Mixture Theory	72
3.2.3 S	Shell model	73
3.2.4 S	Simulations	74
3.	.2.4.1 Frequency spectrum with different conductivity medium	74
3.	.2.4.2 Frequency spectrum with different cell parameters	76
3.3 Single	e-cell Mechanics: Theory and Models	80
3.3.1 Y	/oung's modulus	80
3.3.2 S	Solid model of cells	80
3.4 Micro	ofluidics	81
3.4.1 L	_aminar flow	82
3.4.2 S	Sheath flow focusing	83
3.4.3 lr	nertial focusing	85
3.4.4 V	/iscoelastic focusing	89
3.4.5 S	Shear flow-induced deformation	92
3.4.6 E	Extensional flow-induced deformation	94
3.4.7 F	Fluid selection	96
3.5 Cell S	Sorting	96
3.5.1 M	Membrane pump for local-flow control	97
3.5.2	Deflection of a circular membrane	98
3.5.3 S	Simulation of circular membrane1	00
3.5.4 S	Simulation for fluid in the sorter1	01
3.6 Discu	ussion1	05
Chapter 4	Electro-Optical Deformability MIC system1	07
4.1 Introd	duction1	07
4.2 Syste	em Overview1	80
4.2.1 E	Electrodes configuration and electrical deformability 1	80
4.2.2 Ir	mage acquisition and processing and optical deformability 1	10
4.	.2.2.1 Triggering principle 1	12

		4.2.2.2	Image processing	115
	4.2.3	Electro-	-Optical data matching and system calibration	119
4.3	В Ехр	eriment	Setup	121
	4.3.1	Experim	nent procedure	121
	4.3.2	HL60 ce	ell culture	122
	4.3.3	Cell trea	atment	123
		4.3.3.1	Cytochalasin D and Latrunculin B	123
		4.3.3.2	Glutaraldehyde	126
4.4	Res	sults		126
	4.4.1	Correla	tion between electrical and optical techniques	126
	4.4.2	Deform	ability distribution between optical and electrical measuren	nents 131
	4.4.3	Optical-	-electrical deformability measurements for HL60 cells with o	disrupting
		cytoske	eleton	133
	4.4.4	Optical-	-electrical deformability measurements for fixed HL60 cells	135
4.5	i Dis	cussion		138
Cha	pter	5 Singl	e-cell Spectroscopy of Nucleated Cell	140
5.1	Inti	roductio	n	140
5.2	2 Sys	stem Ove	erview	141
	5.2.1	Electro	de configuration	141
	5.2.2	Measur	rement principles and data processing	143
		5.2.2.1	Complex permittivity and differential current measuremen	nt 144
		5.2.2.2	Gating and calibration	146
		5.2.2.3	Madal fitting	147
5.3		5.2.2.5	Model fitting	
5.3	B Cel		ent and Media Preparation	
5.3		ll Treatm		150
5.3	5.3.1	I l Treatm THP-1 c	ent and Media Preparation	150 151
5.3	5.3.1 5.3.2	I l Treatm THP-1 c Media p	cells and macrophages	150 151
5.3	5.3.15.3.25.3.3	THP-1 c Media p HL60 ce	cells and macrophages	150 151 151 152

	5.4.1	Mean dielectric properties and influence of suspending media conductive	vity
		153	
	5.4.2	Single-cell spectroscopy for fixed HL60 cells	158
	5.4.3	Single-cell spectroscopy for differentiation into macrophages	162
5.5	5 Dis	cussion	165
Cha	apter 6	Single-cell Sorting System Based on deformability MIC1	167
6.1	l Intr	oduction	167
6.2	2 Sor	ting System	167
	6.2.1	Electrode configuration	167
		System setup	
		6.2.2.1 Real-time triggering algorithm to solve conflicts	
		6.2.2.2 Driving pulse circuit	174
		6.2.2.3 Piezo actuator assembly	175
	6.2.3	Sorting chip design and fabrication	
		6.2.3.1 Prototype design	178
		6.2.3.2 Final design	180
6.3	3 Ехр	periment Setup	182
	6.3.1	Sample preparation	182
		Sorting process	183
6.4	1 Sor	ting Evaluation Result	183
		Fluorescence beads test	
		Cell deformability sorting	
6.5		cussion	
		7 Conclusions and Future Work1	
	-	e 201	ספו
1761	GI CIIC	G ZVI	

Table of Tables

Table of Tables

Table 2.1 Summry table for deformability MIC metioned in this section53
Table 4.1 Definition of electrical deformability (ED) and the range of ED values for cells in undeformed and deformed states
Table 4.2 Definition of electrical deformability (OD) and cases for cells in different states 118
Table 4.3 The mean ± SD value of ED and OD plotted in Figure 4.25
Table 4.4 The mean ± SD value of ED and OD plotted in Figure 4.27
Table 4.5 The number of cells used in Figure 4.27 and Table 4.4
Table 4.6 The mean ± SD value of OD for untreated and treated HL60 cells for three repeats at 10µL/min in Figure 4.32(a).
Table 4.7 The mean ± SD value of ED for untreated and treated HL60 cells for three repeats at 10μL/min in Figure 4.32(b).
Table 4.8 The mean ± SD value of ED for unfixed and fixed HL60 cells for three repeats at 5µL/mir in Figure 4.33(b).
Table 4.9 The mean ± SD value of OD for unfixed and fixed HL60 cells for three repeats at 5µl/mir in Figure 4.33(b).
Table 5.1 An example of initial values and set range for cell parameters when running the "pattern search" function in MATLAB
Table 5.2 The setting dielectric parameters of the generated dataset in Figure 5.5 and the output results from the "pattern search" fitting program149
Table 5.3 Fitting results for unfixed and fixed HL60 cells in different conductivity saline shown in Figure 5.8 with confidence interval (CI)
Table 5.4 Fit results of untreated and CytoD-treated HL60 cells shown in Figure 5.12(a) with confidence interval (CI).
Table 5.5 Fitting results for untreated and fixed single-cells in 0.32 S/m and 1.6 S/m saline (Figure 5.14), with confidence interval (CI)
Table 5.6 Single-cell fitting results (mean ± SD) for untreated and fixed cells in two different conductivity saline (Figures 5.15 and 5.16). CV stands for coefficient of variation
Table 6.1 Purity of 10 μ m beads with two different ratios of N_{pre10} to N_{pre6} and different pulse widths.

Table of Tables

Table 6.2 Sorting efficiency for 10 μ m beads with two different ratios of $N_{ extit{pre10}}$ to $N_{ extit{pre6}}$ and different
pulse widths. The data is plotted in Figure 6.19
Table 6.3 The purity for 10 μ m beads with the ratio of N_{pre10} to N_{pre6} 3:2 and 2 ms pulse widths. The
data was plotted in Figure 6.21 187

mammalian cells4
Figure 2.2 (a) Atomic Force Microscopy. A micron-sized tip connects to a micro-fabricated
cantilever to deform and interact with the sample. A laser beam is reflected from
the cantilever and collected by a detector, which measure the displacement
The real-time force is recorded. (b) Optical Tweezers. Microbeads are attached
to the measured cell. A laser beam traps one of the beads and an elongation is
induced in the cell. The escape force (F) of the trapped bead and dimensiona
alterations of cell (D_a and D_t) are used to evaluate the elastic or bending modulus
of the membrane through a deformation model. (c) Micropipette Aspiration.
cell partially or completely enters the micropipette with a radius $R_{\text{\tiny p.}}$ It
deformability is determined through the relationship between the shear modulu
μ , the suction pressure (P) and the length of the protrusion (L). (d) Acoustic
Scatter. A particle interacts with acoustic fields (black waves) produced by SWI
vibration (black arrows) at the resonant frequency f. The interaction between the
particle and the surrounding fluid induces acoustic scattering (blue waves)
resulting in a shift in the resonant frequency (Δf). (a), (b)and (c) are adopted fron
(Matthews et al. 2022), (d) is adopted from (Kang et al. 2019)4
Figure 2.3 Operating principle of cDC, sDC and xDC. (a) cDC. A cell passes through a constriction
smaller than its diameter, and the transit time is measured to determine
deformability. (b) sDC. A cell passes through a contactless channel and shea
deformability. (b) sDC. A cell passes through a contactless channel and shea
deformability. (b) sDC. A cell passes through a contactless channel and shea force is applied to its surface. The deformability is determined from optical
deformability. (b) sDC. A cell passes through a contactless channel and sheat force is applied to its surface. The deformability is determined from optical images. (c) xDC. An extensional flow along with a cross-slot microfluidice.
deformability. (b) sDC. A cell passes through a contactless channel and sheat force is applied to its surface. The deformability is determined from optical images. (c) xDC. An extensional flow along with a cross-slot microfluiding architecture induces extensional deformation of a cell and the deformability is
deformability. (b) sDC. A cell passes through a contactless channel and shear force is applied to its surface. The deformability is determined from optical images. (c) xDC. An extensional flow along with a cross-slot microfluiding architecture induces extensional deformation of a cell and the deformability is determined by optical images. Copied from (Urbanska et al. 2020) (d) The
deformability. (b) sDC. A cell passes through a contactless channel and shear force is applied to its surface. The deformability is determined from optical images. (c) xDC. An extensional flow along with a cross-slot microfluiding architecture induces extensional deformation of a cell and the deformability is determined by optical images. Copied from (Urbanska et al. 2020) (d) The extensional forces dominate in the short hyperbolic channel so that cells
deformability. (b) sDC. A cell passes through a contactless channel and shear force is applied to its surface. The deformability is determined from optical images. (c) xDC. An extensional flow along with a cross-slot microfluiding architecture induces extensional deformation of a cell and the deformability is determined by optical images. Copied from (Urbanska et al. 2020) (d) The extensional forces dominate in the short hyperbolic channel so that cells perform elliptical deformation patterns. Copied from (Piergiovanni et al. 2020)
deformability. (b) sDC. A cell passes through a contactless channel and sheat force is applied to its surface. The deformability is determined from optical images. (c) xDC. An extensional flow along with a cross-slot microfluidical architecture induces extensional deformation of a cell and the deformability is determined by optical images. Copied from (Urbanska et al. 2020) (d) The extensional forces dominate in the short hyperbolic channel so that cells perform elliptical deformation patterns. Copied from (Piergiovanni et al. 2020)
deformability. (b) sDC. A cell passes through a contactless channel and shear force is applied to its surface. The deformability is determined from optical images. (c) xDC. An extensional flow along with a cross-slot microfluiding architecture induces extensional deformation of a cell and the deformability is determined by optical images. Copied from (Urbanska et al. 2020) (d) The extensional forces dominate in the short hyperbolic channel so that cells perform elliptical deformation patterns. Copied from (Piergiovanni et al. 2020)
deformability. (b) sDC. A cell passes through a contactless channel and shear force is applied to its surface. The deformability is determined from optical images. (c) xDC. An extensional flow along with a cross-slot microfluiding architecture induces extensional deformation of a cell and the deformability is determined by optical images. Copied from (Urbanska et al. 2020) (d) The extensional forces dominate in the short hyperbolic channel so that cells perform elliptical deformation patterns. Copied from (Piergiovanni et al. 2020) Figure 2.4 The structure and principle of the Coulter counter. As a particle passes through the tube, the generated current is recorded to count the number and deduce its size.

increase were determined, and foetal/neonatal and adult RBCs were classified

successfully. Picture from (Zheng et al. 2012)50
natic of the microfluidic impedance systems developed by Zhou et al. (Zhou et al 2018). (a) Total passage time was used to reflect the undeformed state of cells (b) Entry time was used to characterise the deformability of cells. (c) Transit time was used to identify the fractional properties of cells
matic illustration the system from Petchakup et al. (Petchakup et al. 2022). Cells were subjected to the dominant shear force and the cell shape changes were assessed by comparing impedance signals before and after the cross-shaped channel. Size, deformability, and electrical opacity were defined by impedance at different frequencies.
eformability MIC with hyperbolic channel proposed by Reale et al. (Reale et al 2022) i. The device geometry which contains a hyperbolic channel and four coplanar electrodes in cross configuration to probe the cell along the direction of flow and along the direction transverse to flow. ii. $I_F = I_T$, when a spherical particle passes through. iii. $I_F \neq I_T$, when an elongated particle passes through. (b) Schematic illustration of the channel design from (Jarmoshti et al 2024). Deformation of cells under viscoelastic hyperbolic extensional flow alters their anisotropy index (AI), defined as the ratio of length (A) to width (B) in the flow direction. Cells were measured using a three-electrode configuration to measure three stages of deformation: pre-deformation, deformation and recovery.
patch-clamp technique used to measure single-cell electrical properties Schematic circuit diagram of current recording from a patch of membrane with an extracellular pipette. VC, a two-microelectrode voltage clamp circuit to provide a fixed value of the membrane potential of the fibre. P, pipette applied closely onto the muscle fibre within 200µm of the intracellular clamp electrodes VG. Virtual ground circuit that measured the membrane current with an optional amplifier and a feedback resistor. Picture from (Neher and Sakmann 1976)54
Overview of the device developed by Malleo et al. (Malleo et al. 2010) to measure the time-dependent impedance of single cells to dynamic chemical perturbations. Cells were hydrodynamically trapped on top of a pair of electrodes. (g) Schematic diagram of the electrical impedance spectroscopy system designed by Mansoorifar et al. (Mansoorifar et al. 2018). Cells are trapped in the electro-activated microwells and for dielectric spectroscopy

	measurements. Spectra are fitted to an equivalent circuit model to extract cell
	membrane capacitance and cytoplasmic conductivity 55
Figure 2.11 (a) S	Schematic diagram of a chamber used to generate the rotating electric field. Four
	electrodes are driven by equal voltages with four phases shifted by 90°. The
	frequency of maximum rotation speed was recorded for different suspension
	conductivities in order to derive the cell membrane capacitance (Arnold and
	Zimmermann 1982a). (b) Schematic diagram of the electrorotation device
	designed by Kawai et al. (Kawai et al. 2020). Hematopoietic cells in the 3D-array
	microwells rotate, and the measured spectra used to extract membrane
	capacitance and cytoplasmic conductivity55
Figure 2.12 (a) 5	Schematic diagram of the MIC device designed by Gawad et al. (Gawad, Schild,
, ,	and Renaud 2001). Three coplanar electrodes were fabricated in the channel to
	generate the differential impedance signal shaped as an anti-symmetric
	Gaussian signal. (b) MIC scatter plot of low frequency (LF) phase versus high
	frequency (HF) phase for mixed ghosts and erythrocytes. Ghosts had a lower
	HF/LF ratio56
F: 0.40.0	
Figure 2.13 Sca	tter plot of a mixture of the T-lymphocytes, monocytes, neutrophils and 5.62µm
	diameter latex beads from (Holmes et al. 2009). (a) Opacity ($ Z_{1707kHz} / Z_{530kHz} $) vs
	low frequency impedance magnitude ($ Z_{503kHz} $). (b) FACS analysis of the same
	sample showing forward and side scatter of the cells; colour coded according to
	fluorescence57
Figure 2.14 Scat	tter plot of phase versus amplitude of impedance at 6MHz showing discrimination
	between necrotic and viable U937 human lymphoma cells (Ostermann et al.
	2020)
Figure 2.15 (a) C	Comparisons of MLS, Pspice circuit simulations and conventional AC frequencies
	(Sun et al. 2007). These three methods had good agreements. (b) The impedance
	spectrum example of the four-frequency impedance signal fitting of a single
	fabricated liposome particle (Chai et al. 2023)58
Figure 2.16 (a)	-i. Schematic diagram of the MIC device to determine specific membrane
	capacitance (C_{sm}) and cytoplasm conductivity (σ_{cy}). (a)-ii. The equivalent circuit
	was used to fit the measured impedance and derive the parameters. S_{ch} – cross-
	section area of the side constriction channel. L_{ch} – the length of the major
	constriction channel along the direction of the side channel. M_f – modification
	factor obtained based on numerical simulations. Four parameters including
	cytoplasm resistance (P) and membrane canacitance (C) were obtained

Copied from (Zhao et al. 2018) (b) The shell model used to represent yeast cells

	(Haandbæk et al. 2016). R_i , ε_i , σ_i – Inner radius, permittivity, conductivity; ε_w , σ_w – Cell wall permittivity and conductivity; ε_m , σ_m – Cell membrane permittivity and
Figure 2.17 (a) \$	conductivity; D_w , D_m – Thickness of the cell wall and cell membrane59 Schematic diagram of the impedance spectroscopy system proposed by Spencer
G * 3 (4)	and Morgan (Spencer and Morgan 2020). Eight frequencies ranging from 200kHz
	to 50MHz were applied to the microelectrodes simultaneously, and the
	spectrum of each single cell was fitted to a single-shell model to extract the
	dielectric parameters, including cell diameter, membrane capacitance and
	cytoplasm permittivity and conductivity. (b) Scatter plot for 1000 RBCs (red dots)
	and 1000 ghosts (blue dots). The bottom right plot is an example impedance
	spectrum for a ghost cell, showing an excellent fit to the single-shell model59
Figure 2.18 (a) 9	Schematic diagram of a microfluidic fluorescent-based sorting system. Cells were
1 18410 2110 (4)	encapsulated in droplets, and those with target antibodies produced increased
	fluorescence signals after off-chip incubation. (b) From i to iii, the whole process
	of sorting. Copied from (Mazutis et al. 2013)61
Figure 2 19 (a) 9	Schematic of a fluorescence sorting system developed by Li et al. (Li et al. 2019).
1 16410 2:10 (4)	(b) The chip image. (c) The microscope image of the channel and sorting region.
	Stained cells were forced by the acoustic waveform generated by the FIDT
	toward the target outlet
Eiguro 2.20 Mi	croporous membrane filtration of whole blood using cross flow filtration to
rigule 2.20 Mi	maximise yield or reduce processing time. This method achieved high isolation
	efficiency by minimising the accumulation of fouling elements, such as RBCs, at
	the filter face. Copied from (Crowley and Pizziconi 2005)
Eiguro 2 21 Sok	nematic of a DLD separating system. The critical diameter of the system is D $_{ m c}$,
rigule 2.21 oci	which can be evaluated. Cells with size larger than D_c move in a direction
	dictated by the arrays, while cells smaller than D_C move with the convective flow.
	Copied from (Xavier et al. 2019)64
Figure 2.22 An	inertial microfluidic sorting device with spiral channel. A set of micro-obstacles
	integrated into the spiral channel results in an enhanced performance. Three
	outlets for specific particle separation and collection. The sorting efficiency was
	99.8% for sorting polymeric particles, CTCs and blood cells. Copied from (Shen et al. 2017)
E	
Figure 2.23 (a)	Two sets of integrated electrodes in the sidewalls of the microchannel generate

negative DEP forces with different directions to push particles away from the

	sidewall. Particles position at different equilibrium points along the width by the $$
	coupled DEP forces, flowing to a target outlet. (b) Sorting principle of DEP-FFF
	proposed by Vykoukal et al. (Vykoukal et al. 2008). i. An array of electrodes
	positions cells to equilibrium positions above the bottom of the channel
	according to their type. ii. Cells sorted by propelling them through the channel at
	rates according to their distance from the wall. Image is copied from (Wyatt
	Shields Iv, Reyes, and López 2015)65
Figure 2.24 (a) N	am et al. separated platelets from blood cells by a SAW device (Nam et al. 2011).
	Sheath flow was used to focus the cells into a confined band. Larger cells, such
	as leukocytes and erythrocytes, experienced greater acoustic radiation forces,
	thereby migrating farther than the surrounding platelets. (b) Components of the
	microfluidic device66
Figure 2 25 Intel	lligent image-based deformation-assisted cell sorting with molecular specificity
Tiguro 2.25 into	(fluorescence signal) proposed by Nawaz et al. (Nawaz et al. 2020). The sorter
	used SSAW to change the direction of target cells
Figure 2.26 (a) S	chematic diagram of the impedance-based peripheral blood mononuclear cells
	(PBMC) isolation system proposed by Zhong et al. (Zhong, Li, et al. 2021). (b) Choi
	et al. (Choi et al. 2020) proposed a microfluidic deformability-activated sorting
	system of single particles. Poly (ethylene glycol) diacrylate (PEGDA) beads were
	created as the deformability model for device validation and performance
	evaluation. The deformability was measured according to the transit time of
	particles passing through the constriction
Figure 2.27 (a) L	i and Ai (Li and Ai 2021) proposed an acoustic sorting system based on MIC using
	impedance and mechanical characteristics. (b) High-throughput automated
	droplet screening using impedance to reduce false positive events and improve
	efficiency and stability. Copied from (Panwar et al. 2023)67
Figure 2.28 (a)	Chen et al. developed a membrane pump sorter using a piezoelectric (PZT)
· · · · · ·	actuator (Chen et al. 2009). As the particles enter the sorting junction, the
	bending motion of the PZT actuator temporarily disturbs fluid flow, deflecting
	target particle to the left-right channels. When the PZT was not triggered,
	unwanted particles stayed in the centre streamlines towards the middle waste
	channel. (b) Rajauria et al. developed a high-speed sorting system with a pair of
	PZT actuators, with a throughput of 60000 particles/min
F 1. 6 .5.4.3	
Figure 2.29 (a)	Conceptual image of the on-chip cell sorter using dual-membrane pumps
	proposed by Sakuma et al. (Sakuma et al. 2017). The membrane pumps were

	fabricated on the chip and the membrane deflection was driven by the
	piezoelectric actuator. (b) Nitta et al. (Nitta et al. 2018) integrated high-speed
	intelligent image-based detection69
Figure 3.1 Diagr	am of the parallel plate capacitor. A is the plate area, D is the separated distance,
	$arepsilon$ is permittivity, and σ is the conductivity of the dielectric72
Figure 3.2 Sche	ematic diagram of (a) single-shell model and (b) double-shell model. ϵ_i is the
	permittivity and σ_i is conductivity. Subscript 1: cell membrane, 2: cytoplasm, 3:
	nuclear envelope, 4: nucleoplasm, med: media. r_{cell} is the radius of cell, d_1 is
	membrane thickness, $Ra = r_{cell} - d_1$, d_3 is thickness of nuclear envelope, R_b is the
	radius of the nucleus, $R_c = R_b - d_3$
Figure 3.3 Real	and imaginary parts of $fCM(cell)*$ for a single shell model when changing the
	media conductivity $\sigma_{\it med}$ from 0.32 S/m to 1.6 S/m. The cell dielectric parameters
	are: $\varepsilon_{med} = 80\varepsilon_0$, $\varepsilon_1 = 7\varepsilon_0$, $\sigma_1 = 3.14 \times 10^{-5}$ S/m, $\varepsilon_2 = 60\varepsilon_0$, $\sigma_2 = 0.3$ S/m, $d_1 = 5$ nm, r_{cell}
	(cell radius) = 6 μ m. Subscript: "med" – media, "1" – cell membrane, "2" –
	cytoplasm75
Figure 3.4 Real	and imaginary parts of $fCM(cell)*$ for a double shell model for different media
	conductivity σ_{med} from 0.32 S/m to 1.6 S/m. The dielectric parameters are: ε_{med} =
	$80\varepsilon_0$, $\varepsilon_1 = 7\varepsilon_0$, $\sigma_1 = 3.14 \times 10^{-5}$ S/m, $\varepsilon_2 = 60\varepsilon_0$, $\sigma_2 = 0.3$ S/m, $\varepsilon_3 = 52\varepsilon_0$, $\sigma_3 = 1.8 \times 10^{-3}$
	S/m, ε_4 = 120 ε_0 , σ_4 = 0.82 S/m, d_1 = 5nm, d_3 = 20nm, r_{cell} (cell radius) = 6 μ m, R_b
	(nucleus radius) = $4\mu m$. Subscript: "med" – media, "1" – cell membrane, "2" –
	cytoplasm, "3" – nuclear envelope, "4" – nucleoplasm
Figure 3.5 Real	and imaginary parts of $f\mathit{CM}(\mathit{cell})$ $*$ for a single shell model in physiological saline
	when modifying cell diameter (d, $8\mu m\sim 24\mu m$, orange region), membrane
	capacitance (C_1 , 5.3mF/m ² ~19.53mF/m ² , red region) and cytoplasm
	conductivity (σ_2 , 0.2 S/m~0.4 S/m, blue region). Other parameters are the same
	as the "typical" setting for the black curve. Cell dielectric parameters for the
	black curve: $\varepsilon_1 = 7\varepsilon_0$ ($C_1 = 12.4$ mF/m ²), $\sigma_1 = 3.14 \times 10^{-5}$ S/m, $\varepsilon_2 = 60\varepsilon_0$, $\sigma_2 = 0.3$
	S/m, d_1 = 5nm, r_{cell} (cell radius) = 6 μ m. Subscript: "1" – cell membrane, "2" –
	cytoplasm76
Figure 3.6 Real	and imaginary parts of $f\mathit{CM}(\mathit{cell})$ $*$ for a single shell model in physiological saline
	when modifying cell diameter (d, 8 μ m~24 μ m, orange region), membrane
	capacitance (C_1 , 5.3mF/m ² ~19.53mF/m ² , red region) and cytoplasm
	conductivity (σ_2 , 0.2 S/m~0.4 S/m, blue region). Other parameters are the same
	as the "typical" setting for the black curve. Cell dielectric parameters for the
	black curve: $\varepsilon_1 = 7\varepsilon_0$ ($C_1 = 12.4$ mF/m ²), $\sigma_1 = 3.14 \times 10^{-5}$ S/m, $\varepsilon_2 = 60\varepsilon_0$, $\sigma_2 = 0.3$

S/m, ε_3 = 52 ε_0 , σ_3 = 1.8×10⁻³ S/m, ε_4 = 120 ε_0 , σ_4 = 0.82 S/m, d_1 = 5nm, d_3 = 20nm, r_{cell} (cell radius) = 6 μ m, R_b (nucleus radius) = 4 μ m. Subscript: "med" – media, "1" – cell membrane, "2" – cytoplasm, "3" – nuclear envelop, "4" – nucleoplasm. .77

- Figure 3.8 Real and imaginary parts of fCM(cell) * for a single shell model in low-conductivity (0.32 S/m) media when modifying cell diameter (d, 8 μ m~24 μ m, orange region), membrane capacitance (C_1 , 5.3mF/m²~19.53mF/m², red region) and cytoplasm conductivity (σ_2 , 0.2 S/m~0.4 S/m, blue region). Other parameters are the same as the "typical" setting for the black curve. Cell dielectric parameters for the black curve: ε_1 = 7 ε_0 (C_1 = 12.4 mF/m²), σ_1 = 3.14×10⁻⁵ S/m, ε_2 = 60 ε_0 , σ_2 = 0.3 S/m, ε_3 = 52 ε_0 , σ_3 = 1.8×10⁻³ S/m, ε_4 = 120 ε_0 , σ_4 = 0.82 S/m, d_1 = 5nm, d_3 = 20nm, r_{cell} (cell radius) = 6 μ m, R_b (nucleus radius) = 4 μ m. Subscript: "med" media, "1" cell membrane, "2" cytoplasm, "3" nuclear envelope, "4" nucleoplasm.78
- Figure 3.10 Real and imaginary parts of fCM(cell) * for double-shell model in low-conductivity media when modifying the nuclear envelope permittivity (ε_3 , $36\varepsilon_0\sim68\varepsilon_0$, grey region) and conductivity (σ_3 , $0.6\times10^{-3}\sim3\times10^{-3}$ S/m, light blue region), and nucleoplasm permittivity (ε_4 , $100\varepsilon_0\sim140\varepsilon_0$, green region) and conductivity (σ_4 , $0.54\sim1.1$ S/m, purple region). Other parameters are the same as the "typical" setting for the black curve. Cell dielectric parameters for the black curve: $\varepsilon_1=7\varepsilon_0$ ($C_1=12.4$ mF/m²), $\sigma_1=3.14\times10^{-5}$ S/m, $\varepsilon_2=60\varepsilon_0$, $\sigma_2=0.3$ S/m, $\varepsilon_3=52\varepsilon_0$, $\sigma_3=1.8\times10^{-3}$ S/m, $\varepsilon_4=120\varepsilon_0$, $\sigma_4=0.82$ S/m, $\sigma_1=5$ nm, $\sigma_2=1.8\times10^{-3}$ S/m, $\sigma_3=1.8\times10^{-3}$ S/m, $\sigma_3=1.8\times10^{-3}$

Figure 3.11 Two	Voigt Model
Figure 3.12 (a) S	Schematic of 2D focusing. Arrows for "Inlet" and "Side" are the direction of fluid. The channel width is represented as w_c and w_f is the width of the focused inlet stream. (b) Confocal scanning microscopy fluorescence images of focusing with inlet pressure $P_i = 5$ psi and the ratio of the side pressure to the inlet pressure is (i) 0.5 (ii) 1.0 (iii) 1.1 and (iv) 1.2. Each 3D rendering consists of approximately 30 separate 2D images acquired at regular intervals in depth. Copied from (Knight et al. 1998).
Figure 3.13 3D	hydrodynamic focusing chips: one top and bottom sheath flow entering perpendicular to the sample flow direction. Copied from (Sundararajan et al. 2004).
Figure 3.14 Isor	etched into both the superior and inferior channel walls, producing fluidic pathways that guide sheath flows from lateral positions toward the superior and inferior midplanes of the sample stream (Howell et al. 2008)
Figure 3.15 Sch	ematic of the non-coaxial sheath flow cell (Hairer et al. 2008). The sample was introduced through the inlet, while the sheath flow entered via the rear inlet and lateral hydrodynamic focusing was achieved.
Figure 3.16 Sch	nematic of the improved sheath flow cell. A lifting sheath inlet was added to navigate the sample liquid in the horizontal direction (Hairer and Vellekoop 2009)
Figure 3.17 Sche	ematics describing the dominant forces in inertial focusing systems. (a) is the wall interaction force which is generated when particle-wall interactions create localised pressure gradients. (b) is the shear gradient lifting force originated from velocity profile curvature in Poiseuille flow. Copied from (Martel and Toner 2014).
Figure 3.18 In th	ne square channel, random distributed particles are focused to four equilibrium regions at a moderate Reynolds number and the distribution of equilibrium exhibits four-fold symmetry. The simulated force field on a particle over a fourth of a channel cross-section is shown (Di Carlo 2009).
Figure 3.19 In a	rectangular channel with a large aspect ratio (very wide or very high channel), the number of equilibrium positions are decreased to two and centred at the long face of the channel (Martel and Toner 2014).

Figure 3.20 Fu	uorescence image of inertial focusing of particles of three sizes (2um,10um and
	24um) (Hansson et al. 2011). Smaller particles migrate to four symmetric
	equilibrium positions around the channel central line, while larger particles
	settled into two equilibrium positions aligned with the long-wall midpoints. Very
	small particles remain unfocused88
Figure 3.21 S	chematic of a spiral microparticle separator proposed by Kuntaegowdanahali
	(Kuntaegowdanahalli et al. 2009)88
Figure 3.22 Th	e channel length the system needs for different sizes of particles when the channel
	size is 50umx30um and the flow rate is 90ul/min. Larger particles need shorter
	channel length to achieve inertial focusing equilibrium positions (Di Carlo 2009).
	89
Figure 3.23 P	article equilibrium positions in inertial dominant focusing, elasticity dominant
	focusing, and inertia-elastic focusing (Yuan et al. 2018). The equilibrium
	positions are different because of varing inertial and elastic effects. W_i is
	Weissenberg number which referres to elasticity while the Reynolds number Re
	characterises the ratio between the inertial and viscous force90
Figure 3.24 Cr	oss-sectional distribution of particles of blockage ratio (ratio of particle diameter
	to cahnnel height) β =0.1 and β =0.17 in a square channel flow of an elasticity
	dominant fluid at different flow rates . In 8% polyvinylpyrrolidone (PVP), an
	elasticity-dominant fluid, focusing was enhanced by increasing the flow rate and
	blockage ratio (Seo, Kang, and Lee 2014)90
Figure 3.25 Cro	oss-sectional distributions of particles of eta =0.1 and eta =0.17 in a square channel flow
	of a shear-thinning fluid at low flow rate conditions (20ul/min and 100ul/min) and
	high flow rate conditions (500ul/min and 1000ul/min), where the elastic and
	inertial effects are comparable and the inertial effect is dominant respectively.
	(Seo, Kang, and Lee 2014)91
Figure 3.26 Sh	ear-gradient lift and wall repulsion working in the direction opposite to that of the
	elastic force becomes stronger as the flow rate increases. As a result, focussed
	particles at the channel centre disperse again at high flow rate in a shear-
	thinning fluid. FE , FL , and FW represent the elastic force, shear-gradient lift,
	and wall repulsion. Adapted from (Seo, Kang, and Lee 2014)91
Figure 3.27 (a)	A red cell is distorted by the drag force in the channel. (b) Simulation showing that
	the highest stresses occur in the red blood cell membrane regions closest to the
	channel walls (Xu et al. 2018)93

Figure 3.28 Det	formation of an elastic sphere and a thin elastic shell with and without surface
	tension generated by the hydrodynamic loading in a cylindrical channel.
	Representative example shapes for relative cell sizes $\lambda=0.7$ and $\lambda=0.9$. λ is
	the ratio of the sphere's radius and the channel radius. In each row, materia
	parameters were chosen such that shapes have the same deformation d . The
	curvature ξ changes between different models (Mietke et al. 2015b)93
Figure 3.29 (a)	Isoelasticity lines of a solid elastic sphere with data points representing agarose
84 00 (4)	bead (blue circles) and HL60 cells (red squares). $E0 \approx 270$ Pa. (b) Isoelasticity
	lines of a thin elastic shell without surface tension with data points representing
	· · · · · · · · · · · · · · · · · · ·
	HL60 cells (red squares). $(Eh)0 \approx 3.4 \text{ nN/um}$ (Mietke et al. 2015a)94
Figure 3.30 Hyp	perbolic converging microfluidic channel proposed by Lee et al. (a) Velocity field
	flow rate $Q=1\mathrm{ul/min}$. (b) Velocity of the x-axis direction at the centerline of the
	channel. The slope of this graph implies the extensional rate, which is a constant
	Copied from (Lee et al. 2009)95
Figure 3.31 Ima	ages of two modes of deformation shapes occurring in different geometries. The
	top one is a short hyperbolic channel, the middle one is a long hyperbolic
	channel, and the last one is a straight channel. The extensional forces are
	prevalent in the short hyperbolic channel, causing cells to adopt elliptical
	deformation. Long and straight hyperbolic channels are primarily influenced by
	shear forces, resulting in bullet-shaped cell deformation. (Piergiovanni et al
	2020)
Figure 3.32 Sch	nematic diagram of membrane pump when the sorter is inactivated. (a) Side view
	along the cross-section line shown in (b). In a stable inactivated state, the liquid
	flows inside the main channel and spreads to two outlets at the end. The two
	chambers covered by a thin membrane are filled with the local flow, which car
	be pumped into the main channel when the sorter is activated, but it is stagnant
	in the inactivated state. (b) Top view. The part connecting the main channel and
	the chamber is the sorting channel97
Figure 3.33 Sc	hematic diagram of the pump showing how the sorting works (chambers and
	membranes are not shown in this diagram). (a) "Ready to activate" state. The
	pressure of the inlet (P_1) and two outlets $(P_2$ and $P_3)$ are controlled by the pressure
	pump. In this state, the particles in the main flow target the upper outlet. (b)
	"Activated" state. The red outlined region is sorting ROI. When the membrane
	covering the upper pump is triggered by a pulse, the local flow stored in the upper
	chamber is pumped into the main channel. The particles flow in the main flow

Figure 3.34 Scl	mematic of a circular membrane deflection model. The radius of the circular membrane is "a", and the applied central point load is "F". "r" is the distance from a point on the membrane to the central point, and w_0 is the deflection displacement when r =0. Copied from Wan (Wan 1999)99
Figure 3.35 The	e 3D geometry model was created in COMSOL. The diameter of the circular membrane was 2mm, and the thickness was 170 μ m, the same as the normal cover slip made from borasilicate with Young's modulus $G = 64$ Gpa; Poisson's ratio $u = 0.2$. The point load ($F = 20$ N) was applied at the central point of the memrbane to simplify the simulation. The blue region represents the polygon that is clamped and set to be "Fixed Constraint"
Figure 3.36 (a)	The surface displacement and (b) the slice view of the displacement magnitude. The displacement at the central point of the membrane (<i>r</i> =0) is higher than other points on the same surface and the surface in direct contact with the point load exhibits maximum displacement magnitude which is around 23µm
Figure 3.37 3D g	geometry model used for the fluidic simulation. (a) Whole microfluidic domain. To simplify the simulation, the contralateral chamber is neglected. (b) The dimension of the radial section AB. The overall height is $700\mu m$, and the height of the main channel is $30\mu m$. (c) The dimension of the sorting ROI. w_L is the width of the sorting channel; w_D is the distance between the outlet junction and the centre of the sorting channel; w_m is the width of the main channel
Figure 3.38 (a)	The initial and applied conditions for the model. (b) The rectangular pulse generated an external velocity v_{mem} = 0.001× $rect1(t)$ [m/s], which is set as a "Normal inflow velocity" condition in the inlet boundary (top surface of the chamber). Because the signal was symmetric about t =2 m s, the fluidic changes at t = 0 m s, t = 1 m s, and t = 2 m s were focused.
Figure 3.39 Nur	merical characterisation of the fluidic velocity field and path of the streamlines originating at the main channel when an external force pulse is applied at different time points: (a) $t = 0$ ms; (b) $t = 1$ ms; (c) $t = 2$ ms
Figure 3.40 Sim	aulations when w_D was set to (a) 50µm (b) 100µm (c) 150µm at $t = 2$ ms. The red arrows indicated the tangential direction of the centre streamline at the middle of the channel, demonstrating the magnitude of the fluid deflection angle within the main channel. For a changing w_D , there is no significant difference on the positional interference concluded by the angular perturbations

Figure 3.41 Sim	ulation after changing w_m from 100 μ m to 40 μ m at (a) t = 0ms; (b) t = 1ms; (c) t =
	2ms. The v_{mem} was too high to achieve successful sorting. The main flow changes
	its direction, as shown by red arrows105
Figure 3.42 Nur	merical characterisation of the fluidic velocity field and path of the streamlines
	originating at the main channel when an external force pulse is applied at
	different time points after decreasing the magnitude of v_{mem} from 0.001 to 0.0002
	m/s at (a) $t = 0$ ms; (b) $t = 1$ ms; (c) $t = 2$ ms
Figure 4.1 Can	ncerous cells have differences in rheological behaviours. Actin stress fibres
	contribute to cell deformability. Cancerous cells have less dense and less
	organised fibres compared with normal cells. Adapt from (Alibert, Goud, and
	Manneville 2017)107
Figure 4.2 Elect	trode configurations and the calculation of the electrical deformability. (a) Two
	configurations of electrodes and deformed cells pass through the channel from
	position ① to ④. The differential current generated from the first set is $\Delta I_1 $, and
	the second set is $\Delta I_2 $. (b) The waveform of the output differential current. The
	final output curret is the sum of $\Delta I_1 $ and $\Delta I_2 $ 108
Figure 4.3 2D si	imulation of the electrode configurations. Applied voltage $V_{\scriptscriptstyle in}$ is 1V at frequency
	500kHz, and the channel dimension is 30μm high and 430μm long. The
	permittivity of the suspension media is $80\varepsilon_{o}$ and the conductivity is 1.6 S/m. The
	particle has a permittivity $2.5\epsilon_{0}$ and conductivity $10^{\text{-}11}\text{S/m}$ with a diameter of
	10μm. Electrical potential and current density streamlines when the particle is
	in configuration (a) 1 and (b) 2109
Figure 4.4 Illust	tration of how a cell is deformed when it flows from pre-detection to detection
	regions of the microchannel. To simplify the diagram, GND electrodes are not
	shown here. The dark blue region in the centre of the channel, corresponding to
	the central region that will be mentioned in section 4.4.2. The focusing plan
	induced by the viscoelastic flow in this case is parallel to the x-y plan and located
	at the centre of the channel height (z-axis)110
Figure 4.5 Syste	em overview. Cells suspended in a viscoelastic fluid are pumped through the
	"detection region" of the channel (40μm×30μm) where they deform and become
	elongated. The electrodes are connected to amplifiers and a lock-in to extract
	the impedance signals. The lock-in also provides a trigger signal. (b) The
	detection region is divided into two parts: the electrical impedance sensing zone
	and the optical image capture zone. The two electrode configurations measure

	ertical ($\Delta I_1 $) and horizontal ($\Delta I_2 $) impedance of the cell. An image is focused a simple CMOS camera with a X20 objective111
(diffe the p peak The p the tr (34µr elect	showing the principle of the triggering mechanism. The impedance rential current) of the first configuration is used to calculate the velocity of article, obtained from the ratio of the distance between the impedance and valley (D_1) and the transit time (Δt_1) obtained from the impedance signal oredicted time to trigger Δt_2 is then calculated with known distance D_2 and rigger pulse generated to drive the LED. The red rectangle defines the ROI in wide, 80µm long) of the optical image capture zone. Only two pairs of rodes in the first configuration are shown in the diagram because the other not used for triggering.
differ Finall	chart of the peak-valley detection algorithm. The data is processed by encing operation twice, and the results of each differencing are binarised. by, the values of 2 or -2 in the results are used to determine the peaks and so of the original signal
flow	of experimental cell position illuminated by the LED at (a) 5 and (b) 10 µL/min rates. Data for 500 cells for each plot. The x-axis labelled "Position" sponds to the x coordinate within the optical window shown in Figure 4.6.
	nart of image processing. (a) – (e) corresponds to the label number of the essed result image at each stage
incre	e (a) and the resulting image (b) after processing by a Gaussian filter and asing contrast. The image is blurrier than the raw image because the filter ved noise and smoothed the edges.
- , ,	in the last stage and the resulting image (c) after being processed by the detection function
Figure 4.12 Example o	of eliminating spur pixels using the morphological operation
morp	c) from Figure 4.11 and the resulting image (d) after applying the hological operation to eliminate spurred pixels
	in Figure 4.13 and its resulting image (e) after extracting the target particle.
scrip	ntour, major axis and minor axis extracted by the MATLAB image processing t. The contour is determined by the edge detection algorithm; major and r axis are determined with the "regionprops" function118

Figure 4.16 Exa	mple of impedance (blue line) coincidence with the corresponding trigger signal
	(brown). The time interval between these two particular events is 1.53 ms 120
Figure 4.17 (a)	The scatter plot of $3\Delta I1 $ versus ED for untreated cells at 5 mL/min before
	calibration. (b) The scatter plot of Electrical Diameter for those cells after
	calibration
Figure 4.18 Sca	tter plot of optical diameter versus OD for untreated cells at 5 µL/min before and
	after calibration. The mean OD of the gated bead before calibration was 1.03 and
	after calibration was 1.0; the mean OD of the gated cell before calibration was
	1.19 and after calibration was 1.15121
Figure 4.19 The	diagram of the barbed end capping mechanism of Cytochalasin D (CytoD) that
	inhibits the polymerisation of F-actin
Figure 4.20 The	microscope images of changes in the organisation of the actin cytoskeleton at
	various concentrations of CytoD. The cells were incubated with 0.1% DMSO (A,
	control), 200pM (B), 900pM (C), 4nM (D), 20nM (E), 90nM (F), 400nM (G) and $2\mu M$
	(H) for 30 minutes. At a CytoD concentration of $2\mu M$, almost all the long actin
	filaments were disrupted and replaced by large focal aggregates of F-actin. Scale
	bar: 50µm. The image is adapted from (Wakatsuki et al. 2001)
Figure 4.21 The	diagram of the capping mechanism of Latrunculin B (LatB) that inhibits G-actin.
	125
Figure 4.22 The	microscope images of changes in the organisation of the actin cytoskeleton at
	various concentrations of LatB. The cells were incubated with 10 nM (A), 40 nM
	(B), 160 nM (C), 630 nM (D), 2 μ M (E), 10 μ M (F) for 30 minutes. At a LatB
	concentration of 2 $\mu\text{M}\textsc{,}$ almost all the long actin filaments were disrupted and
	replaced by large focal aggregates of F-actin. Scale bar: 50µm. The image is
	adapted from (Wakatsuki et al. 2001)
Figure 4.23 Cor	relation between electrical and optical properties of untreated HL60 cells and
	beads at a flow rate of 5 μ L/min. (a) and (b) are scatter plots of Electrical and
	Optical Diameter versus ED and OD, together with histograms of deformability.
	10µm polystyrene beads were used as calibration particles for both size and
	deformability. (c) Scatter plot of electrical diameter versus optical diameter, with
	a fitted straight line y=0.98x, R ² >0.90127
Figure 4.24 Cor	relation of electrical and optical diameter for untreated HL60 cells at (a) 10 µL/min
	and (b) 15µL/min. Data was obtained for the same day as the correlation plot in
	Figure 5.6 (c) but at different flow rates128

Figure 4.25 Co	rrelation between the mean ± SD value of ED vs OD for beads and untreated HL60
	cells at different flow rates (5, 10, and 15 μ L/min) for three repeats
Figure 4.26 Ex	ample images of a single HL60 cell deforming in the channel at a 10 $\mu L/min$ flow
	rate129
Figure 4.27 Co	orrelation between the ED and OD for HL60 cells (Untreated, GA fixed and CytoD
	treated) with 10 μm rigid spherical beads at a 10 $\mu L/min$ flow rate. Data is the
	mean ± SD of three biological repeats (n = 3). The correlation between the two
	methods is given by the solid line ($R^2 = 0.98$)
Figure 4.28 Sc	hematic diagram showing channel cross section and dimensions. The shaded box
	(-6.3μm to +6.3μm) defines the ROI within which cells were measured. Those
	near the walls were discarded131
Figure 4.29 Co	omparison between (a) OD and (b) ED for HL60 cells treated with CytoD and LatB
	demonstrating how cell deformation depends on lateral position in the channel
	at a 10 µL/min flow rate132
Figure 4.30 Im	nages of cells located at different Y-position in the ROI (-17µm to +17µm) and
	different treatments. Cells are treated with 1µM CytoD and 25nM LatB 132
Figure 4.31 Sca	atter plots of ED v.s. OD for (a) untreated HL60 cells and treated with (b) CytoD and
	(c) LatB at a 10 μ L/min flow rate. The results are filtered according to the Y-
	position in the channel to exclude cells close to the channel walls, i.e. outside
	the shaded region in Figure 4.29 133
Figure 4.32 Bo	x charts of (a) ED and (b) OD (n = 3). Data are mean \pm SD. The statistic analysis is
	the student t-test, ** p \leq 0.01, *** p \leq 0.001, compared with the untreated group.
	The flow rate is 10 μ L/min134
Figure 4.33 (a)	The contour plots of ED vs OD for HL60 cells treated with different concentrations
	of GA at a flow rate of 5 µL/min. (b) Dose-response curves of ED and OD for three
	repeated experiments at a flow rate of 5μL/min (n = 3). P- values are relative to
	the unfixed group, where *** p \leqslant 0.001, ** p \leqslant 0.01, * p \leqslant 0.05 and ns is not
	significant135
Figure 4.34 The	e contour plots of ED vs OD for HL60 cells treated with different concentrations of
	GA at flow rates of (a)10 μL/min and (b) 15 μL/min137
Figure 4.35 Do	ose-response curves of ED and OD for three repeated experiments (n = 3) at flow
-	rates (a) 10 and (b) 15 µL/min. P- values are relative to the unfixed group, where
	*** p \leq 0.001, ** p \leq 0.01, * p \leq 0.05 and ns stands for not significant 138

Figure 5.1 (a) II	ne electrode configuration of this single-cell spectroscopy. Cells suspended in the
	saline with different conductivities pass through the channel from position ${\color{black} \textcircled{1}}$ to
	${\it \textcircled{8}}$ (centre position of electrodes) at a flow rate of 30µL/min. AC voltage V, and V.
	have inverted phases and were applied to some electrodes. Their parallel
	electrodes were sensing ones and output the differential current. (b) The ideal
	output waveform for a single event. It is a central symmetric form with peaks and
	valleys that matches the position ${ ext{@}}$ to ${ ext{@}}$ at (a). (c) Convolution template
	generated according to the electrode encoding, channel dimension and the flow
	rate used in the experiments. Fifty normalised templates are multiplied to the
	raw data stream within a fixed size of window and the maximum result is the
	matched impedance of this event
Figure 5.2 Sys	tem conceptional overview and measurement principle. (a) Cells suspended in
	saline flow along the microchannel (40µm×30µm) where electrodes measure
	the impedance at discrete frequencies ranging from 250kHz to 550MHz. After
	Gating and calibration, the frequency spectrum was fitted to the double-shell
	model to give cell diameter d, membrane capacitance ($C_{\it mem}$) and cytoplasm
	conductivity (σ_{cyt}). (b) To simplify the diagram, not all electrodes are shown here.
	The detailed wiring scheme is shown in Figure 5.1 (a) 144
Figure 5.3 (a) <i>A</i>	An example impedance phase scatter plot of beads and cells used in the "gating
	and calibration" step. For the population mean method, this is the plot at
	reference frequency 18MHz; for the single-cell method, this is the plot at around
	7MHz. This plot is used to gate beads and cells. (b)Histogram of gain* $3 Z_{18MHz} $ at
	18MHz. The noise, beads and cells are gated as blue, red and yellow
	subpopulations. The population mean square ratio of noise impedance to the
	particle impedance is SNR146
Figure 5.4 Exar	mple normalised $fCM(cell)$ st spectrum of untreated HL60 cells from two different
	methods: (a) population mean method and (b) single-cell method, in 0.32 S/m
	conductivity saline. Blue circles and lines represent the real part, and red
	represents the imaginary part. For further analysis, see the results in section 5.4.
	147
Figure 5.5 A ge	nerated data set of normalised $fCM(cell)$ st (solid dots) and its fitting curve in 0.32
.6 0 0.0 / 180	S/m conductivity media with the double-shell model at the frequency range of
	100kHz to 1GHz. Blue is for the real part, and red is for the imaginary 149
Figure 5 6 The	procedure of THP-1 differentiation treatment. Three different groups awaiting to
i-iguie 5.6 IIIe	suspend in the measurement media: 1) - THP-1 cells in culture media with

	DMSO; ② - M0 cells differentiated from THP-1 cells treated with PMA in culture
	media; $\ensuremath{\mathfrak{3}}$ - Harvested THP-1 cells treated with TrypLE than moved in culture
	media
Figure 5.7 Image	es of THP-1 and M0 cells at 48h in the culture media before harvesting. THP-1 cells
	have regular round shapes and float in the flask, while M0 cells attach to the flask
	bottom and have a spreading morphology153
Figure 5.8 Plots	of the normalised Clausius Mossotti factor (real and imaginary parts) for HL60
	cells in control (solid lines with dots) and fixed group (dashed lines with unfilled
	circles) suspending in (a) high conductivity saline: 1.6 S/m with 5mm diameter
	beads and (b) low conductivity saline: 0.32 S/m with 7 mm diameter beads. 154
Figure 5.9 The c	lose-response plot of CytoD-treated HL60 cells for opacity. Adapted from (Chen
	et al. 2024)
Figure 5.10 Scat	tter plot of electrical diameter ($gain*3 Z150kHz $) versus opacity ($ Z_{3MHz} / Z_{150kHz} $)
	for untreated and CytoD-exposed HL60 cells measured in 0.32 S/m saline. Data
	were repeated three times. The means of the populations show that the opacity
	had a slight change
Figure 5.11 Erro	or bar chart of opacity for untreated and CytoD-treated cells (n=3). Data was
	statistically analysed by students' t-test (*, p \leq 0.05)157
Figure 5.12 (a)	Normalised Clausius Mossotti factor spectra (real and imaginary parts) for
	untreated (solid lines with dots) and CytoD-treated group of HL60 cells (dashed
	lines with unfilled circles) suspending in 0.32 S/m conductivity saline. (b) Mean ${\bf m}$
	and S.D. of $C_{\mbox{\scriptsize mem}}$ for untreated and CytoD-treated cells demonstrated a
	significant change (***, p < 0.005)
Figure 5.13 Sca	tter plot of electrical diameter versus phase at different frequencies (left column:
	760kHz; right column: 575MHz) for mixture samples (50%/50% normal and fixed
	cells) suspended in different conductivity media (top row: 0.32 S/m; bottom row:
	1.6 S/m). The subpopulations of the mixture can be discriminated in low-
	conductivity saline at very low frequency (750kHz) but are difficult to distinct in
	high-conductivity saline even at high frequencies (575MHz)159
Figure 5.14 Ex	amples of normalised $f\mathcal{C}M(cell)*$ (blue: real part, red: imaginary part) for
	untreated (solid lines with dots) and fixed cells (dashed lines with unfilled circles)
	measured in saline of conductivity (a) 0.32 S/m and (b) 1.6 S/m, respectively.

Figure 5.15 Sin	gle-cell fitting results in physiological saline. (a) Scatter plot (d vs C_{mem}) for 1000
	individual untreated (blue) and fixed (red) HL60 cells. (b) Histogram of $\sigma_{\text{cyt}}.$ Mean
	± SD are summarised in Table 5.6. 161
Figure 5.16 Sing	gle-cell fitting results in 0.32 S/m conductivity saline. (a) Scatter plot (d vs $C_{\mbox{\scriptsize mem}}$) for
	1000 individual untreated (blue) and fixed (red) HL60 cells. (b) Histogram of $\sigma_{\text{cyt}}.$
	Mean ± SD are summarised in Table 5.6. 161
Figure 5.17 An i	mage of M0 cells in the culture media at 24h before harvesting. Cells adhere to the
	bottom without many protrusions around the membrane 162
Figure 5.18 The	mean value of single-cell normalised $fCM(cell)*$ for three different groups in (a)
	real part and (b) imaginary part after 24h treatment. The three groups are nearly
	overlapped163
Figure 5.19 The	mean value of single-cell normalised $fCM(cell)*$ for three different groups in (a)
	real part and (b) imaginary part after 48h treatment. THP-1 and THP-1 + TrypLE
	groups overlap but data of M0 cells are significantly different from them 163
Figure 5.20 (a)	and (b) are images of cells dyed with Trypan blue after harvesting from the plates
	and ready to be measured. The average diameter (mean±SD) of 30 THP-1 cells is
	14.3±1.4mm and 18.0±2.9mm for 30 M0 cells
Figure 5.21 Sing	gle-cell fitting results of THP-1 cells differentiated into macrophages (M0) following
	48h exposure to PMA in low conductivity saline (0.32 S/m). (a) Scatter plots (d vs
	C_{mem}) of 1,000 individual THP-1 cells (blue) and M0 cells (red). (b) Histogram of
	σ_{cyt} for two different cell subpopulations
Figure 5.22 Sta	tistical analysis of d, C_{mem} and σ_{cyt} for three repeat experiments with student's t-
	test (*, p≤0.05; **, p≤0.01; ns, not significant)
Figure 6.1 2D s	imulation of the electrode configuration introduced in Chapter 4 . Applied voltage
	$V_{\it in}$ is 1V at frequency 500kHz, and the channel dimension is 30 μ m high and
	430µm long. The permittivity of the suspension media is $80\epsilon_{0}$ and the
	conductivity is 1.6 S/m. The particle has a permittivity 2.5 ϵ_{0} and conductivity 10 $^{\text{-}}$
	$^{11}\mbox{S/m}$ with a diameter of 10 $\mu\mbox{m}$. (a) Electrical potential and current density
	streamlines when the particle is in configuration 1 and 2. (b) Output differential
	current plotted as a function of the particle position when it moves from x=11 to
	x=421. Only the real part of the current is presented because at low frequency
	the imaginary part is extremely small. ΔI_1 and ΔI_2 are the current of configuration
	1 and configuration 2

Figure 6.2 2D C	OMSOL simulation of the optimised electrode configuration used in this chapter.
	(a) Electrical potential and current density streamlines when the particle is
	placed in the configuration 1 and 2. (b) The output differential current plotted as
	a function of the particle position when it flows from $x=11$ to $x=461$. Only the real
	part of the current is plotted because at low frequency the imaginary part is
	extremely small. ΔI_1 and ΔI_2 are the current of configuration 1 and configuration
	2. The figure shows that the offset is close to zero
Figure 6.3 Sche	matic illustration of the sorting system. (a) Pressure pump regulates the pressure
	of the inlet $\ensuremath{\mathfrak{B}}$ and two outlets, $\ensuremath{\mathfrak{D}}$ and $\ensuremath{\mathfrak{A}}$, directing particles toward outlet $\ensuremath{\mathfrak{A}}$
	during the "Ready to activate" state. The impedance signals from the detection
	region are collected by the lock-in amplifier and sent to the MCU to be processed
	in real-time. MCU generated trigger signals drive a pulsed voltage circuit, which
	is subsequently amplified by a voltage amplifier (gain factor = 15) to meet the
	operational requirements of the piezo actuator. The customised optical pathway
	of fluorescence detection consists of an LED that generates excitation light, a
	dichroic mirror for spectral separation, an objective, and a camera to capture the
	emission images at 250 fps. (b) Illustration of the sorting chip. The membrane-
	pump sorter is downstream of the impedance detection region (40μm×30μm) on
	the chip. Grounded electrodes are omitted. The piezo actuator is controlled by
	the impedance measurement, it provides an external force to deflect the
	membrane170
Figure 6.4 Imp	pedance signals from 6µm and 10 µm beads. (a) Impedance signals (blue)
	transmitted from the lock-in auxiliary output port to the MCU and the threshold
	(orange) for triggering. (b) Synchronised impedance-pulse (blue-green)
	correlation depicting two operational scenarios:
Figure 6.5 Deta	ailed plots of impedance-pulse signals in two different scenarios mentioned in
	Figure 6.4(b). (a) Scenarios $\textcircled{1}$ and (b) Scenarios $\textcircled{2}$. The time interval between
	the impedance and trigger pulse is denoted " $\tau_{\it d}$ " which includes the calculated
	particle transit time and an offset to compensate for the program execution
	delay172
Figure 6.6 (a) Pr	rogram execution timeline before optimisation. The program has one thread, and
	the order of execution is ADC, peak detection, $ au_d$ generation and finally digital
	pulse output. These processes are in serial. (b) Optimised program execution
	timeline. There are three parallel threads: Processing thread, Trigger thread $\ensuremath{\mathfrak{I}}$
	and Trigger thread ②. The processing thread achieves ADC, peak detection and
	generating τ_d . An event counter is used in this thread to index the impedance

signal. Trigger thread ${\color{black} \textcircled{1}}$ and ${\color{black} \textcircled{2}}$ monitor the parity of parameter "count" and

	output of τ_d . Once the generated τ_d is detected by the trigger thread, and the
	parameter count is an odd number, trigger thread ① produces a digital pulse.
	Conversely, trigger thread ② produces the pulse when parameter count is an
	even number173
Figure 6.7 Custo	om circuit for generating driving pulses. 3.3V DC voltage from the MCU is amplified
	via an operational amplifier (op-amp), with gain adjustable by potentiometer
	resistance (R_f =250 Ω). The digitalised MCU output pulses control the
	electromagnetic switch of the reed relay, generating rectangular waveforms with
	desired triggering patterns. Finally, the output pulse is sent to a commercial
	amplifier with a gain of 15. R_1 = 100 Ω , R_2 = 22k Ω
Figure 6.8 Gene	erated pulse before being amplified by the power amplifier. (a) An impedance
	signal (blue) and its synchronised trigger pulse (brown). (b) Details for the
	triggering signal. During low-level MCU digital signals ($t < 5.41185$ s), the reed
	relay maintains an open (Voltage = 0V) state. Upon transitioning to a high-level
	signal, magnetically induced current activates the reed relay, resulting in switch
	closure to conduct the output amplified voltage from operational amplifier. The
	level transition demonstrates a 10 μ s switching delay (from t = 5.41185 to t =
	5.41186 s)
Figure 6.9 Piezo	o actuator assembly integrated into the impedance cytometry system. (a) CAD
	model of the system. The microfluidic impedance chip (omitted) is placed in the
	plastic holder and mechanically secured via a metal cover to maintain leak-free
	fluidic connections. The top and bottom PCB boards are fixed to the holder to
	ensure electrical continuity. The piezo actuator assembly is integrated on the
	metal cover and aligned precisely with the membrane pump of the impedance
	chip by using locating holes. (b) Photograph of the sorting system
Figure 6.10 (a)	CAD module of the holder. The centre rectangular slot is used to place the
	impedance chip and enable fluidic connections. (b) PCB geometry design. The
	spring connector on it is to connect the electrode pads of the impedance chip
	and send the signal to the lock-in amplifier via the PCB circuit
Figure 6.11 (a) I	Detailed illustration of metal cover. Two rods are used as alignment guides and
	secure the piezo actuator assembly while maintaining precise vertical
	positioning of the actuator cap over the membrane pump. M3 screws
	mechanically couple the cover to the holder; M2 screws rigidly fix the actuator
	assembly. (b) Detailed illustration of piezo actuator assembly. It comprises a
	brass holder with a precision-machined slot for actuator housing. On top of the

holder, there is a threaded hole for the spring screw to fix the actuator. The spring

	screw provides a preload for the actuator and the spring inside eliminates		
	damping. Between the actuator and the spring screw, a small piece of foam is		
	added as a buffer, preventing surface damage to the actuator caused by the		
	spring screw. The cap is fitted to the hemispherical end and its flat underside is		
	glued to a ball bearing (not shown) that touches the surface of the chip 177		
Figure 6.12 The design of the sorting chip without electrodes. (a) The features in pink define the			
	fluidic layer. Dimensions of the sorter: radius of the chamber a_{pump} = 1mm, main		
	channel width w_{m} = 100 μ m, sorting channel width w_{L} = 50 μ m, distance between		
	the centre of the sorting channel and the outlet junction is w_D = 280 μ m. These		
	dimensions are the same as used for the simulation in section 3.6, with the		
	exception of $w_{\scriptscriptstyle D}$, which has no effect on sorting performance. The serpentine		
	$microchannels\ provide\ sufficient\ flow\ resistance,\ preventing\ local\ flowback.\ (b)$		
	Wafer layout		
Figure 6.13 Phot	tograph of the chips. There are two different designs, (a) one has dual membrane		
	pumps and (b) the other one has single membrane pump 179		
Figure 6.14 The frames of bead movement using a single-pump prototype sorting chip.			
	Specific frames of the bead position. The blue line in (d) is the trace of the bead $$		
	from t = 0.542 s and t = 0.576 s. It is clear to see that after a subtle deflection, the		
	beads returned to its original path when using the single-pump chip 179		
Figure 6.15 (a) M	lask design of the final version of the chips. This version integrated the electrodes		
	(purple region). The features in pink are fluidic regions. (b) There are two different		
	designs with the main channel width w_{m} = 100 μ m (wide channel) and w_{m} = 40 μ m		
	(narrow channel). The distance between the centre of the sorting channel and $% \left(1\right) =\left(1\right) \left(1$		
	the outlet junction w_{D} was shorten to 80 μm because the simulation in Chapter		
	${f 3}$ shows w_{D} has no significant influence on the sorting performance. (c) The		
	electrode array consists of 10 electrodes $30\mu m$ in width and $10\mu m$ gap 180		
Figure 6.16 (a)	Schematic of the MIC sorting chips with internal microchannel networks and		
	electrode arrays omitted. Two holes are drilled in the pump chamber with a laser $$		
	cutter. A 170 μm thick cover slip was bonded to the glass sealing the holes and		
	producing the deformable membrane. The inlet/outlet ports and local flow port		
	are drilled on the reverse surface of the chip. (b) Image of a chip181		
Figure 6.17 The flow chart of post-processing chips after fabrication in the cleanrooms. Details			
	are described in the text		

Figure 6.18 Def	inition of the efficiency and purity used to evaluate the system performance. E is	
	the efficiency; P_{pre} and P_{pos} are pre-sorting and post-sorting purity. N_{pre6} and N_{pre10}	
	are the numbers of 6 μ m and 10 μ m beads before sorting, respectively. N_{u6} and	
	N_{u10} are 6 μ m and 10 μ m beads directed to the upper outlet; N_{l6} and N_{l10} are 6 μ m	
	and 10µm beads directed to the lower outlet184	
Figure 6.19 Wid	e channel purity for two different N_{pre10} to N_{pre6} ratios with different pulse widths of	
	actuator driving signal. The purity increased from around 60% (N_{pre10} : N_{pre6} = 3:2)	
	and 40% (N_{pre10} : N_{pre6} =2:3) to approximate 97%. Data are summarised in Table	
	6.1.	
Figure 6.20 So	rting efficiency ($E = N_{l10}/N_{pre10}$) of the 10µm beads under different conditions	
	including two distinct N_{pre10} to N_{pre6} ratios (3:2 and 2:3) and different pulse width.	
	It was achieved above 70% by using 1.5 ms and 2 ms pulse width, while under	
	the 1 ms pulse width condition, the sorting efficiency showed a significant drop,	
	falling below 50%. The data is summarised in Table 6.2.	
Figure 6.21 Nar	row channel purity when N_{pre10} to N_{pre6} ratio was 2:3 with the pulse widths of the	
	actuator driving signal 2 ms. The values are summarised in Table 6.3 187	
Figure 6.22 Exa	mple images of a sorting a 10 μ m bead towards the lower outlet. At t = 32 ms, a	
	$6\mu m$ bead entered the channel without being sorted. The system applied the 2ms	
	pulse width driving voltage188	
Figure 6.23 Sigr	nal output from the MCU serial port after the raw impedance signal was filtered by	
	a custom FIR for (a) 10 μ m bead, (b) untreated HL60 cell, (c) fixed HL60 cell. Each	
	signal has two peaks, from electrode configuration 1 and 2. The peak detection	
	results from the MCU were: (a) pk1 is 0.55, pk2 is 0.35, real-time ED is 1.59; (b)	
	pk1 is 0.46, pk2 is 0.19, real-time ED is 2.37; (c) pk1 is 0.54, pk2 is 0.34, real-time	
	ED is 1.61	
Figure 6.24 Rea	l-time ED evaluation of beads used to set a threshold for sorting. (a) Scatter plot	
	of pk1 versus Real-time ED. Cells in the red circle were gated (614 beads) to do	
	further analysis. (b) The Real-time ED distribution of gated beads. Threshold	
	(dashed red line) is the mean Real-time ED value of the gated beads (1.68), with	
	78% of beads exhibiting a lower Real-time ED than 1.68	
Figure 6.25 Scatter plot of pk1 versus Real-time ED for untreated cells (orange dots). The bea		
	population (dark blue dots) in Figure 6.21(a) overlaps. The red line is the	
	threshold obtained from the beads assessment in Figure 6.21	

Figure 6.26 Scatter plot of pk1 versus Real-time ED for fixed cells (pink dots). The untreated ce		
	population (orange dots) in Figure 6.23(a) overlaps. The red line is the threshold	
	obtained from the beads assessment in Figure 6.22. 191	
Figure 6.27 The	e distribution of Real-time ED for gated fixed cells shown in Figure 6.26. The	
	discrimination criterion was set to "Real-time ED that below threshold". 58% of	
	fixed cells were identified by this condition191	
Figure 6.28 Images of an example bead in "Ready to activate" state. The bead is circled with the		
	red dashed lines and directed to the upper outlet	
Figure 6.29 Beads in "Activated" state. (a) and (b) are two example beads with different velocities.		
	At $t = 0$ ms, beads were approaching the sorting ROI and successfully being	
	sorted at $t = 4$ ms and 6 ms respectively	
Figure 6.30 Images of an example sorting scenario that an untreated live cell (circled with dashed		
	$red\ line)\ is\ directed\ toward\ the\ upper\ outlet\ with\ high\ velocity,\ and\ a\ subsequent$	
	fixed cell (circled with solid red line) is sorted to the lower outlet. The cells are	
	successfully sorted based in deformability194	
Figure 6.31 Results of commercial flow cytometer test. (a) The Forward scatter (FSC) in BL1-A		
	channel of the fixed cells sample. The single population represented fixed cells.	
	(b) The FSC in BL1-A channel of the untreated and fixed cell mixture before	
	sorting. The circled subpopulation is fixed cells by comparing with (a). The	
	percentage of this population is 32.6%. (c) The FSC in BL1-A channel of the upper	
	outlet suspension after sorting. The percentage of fixed cells is decreased to	
	25.4%	

Research Thesis: Declaration of Authorship

Research Thesis: Declaration of Authorship

Print name: Xueping Zou

Title of thesis: Single-cell Impedance Analysis and Sorting

I declare that this thesis and the work presented in it are my own and have been generated by me

as the result of my own original research.

I confirm that:

1. This work was done wholly or mainly while in candidature for a research degree at this

University;

2. Where any part of this thesis has previously been submitted for a degree or any other

qualification at this University or any other institution, this has been clearly stated;

3. Where I have consulted the published work of others, this is always clearly attributed;

4. Where I have quoted from the work of others, the source is always given. With the exception

of such quotations, this thesis is entirely my own work;

5. I have acknowledged all main sources of help;

6. Where the thesis is based on work done by myself jointly with others, I have made clear

exactly what was done by others and what I have contributed myself;

7. Parts of this work have been published as:

(1) A combined electro-optical deformability micro-cytometer. Xueping Zou, Daniel

Spencer, Junyu Chen and Hywel Morgan, 2024, RSC advances, 14, 34270.

(2) Single-cell electro-mechanical shear flow deformability cytometry. Junyu Chen,

Xueping Zou, Daniel Spencer and Hywel Morgan, 2024, Microsystems & Nanoengineering,

10(1), 173.

(3) Single-cell Impedance spectroscopy of nucleated cells. Xueping Zou, Daniel Spencer

and Hywel Morgan, 2025, Lab on a Chip, 25(12), 2939

Signature:

Date: 02/04/2025

33

Acknowledgements

I would like to express my gratitude to my supervisor, Professor Hywel Morgan, for his invaluable guidance and support over the past four years. When I was interviewed four years ago, I still had a bit of uncertainty about whether I could complete my doctoral studies. It was he who encouraged me that as long as I didn't give up on learning, all of this could be overcome. I must also thank Dr. Daniel Spencer, my second supervisor. His ingenious insights always amaze me and have helped me resolve many technical issues in my experiments. They took the time to meet with me regularly every week to discuss experimental results and refine the experimental plan. It was this rigorous training that enabled me to complete my studies on time.

I am also deeply grateful for the members of the Center for Hybrid Biodevices (CHB), from Katie Chamberlin, who fabricated chips for my experiments, to colleagues who provided technical guidance, including Dr. Jonathan Butement, Dr. Fernando Garcia Garcia, Dr. Raul Feranadez-Mateo, Dr. Junyu Chen, Dr. Max Saito, and Dr. Xiang Wang. I would also like to thank Anika Assaraf for coordinating the use of Lab 4 with me, as well as Daniel Cancado and Yachong Deng for sharing the daily joys and challenges of our experiments. I would also like to thank the technicians in the ECS mechanical workshop for fabricating the mechanical components needed for my experiments. Obviously, this list does not include all the names of those who have helped me over the past four years in Southampton.

On a personal note, I extend my deepest gratitude to my family and friends in China. Their unwavering care and encouragement have been the bedrock that sustained me through countless challenging and stressful days, providing me with steadfast support throughout this journey.

Last but not least, I would like to thank myself - for standing by the choice I made four years ago, for staying resilient through the tough times, and for embracing this deeply rewarding journey. Perhaps, having completed my PhD, I will now face future difficulties with greater courage and a more rational approach to solving problems, both of which are invaluable assets in my life.

List of Symbols

τ	relaxation time constant
<i>Z</i> *	complex impedance
$oldsymbol{arepsilon}^*$	complex permittivity
$arepsilon_{mix}^*$	complex permittivity of a particle suspension
f_{CM}^*	Claisous-Mossotti facor
$arepsilon_{med}^*$	complex permittivity of media
$arphi_{cell}$	volume fraction
$arepsilon_{cell}^*$	complex permittivity of a cell
$arepsilon_i^*$	complex permittivity of the interior, 1: cell membrane,
	2:cytoplasm, 3: nuclear envelope, 4: nucleoplasm
$\boldsymbol{arepsilon}_i$	permittivity of the interior
σ_i	conductivity of the interior
d_1	cell membrane thickness
d ₃	nuclear envelope thickness
r_{cell}	cell radius
R_b	nucleus radius
d	cell diameter
$C_{\it mem}$	cell membrane capacitance
σ_{cyt}	cytoplasm conductivity
G	Young's modulus
$ec{v}$	velocity of the fluid
ρ	fluid density
p	pressure
η	dynamic viscosity
$ec{f}$	applied force
Re	Reynolds number
F_{wl}	wall interaction force

List of Symbols

 F_{SG} shear gradient lift force

 F_{CL} cross-lateral force

 F_E elastic force

 F_L inertial force

 F_W wall repulsion

P₁, P_{inlet} inlet pressure

 P_2 , P_{o1} upper outlet pressure

 P_3 , P_{o2} lower outlet pressure

D membrane deflection

E elastic modulus

u Poisson's ratio

h thickness of the membrane

F point force

w(r) blister deflection, r is the distance from the point on the

membrane to the central point

 w_0 central deflection

N average stress

 N_r radial stress

 N_t tangential stress

a radius of the membrane

 C_{ν} volume change of local-flow

 w_L width of the sorting channel

 w_D distance between the outlet junction and the centre of the sorting

channel

 w_m main channel width

 a_{pump} membrane pump radius

 V_{mem} membrane velocity profile

 $\Delta |I_1|$ differential current of configuration 1

 $\Delta |I_2|$ differential current of configuration 2

List of Symbols

 F_d sampled data stream Z_{mix}^* impedance of a mixture V, V_{in} applied voltage complex system transfer function, ω angular frequency $S^*(\omega)$ constant depending on the electrode and gap dimensions κ Δi_{cell}^* differential complex current of the cell Δi_{bead}^* differential complex current of the bead vector of initial values for model fitting X_0 $[\mathbf{b}_{l} \, \mathbf{b}_{u}]$ set range for model fitting $\{r_i^*\}$ residual set, difference between measured and fitted bootstrap dataset $(f_{CM}^*)_{i(bootstrap)}$ time delay between a matched impedance-pulse signal τ_d P_{pre} pre-sorting purity P_{pos} post-sorting purity numbers of 6µm beads before sorting N_{pre6} numbers of 10µm beads before sorting N_{pre10} N_{u6} numbers of 6µm beads directed to the upper outlet N_{u10} numbers of 10µm beads directed to the upper outlet numbers of 6µm beads directed to the lower outlet N_{l6} numbers of 10µm beads directed to the lower outlet N_{l10} Ε sorting efficiency

the first peak of real-time ED

the second peak of real-time ED

pk1

pk2

List of Abbreviations

AFM Atomic force microscopy

ADC Analogue-to-Digital Converter

AC Alternating Current

cDC Constriction-based deformability cytometry

CytoD Cytochalasin D

CTCs Circulating Tumour Cells

CAR-T Chimeric Antigen Receptors-T cells

CAD Computer Aided Design

CMOS Complementary Metal Oxide Semiconductor

CI Confidence Interval

DMSO Dimethylsulfoxide

DPBS Dulbecco's Phosphate Buffered Saline

DEP Dielectrophoresis

DC Deformability Cytometry

EC₅₀ Half maximal effective concentration

EIS Electrical Impedance Spectroscopy

ED Electrical Deformability

FACS Fluorescence-Activated Cell Sorting

FEM Finite Element Method

FSC Forward Scatter

FIR Finite Impulse Response filter

GA Glutaraldehyde

LatB Latrunculin B

MIC Microfluidic Impedance Cytometry

MC Methylcellulose

MCU Microcontroller Unit

List of Abbreviations

OD Optical Deformability

PoC Point of Care

PEO Polyetheme oxide

PCB Printed Circuit Board

PMA Phorbol 12-myristate 13-acetate

PVP Polyvinylpyrrolidone

RBCs Red Blood Cells

RT-DC Real-time Deformability Cytometry

ROT Electrorotation

ROI Region of Interest

SMR Suspended Microchannel Resonator

sDC Shear flow Deformability Cytometry

SNR Signal-Noise-Ratio

SD Standard Derivation

xDC extensional flow Deformability Cytometry

Chapter 1 Introduction

1.1 Background

Point-of-care (PoC) testing plays an important role in medicine and health care. Microfluidic PoC platforms, in particular, provide opportunities for the rapid detection of disease at low cost, and are portable devices for home use, increasing the efficiency of real-time monitoring and diagnosis. For example, PoC analysis of cells can be used to diagnose infectious diseases, cardiovascular diseases, tumours (cancer) and chronic diseases. The advantages of microfluidic PoC devices originate from the label-free technique, where biophysical properties can serve as ideal choices for label-free cell analysis and sorting.

Cellular systems have a wide degree of heterogeneity, and intrinsic biophysical markers of cells can be used to distinguish type, state and even function. Bio-mechanical and bio-electrical properties of cells are linked to disease presentation, progression, and treatment response. For example, the differentiation potential of mesenchymal stromal/stem cells is strongly dependent reflected in their elastic and viscoelastic properties (Lin et al. 2017; González-Cruz, Fonseca, and Darling 2012), and the cytoplasm conductivity and membrane permittivity of red blood cells can be used to diagnose *Plasmodium* infection (Zhu et al. 2021). Thus, there is an interest in identifying and sorting specific cells based on biophysical properties from heterogeneous populations for emerging PoC applications.

1.2 Current Challenges and Motivation

Quantifying cell phenotypic heterogeneity based on biophysical properties, including dielectric and mechanical characteristics, is used to investigate cellular physiological responses to the cell environments and can be used to identify functionally distinct cells in a label-free way. Early studies (Gawad, Schild, and Renaud 2001; Lekka et al. 2005; Dulińska et al. 2006) demonstrate how techniques, such as atomic force microscopy and impedance spectroscopy, can measure cell biophysical properties, but these methods are either low throughput or only measure population average, which is time-consuming, inefficient and cannot unravel the unique properties of rare cells, such as early-stage embryos or circulating tumour cells (CTCs) (Fuchs et al. 2021; Kong et al. 2020). Thus, single-cell biophysical analysis and sorting are urgently needed because they can enhance measurement accuracy, thereby emphasising the heterogeneity of individual cells which is overlooked by population mean analysis.

Current single-cell label-free microfluidic cytometry measures the biophysical properties using complicated systems and operations. For example, the popular microfluidic cytometry to

measure the single-cell deformability couple with a massive optical image system because the deformability is derived from the area and perimeter of each cell (Otto et al. 2015; Urbanska et al. 2020). A huge amount of image data is usually to be processed which is a time-consuming work. The example on dielectric measurement is the single-cell electrorotation microfluidic devices (Kawai et al. 2020; Keim et al. 2019). These devices need to control cells movement in the channel, which requires skilled operators. These drawbacks hindered their development into clinical rapid diagnosis devices for PoC. Microfluidic impedance cytometry (MIC) provides an alternative method for analysing biophysical parameters in a rapid, easy to operate and time-saving way because the electrodes for detection are integrated inside the microchannel, no other complicated peripheral is required. Also, the data processing for impedance is much quicker than other data types, such as images. However, the mechanical and dielectric analysis by the MIC system still has some unexplored areas, such as how the deformability measured from the impedance method is correlated with the results from the optical method? Can the impedance spectroscopy based on MIC be improved with a broader frequency range than current studies when obtaining the spectra? These are the main points for single-cell impedance analysis shown in this thesis.

Single-cell impedance sorting retains the advantages of the previously mentioned MIC analysis system while also enabling subsequent molecular-level analysis of cells from the same subpopulation, such as DNA expression. Microfluidic techniques are being developed for cell sorting because of low contamination risk, ease of operation and low sample volume requirement. The sorting method can be categorised into passive and active. Passive sorting does not use an external force field. It relies on fluidic properties and channel geometry and examples include inertial sorting (Yang et al. 2011), deterministic lateral displacement (Xavier et al. 2019; Xavier et al. 2016) or simple microfiltration. These sorting methods are generally based on cell size. Active sorting with external fields can deflect target cells to specific outlets. These active sorters can combine electrophoresis (An et al. 2009; Thomas et al. 2019; Hattori and Yasuda 2010), fluorescence (Li et al. 2019) and optical images (Isozaki et al. 2019) to determine single-cell phenotype isolate specific cells. Fluorescence-activated cell sorting (FACS) and magnetically activated cell sorting (MACS) have been widely used. However, they require molecular labels which can alter cell states and affect their viability. Optical image analysis usually requires highspeed cameras to collect many images. Microfluidic label-free cell sorting systems have many advantages compared with these methods including non-invasive detection and maintaining cell viability for further analysis. These points are important for rare cells, as obtaining enough number of cells for measurements requires a large sample volume. As a label-free method, MIC is of interest to employ a single-cell sorting system based on biophysical analysis.

1.3 Objective

The main objective of this project is to establish new approaches for measuring both cellular mechanical and dielectric parameters based on the MIC technique while integrating a novel real-time single-cell sorting method according to their electro-mechanical phenotype. The specific objectives are as follows:

- 1. To establish an electro-optical deformability MIC system:
 - Utilise MIC to measure the mechanical deformability of HL60 cells subjected to chemical treatments that modify cell stiffness.
 - Simultaneously capture optical images of cell deformation under flow to correlate optical and electrical deformability.
 - Validate the accuracy of impedance-based deformability measurements by comparing them to optical deformation metrics.
 - Provide a foundation for developing future rapid PoC devices for cancerous cell identification.
- 2. Extend MIC for single-cell dielectric spectroscopy:
 - Perform high-frequency impedance measurements up to hundreds of MHz to enable comprehensive dielectric characterisation of single, nucleated cells.
 - Fit measured spectra to the double-shell model, extracting subcellular dielectric parameters (e.g., membrane and cytoplasmic properties).
 - Improve system sensitivity and data processing algorithms to allow detection of subtle dielectric parameter shifts following chemical treatments (e.g., glutaraldehyde and cytochalasin D).
 - Explore the potential applications of this method for disease diagnostics and drug screening based on dielectric profiling.
- 3. Develop and integrate an active single-cell sorting strategy:
 - Implement a chip-integrated active sorting mechanism using an external actuator,
 which redirects selected cells toward a target outlet by altering flow paths.
 - Evaluate the efficiency and purity of the sorting performance using polystyrene beads and treated cell models.
 - Demonstrate the integration of the active sorter into MIC chips with acceptable throughput and reliability.
 - Enable real-time identification and enrichment of rare cells from mixture samples, supporting future PoC diagnostic applications.

By achieving the above objectives, this project aims to enhance the capability of MIC-based systems for label-free, real-time single-cell analysis and sorting, bridging the gap between impedance-based cell phenotyping and clinical applicability.

1.4 Thesis outline

The thesis is organised as follows:

Chapter 2 Literature review. Summarises methods for analysing the mechanical and electrical properties of single cells, mainly focusing on microfluidic cytometry. It also describes recent microfluidic cell sorting techniques.

Chapter 3 Theory and simulations. It introduces the electrical theory and the shell model. Single-cell mechanics are covered together with the principles of microfluidics. Finally, this chapter outlines the working principle of the sorter together with simulations.

Chapter 4 describes the electro-optical deformability system, which correlates electrical and optical deformability. This sheath-less system uses a viscoelastic flow to induce cell deformation. A triggering algorithm is used to switch on an LED depending on the velocity of individual cells.

Chapter 5 presents experimental results of single-cell impedance for nucleated cells. The spectra of single cells are measured up to 550MHz, and the dielectric properties of cells are derived from the spectrum fitting. It is shown that suspending cells in a low-conductivity medium can enhance the discrimination of different cells and cell treatment.

Chapter 6 describes the design and experimental verification of the sorting system. An impedance measurement system provides signals that control a downstream sorter. The system was validated using fluorescence bead mixtures of fixed and normal cells.

Chapter 7 summarises the thesis with perspectives for future work.

Chapter 2 Literature Review

2.1 Introduction

This thesis focuses on the application of microfluidic impedance cytometry (MIC) for biomechanical and bio-electrical label-free analysis of cells together, with the implementation of single-cell sorting based on MIC.

The operational principle of MIC is based on measuring the electrical impedance of cells that pass along a microchannel with integrated electrodes. Low-frequency measurements characterise the geometric properties of cells, such as size, volume and even mechanical properties like deformability, while high-frequency measurements probe the intrinsic dielectric properties of cells, including membrane capacitance and cytoplasm conductivity. This chapter gives an overview of existing methods for measuring cell properties and microfluidic cell sorting. Key performance indicators such as single-cell resolution and non-invasive operation with high throughput are discussed.

2.2 Single-cell Biophysical Properties and Measurements

A cell is the basic unit of life and varies in size across organisms (**Figure 2.1**), with a typical size of a mammalian cell around $5\sim30~\mu m$.

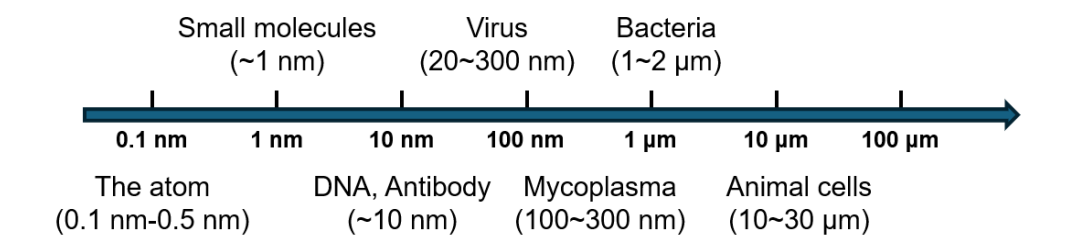


Figure 2.1 Size and dimensions of biological particles, ranging from small molecules to large mammalian cells.

At the sub-microscopic structural level, eukaryotic cells can be categorised into three principal components: the plasma membrane (cell membrane), cytoplasm and nucleus. The plasma membrane coordinates transmembrane transport of biomolecules and mediates signal transduction through integrated receptors; the cytoplasm houses a dynamic array of membrane-bound organelles (e.g. endoplasmic reticulum, Golgi apparatus) that execute biosynthetic and metabolic processes; the nucleus is a double-membrane enclosed compartment specialising in the regulation of genetic information flow, including DNA replication, transcription and RNA processing/export. Cellular heterogeneity is through the stochastic expression of genes, proteins,

and metabolites, exhibiting intercellular variations in structural organisation, biochemical composition and functional capacities (Ren et al. 2019; Bao et al. 2011; Zhou et al. 2017).

2.2.1 Mechanical properties and characteristics

Cell mechanical parameters are important in understanding the biophysics of cells (Azubuike and Tanner 2023; Nyberg et al. 2016). In the cytoplasm, there exists a cytoskeletal system, assembled from a series of proteins which serves as a scaffold for maintaining cell morphology and the organisation of internal structures. In a microenvironment, cells have viscoelastic mechanical properties, including stiffness, adhesion, and viscosity. These properties are closely linked to the fundamental structure and function of cells (Hao et al. 2020; Maremonti et al. 2022; Belotti et al. 2019). Emerging biomechanical evidence has established that the cytoskeleton, particularly the cortical actin meshwork, plays a crucial role in defining cell stiffness. Its disassembly leads to cell fluidisation, while its stabilisation or enhanced assembly increases cell rigidity (Galie, Georges, and Janmey 2022; Luna and Hitt 1992; Nematbakhsh and Lim 2015). Cell stiffness has attracted significant attention from researchers and interconnects to many physiological processes, including the cell cycle (Gupta and Chaudhuri 2022; Gerum et al. 2022), cancer immune cell activation (Suresh 2007; Tse et al. 2013; Gossett et al. 2012; Zak et al. 2021; Bufi et al. 2015) and stem cell differentiation (Gossett et al. 2012; Sliogeryte et al. 2014). Observing irregular alteration in cell deformability can help uncover the underlying mechanism of various diseases, including atherosclerosis, fibrosis, cardiac hypertrophy, muscular dystrophy and others (Panciera et al. 2017; Li et al. 2024).

Conventional single-cell deformability measurements include atomic force microscopy (AFM) (Radmacher 2007; Shan and Wang 2015), optical tweezers (Guck et al. 2001), micropipette aspiration (Hochmuth 2000) and acoustic scatter (Kang et al. 2019). These methods enable precise quantification of a few individual cells.

Atomic force microscopy (AFM) quantifies cell membrane deformability via a cantilever scanning probe (Matthews et al. 2022; Dulińska et al. 2006; Lekka et al. 2005). An incident laser beam undergoes reflection from the cantilever, with the resultant signal monitored via a detector (Figure 2.2(a)). Tip-sample interactions induce cantilever deflection, modulating the reflection trajectory of the laser beam with sub-nanometer resolution. The bending displacement of the cantilever is converted to interaction force using its spring constant. A closed-loop feedback system dynamically adjusts the up and down position to maintain preset deflection thresholds, enabling real-time force regulation during scanning. The AFM force-indentation curve on the cell is fitted to a model to estimate cell elasticity (Moeendarbary and Harris 2014). AFM is an extremely sensitive technique because it can achieve sub-nanometer and pico-Newton

resolution. A recent study presented its capacity to discriminate red blood cells (RBCs) treated with ultralow glutaraldehyde (0.001%v/v) from controls (Abay et al. 2019).

Optical tweezers uses a laser to manipulate microbeads attached to the cell membrane and induce an elongation (**Figure 2.2(b)**). The calibrated force imposed by a focused laser beam on a microbead determines the escape force required for the trapped bead. When the laser beam holds the trapped bead, the microscope stage movement elongates the cell via the bead fixed to the stage. The applied force (F) of the stage movement is increased until the trapped bead just escapes the optical trap. Then, the transverse (D_t) and axial diameters (D_a) of cells are tracked by images (Matthews et al. 2022). From these parameters, the elastic shear modulus or bending modulus of the membrane can be determined through a deformation model (Mills et al. 2004). Optical tweezers allow the selection of rare cells for measurement and integration with other measurement modalities, such as Raman spectroscopy (Wood et al. 2007).

Micropipette aspiration has been used to determine cell biomechanics for over 50 years. It quantifies the extensional rigidity (shear modulus μ) of individual cells by analysing their uniaxial elongation or shear deformation of the membrane (**Figure 2.2(c)**). A cell is aspirated into a glass micropipette with an internal radius (R_p) smaller than its own radius. As the cell partially enters the micropipette, the relationship between the suction pressure (P) and the length of the protrusion (L) is utilised to determine its intrinsic deformability through the shear modulus μ .

Compared with the previous three methods, acoustic scattering is a non-invasive technique that can probe and monitor cell mechanics in a short time period (Kang et al. 2019). The vibration of a suspended microchannel resonator (SMR) is used as an acoustic source, and the investigation of the acoustic scattering shift in resonant frequency (Δf) at the node of a suspended microchannel resonator is used to determine the cell cortex mechanical properties with size normalisation.

The sensitivity of these systems is high enough to probe the nano-scale deformation of cells. However, these single-cell methods suffer from limitations such as low analysis speed and low throughput, which hinders their ability to profile heterogeneous cell populations, and the complexity of manipulation is unsuitable for clinical or point-of-care (POC) analysis. Microfluidic techniques have the potential to solve these limitations by allowing simpler measurements. Microfluidic deformability methods are introduced in section 2.2.2.

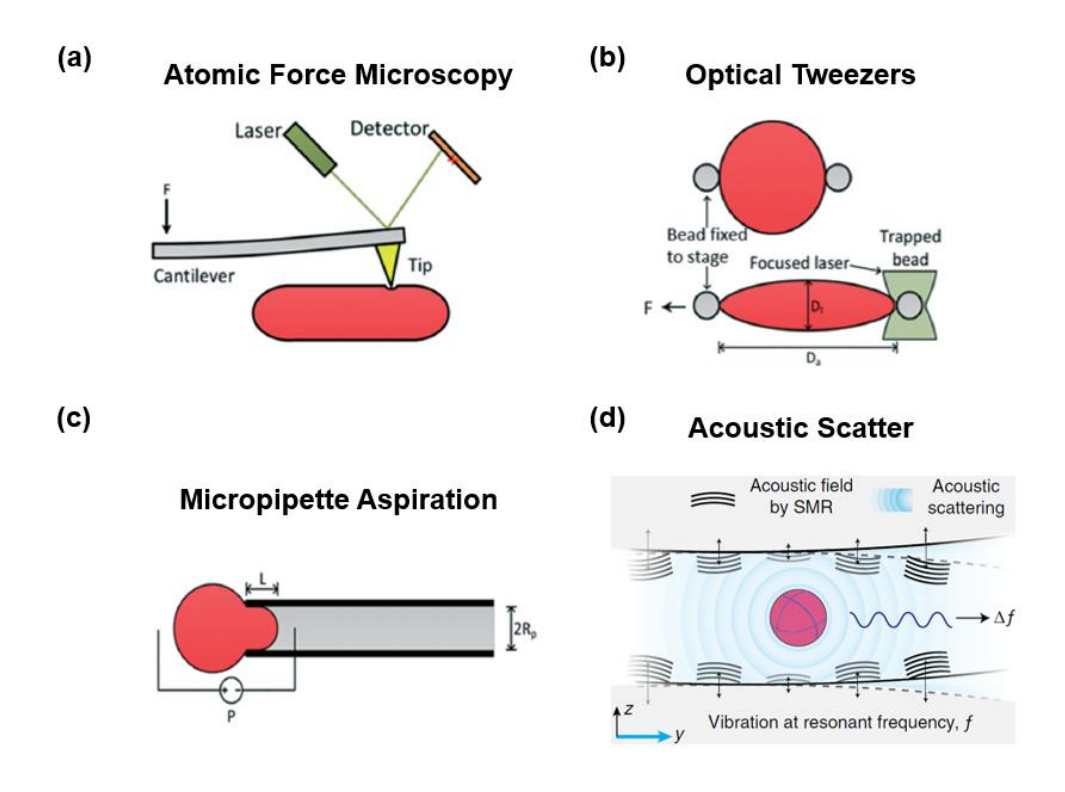


Figure 2.2 (a) Atomic Force Microscopy. A micron-sized tip connects to a micro-fabricated cantilever to deform and interact with the sample. A laser beam is reflected from the cantilever and collected by a detector, which measure the displacement. The real-time force is recorded. (b) Optical Tweezers. Microbeads are attached to the measured cell. A laser beam traps one of the beads and an elongation is induced in the cell. The escape force (F) of the trapped bead and dimensional alterations of cell (D_a and D_t) are used to evaluate the elastic or bending modulus of the membrane through a deformation model. (c) Micropipette Aspiration. A cell partially or completely enters the micropipette with a radius R_p . Its deformability is determined through the relationship between the shear modulus μ , the suction pressure (P) and the length of the protrusion (L). (d) Acoustic Scatter. A particle interacts with acoustic fields (black waves) produced by SWR vibration (black arrows) at the resonant frequency f. The interaction between the particle and the surrounding fluid induces acoustic scattering (blue waves), resulting in a shift in the resonant frequency (Δf). (a), (b)and (c) are adopted from (Matthews et al. 2022), (d) is adopted from (Kang et al. 2019)

2.2.2 Single-cell microfluidic deformability cytometry

Single-cell microfluidic deformability cytometric methods have been developed to enable rapid assessment of cells with high throughput. Most of these techniques require high-speed optical systems to determine deformability. Urbanska et al. (Urbanska et al. 2020) showed that there are three major types of microfluidic deformability cytometry, which vary by the magnitude of applied stress to the way deformability is measured. The first class is constriction-based deformability cytometry (cDC), forcing single cells through a constriction smaller than their diameter (Rosenbluth, Lam, and Fletcher 2008; Lange et al. 2015; Nyberg et al. 2017). The transit time is measured by recording frequency changes (Urbanska et al. 2020), optical imaging (Lange et al. 2015) or electrical resistance changes (Adamo et al. 2012) (**Figure 2.3(a)**). This method has been developed to characterise both electrical and mechanical metrics of individual cells, including

Young's modulus and capacitance (Feng et al. 2023; Feng, Chai, et al. 2022). However, this device is easy to block by particles and removing particle clusters within the channel is difficult (Petchakup et al. 2022). Furthermore, cell transit time is influenced not only by deformability but also by cell volume and membrane-wall friction and interactions.

To address these drawbacks, contactless methods integrated with high-speed camera and image processing were developed. Shear flow deformability cytometry (sDC) and extensional flow deformability cytometry (xDC) use hydrodynamic flow to induce cell deformation, eliminating the interaction between the cell and the channel wall. sDC uses shear flow to deform cells in a long, narrow channel. Deformability is defined by the relationship between cell contour area and perimeter obtained from optical images (Figure 2.3(b)). A widely used example is real-time deformability cytometry (RT-DC). Otto et al. (Otto et al. 2015) introduced RT-DC for continuous cell deformability characterisation with a high throughput. It is proven to be sensitive to cytoskeletal alterations and can distinguish cell-cycle phases and identify cell populations in whole blood. xDC combines extensional flow with the cross-slot microfluidic design. The cells are delivered to the cross junction of the channel, where images are recorded for analysis. The deformability is defined as the maximal aspect ratio observed in the images (Figure 2.3(c)). Urbanska et al. found this method can detect change of deformability altered by osmotic changes, but the deformability increase due to actin disassembly was not detected. Armistead et al. (Armistead et al. 2019) developed a device capable of spanning both high- and low-strain flow regimes, encompassing both shear- and inertia-dominant conditions. Their findings revealed that different flow regimes probe different aspects of cell structure, with a shear-dominant, low-strain regime proving to be the most sensitive to cytoskeletal changes. A comparison between sDC and xDC by Urbanska et al. (Urbanska et al. 2020) confirmed that the higher strain rate of xDC makes measurement of cytoskeletal changes challenging, probably due to cytoskeletal fluidisation (Armistead et al. 2019). There is another channel shape, the hyperbolic channel, applying the extensional flow to deform cells without contacting the channel walls. Piergiovanni et al. (Piergiovanni et al. 2020) explored the deformability of nucleated cells by images and found that a hyperbolic channel can lead to elliptical deformation patterns (Figure 2.3(d)). Moreover, these single-cell microfluidic deformability systems require a high-speed imaging system with expensive and complicated microscopy and high-speed imaging. With the development of impedance-based flow cytometry, probing cellular mechanics through electrical measurement is of great interest to replace optical systems.

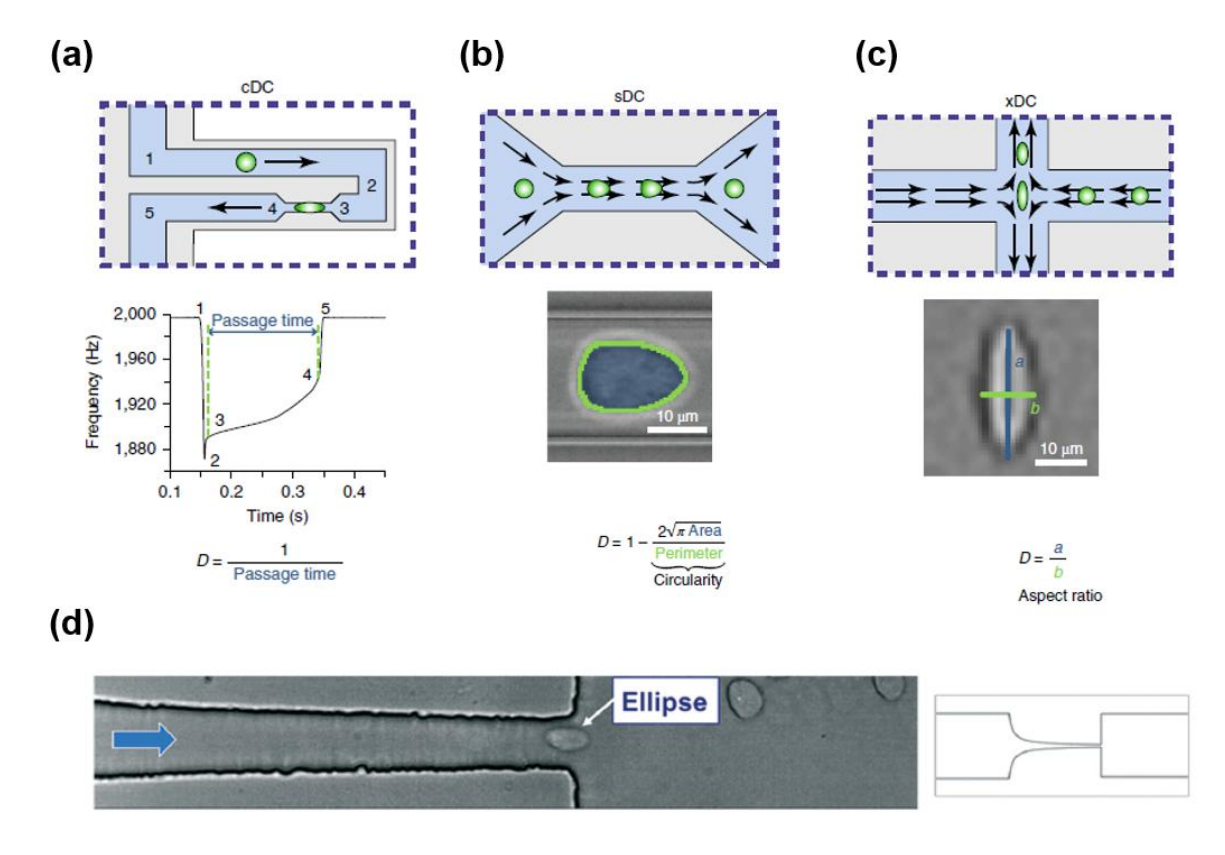


Figure 2.3 Operating principle of cDC, sDC and xDC. (a) cDC. A cell passes through a constriction smaller than its diameter, and the transit time is measured to determine deformability. (b) sDC. A cell passes through a contactless channel and shear force is applied to its surface. The deformability is determined from optical images. (c) xDC. An extensional flow along with a cross-slot microfluidic architecture induces extensional deformation of a cell and the deformability is determined by optical images. Copied from (Urbanska et al. 2020) (d) The extensional forces dominate in the short hyperbolic channel so that cells perform elliptical deformation patterns. Copied from (Piergiovanni et al. 2020).

Microfluidic impedance cytometry (MIC) has been developed for decades, and is based on the Coulter counter principle, the first technology that uses electrical methods to measure the properties of a single particle (Coulter 1956) (**Figure 2.4**). The Coulter device consists of two electrically isolated fluid-filled chambers with a pair of electrodes, and the DC (Direct Current) resistance is measured as particles flow through a small tube. The current pulse corresponds to the movement of a single particle and the magnitude is proportional to the amount of fluid displaced, i.e. cell size (Sun and Morgan 2010).

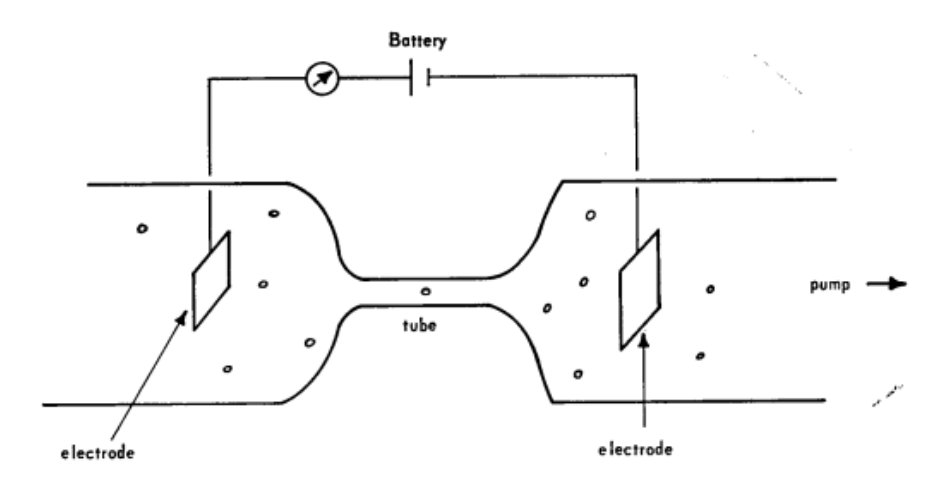


Figure 2.4 The structure and principle of the Coulter counter. As a particle passes through the tube, the generated current is recorded to count the number and deduce its size. Copied from (Hurley 1970)

The first Coulter counter integrated with a microchannel was developed by Larsen et al (Larsen, Blankenstein, and Branebjerg 1997). MIC is based on a microfluidic device integrated with microelectrodes to detect the impedance of a microchannel when cells pass through successive pairs of electrodes. The transit time determined from the impedance signal can be used to estimate the deformability. This is an example of cDC. Zheng et al. (Zheng et al. 2012) (**Figure 2.5**) developed a microfluidic system capable of measuring multiple biophysical parameters of single RBCs, including transit time, amplitude ratio and phase of the impedance signal. The transit time reflects cell membrane stiffness and the friction between the membrane and channel wall. The impedance amplitude ratio and phase were used to determine the volume, the membrane conductivity and the haemoglobin density of RBCs. They used multiple parameters to classify foetal/neonatal and adult RBCs.

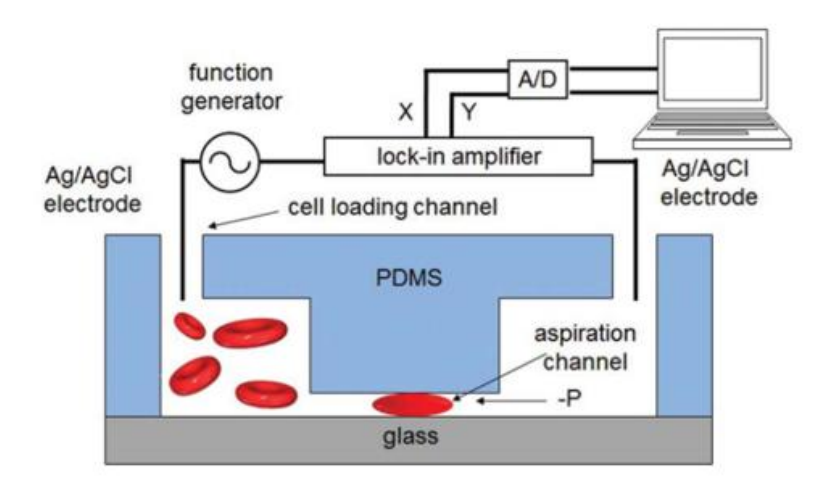


Figure 2.5 Schematic of a microfluidic system for electrical and mechanical characterisation of RBCs. The transit time, impedance amplitude ratio and impedance phase increase were determined, and foetal/neonatal and adult RBCs were classified successfully. Picture from (Zheng et al. 2012)

Zhou et al.(Zhou et al. 2018) proposed a deformability MIC with multiple pairs of electrodes as shown in **Figure 2.6**. This measured the impedance of undeformed and deformed cells simultaneously for the first time. The system used cDC to squeeze cells through a constriction smaller than the cell size. The cellular models were extended to MCF-7 breast cancer cells. The differential impedance simplified measurement of passage time (**Figure 2.6(a**)), entry time (**Figure 2.6(b**)) and transit time (**Figure 2.6(c**)). The entry time was used to characterise the ability to deform, and the transit time was governed by the frictional properties of the cell membrane. The impedance measured from electrode configurations in **Figure 2.6(a**) and **(c)** were utilised to analyse undeformed and deformed cells simultaneously. However, their system still relies on cell transit time detection and the deformability is still not directly defined by the impedance signal.

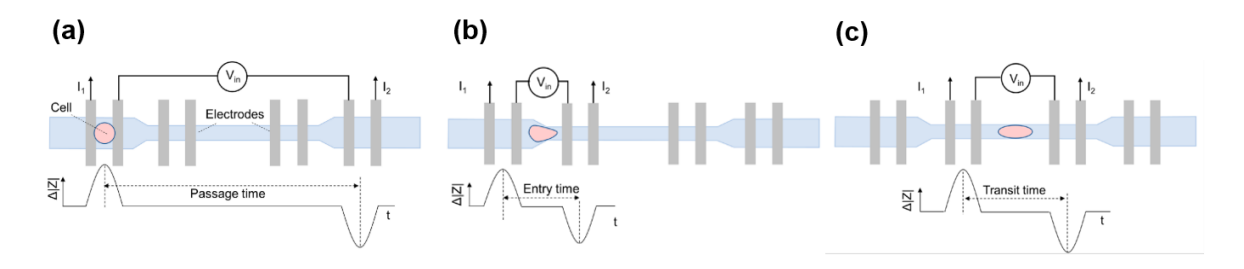


Figure 2.6 Schematic of the microfluidic impedance systems developed by Zhou et al. (Zhou et al. 2018). (a) Total passage time was used to reflect the undeformed state of cells. (b) Entry time was used to characterise the deformability of cells. (c) Transit time was used to identify the fractional properties of cells.

Petchakup et al. (Petchakup et al. 2022) developed a deformability MIC using microfabricated coplanar electrodes to quantify size, deformability and membrane properties of neutrophils, demonstrating alterations upon activation (**Figure 2.7**). This system used viscoelastic-inertial sheath flow to focus cells into a narrow stream, guiding them through a cross-junction where they were deformed by the squeezing forces of the sheath fluids. Inside the microchannel, shear force dominated, and the cell shape changes were assessed by comparing impedance signals before (native state) and after (deformed state) the cell flowed along the cross-shaped channel.

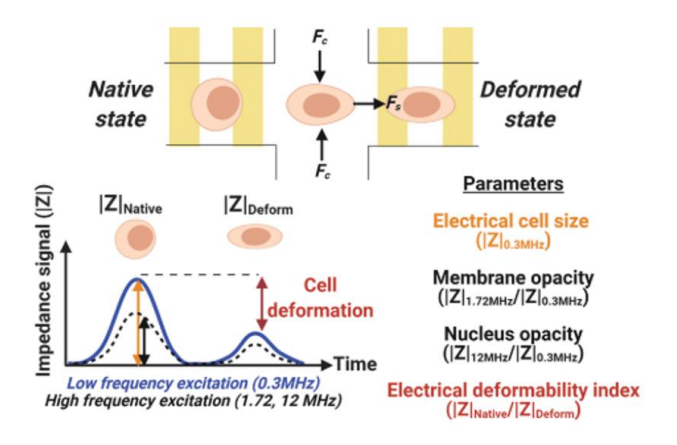


Figure 2.7 Schematic illustration the system from Petchakup et al. (Petchakup et al. 2022). Cells were subjected to the dominant shear force and the cell shape changes were assessed by

comparing impedance signals before and after the cross-shaped channel. Size, deformability, and electrical opacity were defined by impedance at different frequencies.

Reale et al. (Reale et al. 2022) used a hyperbolic channel to induce cell deformation by extensional flow (Figure 2.8(a)). Four coplanar electrodes are integrated into the cross configuration to probe the cell along the direction of flow and along the direction transverse to flow. Jarmoshti et al. (Jarmoshti et al. 2024) from the same group kept the hyperbolic channel design, but they used a three-electrode configuration to measure pre-deformation, deformation, and recovery of a cell when it passed along the channel. A multilayer perceptron neural network was utilised to train raw impedance signals from cells under extensional flow along with their image metrics, deriving metrics to quantify cell deformability over wide anisotropy ranges with minimal errors from cell size distribution (Figure 2.8(b)).

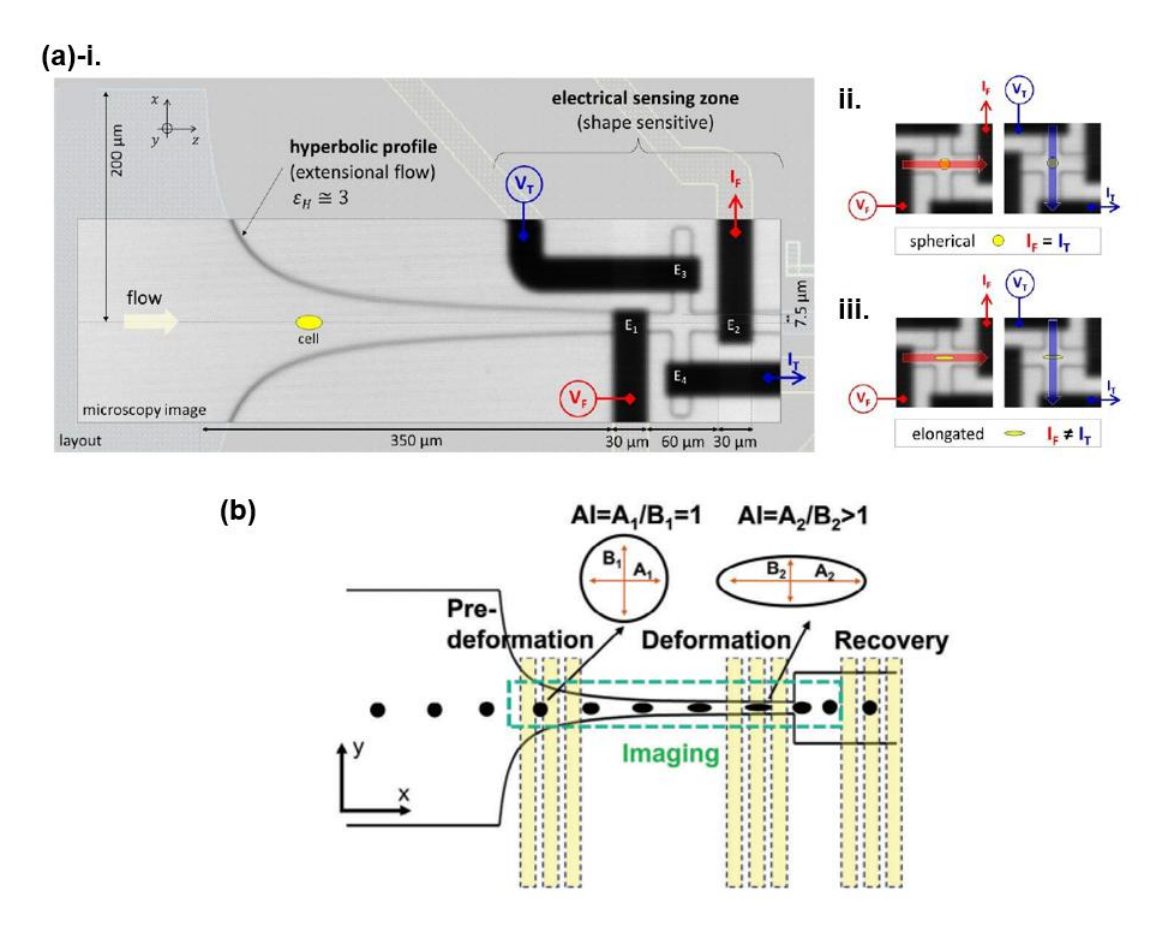


Figure 2.8 (a) Deformability MIC with hyperbolic channel proposed by Reale et al. (Reale et al. 2022) i. The device geometry which contains a hyperbolic channel and four coplanar electrodes in cross configuration to probe the cell along the direction of flow and along the direction transverse to flow. ii. $I_F = I_T$, when a spherical particle passes through. iii. $I_F \neq I_T$, when an elongated particle passes through. (b) Schematic illustration of the channel design from (Jarmoshti et al. 2024). Deformation of cells under viscoelastic hyperbolic extensional flow alters their anisotropy index (AI), defined as the ratio of length (A) to width (B) in the flow direction. Cells were measured using a three-electrode configuration to measure three stages of deformation: pre-deformation, deformation and recovery.

Table 2.1 Summary table for deformability MIC mentioned in this section.

Main metric	Channel type	Cell type	Aim of the work	Ref
Transit time	Aspiration channel	RBCs	Used multiple parameters to classify foetal/neonatal and adult RBCs	Fig 2.5 (Zheng et al. 2012)
	Constriction channel	MCF-7 breast cancer cells	Characterise the ability to deform and fractional properties of the cell membrane	Fig 2.6 (Zhou et al. 2018)
Deformability index	Cross-junction channel	HL-60 cells, Neutrophil	Quantify size, deformability and membrane properties of neutrophils after activation	Fig 2.7 (Petchakup et al. 2022)
	Hyperbolic channel	RBCs	Characterise the deformed cell shape of healthy and chemically stiffened RBCs	Fig 2.8 (a) (Reale et al. 2022)
		Cancer and cancer associated fibroblasts cells	Characterise the pre- deformation, deformation and recovery of a cell, and the support vector machine model is used for multiparametric classification	Fig 2.8 (b) (Jarmoshti et al. 2024)

2.2.3 Characterisation of cell electrical properties

Cell electrical parameters (conductivity and permittivity) are governed by structural and dynamic characteristics (Zhong, Yang, et al. 2021; Shi et al. 2015; Mansoorifar et al. 2018). The electrical properties of the cell membrane are primarily determined by membrane surface morphology, lipid bilayer composition and thickness, and the presence of membrane proteins (Yang et al. 1999; Wang et al. 1994; Zimmermann et al. 2008). The cytoplasm dielectric properties are influenced by the structural organisation of intracellular components and dynamic biochemical conditions, most notably the concentration of various ionic species within the cellular environment (Huang et al. 1995; Hölzel 1999; Duncan et al. 2007). These factors are related to the physiological process of cells, including cell viability (Zhong, Yang, et al. 2021; Feng, Cheng, et al. 2022), leukocyte types in whole blood (Holmes et al. 2009; Prieto et al. 2016), the activation state of

macrophages (Torres - Castro et al. 2023; Salahi, Rane, et al. 2022), parasite invasion of red blood cells (Honrado et al. 2018; Du et al. 2013), cancer cells (McGrath et al. 2020; Chiu et al. 2017) and antimicrobial susceptibility (Spencer et al. 2020; Tang et al. 2023).

Early work on measuring single-cell electrical properties with patch-clamp was developed in 1976 by Neher and Sakmann (Neher and Sakmann 1976). The method used a pipette (P) with a DC resistance of 2-5M Ω and a 3-5 μ m opening. It contained Ringer's solution and was applied close onto muscle fibres within 200 μ m of intracellular clamp electrodes. A virtual ground circuit was used to measure the membrane current with an operational amplifier and a feedback resistor. However, this method took about ten minutes to measure one cell (**Figure 2.9**).

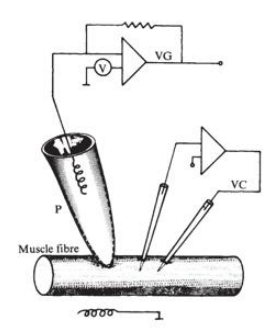


Figure 2.9 The patch-clamp technique used to measure single-cell electrical properties. Schematic circuit diagram of current recording from a patch of membrane with an extracellular pipette. VC, a two-microelectrode voltage clamp circuit to provide a fixed value of the membrane potential of the fibre. P, pipette applied closely onto the muscle fibre within $200\mu m$ of the intracellular clamp electrodes. VG. Virtual ground circuit that measured the membrane current with an optional amplifier and a feedback resistor. Picture from (Neher and Sakmann 1976).

Other methods for analysing cell electrical properties include electric impedance spectroscopy (EIS) and single cell electrorotation (ROT).

EIS is a technique that applies an electric field to many cells to measure the current at different frequencies. Various cell trapping mechanisms integrated with microfabricated electrodes have been developed to measure single cells (Tan et al. 2012). Malleo et al. (Malleo et al. 2010) developed a device that implemented hydrodynamic cell trapping for continuous differential impedance analysis of single cells. The current from two closely positioned electrode pairs, one empty (reference) and one containing a cell, were recorded, and time-dependent impedance responses to dynamic chemical perturbations of single cells were measured. This design recorded multiple signals from multiple trapping sites (Figure 2.10(a-f)). Mansoorifar et al. (Mansoorifar et al. 2018) designed an electro-activated microwell array for cell capture, dielectric spectroscopy analysis, and release. Using equivalent circuit modelling, the membrane capacitance and cytoplasmic conductivity were extracted from the impedance spectra. The results showed that this system can monitor the response of cells to external stimuli, such as alterations in the buffer conductivity and pH (Figure 2.10(g)).

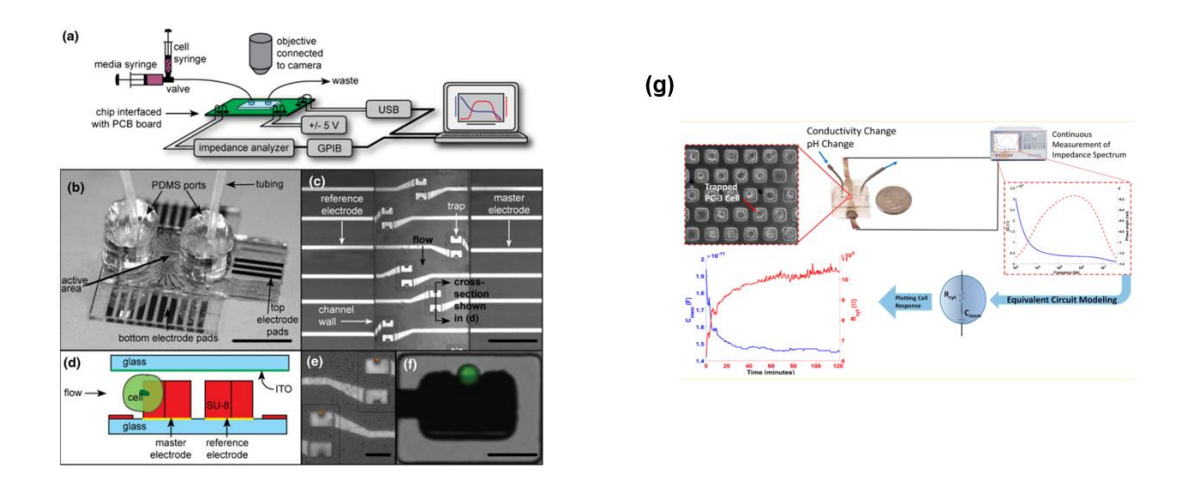


Figure 2.10 (a-f) Overview of the device developed by Malleo et al. (Malleo et al. 2010) to measure the time-dependent impedance of single cells to dynamic chemical perturbations. Cells were hydrodynamically trapped on top of a pair of electrodes. (g) Schematic diagram of the electrical impedance spectroscopy system designed by Mansoorifar et al. (Mansoorifar et al. 2018). Cells are trapped in the electro-activated microwells and for dielectric spectroscopy measurements. Spectra are fitted to an equivalent circuit model to extract cell membrane capacitance and cytoplasmic conductivity.

ROT uses a non-uniform electrical field to generate a rotation torque on a cell. The cell rotation speed is related to the electrical parameters of the cell and suspension media. The cell dielectric parameter (membrane capacitance) are derived from the rotation spectrum which gives the imaginary part of the Clausius Mossotti factor (Arnold and Zimmermann 1988, 1982b, 1982a). (Wang, Pethig, and Jones 1992). Arnold et al. (Arnold and Zimmermann 1982a) developed a device consisting of a chamber with four electrodes driven by sinusoidal voltages with 90° phase differences around the chamber (Figure 2.11(a)). A cell in the chamber rotates due to the induced dipole. The frequency of maximum rotation for different conductivities were recorded, and the gradient yielded the membrane capacitance. Kawai et al. (Kawai et al. 2020) used a 3D-array device to measure the membrane capacitance and cytoplasmic conductivities of hematopoietic cells (Figure 2.11(b)). ROT requires skilled operators and is not high throughput. Moreover, cells may be damaged or even dead after the ROT (Li et al. 2024).

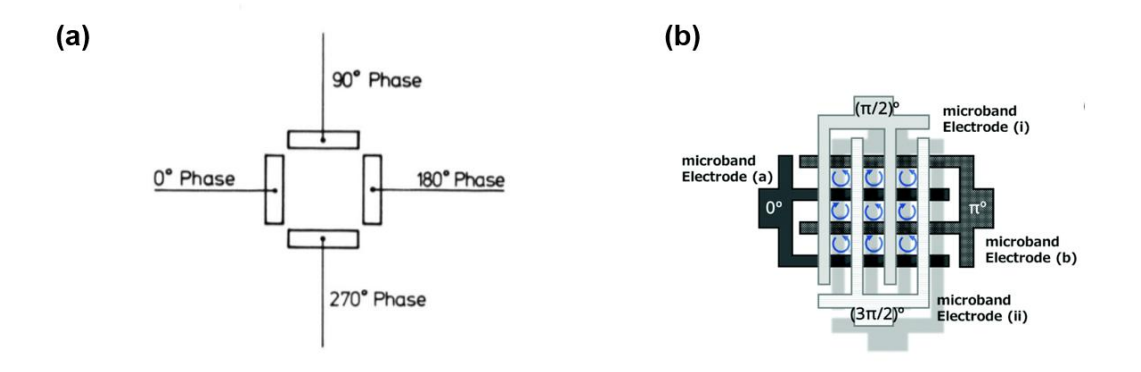


Figure 2.11 (a) Schematic diagram of a chamber used to generate the rotating electric field. Four electrodes are driven by equal voltages with four phases shifted by 90°. The frequency of maximum rotation speed was recorded for different suspension conductivities in order to derive

the cell membrane capacitance (Arnold and Zimmermann 1982a). (b) Schematic diagram of the electrorotation device designed by Kawai et al. (Kawai et al. 2020). Hematopoietic cells in the 3D-array microwells rotate, and the measured spectra used to extract membrane capacitance and cytoplasmic conductivity.

2.2.4 Single-cell microfluidic impedance cytometry

Unlike EIS and ROT, MIC has high throughput because particles flow through a channel at high flow rates. In MIC, cells are typically measured at two or at most three discrete frequencies, with classification based on the value of the impedance signals, for example, amplitude, phase, and/or electrical opacity (the ratio of high- to low-frequency impedance).

Gawad et al. (Gawad, Schild, and Renaud 2001) used a coplanar electrode configuration to measure erythrocytes and ghosts, and presented the data as a scatter plot of low-frequency phase (LF) versus high-frequency phase (HF) (**Figure 2.12**). When the ratio of ghosts to erythrocytes was 1:4, ghost cells had a lower HF/LF ratio because their cytoplasm conductance was similar to that of the buffer solution.

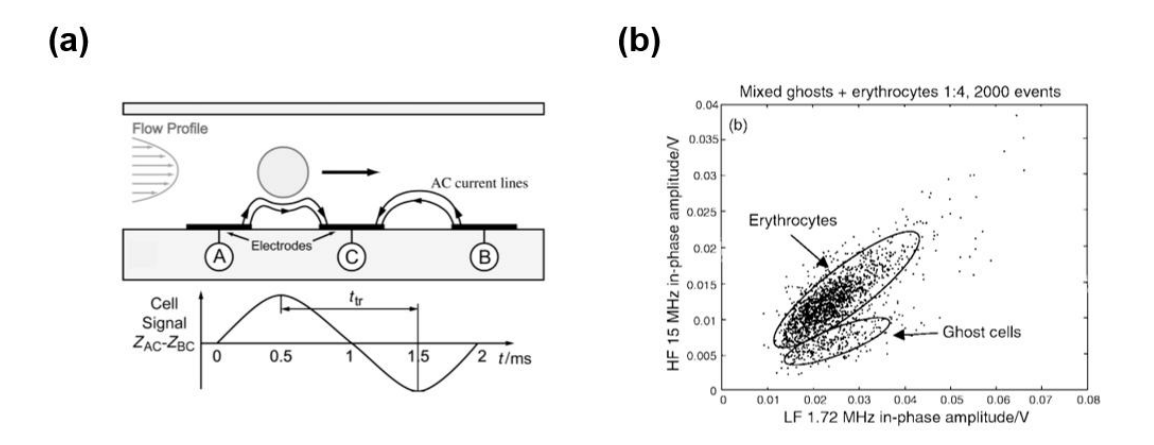


Figure 2.12 (a) Schematic diagram of the MIC device designed by Gawad et al. (Gawad, Schild, and Renaud 2001). Three coplanar electrodes were fabricated in the channel to generate the differential impedance signal shaped as an anti-symmetric Gaussian signal. (b) MIC scatter plot of low frequency (LF) phase versus high frequency (HF) phase for mixed ghosts and erythrocytes. Ghosts had a lower HF/LF ratio.

Holmes et al. (Holmes et al. 2009) used electrical opacity to discriminate subpopulations of cells (**Figure 2.13**). They mixed antibody-conjugated beads with cells, and beads were bound to the target population, thereby altering the electrical properties of cells. In human blood samples, CD4 T-lymphocyte subpopulations were identified after adding CD4 beads, and it had a higher opacity compared to lymphocytes and granulocytes & monocytes subpopulations.

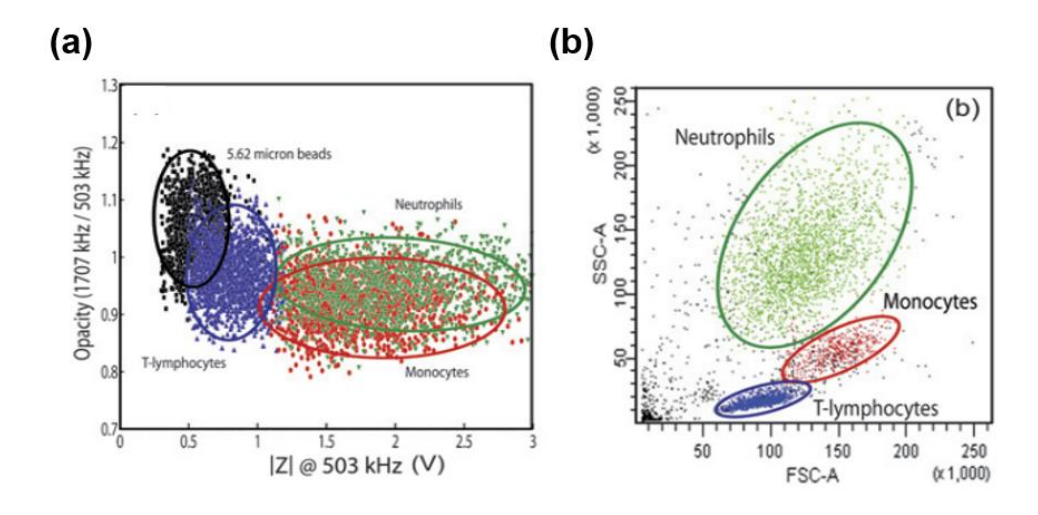


Figure 2.13 Scatter plot of a mixture of the T-lymphocytes, monocytes, neutrophils and 5.62 μ m diameter latex beads from (Holmes et al. 2009). (a) Opacity ($|Z_{1707kHz}|/|Z_{530kHz}|$) vs low frequency impedance magnitude ($|Z_{503kHz}|$). (b) FACS analysis of the same sample showing forward and side scatter of the cells; colour coded according to fluorescence.

Ostermann et al. (Ostermann et al. 2020) demonstrated that the phase at 6 MHz enabled the characterisation of the necrotic and viable U937 human lymphoma cells. A significant discrimination between two different subpopulations of cells was observed from the scatter plot (**Figure 2.14**).

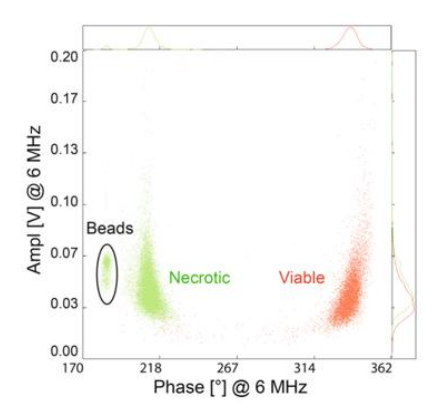


Figure 2.14 Scatter plot of phase versus amplitude of impedance at 6MHz showing discrimination between necrotic and viable U937 human lymphoma cells (Ostermann et al. 2020).

The examples mentioned above are just a few limited cases of MIC measurements at dual frequencies. In fact, there are many studies which attempted to use impedance signals including opacity or phase to assess various types of cells, such as macrophage activation by *ex vivo* intervertebral discs (Salahi, Rane, et al. 2022) and lymphocyte activation (Petchakup et al. 2021).

However, measurements at only two or three frequencies are inadequate to obtain the intrinsic electrical properties of individual cells. This limitation arises because determining cellular dielectric parameters requires fitting the frequency-dependent impedance spectra to a set of

Debye relaxations (Morgan and Green 2003). This analytical process is typically implemented through established modelling such as multi-shell theory or equivalent circuit. To address this, the properties of single cells need to be measured across a wide range of frequencies.

Early work by Sun et al. (Sun et al. 2007) used maximum length sequence (MLS) analysis to measure the properties of polystyrene beads with 512 evenly distributed frequencies between approximately 1kHz and 500kHz (**Figure 2.15(a**)). It demonstrated that the MLS technique could give multi-frequency measurements in a short period of time (ms), and validation was conducted with polystyrene beads, showing a good agreement between the MLS data and both circuit simulations and conventional AC signal measurements (average signal for 200 beads at every frequency).

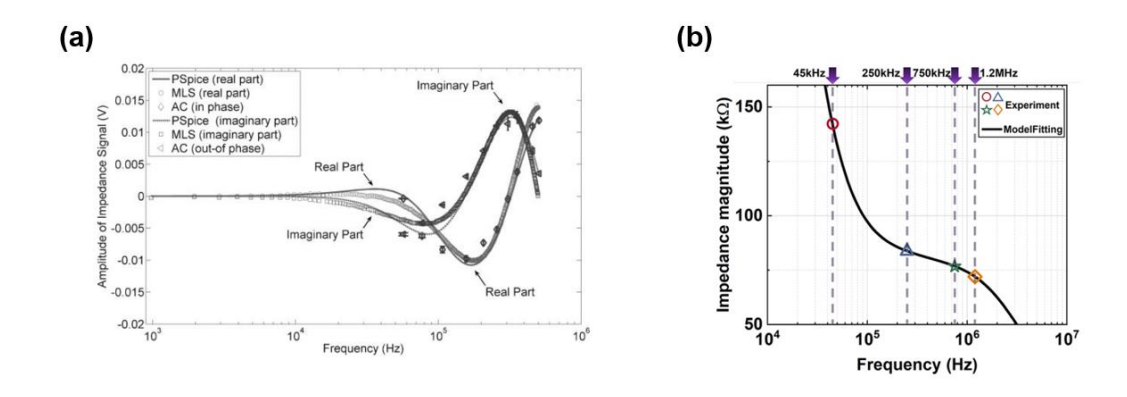


Figure 2.15 (a) Comparisons of MLS, Pspice circuit simulations and conventional AC frequencies (Sun et al. 2007). These three methods had good agreements. (b) The impedance spectrum example of the four-frequency impedance signal fitting of a single fabricated liposome particle (Chai et al. 2023).

Some groups attempted to extrapolate particle dielectric parameters from a very limited range of frequencies. For example, Chai et al. (Chai et al. 2023) used giant liposomes of known radius, membrane permittivity and cytoplasm conductivity and fitted a single dispersion to only four discrete frequencies up to 1.2MHz. The dielectric properties of the liposomes were extracted using the single-cell equivalent circuit model (Figure 2.15(b)). They optimised the geometry of the channel and demonstrated that IFC achieved less than 10% relative error in characterising intrinsic electrical properties when the sensing zone dimensions approximate to the target particle diameter. Zhao et al. (Zhao et al. 2013; Zhao et al. 2018) used a constriction channel to measure the capacitance of single cells at two low frequencies, up to 250kHz (Figure 2.16(a)), and the raw data were fitted to equivalent electrical circuits without considering the nucleus in the model. They claimed to extract the cell specific membrane capacitance (C_{sm}). Haandbæk et al. (Haandbæk et al. 2016) characterised different yeast cell phenotypes at frequencies up to 20MHz, fitting data to a shell model, including the cell wall layer (Figure 2.16(b)). They demonstrated the cell wall conductivity and thickness and cytoplasm conductivity for characterising different species of yeast cells with large differences in morphology.

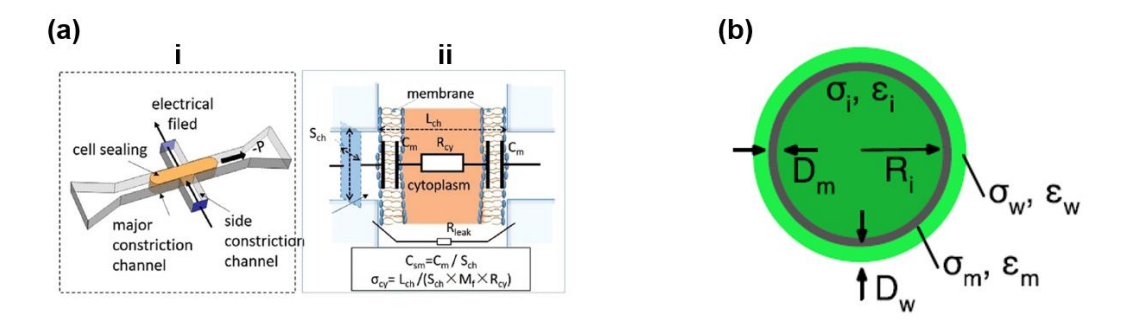


Figure 2.16 (a)-i. Schematic diagram of the MIC device to determine specific membrane capacitance (C_{sm}) and cytoplasm conductivity (σ_{cy}). (a)-ii. The equivalent circuit was used to fit the measured impedance and derive the parameters. S_{ch} – cross-section area of the side constriction channel. L_{ch} – the length of the major constriction channel along the direction of the side channel. M_f – modification factor obtained based on numerical simulations. Four parameters including cytoplasm resistance (R_{cy}) and membrane capacitance (C_m) were obtained. Copied from (Zhao et al. 2018) (b) The shell model used to represent yeast cells (Haandbæk et al. 2016). R_i , ε_i , σ_i – Inner radius, permittivity, conductivity; ε_w , σ_w – Cell wall permittivity and conductivity; ε_m , σ_m – Cell membrane permittivity and conductivity; D_w , D_m – Thickness of the cell wall and cell membrane.

Spencer and Morgan (Spencer and Morgan 2020) developed a single-cell dielectric spectroscopy system which employed eight frequencies simultaneously to probe the impedance response over a frequency range from 200kHz to 50MHz (**Figure 2.17**). They measured thousands of single cells without nuclei (RBCs and ghosts) at a high throughput, up to 50MHz, sufficient to fit the data to the single-shell model. The radius, membrane capacitance and cytoplasm permittivity and conductivity of cells were extracted for each individual cell.

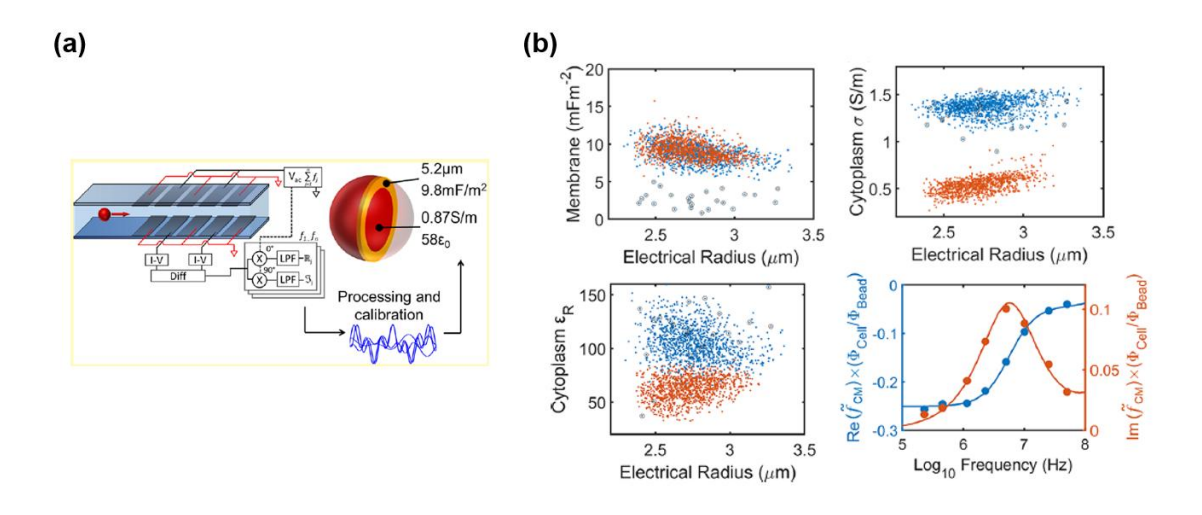


Figure 2.17 (a) Schematic diagram of the impedance spectroscopy system proposed by Spencer and Morgan (Spencer and Morgan 2020). Eight frequencies ranging from 200kHz to 50MHz were applied to the microelectrodes simultaneously, and the spectrum of each single cell was fitted to a single-shell model to extract the dielectric parameters, including cell diameter, membrane capacitance and cytoplasm permittivity and conductivity. (b) Scatter plot for 1000 RBCs (red dots) and 1000 ghosts (blue dots). The bottom right plot is an example impedance spectrum for a ghost cell, showing an excellent fit to the single-shell model.

2.2.5 Discussion

Section 2.2 described the biophysical characteristics, including mechanical (e.g. deformability) and electrical parameters (e.g. membrane capacitance and cytoplasm conductivity) of cells. Measurement of cellular biophysical properties offers novel insights into technology for disease diagnosis, drug development, bioengineering and clinical therapy. Although studies have indicated the potential of cellular biophysical properties as biomarkers for cell identification, early detection methods often rely on costly equipment, complex procedures, and specialised researchers, limiting their feasibility for on-site, high-throughput analysis of large sample volumes. The emergence of microfluidic techniques provides the possibility to address this limitation.

In deformability measurements, cell deformation is induced by different channel structures or specialised fluids as they flow through the channels of a microfluidic cytometer. Deformability can be directly quantified from images captured by high-speed cameras or derived from indirect measurement parameters, such as cell transit time in a constricting channel. These methods require complicated microscope systems and a large amount of image data to be processed. Additionally, a constricting channel may cause microchannel clogging, thereby decreasing throughput. In the dielectric parameter measurements, early microfluidic devices manipulated trapped cells to obtain their frequency-dependent spectrum and determine their properties. Low throughput and complex operation procedures hinder the application of these measurement systems in rapid clinical diagnosis.

Microfluidic impedance cytometry (MIC) provides an alternative approach to measuring the biophysical properties of cells. This high-throughput, label-free method can maintain cell viability, which is crucial for the analysis of hard-to-obtain cells, such as circulating tumour cells (CTCs). It is of great interest to develop a deformability MIC system and explore its correlation with optical measurements, as presented in **Chapter 4**. Optimising the microfluidic impedance spectroscopy for nucleated cells is introduced in **Chapter 5**.

2.3 Single-cell Sorting

In applications such as clinical diagnosis, identified target cells need to be purified and isolated from the original sample for specific operations, such as inducing selective differentiation, modifying surface molecules, or even performing advanced procedures such as gene editing and DNA sequencing (Tewhey et al. 2009). Compared with conventional sorting methods, microfluidic cytometry has many advantages, including a higher throughput, lower sample volume requirement, reduced cost and reduced size for operational convenience and portability (Wyatt Shields Iv, Reyes, and López 2015). There are label-based methods and label-free methods.

Fluorescence-based indicators are commonly used in commercial flow cytometry. Other label-based methods include binding magnetic beads onto cell surfaces and forcing target cells sorted by an external magnetic field. Label-free cell sorting using microfluidic cytometry can not only be adapted in passive systems but also in active systems (using external force-fields). It sorts based on a wide range of physical characteristics in such as size, shape, deformability, density etc. This section reviews these two types of sorting methods and introduces some typical examples.

2.3.1 Label-based sorting

Fluorescence-based cell sorting was the first commercial cell sorter invented by Herzenberg et al. in 1969 (Hulett et al. 1969), known as fluorescence-activated cell sorting (FACS). In FACS, cells are labelled with fluorescent probes. The labelled cells are placed in a laminar flow stream and light is scattered from a focused laser beam. The fluorescent signal is analysed to classify each cell for downstream sorting, where each cell is encapsulated into a charged aerosol droplet and sorted electrostatically (Bonner et al. 1972; Wyatt Shields Iv, Reyes, and López 2015). However, due to biosafety concerns during the generation of aerosol droplets, researchers are moving to characterise cells in microfluidic devices (Wyatt Shields Iv, Reyes, and López 2015).

Dielectrophoresis (DEP) and acoustic separation mechanisms are label-free sorting methods (see **section 2.3.2**) when they sort cells based on the intrinsic properties of particles, such as size and shape. These mechanisms can also be utilised to induce displacement of labelled particles to achieve desired sorting. For example, Mazutis et al. (Mazutis et al. 2013) developed a fluorescent droplet-based microreactor integrated with a cell sorter using DEP (**Figure 2.18**). Cells with/without target antibody (Ab-producing cell / non-producer) were encapsulated in droplets with a fluorescent detection antibody and incubated off-chip to produce secretion antibodies. They were sorted based on fluorescence signal.

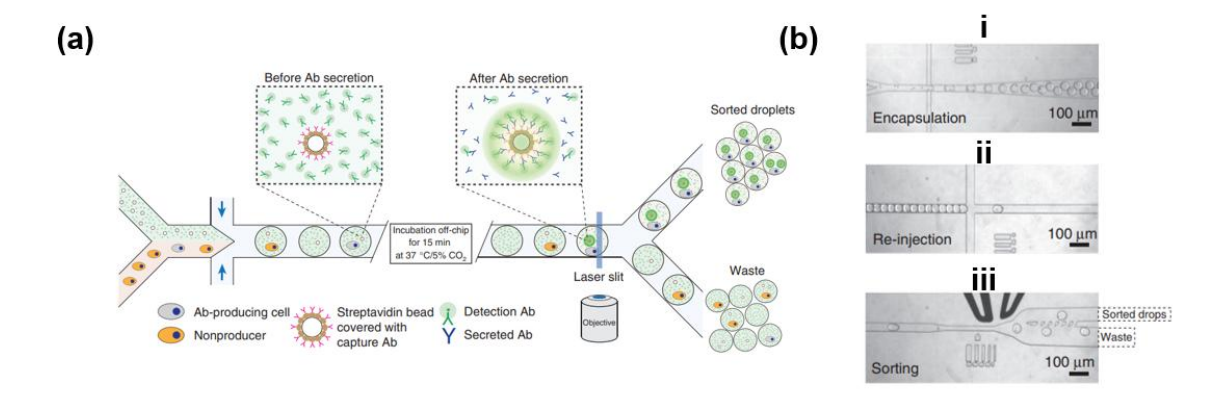


Figure 2.18 (a) Schematic diagram of a microfluidic fluorescent-based sorting system. Cells were encapsulated in droplets, and those with target antibodies produced increased fluorescence signals after off-chip incubation. (b) From i to iii, the whole process of sorting. Copied from (Mazutis et al. 2013).

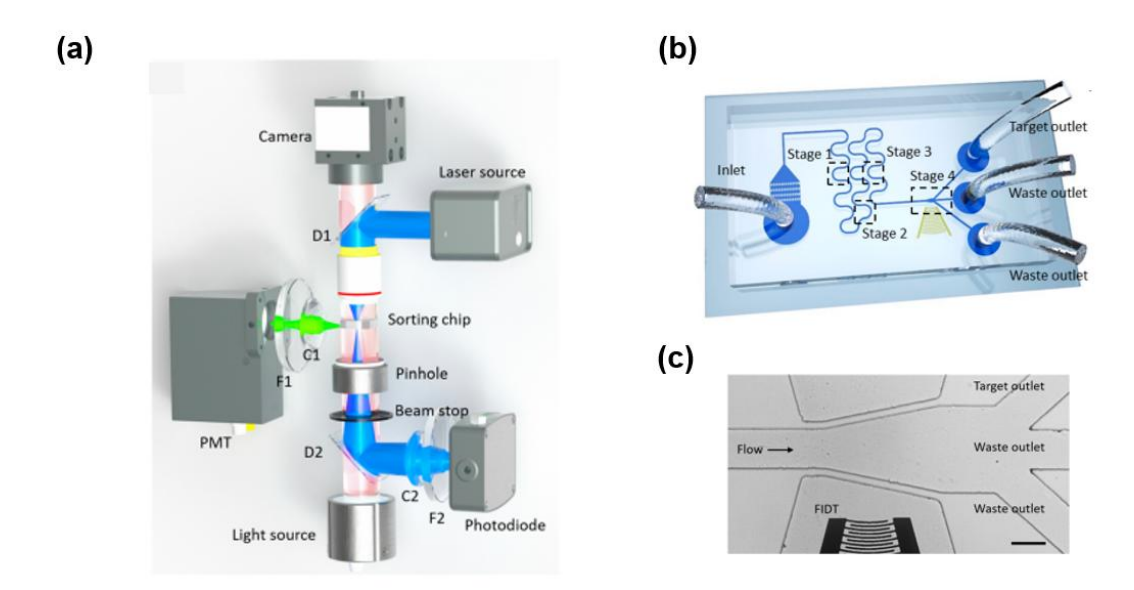


Figure 2.19 (a) Schematic of a fluorescence sorting system developed by Li et al. (Li et al. 2019). (b) The chip image. (c) The microscope image of the channel and sorting region. Stained cells were forced by the acoustic waveform generated by the FIDT toward the target outlet.

Li et al. (Li et al. 2019) developed a fluorescence-activated sorting system integrated with an acoustic sorter. The system used elasto-inertial particle focusing to align stained cells in a single stream, and the selected cells were forced toward the target outlet by the acoustic stream flow and acoustic radiation force (**Figure 2.19**).

Fluorescence-based microfluidic sorting is widely used, but the cytotoxicity of fluorescent dyes may damage DNA and be phototoxic to viable cells (Perry et al. 2011). Magnetic beads can be used to bind target cells for sorting (Evans et al. 2009; Li et al. 2016; Shi et al. 2017; Buryk-Iggers, Kieda, and Tsai 2019). However, magnetic methods have drawbacks such as material limitations, and low response speed. In summary, label-based microfluidic sorting provides reliable performance, but the invasive manipulation of cells limits the application.

2.3.2 Label-free sorting

Label-free microfluidic sorting is simple, cost-effective, and time-efficient. Approaches can be divided into active sorting and passive sorting, depending on whether an external field is applied.

There are several passive label-free sorting methods, including filtration, deterministic lateral displacement (DLD), and inertial microfluidics. These methods have no requirement for external fields, and particles are separated by hydrodynamic forces generated by specialised channel structures or configurations. Microfluidic filtration separates cells based on size, and there are three kinds of filtration: membrane filtration (Fan et al. 2015; Kang et al. 2017; Crowley and Pizziconi 2005), pillar filtration (Sarioglu et al. 2015) and tangential flow filtration (Raub, Lee, and Kartalov 2015). Membrane filtration uses commercial membranes with holes of specific size to isolate larger cells (Lu et al. 2023). Fan et al. (Fan et al. 2015) and Kang et al. (Kang et al. 2017)

isolated circulating tumour cells (CTCs). Pillar filtration generally uses fabricated pillars with different shapes to block cell clusters (Sarioglu et al. 2015; Mehendale et al. 2018). Tangential flow filtration uses an additional sheath flow to provide a pressure gradient in the channel. The target cells flow through small gaps perpendicular to the original direction (Han et al. 2021).

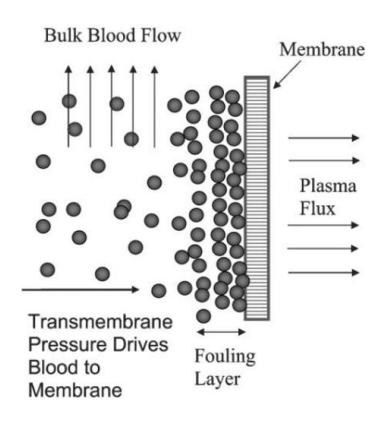


Figure 2.20 Microporous membrane filtration of whole blood using cross flow filtration to maximise yield or reduce processing time. This method achieved high isolation efficiency by minimising the accumulation of fouling elements, such as RBCs, at the filter face. Copied from (Crowley and Pizziconi 2005).

Deterministic lateral displacement (DLD) is a separation technique which uses an array of micropillars to displace larger particles laterally in a bumping migratory flow trajectory (Hochstetter et al. 2020; Smith et al. 2018; Zeming et al. 2016). Huang et al. (Huang et al. 2004) demonstrated that cells with smaller sizes could more easily traverse between obstacles than larger cells, which achieved sorting. The key step is the critical sorting diameter D_c , carefully evaluated by Inglis et al. (Inglis et al. 2006). Particles smaller than D_c , zigzag through the pillar array with no net displacement while particles larger than D_c are displaced from their original lateral position (Xavier et al. 2019) (**Figure 2.21**). This technique was used in many clinical scenarios, such as undiluted whole blood samples and isolating cancer cells (Davis et al. 2006; Huang et al. 2008; Liu et al. 2013). Tottori et al. (Tottori and Nisisako 2020) combined the DLD and inertial focusing, enabling a sorting efficiency of 99% for a mixture of MCF-7 cells (a model of CTCs) and blood cells.

Size-based cell sorting

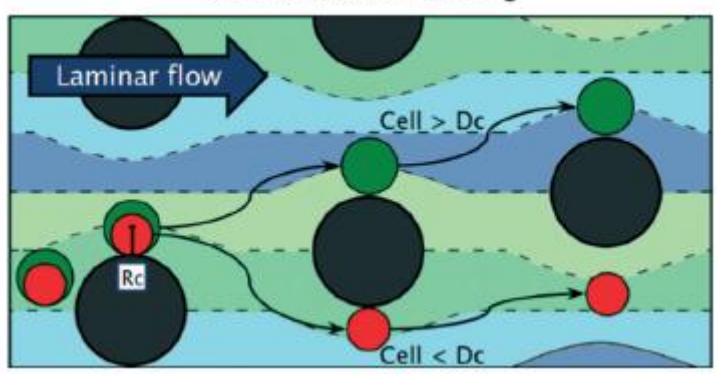


Figure 2.21 Schematic of a DLD separating system. The critical diameter of the system is $D_{\rm C}$, which can be evaluated. Cells with size larger than $D_{\rm C}$ move in a direction dictated by the arrays, while cells smaller than $D_{\rm C}$ move with the convective flow. Copied from (Xavier et al. 2019).

Inertial microfluidic sorting uses hydrodynamic forces acting on particles to produce cell movement. This method differentiates particles by size. Huh et al. (Huh et al. 2007) integrated fluid dynamics with droplet inertia to separate microorganisms and drops, utilised gravity to drive the flow, causing positional deposition difference. Shen et al. (Shen et al. 2017) optimised the channel design to a micro-spiral shape with a set of micro-obstacles integrated into it (**Figure 2.22**), but small particles do not experience sufficient inertial forces, leading to separation failure.

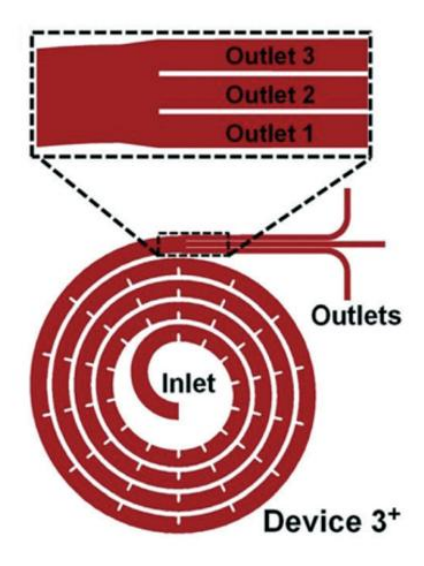


Figure 2.22 An inertial microfluidic sorting device with spiral channel. A set of micro-obstacles integrated into the spiral channel results in an enhanced performance. Three outlets for specific particle separation and collection. The sorting efficiency was 99.8% for sorting polymeric particles, CTCs and blood cells. Copied from (Shen et al. 2017).

Active sorting systems are often integrated with label-free detection methods. Dielectrophoresis (DEP) sorts cells based on their dielectric properties (e.g., polarisability). In a non-uniform electrical field, polarised particles experience a force leading to migration along or against the field gradient depending on the excitation frequency, size and electrode configuration (Velmanickam et al. 2022). Fiedler et al. (Fiedler et al. 1998) achieved particle sorting under

conditions of negative DEP. Various sorting chips based on DEP have been proposed. For example, Wang et al. (Wang et al. 2007) integrated vertical electrodes in the sidewall of microchannels for multiplexed DEP switching of particles to change the equilibrium points for different types of cells or beads (Figure 2.23(a)). However, the DEP technique has several problems, such as Joule heating, limited throughput and the need for a low-conductivity buffer (Lu et al. 2023). Dielectrophoretic cell sorting can be enhanced by field-flow fractionation (FFF), which includes gravitational, centrifugal, thermal, magnetic, and electrical forces. This hybrid approach aims to position cells by height, thereby directing them into distinct laminar flow streams based on the flow velocity gradient inherent to parabolic flow profiles (Roda et al. 2009; Giddings 1993, 1985). Vykoukal et al. (Vykoukal et al. 2008) first developed a DEP-FFF system to separate stem cells from enzyme-digested adipose tissue. The microfluidic platform featured patterned microelectrodes at the bottom of a microfluidic channel, generating negative dielectrophoretic forces counteracting gravity. This allowed each cell type to attain an equilibrium height based on its surface charge, enabling rapid sorting under flow (Figure 2.23(b)).

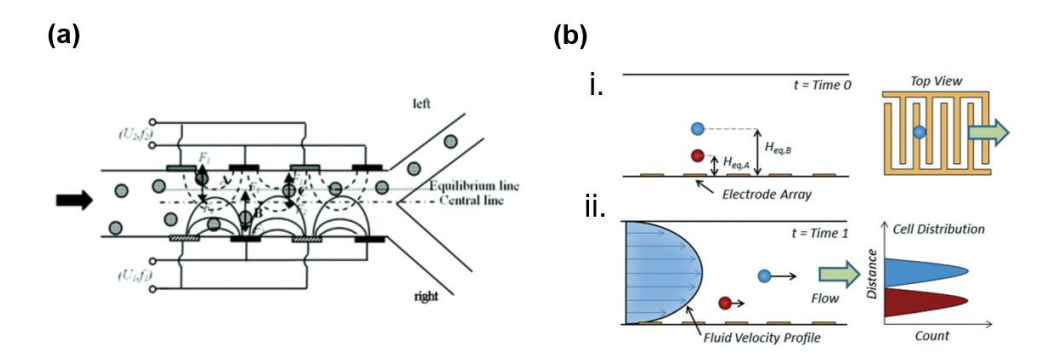


Figure 2.23 (a) Two sets of integrated electrodes in the sidewalls of the microchannel generate negative DEP forces with different directions to push particles away from the sidewall. Particles position at different equilibrium points along the width by the coupled DEP forces, flowing to a target outlet. (b) Sorting principle of DEP-FFF proposed by Vykoukal et al. (Vykoukal et al. 2008). i. An array of electrodes positions cells to equilibrium positions above the bottom of the channel according to their type. ii. Cells sorted by propelling them through the channel at rates according to their distance from the wall. Image is copied from (Wyatt Shields Iv, Reyes, and López 2015). Acoustofluidics uses an external acoustic field to move cells. In general, interdigitated transducers (IDTs) made from a piezoelectric material generate bulk acoustic waves (BAWs) (Petersson et al. 2005; Augustsson et al. 2012; Fong et al. 2014) and surface acoustic waves (SAWs) (Wu et al. 2019; Ding et al. 2014; Li et al. 2015; Nam et al. 2011). These waves form pressure and anti-pressure nodes enabling size or density-based particle separation.

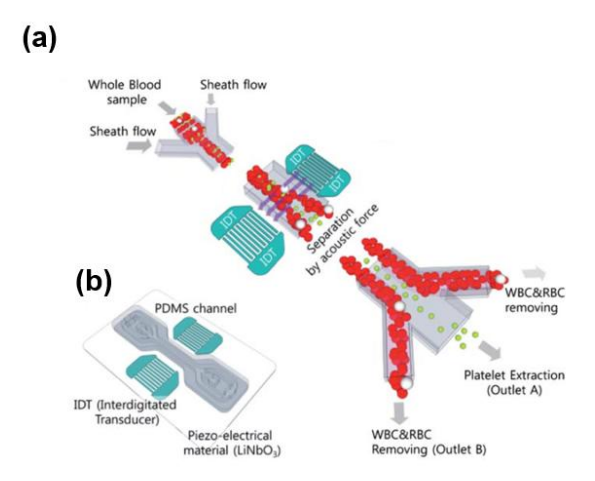


Figure 2.24 (a) Nam et al. separated platelets from blood cells by a SAW device (Nam et al. 2011). Sheath flow was used to focus the cells into a confined band. Larger cells, such as leukocytes and erythrocytes, experienced greater acoustic radiation forces, thereby migrating farther than the surrounding platelets. (b) Components of the microfluidic device.

Label-free sorting methods rely on the differences in forces experienced by cells in an applied field due to their intrinsic properties.

One choice is to use real-time images to trigger a sorter. Sorting systems proposed by Nitta et al. (Nitta et al. 2018) and Isozaki et al. (Isozaki et al. 2019) both used intelligent image-activated methods which is beyond traditional fluorescence-activated ability. It achieves high-content sorting of cells with unique spatial chemical and morphological traits. Nawaz et al. (Nawaz et al. 2020) utilised fluorescence traces and deformability data from real-time images to isolate blood cells (**Figure 2.25**). The sorter was a surface acoustic wave (SSAW). The system also used deep neural network (DNN) to train the raw images to find a predictor for a specific classification without extracting predefined features successfully sorting neutrophils from whole blood without labels.

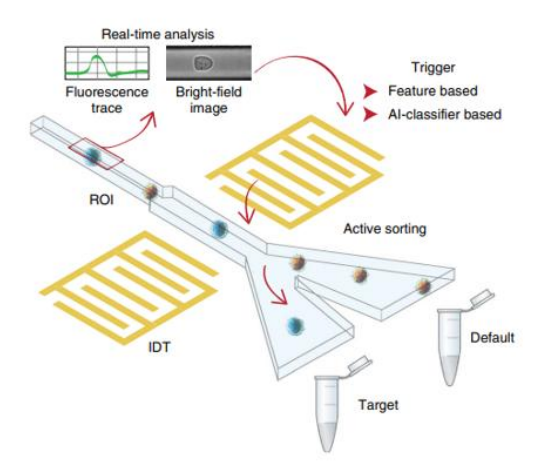


Figure 2.25 Intelligent image-based deformation-assisted cell sorting with molecular specificity (fluorescence signal) proposed by Nawaz et al. (Nawaz et al. 2020). The sorter used SSAW to change the direction of target cells.

Zhong et al. (Zhong, Li, et al. 2021) sorted human peripheral blood mononuclear cells (PBMCs) from dead cells and debris, by combining impedance-based PBMC viability assessment and acoustics cell manipulation (**Figure 2.26(a)**). Choi et al. (Choi et al. 2020) demonstrated the first single-particle-resolved, cytometry-like deformability-activated sorting in a continuous flow on a microfluidic platform. They used poly (ethylene glycol) diacrylate (PEGDA) beads as a deformability model to evaluate sorting performance (**Figure 2.26(b)**).

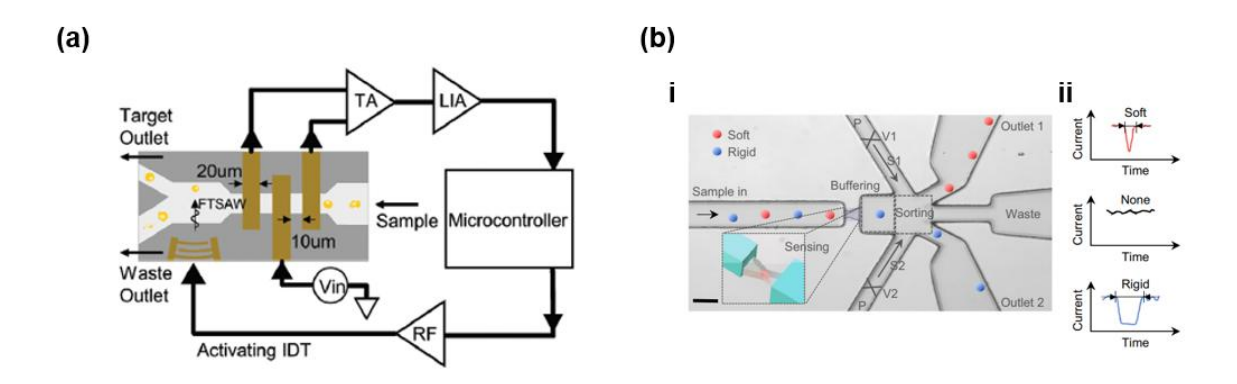


Figure 2.26 (a) Schematic diagram of the impedance-based peripheral blood mononuclear cells (PBMC) isolation system proposed by Zhong et al. (Zhong, Li, et al. 2021). (b) Choi et al. (Choi et al. 2020) proposed a microfluidic deformability-activated sorting system of single particles. Poly (ethylene glycol) diacrylate (PEGDA) beads were created as the deformability model for device validation and performance evaluation. The deformability was measured according to the transit time of particles passing through the constriction.

There are more attempts to integrate MIC with sorting functionality. Single cell differential impedance characteristic and mechanical phenotyping by extracting the transit time were integrated to trigger real-time deformability-based sorting of fixed and live MCF-7 cells mixture (Figure 2.27(a)) (Li and Ai 2021). Panwar et al. designed a novel system that combines MIC sensing with fluorescence-activated DEP sorting, enabling automated, high-throughput screening of droplets (Panwar et al. 2023) (Figure 2.27(b)).

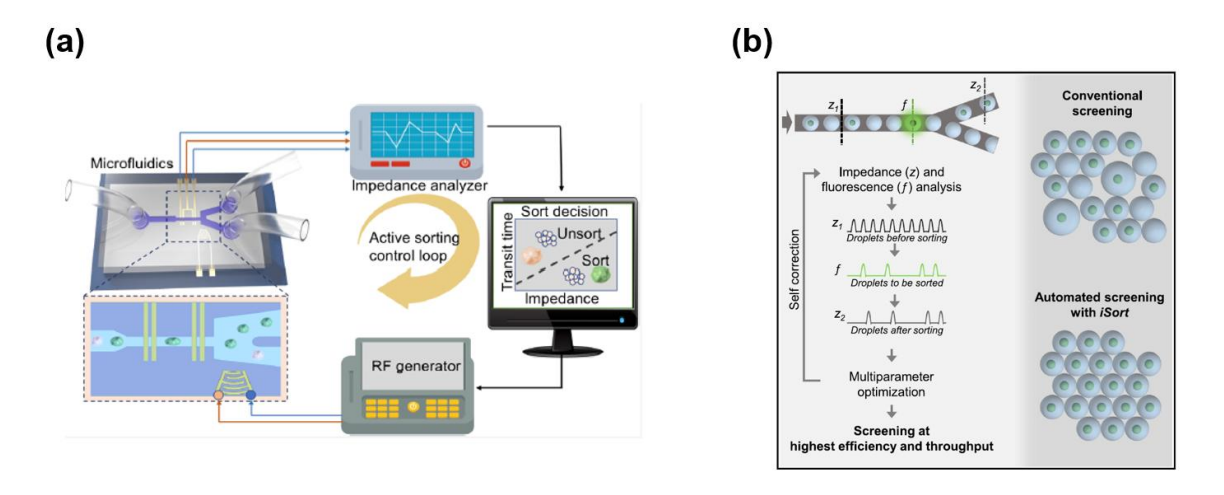


Figure 2.27 (a) Li and Ai (Li and Ai 2021) proposed an acoustic sorting system based on MIC using impedance and mechanical characteristics. (b) High-throughput automated droplet screening

using impedance to reduce false positive events and improve efficiency and stability. Copied from (Panwar et al. 2023).

In general, due to the advantages of the label-free MIC method, MIC-based sorting system is not only as a final step, but also as a pre-processing stage in cell culture and biologics production. Additionally, MIC offers multiparametric data, enabling the sorting system to distinguish and operate on various cell phenotypes based on electrical and mechanical characteristics (Righetto et al. 2025).

A sorter utilising membrane pumps relies on the mechanical actuation of an integrated membrane, where the fluid direction in a main channel is altered by the injected liquid filling the membrane pump. This sorter can be used for both label-based and label-free sorting. One way to form the membrane pump is by integrating a disc transducer which injects and sucks liquid in a side chamber (Chen et al. 2009; Rajauria et al. 2015). Chen et al. (Chen et al. 2009) used this concept to sort *E.coli* at a flow rate of ~2 μ l/min with a throughput of 24 cells/s (**Figure 2.28(a)**). Rajauria et al. (Rajauria et al. 2015) developed a high-speed sorting system based on a pair of disc transducers, enabling a throughput of 60,000 particles/min (**Figure 2.28(b)**).

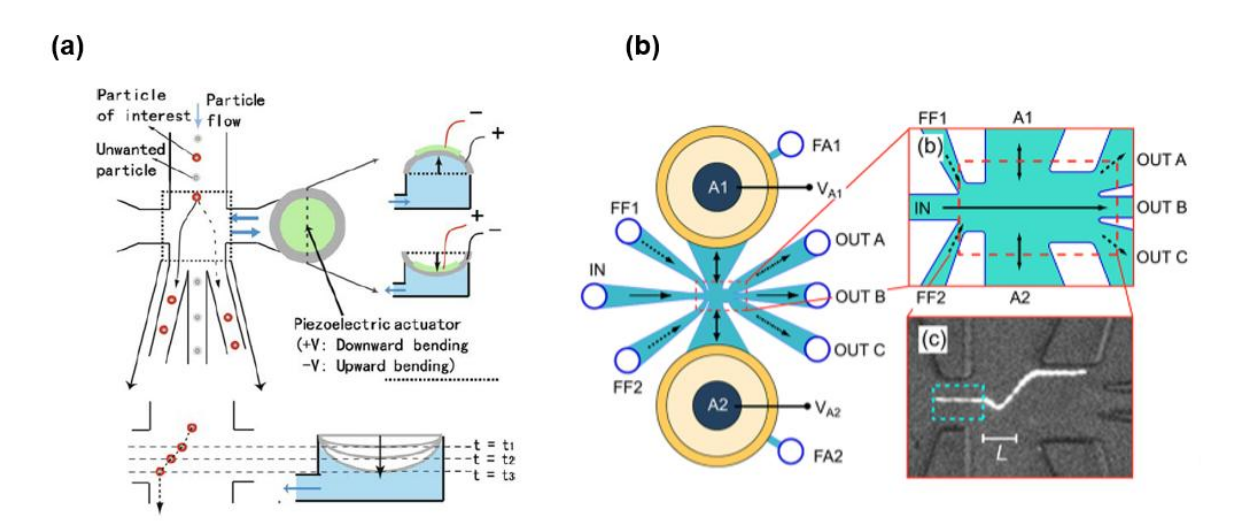


Figure 2.28 (a) Chen et al. developed a membrane pump sorter using a piezoelectric (PZT) actuator (Chen et al. 2009). As the particles enter the sorting junction, the bending motion of the PZT actuator temporarily disturbs fluid flow, deflecting target particle to the left-right channels. When the PZT was not triggered, unwanted particles stayed in the centre streamlines towards the middle waste channel. (b) Rajauria et al. developed a high-speed sorting system with a pair of PZT actuators, with a throughput of 60000 particles/min.

On-chip membrane pumps are fabricated directly into the microfluidic chip, actuated by external drivers, instead of integrated component, such as disc transducers. Sakuma et al. (Sakuma et al. 2017) fabricated chips with membrane pumps, and external piezoelectric actuators to generate a push/pull flow (**Figure 2.29(a**)). This sorter was applied to an intelligent image-based detection mechanism to isolate human platelets (**Figure 2.29(b**)).

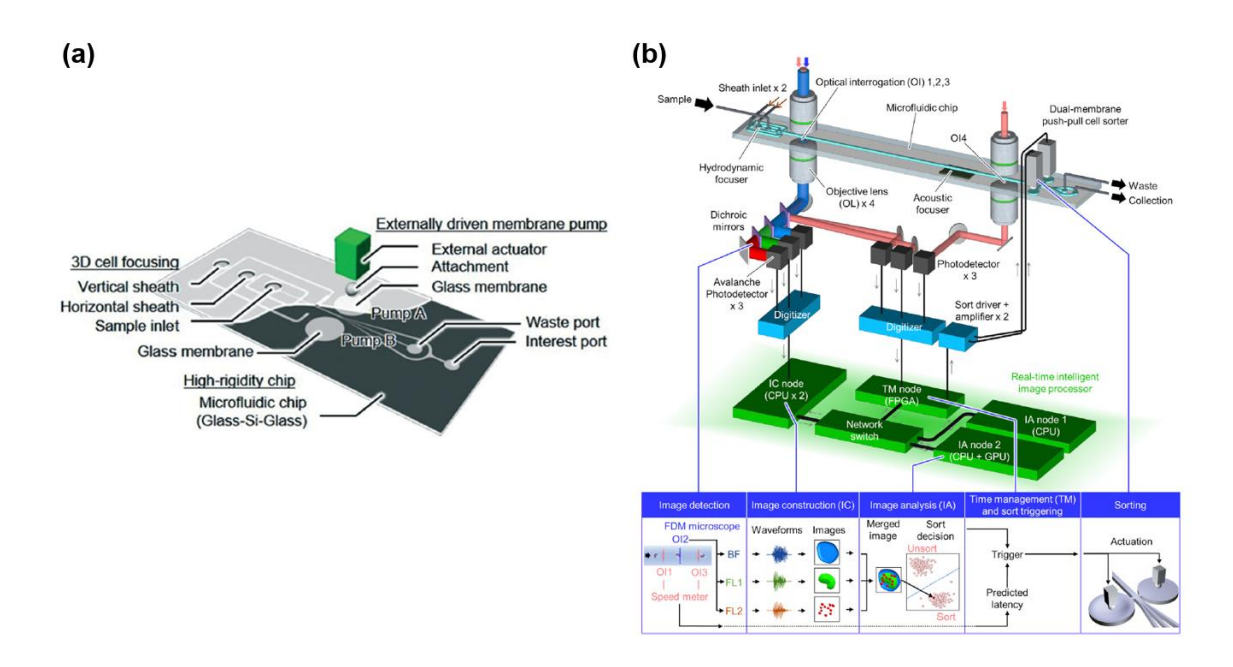


Figure 2.29 (a) Conceptual image of the on-chip cell sorter using dual-membrane pumps proposed by Sakuma et al. (Sakuma et al. 2017). The membrane pumps were fabricated on the chip and the membrane deflection was driven by the piezoelectric actuator. (b) Nitta et al. (Nitta et al. 2018) integrated high-speed intelligent image-based detection.

2.3.3 Discussion

Many label-based and label-free platforms have been developed, integrated with active or passive sorters. Which method is the best remains to be decided, as no single type of sorter can universally meet all requirements due to variability in sample conditions and target cell specifications. Trade-offs between sorting efficiency and purity must be carefully weighed during system selection. Additionally, the implementation of the sorter needs to consider both technical complexity and process feasibility because some sorters are hard to integrate with the pre-existing detection methods.

This project focuses on single-cell MIC analysis, with a separation system based on MIC detection. The selection of a sorter should consider chip dimensions, fabrication cost, production cycle and the ease of integration into the mechanical design of an existing device. Since the fabrication cost of making a batch of chips in the cleanroom is hundreds of pounds, with a production cycle of several weeks, it is necessary to place as many chip as possible on one wafer mask, minimising the chip size within feasible limits to reduce costs and fabrication time. Thus, the on-chip membrane pump shown in **Figure 2.29** was considered to be the optimal solution for the requirement of this project. The design details and experimental verification are presented in **Chapter 6**.

Chapter 3 Theory and Simulation

3.1 Introduction

Label-free microfluidic impedance cytometry (MIC) is a single-cell analysis technique for the non-invasive, high throughput and multiparameter characterisation of cells without requiring fluorescent or chemical labels. This technique differentiates cells according to their intrinsic dielectric signatures (e.g. membrane capacitance) and/or mechanical properties (e.g. deformability). This thesis describes a method for single-cell biophysical analysis, with combined single cell dielectric measurement and deformability measurement, coupled with single-cell sorting.

Chapter 2 reviews previous studies of these fields. Traditional cell dielectric analysis methods such as electrical impedance spectroscopy (EIS) and single-cell electrorotation (ROT) either require complex cell trapping structures or suffer from low throughput and operating difficulty (Kang et al. 2013; Hong, Lan, and Jang 2012; Arnold and Zimmermann 1982a). For deformability assessment, existing microfluidic techniques predominantly use contact-based methods (Lange et al. 2015; Lange et al. 2017; Chen et al. 2011) or sheath flow to induce cell deformation (Petchakup et al. 2022; Urbanska et al. 2020), however, these techniques suffer from issues such as clogging and complicated channel fabrication. Early work on single-cell sorting is based on measuring the impedance magnitude or opacity (Zhu et al. 2024), without incorporating mechanical cellular deformability. The aim of this thesis is to address these limitations and to develop a combined method for real-time sorting of single cells according to their electromechanical phenotypes.

This chapter describes the theoretical foundation for the experimental investigations. It covers three domains: dielectric characterisation of single cells, mechanical modelling of cells, and microfluidic principles. The structural analysis and operational mechanisms of a cell sorting system are modelled using mechanical derivations and computational simulations.

3.2 Single-cell Electrical Theory and Model

The operational principle of MIC originates from dielectric polarisation in an applied alternating electric (AC) fields. Dielectric materials are polarised when they are placed in an electric field and molecules orientate in the direction of the applied field. The polarised systems exhibit relaxation dynamics following Debye's theory, where the relaxation time constant (τ) characterises the time taken for the dipoles to polarise. When subjected to a field with a frequency that is far below the relaxation time, all dipoles have time to orientate, and the polarisation reaches a maximum. As

the frequency increases beyond a critical value $f_c = 1/(2\pi\tau)$, polarisation becomes progressively phase-lagged, resulting in permittivity dispersion. This decline in polarizability reduces energy storage, a phenomenon known as dielectric relaxation. In heterogeneous biological systems, Maxwell-Wagner interfacial polarisation dominates the dielectric response. This interfacial phenomenon arises from conductivity-dielectric contrast between adjacent components. In the experimental configuration used in this thesis, where cells are suspended in electrolyte between planar electrodes, the Maxwell-Wagner interfacial polarisation mechanism leads to frequency-dependent impedance variations in the system. This change in particle-medium dielectric contrast forms the basis of the MIC spectroscopy platform.

The dielectric response of biological suspensions is characterised by the complex permittivity. This is linked to the Clausisu-Mossotti factor through Maxwell's Mixture Theory (MMT). MMT establishes the quantitative relationship between these parameters with multi-particle systems treated as a homogeneous continuum with an effective complex permittivity. This continuum representation enables the derivation of intrinsic cellular dielectric properties when coupled with multi-shell modelling frameworks. Nucleated cells are modelled as a double-shell model, introduced in this section.

The dielectric characteristics of the suspending medium, particularly its ionic conductivity, influence the Clausius-Mossotti factor. The experimental realisation of this principle using is detailed in **Chapter 5**.

3.2.1 Complex permittivity

The polarisation of non-ideal dielectric materials in an alternating electric (AC) field is modelled through parallel-plate capacitor theory. Unlike ideal dielectrics where polarisation arises solely from bound charges, lossy dielectrics exhibit dual charge transport mechanisms: mobile charge carriers and bound polarisation charges. This dual nature necessitates a combined RC circuit representation, where the complex impedance (Z^*) of the system is expressed as a parallel combination of conductive and capacitive pathways (**Figure 3.1**):

$$Z^* = \frac{1}{\frac{1}{R} + j\omega C} = \frac{R}{1 + j\omega RC}$$
 (3.1)

The impedance of the resistor (R) and capacitor (C) are (Morgan and Green 2003):

$$R = \frac{D}{\sigma^A} \tag{3.2}$$

$$C = \varepsilon^* \frac{A}{D} \tag{3.3}$$

where ε^* is the complex permittivity of the dielectric. It is given by:

$$\varepsilon^* = \varepsilon - j \frac{\sigma}{\omega} \tag{3.4}$$

Thus, the total impedance is:

$$Z^* = \frac{D}{\sigma A + i\omega A \varepsilon^*} \tag{3.5}$$

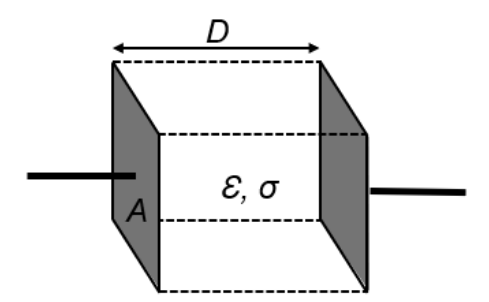


Figure 3.1 Diagram of the parallel plate capacitor. A is the plate area, D is the separated distance, ε is permittivity, and σ is the conductivity of the dielectric.

The frequency-dependent polarisation manifests as a relationship between displacement current (capacitive component) and conduction current (resistive component). The critical frequency (f_c) marking the transition between these mechanisms is determined by:

$$f_c = \frac{\sigma}{2\pi\varepsilon} \tag{3.6}$$

This frequency-dependent behaviour forms the physical basis for dielectric spectroscopy, enabling discrimination between interfacial polarisation (Maxwell-Wagner effect) and bulk dielectric relaxation (Debye mechanism) in biological systems.

3.2.2 Clausius-Mossotti factor and Maxwell Mixture Theory

Dielectric spectroscopy measures the complex permittivity ε^*_{mix} of a particle suspension through Maxwell's Mixture Theory (MMT), which is given by:

$$\varepsilon_{mix}^{*} = \varepsilon_{med}^{*} \frac{1 + 2\varphi_{cell} f_{CM(cell)}^{*}}{1 - \varphi_{cell} f_{CM(cell)}^{*}} = \varepsilon_{med}^{*} \frac{1 + 2\varphi_{cell} \left(\frac{\varepsilon_{cell}^{*} - \varepsilon_{med}^{*}}{\varepsilon_{cell}^{*} + 2\varepsilon_{med}^{*}}\right)}{1 - \varphi_{cell} \left(\frac{\varepsilon_{cell}^{*} - \varepsilon_{med}^{*}}{\varepsilon_{cell}^{*} + 2\varepsilon_{med}^{*}}\right)}$$
(3.7)

where ε^*_{med} is the media complex permittivity, φ_{cell} is the volume fraction that a cell occupies in the suspending medium and the Clausius-Mossotti factor of a cell $f^*_{CM(cell)}$ is defined as:

$$f_{CM(cell)}^* = \frac{\varepsilon_{cell}^* - \varepsilon_{med}^*}{\varepsilon_{cell}^* + 2\varepsilon_{med}^*}$$
(3.8)

Note that the MMT is only applicable with a small volume fraction (φ_{cell} <0.01).

3.2.3 Shell model

The shell-model provides a framework for modelling the stratified dielectric structure of biological cells through concentric layers of homogeneous dielectrics. The multi-shell model developed by Irimajiri et al. (Irimajiri, Hanai, and Inouye 1979) is widely used to determine the dielectric parameters of cells from experimental impedance data. As schematically illustrated in **Figure 3.2**, each cellular compartment (membrane, cytoplasm, etc.) is represented as a discrete shell with distinct complex permittivity parameters. The simplest model is the single-shell model (**Figure 3.2(a**)), which ignores the nucleus and is usually applied to red blood cells. The double-shell model is required to fully describe the nucleated cells.

The single-shell model is briefly introduced here. The complex permittivity of the cell ε_{cell}^* is expressed as:

$$\varepsilon_{cell}^* = \frac{2\varepsilon_1^*(1 - \gamma_a) + \varepsilon_2^*(1 + 2\gamma_a)}{\varepsilon_1^*(2 + \gamma_a) + \varepsilon_2^*(1 - \gamma_a)}$$
(3.9)

where ε_1^* and ε_2^* are complex permittivity of the cell membrane and cytoplasm. The factor γ_a is written as $\gamma_a = (R_a/r_{cell})^3$, with r_{cell} the cell radius, and $R_a = r_{cell} - d_1$, where d_1 is the thickness of cell membrane.

Figure 3.2(b) shows the nucleated cell modelled with four concentric dielectric layers. The membrane thickness is d_1 and the nuclear envelope thickness is d_3 . The cell permittivity is derived through (Mansoorifar et al. 2017; Irimajiri, Hanai, and Inouye 1979):

$$\varepsilon_{cell}^* = \varepsilon_1^* \frac{2(1 - \gamma_a) + (1 + 2\gamma_a)E_a}{(2 + \gamma_a) + (1 - \gamma_a)E_a}$$
(3.10)

where the subscript "1" indicates cell membrane. The factor γ_a is given by $\gamma_a = (R_a/r_{cell})^3$, with r_{cell} the cell radius, and $R_a = r_{cell} - d_1$. The parameter E_a is given by:

$$E_a = \frac{\varepsilon_2^*}{\varepsilon_1^*} \frac{2(1 - \gamma_b) + (1 + 2\gamma_b)E_b}{(2 + \gamma_b) + (1 - \gamma_b)E_b}$$
(3.11)

Here, the subscript "2" stands for cytoplasm, $\gamma_b=(R_b/R_a)^3$, with R_b the radius of the nucleus and

$$E_b = \frac{\varepsilon_3^*}{\varepsilon_2^*} \frac{2(1 - \gamma_c) + (1 + 2\gamma_c)E_c}{(2 + \gamma_c) + (1 - \gamma_c)E_c}$$
(3.12)

The subscript "3" is the nuclear envelope, $\gamma_c=(R_c/R_b)^3$, with $R_c=R_b-d_3$ and d_3 the thickness of the nuclear envelope. Finally, E_c is:

$$E_c = \frac{\varepsilon_4^*}{\varepsilon_3^*} \tag{3.13}$$

and subscript "4" refers to the nucleoplasm. Finally, the complex permittivity of a cell ε_{cell}^* in **equation 3.8** is given by the iterations of inner layers dimensions and dielectric parameters.

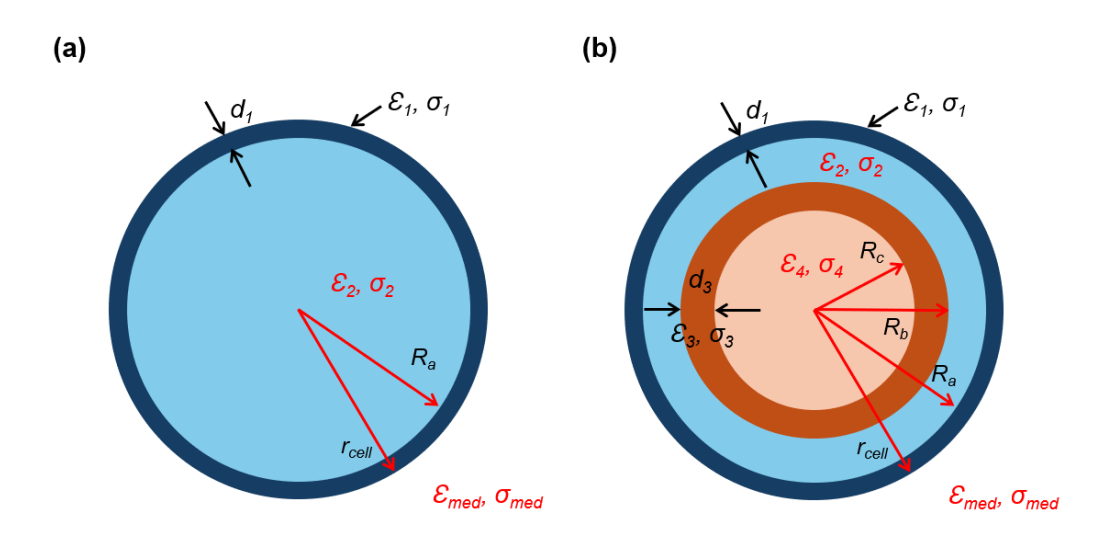


Figure 3.2 Schematic diagram of (a) single-shell model and (b) double-shell model. ε_i is the permittivity and σ_i is conductivity. Subscript 1: cell membrane, 2: cytoplasm, 3: nuclear envelope, 4: nucleoplasm, med: media. r_{cell} is the radius of cell, d_1 is membrane thickness, $R_a = r_{cell} - d_1$, d_3 is thickness of nuclear envelope, R_b is the radius of the nucleus, $R_c = R_b - d_3$.

3.2.4 Simulations

3.2.4.1 Frequency spectrum with different conductivity medium

Physiological saline with a permittivity of $80\varepsilon_0$ and conductivity of 1.6 S/m is usually employed as the standard suspension medium for MIC measurement. The dielectric spectrum is derived through calculations of the Clausius-Mossotti factor $f_{CM(cell)}^*$ (equation 3.8) after obtaining ε_{cell}^* from the multi-shell equation (equations 3.9 and 3.10). This suspending medium contrasts with conventional dielectric measurement protocols (e.g., electrorotation (ROT), dielectrophoresis (DEP)) that typically utilise low-conductivity media (< 0.1 S/m). That is motivated to avoid issues with electrode polarisation, which is much worse for a high conductivity media, to avoid Joule heating and to limit the operating frequency range so that the characteristic relaxation frequencies ($f_c \propto \sigma/\varepsilon$) of cell dielectric parameters decrease to accessible ranges. Nevertheless, for single-cell impedance characterisation, a lower suspension media conductivity leads to a lower current through the micro-channel and SNR (signal-noise-ratio). For example, from the experiments which will be introduced in details in section 5.2.2.2, the SNRs of beads and cells in 0.32 S/m conductivity media are 8.5 dB and 11.4 dB, whilst these values in 1.6 S/m conductivity saline are 13.6 dB and 18.9 dB. There is a trade-off between optimising the suspending media

conductivity for SNR (higher conductivity) and eliminating issues caused by interfacial polarisation (lower conductivity).

The figures below show the frequency spectrum of $f_{CM(cell)}^*$ calculated from single- and double-shell models for different conductivity media.

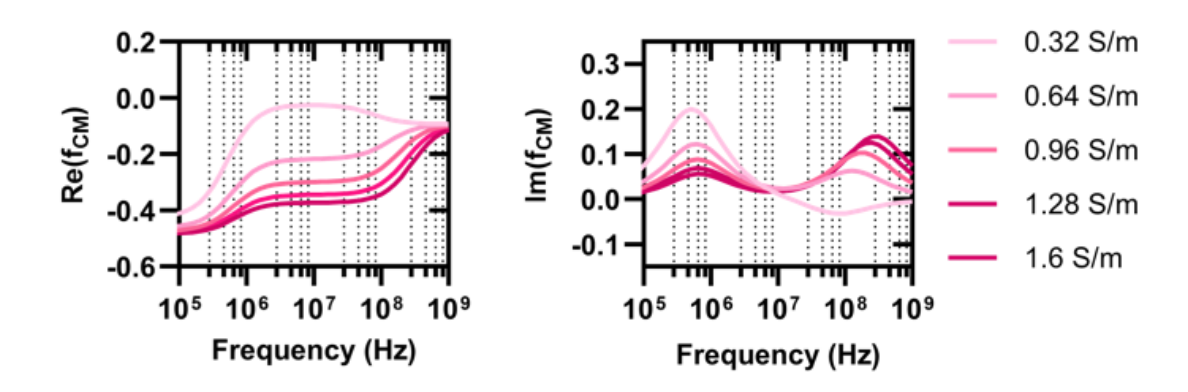


Figure 3.3 Real and imaginary parts of $f_{CM(cell)}^*$ for a single shell model when changing the media conductivity σ_{med} from 0.32 S/m to 1.6 S/m. The cell dielectric parameters are: ε_{med} = 80 ε_0 , ε_1 = 7 ε_0 , σ_1 = 3.14×10⁻⁵ S/m, ε_2 = 60 ε_0 , σ_2 = 0.3 S/m, d_1 = 5nm, r_{cell} (cell radius) = 6 μ m. Subscript: "med" – media, "1" – cell membrane, "2" – cytoplasm.

Figure 3.3 shows a real and imaginary parts of $f_{CM(cell)}^*$ as a function frequency modelled with the single shell for a conductivity from 1.6 to 0.32 S/m, revealing two distinct dielectric relaxations. The one at low frequency is the polarisation between the suspending media and cell membrane, and the higher frequency is between the membrane and the cytoplasm. For the imaginary part, the frequency of the first peak remains invariant with media conductivity. However, as the conductivity decreases, the second peak gradually shifts to the left, indicating that lower conductivity reduces the required maximum frequency for characterising membrane and cytoplasm properties. This reduction helps the measurement process, as generating a lower maximum frequency is easier for the system.

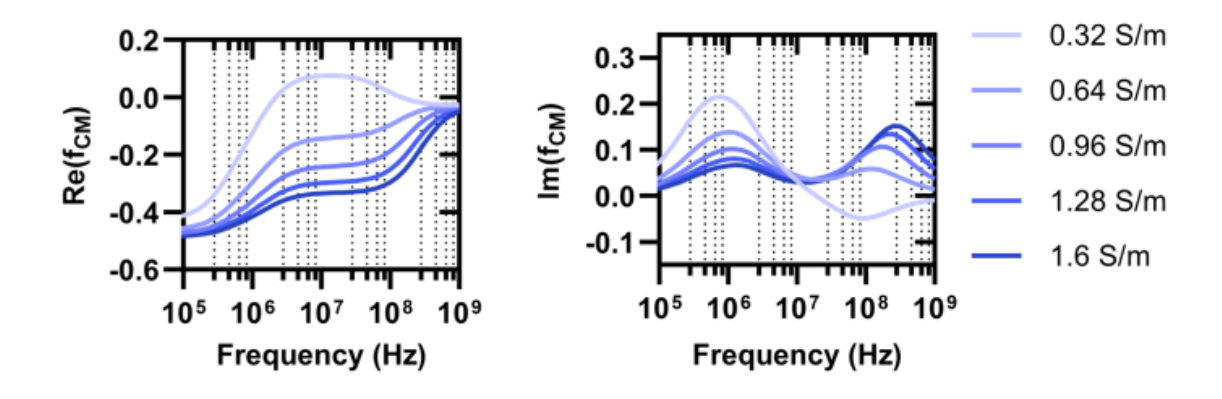


Figure 3.4 Real and imaginary parts of $f_{CM(cell)}^*$ for a double shell model for different media conductivity σ_{med} from 0.32 S/m to 1.6 S/m. The dielectric parameters are: ε_{med} = 80 ε_0 , ε_1 = 7 ε_0 , σ_1 = 3.14×10⁻⁵ S/m, ε_2 = 60 ε_0 , σ_2 = 0.3 S/m, ε_3 = 52 ε_0 , σ_3 = 1.8×10⁻³ S/m, ε_4 = 120 ε_0 , σ_4 = 0.82 S/m, d_1

= 5nm, d_3 = 20nm, r_{cell} (cell radius) = 6 μ m, R_b (nucleus radius) = 4 μ m. Subscript: "med" – media, "1" – cell membrane, "2" – cytoplasm, "3" – nuclear envelope, "4" – nucleoplasm.

The double-shell model simulation for different media conductivity is presented in **Figure 3.4**. The curves are similar to that of the single-shell model simulation. However, the magnitudes of both the real and imaginary components are significantly higher, and the curve shapes at frequencies higher than 10MHz are very different. For example, the imaginary part of the single-shell model is much flattened than the double-shell model. This suggests that the single-shell model is inadequate for accurately modelling a nucleated cell and may lead to erroneous estimations of the dielectric properties of the cell membrane and cytoplasm.

3.2.4.2 Frequency spectrum with different cell parameters

This section presents simulations of single- and double-shell models for high (1.6 S/m) and low (0.32 S/m) conductivity media.

In the first scenario, modifications are made to the properties of the non-nuclear regions of the cell. Variations in cell diameter (d), membrane capacitance ($C_1=\varepsilon_1/d_1$) and cytoplasm conductivity (σ_2) affect different frequency ranges in the plot of $f_{CM(cell)}^*$.

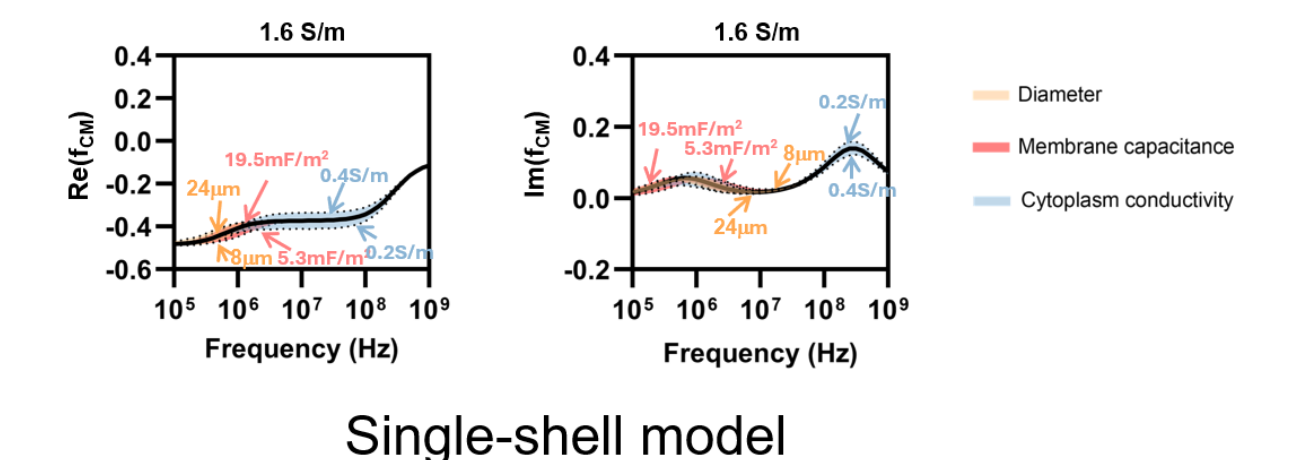
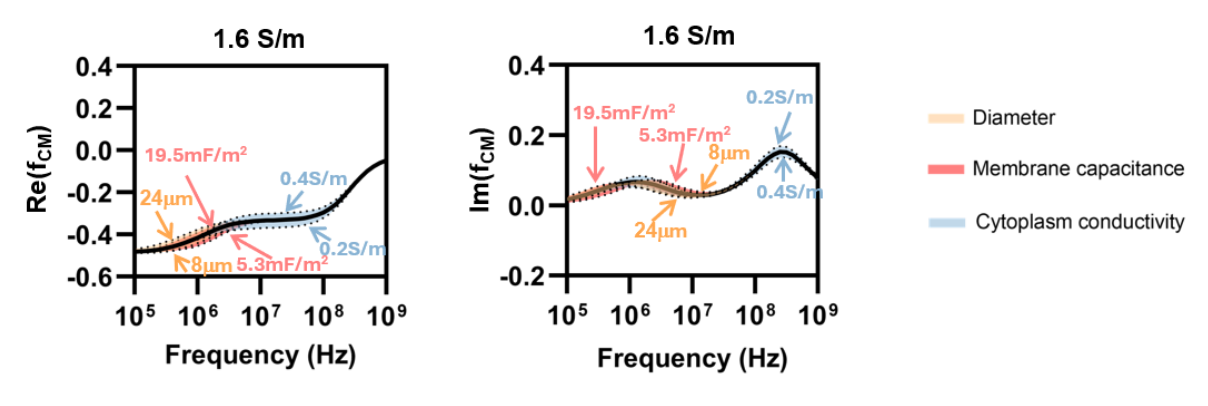


Figure 3.5 Real and imaginary parts of $f_{CM(cell)}^*$ for a single shell model in physiological saline when modifying cell diameter (d, 8µm~24µm, orange region), membrane capacitance (C_1 , 5.3mF/m²~19.53mF/m², red region) and cytoplasm conductivity (σ_2 , 0.2 S/m~0.4 S/m, blue region). Other parameters are the same as the "typical" setting for the black curve. Cell dielectric parameters for the black curve: $\varepsilon_1 = 7\varepsilon_0$ ($C_1 = 12.4$ mF/m²), $\sigma_1 = 3.14 \times 10^{-5}$ S/m, $\varepsilon_2 = 60\varepsilon_0$, $\sigma_2 = 0.3$ S/m, $d_1 = 5$ nm, $d_2 = 6$ 0 cell (cell radius) = 6µm. Subscript: "1" – cell membrane, "2" – cytoplasm.



Double-shell model

Figure 3.6 Real and imaginary parts of $f_{CM(cell)}^*$ for a single shell model in physiological saline when modifying cell diameter (d, 8µm~24µm, orange region), membrane capacitance (C_1 , 5.3mF/m²~19.53mF/m², red region) and cytoplasm conductivity (σ_2 , 0.2 S/m~0.4 S/m, blue region). Other parameters are the same as the "typical" setting for the black curve. Cell dielectric parameters for the black curve: $\varepsilon_1 = 7\varepsilon_0$ ($C_1 = 12.4$ mF/m²), $\sigma_1 = 3.14 \times 10^{-5}$ S/m, $\varepsilon_2 = 60\varepsilon_0$, $\sigma_2 = 0.3$ S/m, $\varepsilon_3 = 52\varepsilon_0$, $\sigma_3 = 1.8 \times 10^{-3}$ S/m, $\varepsilon_4 = 120\varepsilon_0$, $\sigma_4 = 0.82$ S/m, $d_1 = 5$ nm, $d_3 = 20$ nm, r_{cell} (cell radius) = 6µm, R_b (nucleus radius) = 4µm. Subscript: "med" – media, "1" – cell membrane, "2" – cytoplasm, "3" – nuclear envelop, "4" – nucleoplasm.

Figures 3.5 and 3.6 show the $f_{CM(cell)}^*$ spectrum in physiological saline for both single- and double-shell models. The shaded region in the plot illustrates variation in the frequency window resulting from changes in cell diameter (*d*), membrane capacitance (C_1) and cytoplasm conductivity (σ_2). At low frequencies (<1MHz), the impedance is primarily governed by cell dimensions and membrane dielectric properties. In the intermediate frequency range (1MHz~100MHz), multiple factors contribute, including cell dimensions, membrane characteristics, and cytoplasm properties. At higher frequencies (>100MHz), cytoplasm dielectric properties become the dominant factors. The slight difference in curve magnitude between the two models indicates that the presence of a nucleus provides additional information for accurate cell modelling.

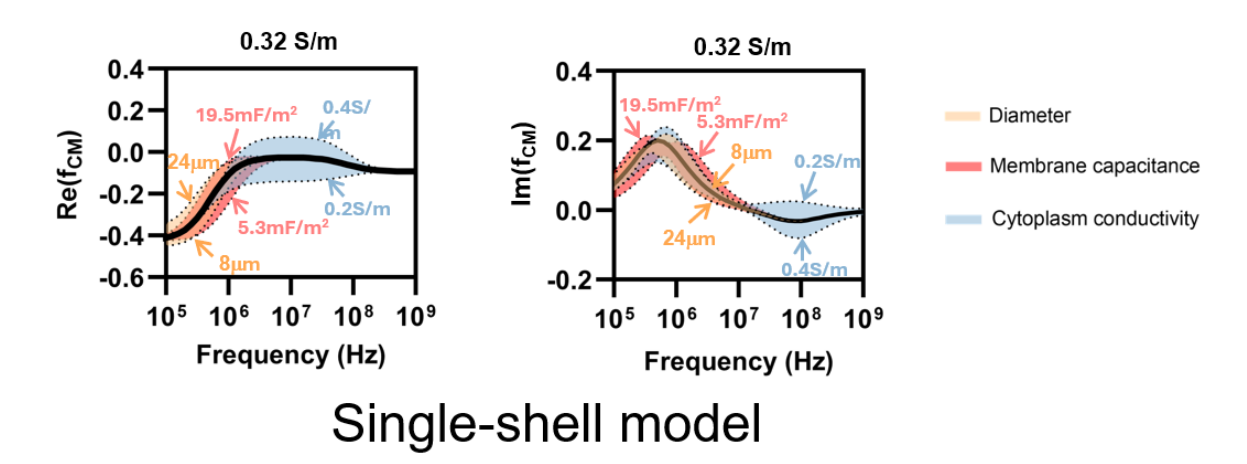


Figure 3.7 Real and imaginary parts of $f_{CM(cell)}^*$ for a single shell model in low-conductivity (0.32 S/m) media when modifying cell diameter (d, 8 μ m~24 μ m, orange region), membrane capacitance (C_1 , 5.3mF/m²~19.53mF/m², red region) and cytoplasm conductivity (σ_2 , 0.2 S/m~0.4

S/m, blue region). Other parameters are the same as the "typical" setting for the black curve. Cell dielectric parameters for the black curve: $\varepsilon_1 = 7\varepsilon_0$ ($C_1 = 12.4$ mF/m²), $\sigma_1 = 3.14 \times 10^{-5}$ S/m, $\varepsilon_2 = 60\varepsilon_0$, $\sigma_2 = 0.3$ S/m, $d_1 = 5$ nm, r_{cell} (cell radius) = 6 μ m. Subscript: "1" – cell membrane, "2" – cytoplasm.

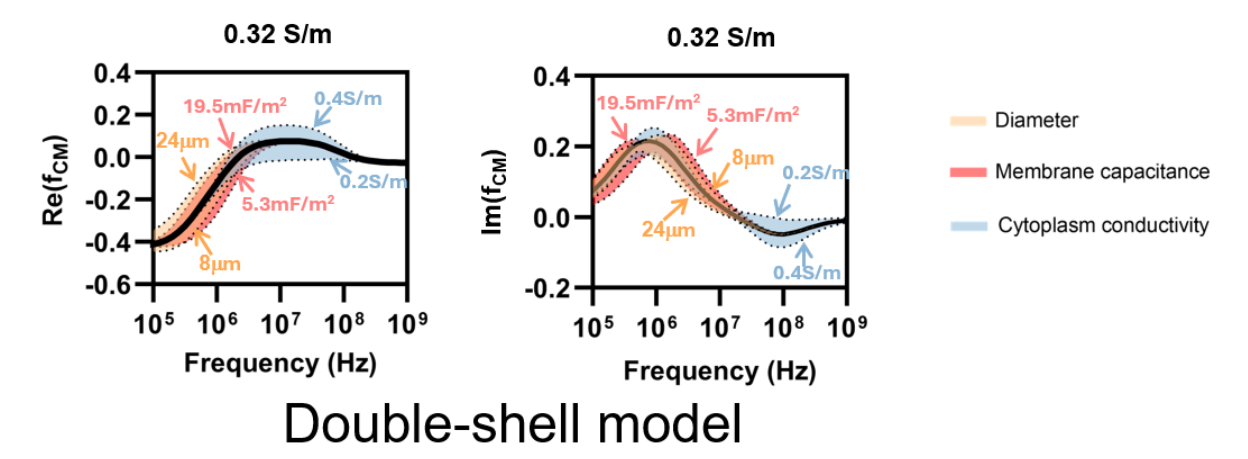
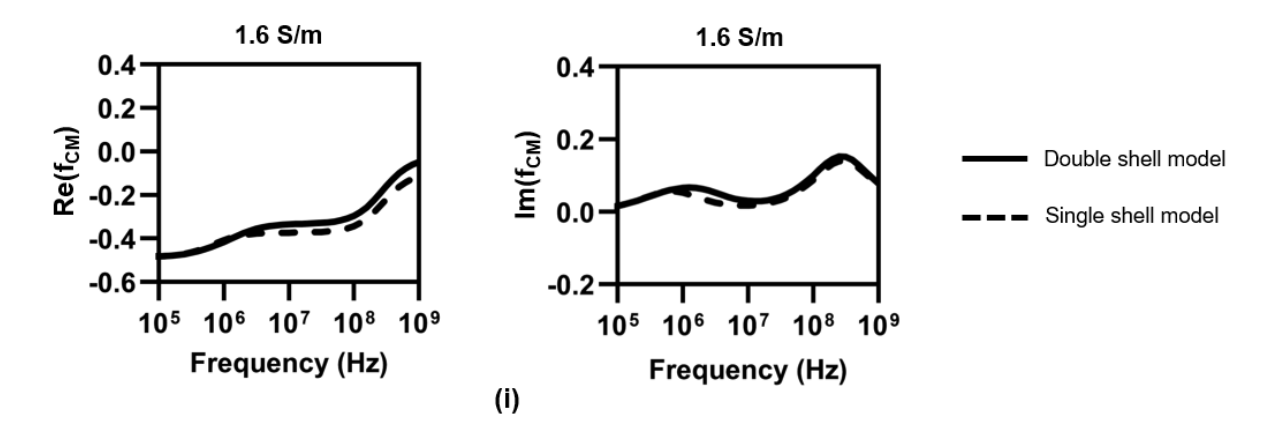


Figure 3.8 Real and imaginary parts of $f_{CM(cell)}^*$ for a single shell model in low-conductivity (0.32 S/m) media when modifying cell diameter (d, 8µm~24µm, orange region), membrane capacitance (C_1 , 5.3mF/m²~19.53mF/m², red region) and cytoplasm conductivity (σ_2 , 0.2 S/m~0.4 S/m, blue region). Other parameters are the same as the "typical" setting for the black curve. Cell dielectric parameters for the black curve: ε_1 = 7 ε_0 (C_1 = 12.4 mF/m²), σ_1 = 3.14×10⁻⁵ S/m, ε_2 = 60 ε_0 , σ_2 = 0.3 S/m, ε_3 = 52 ε_0 , σ_3 = 1.8×10⁻³ S/m, ε_4 = 120 ε_0 , σ_4 = 0.82 S/m, d_1 = 5nm, d_3 = 20nm, r_{cell} (cell radius) = 6µm, R_b (nucleus radius) = 4µm. Subscript: "med" – media, "1" – cell membrane, "2" – cytoplasm, "3" – nuclear envelope, "4" – nucleoplasm.

Figures 3.7 and 3.8 show spectra of the single- and double-shell models in 0.32 S/m conductivity media. Consistent with the results in physiological saline, cell diameter, membrane capacitance, and cytoplasm conductivity remain the dominant factors within their respective frequency ranges. Notably, the variations within the shaded spectral regions are significantly amplified for both single- and double-shell models compared to physiological conditions. This phenomenon suggests that employing low-conductivity media enhances the detection sensitivity of cellular dielectric parameters during impedance spectroscopy measurements.

A difference in magnitude is shown in **Figure 3.9** when overlapping the curve of single- and double-shell models parameterised with the "typical" setting for cell dielectric parameters. The changes are most significance at >1MHz.



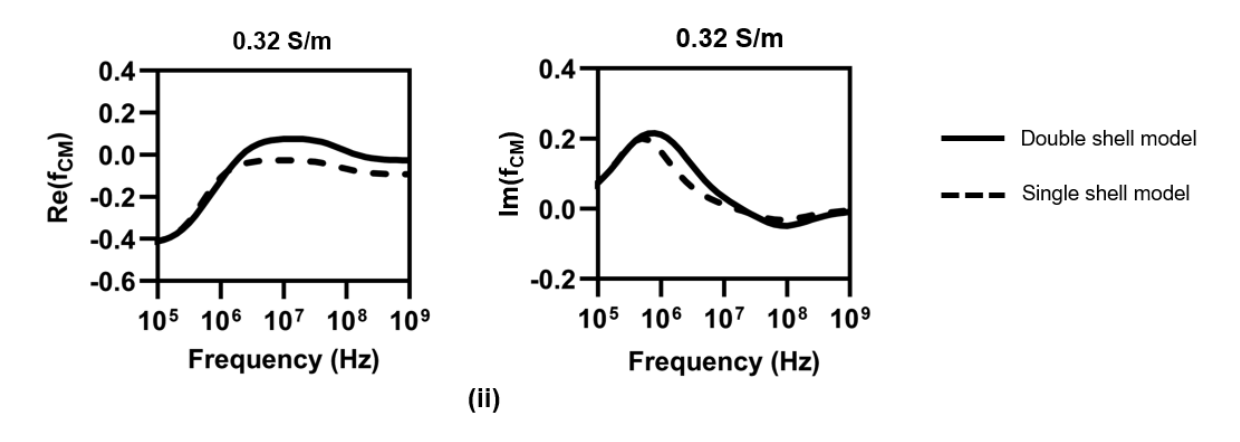


Figure 3.9 The error between single- and double-shell model simulations in (i) physiological saline and (ii) 0.32 S/m conductivity media. The cell dielectric parameters are: $\varepsilon_1 = 7\varepsilon_0$ ($C_1 = 12.4$ mF/m²), $\sigma_1 = 3.14 \times 10^{-5}$ S/m, $\varepsilon_2 = 60\varepsilon_0$, $\sigma_2 = 0.3$ S/m, $\varepsilon_3 = 52\varepsilon_0$, $\sigma_3 = 1.8 \times 10^{-3}$ S/m, $\varepsilon_4 = 120\varepsilon_0$, $\sigma_4 = 0.82$ S/m, $d_1 = 5$ nm, $d_3 = 20$ nm, r_{cell} (cell radius) = 6 μ m, R_b (nucleus radius) = 4 μ m. Subscript: "med" – media, "1" – cell membrane, "2" – cytoplasm, "3" – nuclear envelope, "4" – nucleoplasm.

A secondary effect is due to nuclear dielectric properties. The 0.32 S/m condition demonstrates superior resolution for detecting nuclear envelope changes. Therefore, **Figure 3.10** only focuses on 0.32 S/m conductivity media simulation.

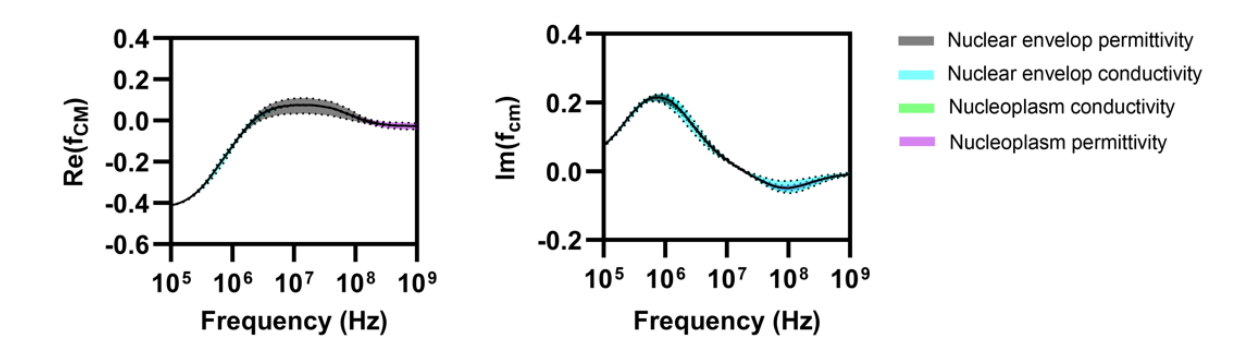


Figure 3.10 Real and imaginary parts of $f^*_{CM(cell)}$ for double-shell model in low-conductivity media

when modifying the nuclear envelope permittivity (ε_3 , $36\varepsilon_0$ ~68 ε_0 , grey region) and conductivity (σ_3 , $0.6 \times 10^{-3} \sim 3 \times 10^{-3}$ S/m, light blue region), and nucleoplasm permittivity (ε_4 , $100\varepsilon_0$ ~140 ε_0 , green region) and conductivity (σ_4 , $0.54 \sim 1.1$ S/m, purple region). Other parameters are the same as the "typical" setting for the black curve. Cell dielectric parameters for the black curve: $\varepsilon_1 = 7\varepsilon_0$ ($C_1 = 12.4$ mF/m²), $\sigma_1 = 3.14 \times 10^{-5}$ S/m, $\varepsilon_2 = 60\varepsilon_0$, $\sigma_2 = 0.3$ S/m, $\varepsilon_3 = 52\varepsilon_0$, $\sigma_3 = 1.8 \times 10^{-3}$ S/m, $\varepsilon_4 = 120\varepsilon_0$, $\sigma_4 = 0.82$ S/m, $d_1 = 5$ nm, $d_3 = 20$ nm, r_{cell} (cell radius) = 6µm, R_b (nucleus radius) = 4µm. Subscript: "med" – media, "1" – cell membrane, "2" – cytoplasm, "3" – nuclear envelope, "4" – nucleoplasm are varied. The nuclear envelope permittivity of the nuclear envelope and nucleoplasm are varied. The nuclear envelope permittivity primarily affects the real part at intermediate frequencies, though its impact is less significant than that of membrane permittivity in the low-frequency range (**Figure 3.7**). Nucleoplasm conductivity slightly influences the imaginary part at frequencies above 1 MHz but has no notable effect on the real part. The effects of nuclear envelope conductivity and nucleoplasm permittivity are minimal, as the nuclear envelope behaves like a capacitor and the nucleoplasm functions as a conductive solution, making these parameters negligible.

3.3 Single-cell Mechanics: Theory and Models

3.3.1 Young's modulus

Young's modulus, also known as elastic modulus, is a mechanical property of a material that indicates its stiffness or resistance to deformation under tensile or compressive stress. It is the ratio of stress to strain within the linear elastic region of the material's stress-strain curve:

$$G = \frac{\sigma_{Stress}}{\varepsilon_{Strain}} \tag{3.14}$$

A higher Young's modulus (*G*) means a stiff material with minor deformation under stress, while lower Young's modulus material can deform significantly under the same conditions. It is a material property and does not depend on the size and shape of the sample.

3.3.2 Solid model of cells

As mentioned in **Chapter 2**, traditional measurement methods, such as AFM, optical tweezers and micropipette aspiration, are used to quantify the mechanical properties of cells, including Young's modulus, compliance and viscosity, with the data fitted to mechanical models.

In cellular rheology, mechanical modelling of living cells primarily follows two principal theoretical frameworks, emphasising either their liquid-like or solid-like properties. Cells demonstrate strain-rate-dependent viscoelastic behaviour under external load, exhibiting characteristics that interpolate between solids and fluids. This biphasic response leads to the development of two distinct models: liquid drop models and solid models. The former considers the cell to have distinct cortical layers with different viscoelastic properties, which increases the difficulty of mathematical analysis. Continuum-based solid models assume material homogeneity through effective medium approximations, achieving significant analytical simplification. Owing to its analytical tractability and empirical validation potential, the solid model is developed here.

Viscoelastic materials are traditionally characterised by time-dependent mechanical responses with mechanical equivalent circuits of connected Hookean elastic springs and Newtonian viscous dashpots (Moeendarbary and Harris 2014). The first well-known model is the Linear Maxwell model, which mathematically proposed the meaning of viscoelasticity. An elastic spring with a constant modulus (Young's modulus), G, is in series with a viscous dashpot element with a viscosity η (Kollmannsberger and Fabry 2011) as shown in **Figure 3.11 (a)**. It illustrates the reaction of steady-state flow and stress relaxation.

Maxwell's model presents the stress relaxation but not the creep behaviour because the strain increases linearly with time rather than becoming constant over time.

Another model is the spring and dashpot parallel configuration called the Voigt model (also known as Kelvin or Kelvin-Voigt model) as shown in **Figure 3.11 (b)**.

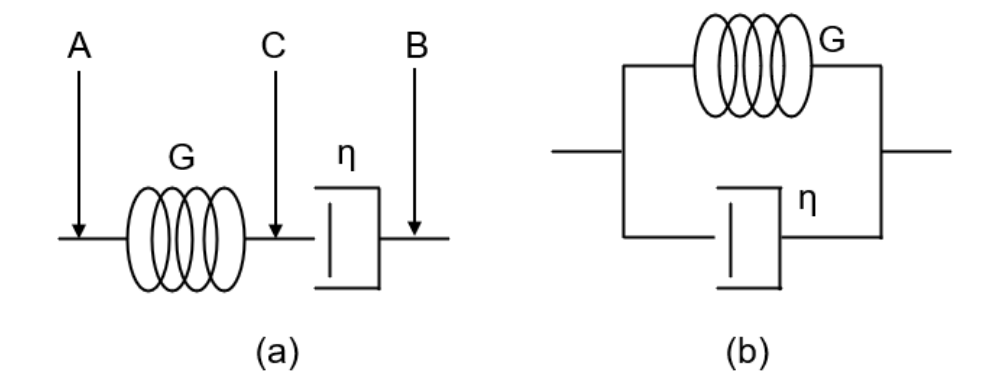


Figure 3.11 Two different standard cases of solid viscoelastic model. (a) Linear Maxwell Model (b) Voigt Model.

This configuration can model creep deformation and elastic recovery yet is inadequate to describe key viscoelastic phenomena including steady-state flow dynamics and stress relaxation behaviour. Thus, complicated configurations of Maxwell and Voigt models are used to simulate stress relaxation, creep and other viscoelastic material properties. These models are derived from transient loading conditions, but cells frequently experience dynamic forces in a physiological environment. The power-law model describes the viscoelastic behaviour of cells by a power law with a single exponent over orders of magnitude of time and frequency. This power-law structural damping is proposed to exhibit behaviours similar to soft glassy materials close to a glass transition (Sollich 1998; Fabry et al. 2001). It has been validated across numerous cell types using various techniques and spanning broad ranges of timescales or frequencies (Hoffman et al. 2006; Fabry et al. 2001; Gerum et al. 2022). However, whole-cell mechanical models are still being developed to meet the requirements of stress and time scales provided by different applied techniques, which means that cell mechanical characterisation is still phenomenological.

The deformability MIC system described in this thesis assumes that the deformation of cells is induced by shear force in a straight channel without contacting walls. The analytical model of this methodology is a solid elastic sphere, introduced in **section 3.4.5**.

3.4 Microfluidics

Compared to fluids at the macro scale, inertia is negligible and viscous forces dominate flow. This section first introduces basic microfluidics principles, such as the continuity equation and Navier-Stokes equation, Reynolds number and laminar flow. Apart from these fundamental principles, there are two essential functions of the fluid that should be taken into consideration:

particle focusing and deformation, which highly influence the impedance measurement in the microchannel of MIC. From **section 3.4.2** to **section 3.4.6**, typical methods of particle focusing and deformation are discussed and the fluid selections for this project are summarised in the **section 3.4.7**.

3.4.1 Laminar flow

The continuity equation is one of the most important equations in fluid mechanics. It describes the conservation of mass. It states that the rate at which mass enters a system is equal to the rate at which mass leaves the system plus the accumulation of mass within the system (Rapp 2022). The continuity equation is written as:

$$\frac{\partial \rho}{\partial t} + \vec{\nabla} \cdot \rho \vec{v} = 0 \tag{3.15}$$

Where \vec{v} is the velocity of the fluid and ρ is the fluid density. If the fluid is incompressible, ρ is a constant and therefore $\frac{\partial \rho}{\partial t} = 0$ and $\vec{\nabla} \cdot \rho \vec{v} = \vec{\nabla} \cdot \vec{v}$. The equation then becomes:

$$\vec{\nabla} \cdot \vec{v} = 0 \tag{3.16}$$

In general, the Navier-Stokes equation describes the conservation of momentum:

$$\rho \left[\frac{\partial v}{\partial t} + (\vec{v} \cdot \vec{\nabla}) \vec{v} \right] = -\vec{\nabla} p + \eta \vec{\nabla}^2 \vec{v} + \vec{f}$$
(3.17)

Where p is the pressure, η is the dynamic viscosity and \vec{f} is the applied force. The left-hand side is the inertial terms, and the force terms are on the right. Inertial terms consist of a change of velocity with time at a fixed point: $\frac{\partial v}{\partial t}$ and convective acceleration which describes change in the direction of motion: $(\vec{v} \cdot \vec{\nabla})\vec{v}$. Pressure gradient $(-\vec{\nabla}p)$, the viscous effects $(\eta \vec{\nabla}^2 \vec{v})$ and other forces (\vec{f}) are force terms.

Reynolds number is dimensionless and defined as the ratio of inertial to viscous forces. It is used to determine whether viscous forces or inertial forces dominate the flow:

$$Re = \frac{inertial\ forces}{viscous\ forces} = \frac{\rho vL}{\eta}$$
 (3.18)

Here ρ is the fluid density, v the characteristic fluid velocity, L the characteristic length of the system, and η the viscosity. In the case of the microfluidic system in this thesis, the length scale L is $\sim 10^{-4} m$, the characteristic velocity v ranges from $\sim 10^{-2} - 10^{-3} m/s$, and for commonly used aqueous solutions, density $\rho = 10^3 kg/m^3$ and $\eta = 10^{-3} kg/(m \cdot s)$. Thus, Re is 0.1 - 0.01. If Re < 1, the viscous terms dominate the dynamics of the fluid, while the Re > 1 the inertial terms dominate. In common microfluidic systems, viscosity dominates. Moreover, a system has

laminar flow if Re is less than ~2000, and when Re > ~2000, the flow can be turbulent (Klein and Dietzel 2021).

The Hagen-Poiseuille equation is a solution under laminar conditions of the Navier-Stokes equations. In this circumstance, the velocity profile is parabolic, and the fastest flow is located in the centre of the channel.

3.4.2 Sheath flow focusing

Sheath flow focusing, is widely used in microfluidic devices, and employs auxiliary sheath fluids to hydrodynamically confine a sample stream to the channel centreline. In this technique one or more sheath flows progressively constrict the sample along the axial direction. Based on the dimensionality of confinement, sheath flow focusing can be categorised into two distinct modalities: 2D focusing and 3D focusing.

2D focusing uses one-dimensional confinement, normally horizontal along the direction of flow. A mathematical model established by Knight et al. (Knight et al. 1998) correlates focused stream width with flow resistance ratios of inlet, side, and outlet channels. They focused the sample flow stream down to approximately 50nm inside a 10µm channel by precisely modulating the pressure ratio of the sample inlet to that of sheath flow channels (**Figure 3.12**).

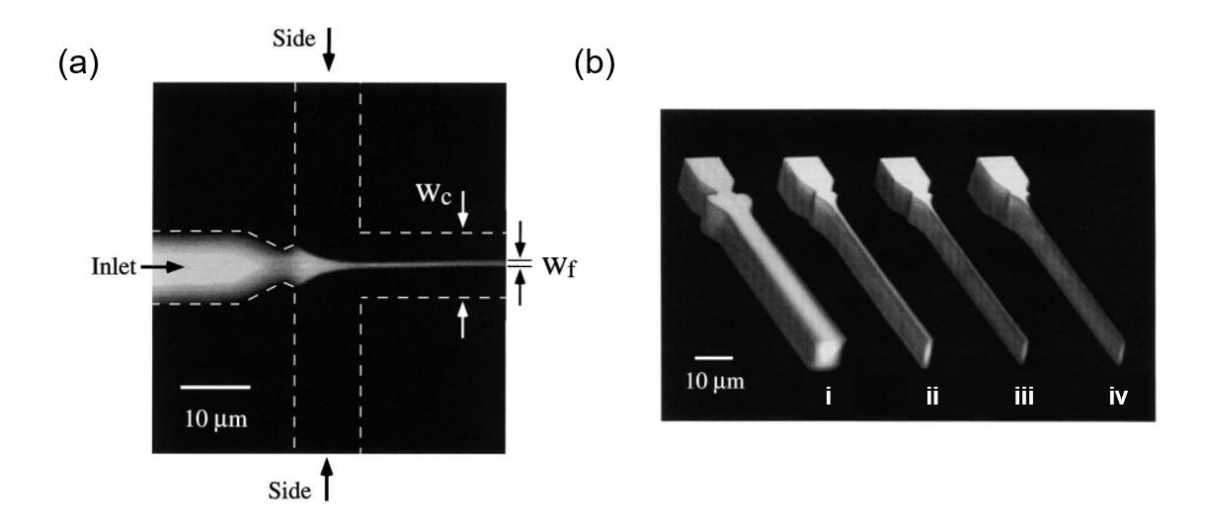


Figure 3.12 (a) Schematic of 2D focusing. Arrows for "Inlet" and "Side" are the direction of fluid. The channel width is represented as w_c and w_f is the width of the focused inlet stream. (b) Confocal scanning microscopy fluorescence images of focusing with inlet pressure P_i = 5 psi and the ratio of the side pressure to the inlet pressure is (i) 0.5 (ii) 1.0 (iii) 1.1 and (iv) 1.2. Each 3D rendering consists of approximately 30 separate 2D images acquired at regular intervals in depth. Copied from (Knight et al. 1998).

However, 2D focusing confines the sample flow solely to the central plane of the channel, while fluid distribution persists across the channel depth. To achieve full three-dimensional particle confinement, 3D focusing was developed to focus particles in both horizontal and vertical directions. Sundararajan et al. (Sundararajan et al. 2004) demonstrated this principle with a

PDMS-based 3D focusing device (**Figure 3.13**). They used five layers to achieve precise focusing, but the fabrication complexity and cost increased significantly compared to 2D systems.

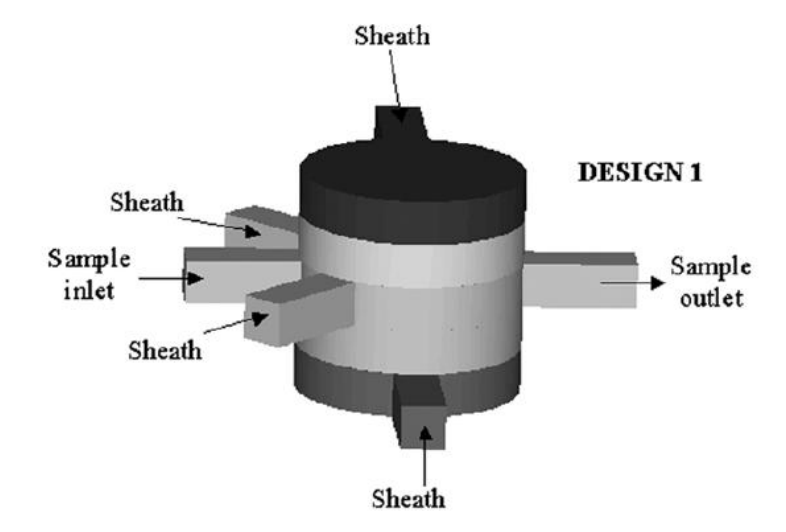


Figure 3.13 3D hydrodynamic focusing chips: one top and bottom sheath flow entering perpendicular to the sample flow direction. Copied from (Sundararajan et al. 2004).

To address these limitations, Howell et al. (Howell et al. 2008) developed a 3D sheath flow focusing method using grooved microchannels (**Figure 3.14**). Chevrons pairs were etched into both the superior and inferior channel walls, creating fluidic pathways that redirected sheath flows from lateral positions toward the superior and inferior midplanes of the sample stream. The area of the focused stream was controlled by the number of chevron pairs and the flow rate ratio between sheath flow and sample flow.

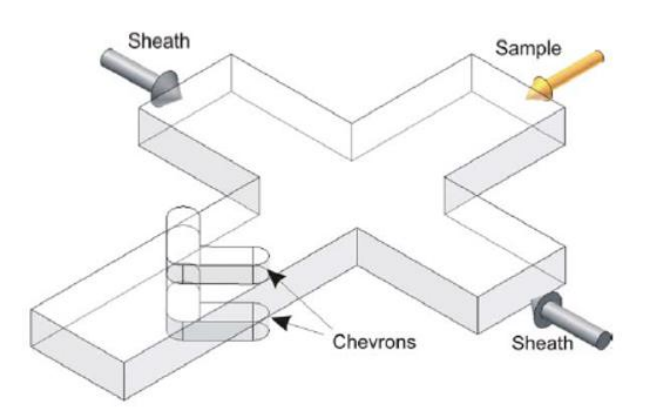


Figure 3.14 Isometric schematic of the chevron-based sheath flow design. Chevrons pairs are etched into both the superior and inferior channel walls, producing fluidic pathways that guide sheath flows from lateral positions toward the superior and inferior midplanes of the sample stream (Howell et al. 2008).

Hairer et al. described a single layer sheath flow focusing system in 2008 (Hairer et al. 2008), with subsequent optimisation in 2009 (Hairer and Vellekoop 2009) through incorporation of a vertical sheath inlet. In the former design (**Figure 3.15**), the sample was injected through the sample inlet while the sheath liquid was introduced via rear inlets. The sheath-to-sample flow rate ratio controlled the vertical sample stream position within the channel, with lateral hydrodynamic

focusing achieved through side sheath inlets. However, this configuration constraints the sample stream to the channel's inferior region (the middle of the bottom of the channel), which is a primary drawback of this design. The 2009 version added another inlet to lift the flowing sample from bottom to centre (**Figure 3.16**), but it still had a high complexity of fabrication.

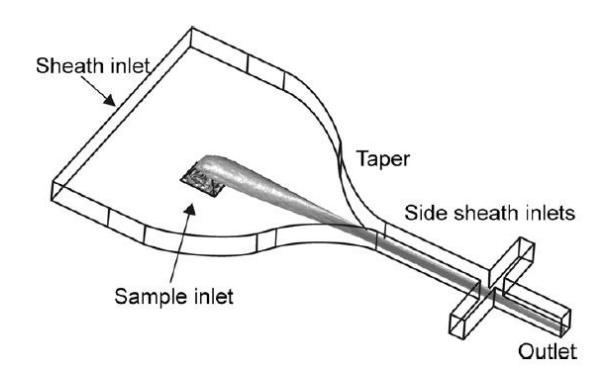


Figure 3.15 Schematic of the non-coaxial sheath flow cell (Hairer et al. 2008). The sample was introduced through the inlet, while the sheath flow entered via the rear inlet and lateral hydrodynamic focusing was achieved.

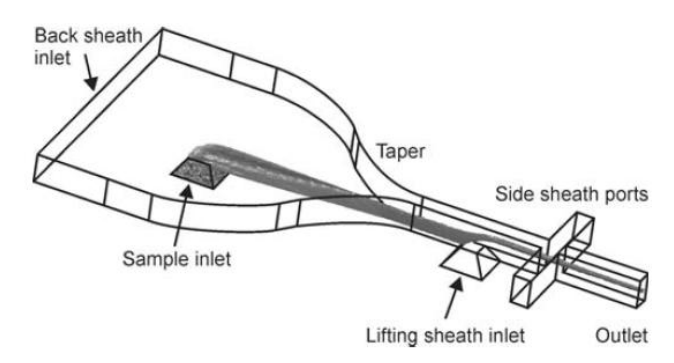


Figure 3.16 Schematic of the improved sheath flow cell. A lifting sheath inlet was added to navigate the sample liquid in the horizontal direction (Hairer and Vellekoop 2009).

In conclusion, sheath flow focusing demonstrates limited applicability in microfluidic systems due to inherent requirement for sophisticated fabrication to realise consistent focusing performance.

3.4.3 Inertial focusing

In 1961 Segré and Silberberg (Martel and Toner 2014) first reported inertial focusing through experimental observation of particles migrating to a stable annular region in laminar pipe flow. Using cylindrical pipes of 1cm diameter, they demonstrated that 1mm particles concentrated at an annular position with a normalized radial distance of 0.6 pipe radii from the centreline. This migration behaviour was attributed to inertial forces governed by the Navier-Stokes equations, specifically arising from two dominant hydrodynamic interactions: a wall interaction force (F_{wl}) and a shear gradient lift force (F_{SG}) (**Figure 3.17**). F_{wl} is generated when particle-wall interactions create localised pressure gradients. As particles travel slower than the surrounding fluid near channel walls, a pressure differential develops between the particle and the wall, generating a

repulsive force directed away from the channel boundaries. F_{SG} originates from velocity profile curvature in Poiseuille flow. Particles experience asymmetric fluid velocities across their surfaces due to the parabolic velocity distribution. The fluid establishes a restorative velocity gradient, inducing a net lift force toward regions of elevated shear rates (typically channel walls in conventional geometries).

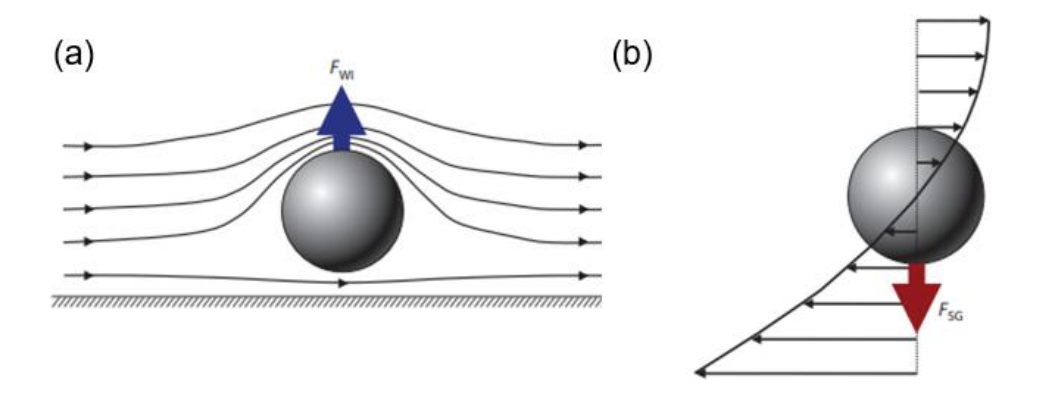


Figure 3.17 Schematics describing the dominant forces in inertial focusing systems. (a) is the wall interaction force which is generated when particle-wall interactions create localised pressure gradients. (b) is the shear gradient lifting force originated from velocity profile curvature in Poiseuille flow. Copied from (Martel and Toner 2014).

Di Carlo et al. (Di Carlo et al. 2007) first demonstrated inertial focusing in rectangular and square channels, mapping three-dimensional equilibrium positions of particles under laminar flow conditions. At a moderate Reynolds number, particles in square channels migrate to equilibrium positions exhibiting four-fold symmetry (**Figure 3.18**). Di Carlo et al. also showed inertial focusing equilibrium positions in a square channel are dependent on particle sizes. However, at different equilibrium positions within the flow, particle velocity in the flow direction remains constant and independent of particle size (Di Carlo et al. 2009).

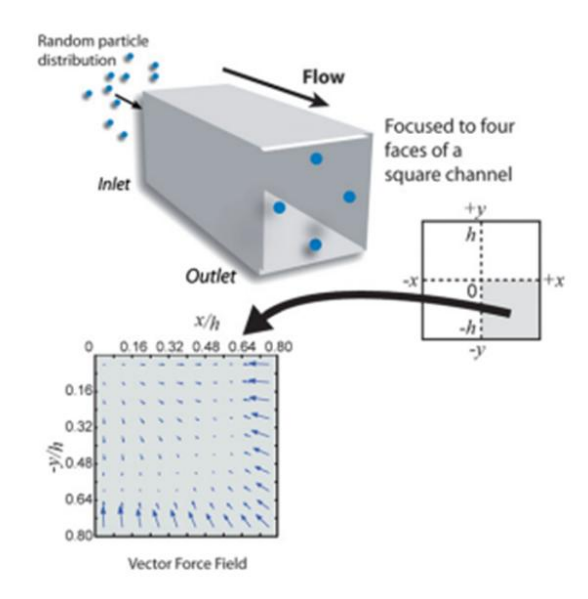


Figure 3.18 In the square channel, random distributed particles are focused to four equilibrium regions at a moderate Reynolds number and the distribution of equilibrium exhibits four-fold symmetry. The simulated force field on a particle over a fourth of a channel cross-section is shown (Di Carlo 2009).

As the aspect ratio of the channel becomes larger (very wide or very high channel), the number of equilibrium positions decreases to two, centred at the long face of the channel (**Figure 3.19**).

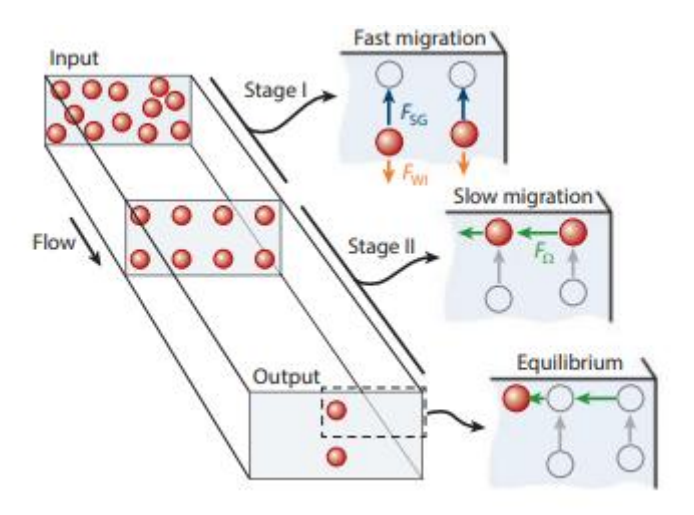


Figure 3.19 In a rectangular channel with a large aspect ratio (very wide or very high channel), the number of equilibrium positions are decreased to two and centred at the long face of the channel (Martel and Toner 2014).

Hansson et al. (Hansson et al. 2011) (**Figure 3.20**) demonstrated that the number of inertial focusing equilibrium positions in rectangular channels is dependent on particle size. Smaller particles migrated to four equilibrium positions symmetric about the channel centreline, but larger particles exhibited dual equilibrium positions aligned with the long-wall midpoints. When decreasing the ratio of height to width, particles were focused in two streams along the centre of the longer wall. Nevertheless, very small particles remain unfocused because of a weak force field.

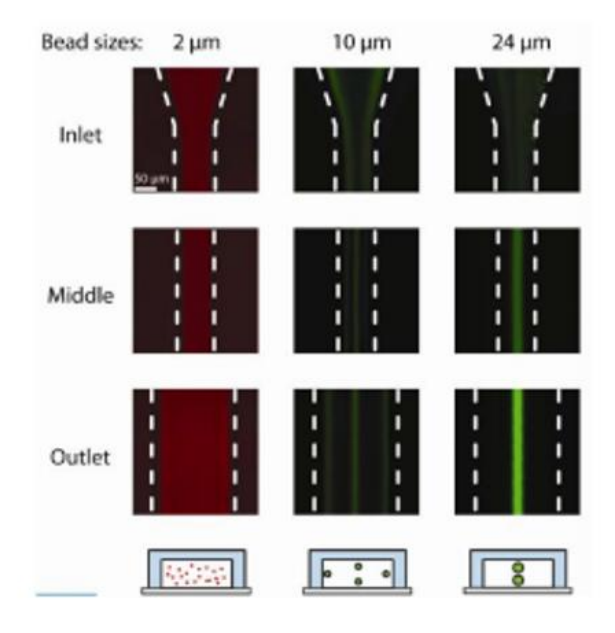


Figure 3.20 Fluorescence image of inertial focusing of particles of three sizes (2um,10um and 24um) (Hansson et al. 2011). Smaller particles migrate to four symmetric equilibrium positions around the channel central line, while larger particles settled into two equilibrium positions aligned with the long-wall midpoints. Very small particles remain unfocused.

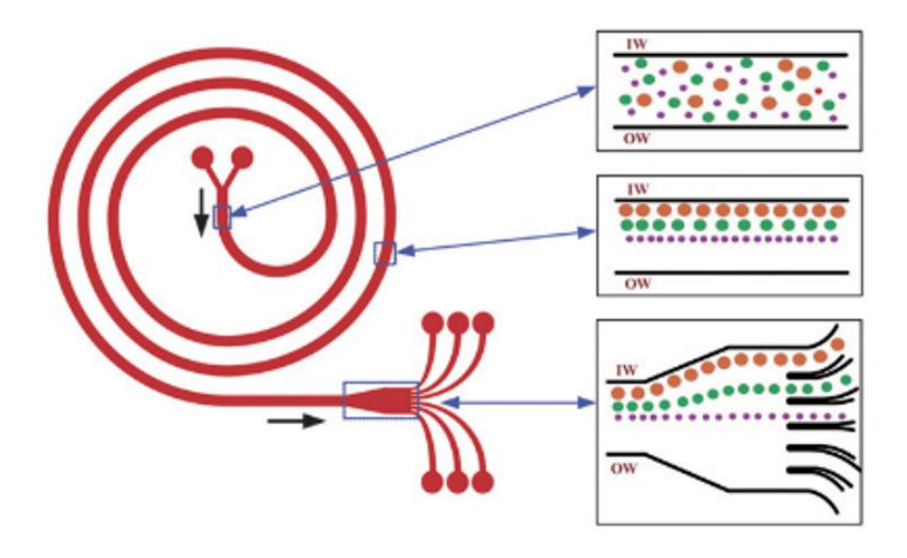


Figure 3.21 Schematic of a spiral microparticle separator proposed by Kuntaegowdanahali (Kuntaegowdanahali et al. 2009).

Inertial focusing was also used in curved microfluidic channels to achieve single-stream particle focusing. This approach exploits curvature-induced Dean vortices to establish size-dependent equilibrium positions, serving as the predominant method for size-based particle differentiation in inertial microfluidics. Kuntaegowdanahalli et al. (Kuntaegowdanahalli et al. 2009) (Figure 3.21) designed a spiral channel and exploited the fact that particle equilibrium positions scale inversely with diameter. Subsequent adaptations enabled high-precision separation resolution in clinical cytometry applications. Hou et al. (Hou et al. 2013) used a optimised spiral channel to isolate CTCs from blood, and the recovery rate was more than 85%.

Although inertial focusing is used in microfluidic cytometry, it is still not a perfect choice for impedance cytometry. Oakey et al. (Oakey et al. 2010) showed decreasing focusing performance for lower particle concentration, which means that a concentration that suits impedance cytometry (<500 particles/µl) leads to a poor focusing. Flow velocity has an inverse relationship with the channel length to attain inertial focusing equilibrium positions. **Figure 3.22** shows the channel length that the system needs for various sizes of particles when the channel size is 50µm×30µm and the flow rate is 90µl/min. It is clear that larger particles need shorter channel lengths.

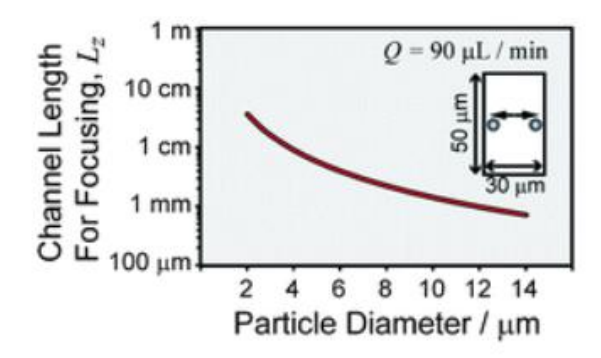


Figure 3.22 The channel length the system needs for different sizes of particles when the channel size is 50umx30um and the flow rate is 90ul/min. Larger particles need shorter channel length to achieve inertial focusing equilibrium positions (Di Carlo 2009).

3.4.4 Viscoelastic focusing

Viscoelastic focusing uses viscoelastic fluids to generate flow-induced elastic lift force, providing precise positional control of suspended particles (Yuan et al. 2018). Viscoelastic fluids are made by dissolving biological or synthetic polymeric substances in Newtonian solvents (Serhatlioglu et al. 2019). Compared to inertial focusing, viscoelastic fluids confine particles at lower flow rates. When the inertial effect is not negligible in the viscoelastic fluids, the fluid is referred to as inertiaelastic focusing which supports high flow rate focusing. Yang et al. (Yang et al. 2011) demonstrated 3D sheath-less focusing in a straight channel using "inertia-elastic focusing". They classified three different focusing regions based on the dominance of elasticity and inertia. In an inertia-dominant flow, there were four equilibrium positions in the square channel. In an elasticity-dominant flow, particles moved to the centre stream and the four corners under pure elastic effects. Finally, the number of equilibrium positions reduced to one for increasing flow rate which influences the dominance of inertial and elastic effects. Figure 3.23 shows these three cases. The Elasticity number, El = Wi/Re, was used to assess the relative magnitude of elastic and inertial forces. Weissenberg number (Wi) refers to elasticity while Reynolds number (Re) is the ratio between the inertial and viscous force. When the elasticity and inertia were combined (Re>0, Wi>0) by increasing flow rate, particles were confined to a certain equilibrium position.

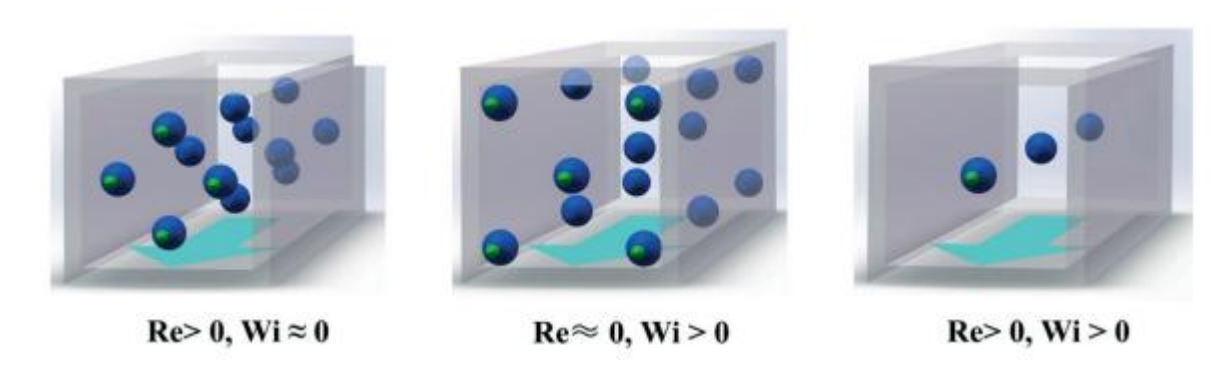


Figure 3.23 Particle equilibrium positions in inertial dominant focusing, elasticity dominant focusing, and inertia-elastic focusing (Yuan et al. 2018). The equilibrium positions are different because of varing inertial and elastic effects. W_i is Weissenberg number which referres to elasticity while the Reynolds number Re characterises the ratio between the inertial and viscous force.

Seo et al. (Seo, Kang, and Lee 2014) investigated the equilibrium position dynamics of particles in three distinct hydrodynamic regimes: inertia dominant, elasticity dominant, and coupled inertia-elastic conditions. They found the effects of the blockage ratio (β , ratio of particle diameter to channel height), flow rate (Q) and shear-thinning property of the viscoelastic fluids on particle focusing position. In 8% polyvinylpyrrolidone (PVP), an elasticity-dominant fluid, focusing was enhanced by increasing the flow rate and blockage ratio (**Figure 3.24**).

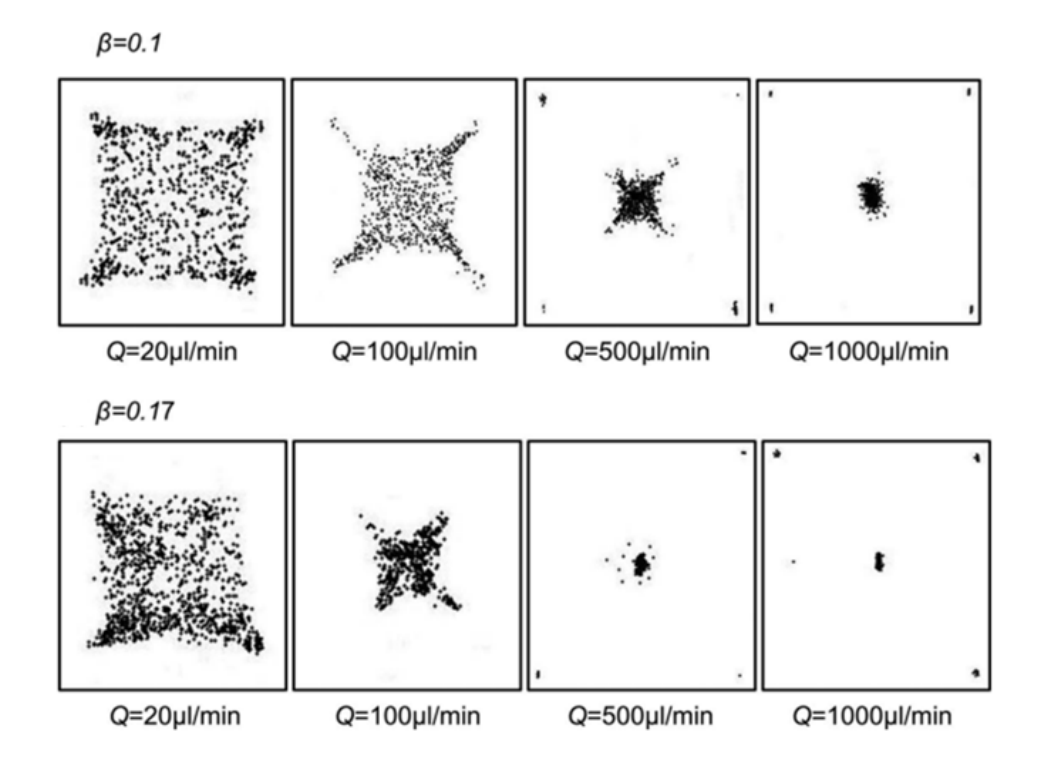


Figure 3.24 Cross-sectional distribution of particles of blockage ratio (ratio of particle diameter to cahnnel height) β =0.1 and β =0.17 in a square channel flow of an elasticity dominant fluid at different flow rates . In 8% polyvinylpyrrolidone (PVP), an elasticity-dominant fluid, focusing was enhanced by increasing the flow rate and blockage ratio (Seo, Kang, and Lee 2014).

The interplay between inertial and elastic forces yields distinct particle focusing dynamics in shear-thinning viscoelastic fluids. Polyethylene oxide (PEO), a shear-thinning viscoelastic fluid, exhibited significant inertial contributions at elevated flow rates. For larger particles, the

combined effect of the cross-lateral lift (F_{CL}) force and strong inward elastic force (F_E) confined most of the particles toward the channel core and the required flow rate was far lower than that used in elasticity-dominant fluid. As the flow rate increased dramatically, the focused particles dispersed again (**Figure 3.25**). This is because the inertial force (F_L) which is in the opposite direction to the elastic force becomes stronger as the flow rate increases due to the significantly decreased viscosity of the PEO solution (**Figure 3.26**). Thus, the strong shear-gradient lift pushes the particles toward the channel wall.

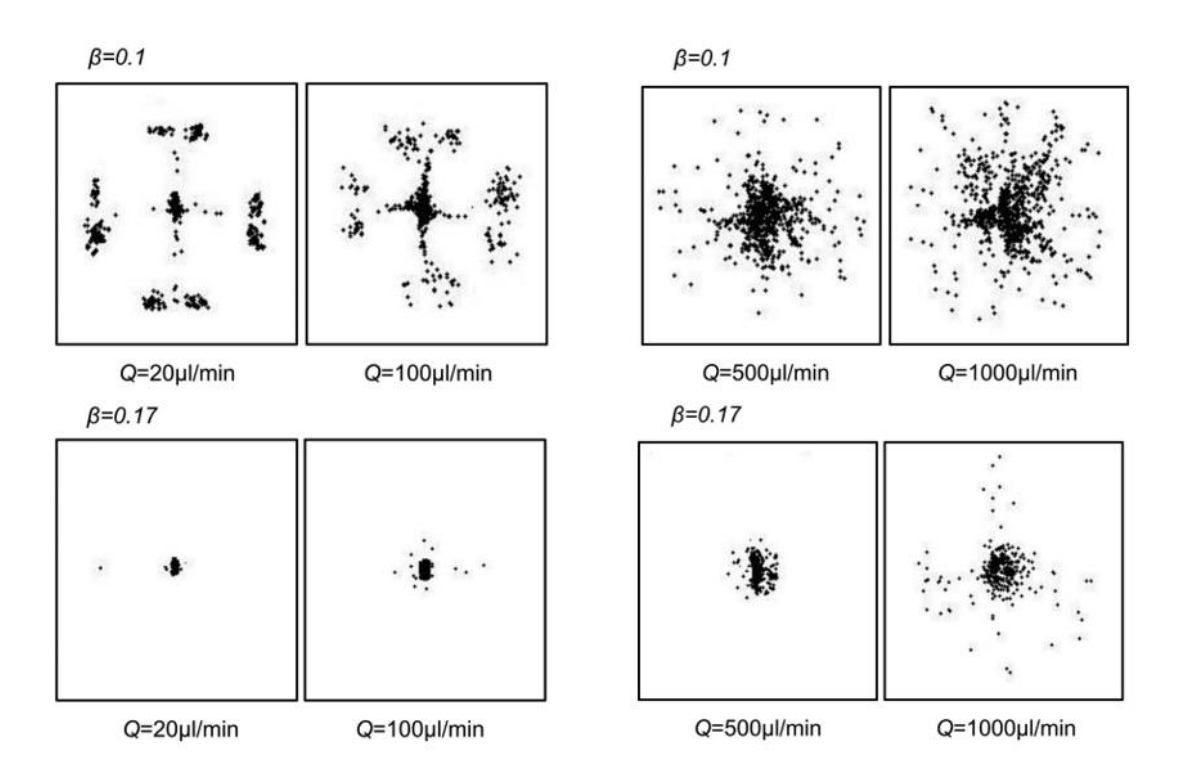


Figure 3.25 Cross-sectional distributions of particles of β =0.1 and β =0.17 in a square channel flow of a shear-thinning fluid at low flow rate conditions (20ul/min and 100ul/min) and high flow rate conditions (500ul/min and 1000ul/min), where the elastic and inertial effects are comparable and the inertial effect is dominant respectively. (Seo, Kang, and Lee 2014)

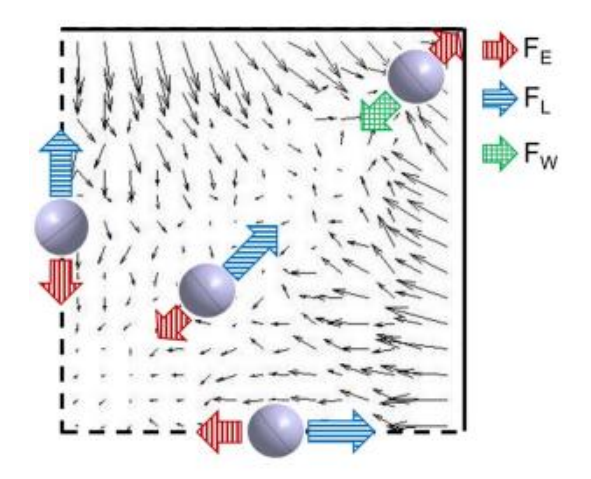


Figure 3.26 Shear-gradient lift and wall repulsion working in the direction opposite to that of the elastic force becomes stronger as the flow rate increases. As a result, focussed particles at the

channel centre disperse again at high flow rate in a shear-thinning fluid. F_E , F_L , and F_W represent the elastic force, shear-gradient lift, and wall repulsion. Adapted from (Seo, Kang, and Lee 2014) Current advancements in viscoelastic and inertia-elastic focusing have demonstrated broad applicability across diverse particulate systems, including synthetic particles (polystyrene beads), biological cells (blood cells, MCF-7 cells, sperm cells), and even bacteria (Serhatlioglu et al. 2019). This technological versatility was exemplified by Holzner et al. (Holzner, Stavrakis, and DeMello 2017), who investigated an inertia-elastic fluidic system within straight rectangular microchannels to achieve high-precision focusing of mammalian cells and bacteria suspensions. Serhatlioglu et al. (Serhatlioglu et al. 2019) first integrated viscoelastic focusing into impedance cytometry, investigating two critical rheological parameters: ionic concentration dependence in polyethylene oxide (PEO) solutions and the dynamic viscosity of different molecular weight PEO.

Their work demonstrated that optimised PEO formulations maintain a constant viscosity over a

wide range of shear rates. This rheological stability enabled high-throughput cellular analysis,

achieving 3,600 cells/min processing rates for red blood cell deformability characterisation.

In summary, viscoelastic focusing meets the requirement for a single stream particle focusing for a microfluidic system with a low flow rate and simplified channel. For impedance cytometry, the system requires a single equilibrium position to reduce the influence of impedance position dependence caused by non-uniform electric field distributions. By constraining particles to a single focal plane, viscoelastic focusing eliminates positional dependence across the channel depth, thus preventing signal distortion. The experimental platforms developed in this work use viscoelastic focusing to achieve robust impedance measurements while maintaining chip design simplicity.

3.4.5 Shear flow-induced deformation

Shear flow in a straight channel is induced by a strong velocity gradient. **Figure 3.27(a)** shows that the highest shear stress occurs on the cell membrane closest to the channel wall and simulation in **Figure 3.27(b)** confirms this phenomenon (Xu et al. 2018).

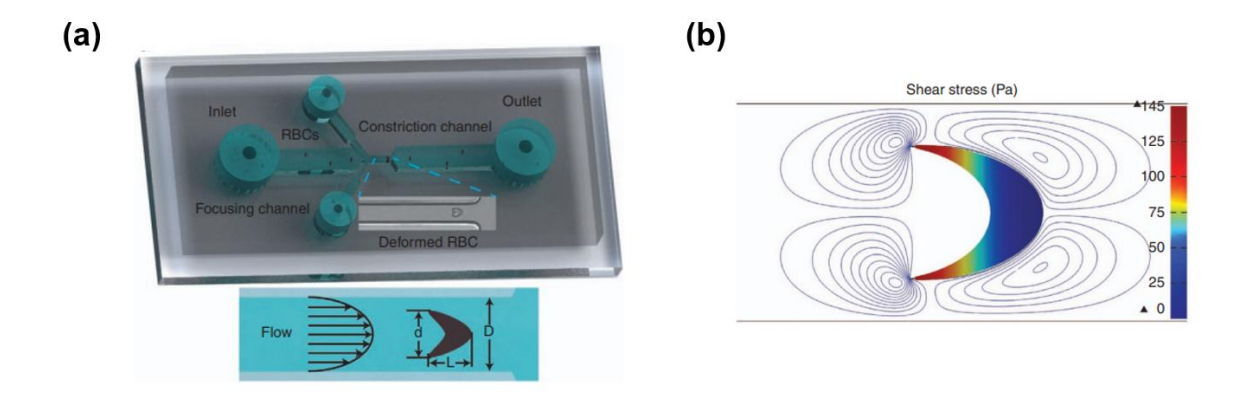


Figure 3.27 (a) A red cell is distorted by the drag force in the channel. (b) Simulation showing that the highest stresses occur in the red blood cell membrane regions closest to the channel walls (Xu et al. 2018).

Mietke et al. (Mietke et al. 2015b) first derived the hydrodynamic stresses on an object surface and quantified deformation based on linear-elasticity theory under high-viscosity conditions (Re<<1). They first calculated the flow field and stresses on the surface of a spherical object. These surface stresses were directly proportional to the peak flow velocity and were adjusted by changing the flow rate. For the particle model, they considered the case of a solid elastic sphere and a thin elastic shell with or without surface tension, and they also assumed the particles were composed of an isotropic elastic material. They then used two deformation measurements: deformation d (d = 1 - c, c is the circularity, defined as $c = 2\sqrt{\pi} \frac{\sqrt{A}}{P}$, where A is the area and P the perimeter of the central cross section of the deformed shapes) and curvature ξ (the fraction between minimal and maximal curvature of the shape boundary of a centred cross section) to differentiate the dependence of sphere shape deformations on sphere architecture (**Figure 3.28**).

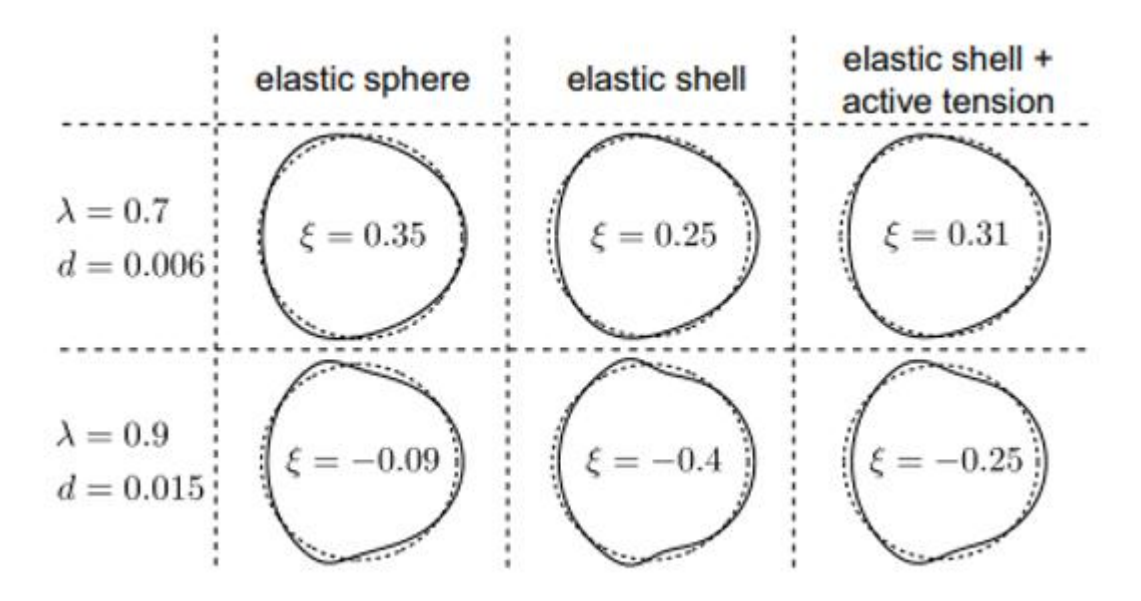


Figure 3.28 Deformation of an elastic sphere and a thin elastic shell with and without surface tension generated by the hydrodynamic loading in a cylindrical channel. Representative example shapes for relative cell sizes $\lambda=0.7$ and $\lambda=0.9$. λ is the ratio of the sphere's radius and the

channel radius. In each row, material parameters were chosen such that shapes have the same deformation d. The curvature ξ changes between different models (Mietke et al. 2015b).

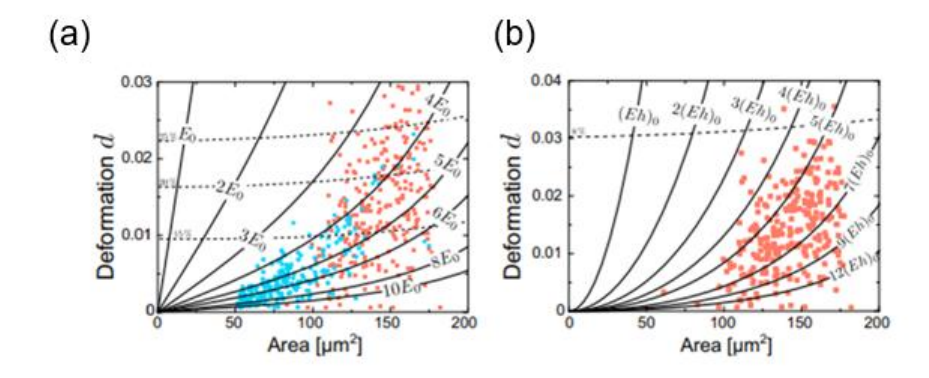


Figure 3.29 (a) Isoelasticity lines of a solid elastic sphere with data points representing agarose bead (blue circles) and HL60 cells (red squares). $E_0 \approx 270$ Pa. (b) Isoelasticity lines of a thin elastic shell without surface tension with data points representing HL60 cells (red squares). $(Eh)_0 \approx 3.4$ nN/um (Mietke et al. 2015a).

Finally, they generated isoelastic lines look-up graphic that was used to determine the cell stiffness using RT-DC (**Figure 3.29**). They verified their theoretical model from deformation measurements of agar beads with known stiffness and also measured the deformation of HL60.

Shear force-induced deformation of cells is commonly measured in a straight microchannel with viscoelastic fluid. As mentioned in **Chapter 2**, sDC uses this deformation generated by a viscoelastic fluid called methylcellulose (MC). This fluid provides constant and significant shear force at low flow rates.

3.4.6 Extensional flow-induced deformation

Two channel designs are used to exploit deformation induced by extensional flow. The first is a cross-slot device which squeezes cells at the stagnation point (Gossett et al. 2012; Bae et al. 2016). The opposite flows from two inlets provide extensional force to particles and they reach the peak deformation at the centre. This method leads to pure extensional stress. Urbanska et al. (Urbanska et al. 2020) compared three different deformability cytometry (DC) and showed that cells in the cross-slot cytometry (xDC) have a high velocity (several meters per second) and the method applies orders-of-magnitude higher stress levels to the cells. Another channel design using extensional flow is a hyperbolically converging geometry. These channels allow observation of the progressive deformation of cells, and maintain a constant extensional rate along the flow axis (Piergiovanni et al. 2020). Thus, they provide spatially uniform stress fields in controlled microenvironments. Lee et al. (Lee et al. 2009) characterised the effect on red blood cell (RBC) deformability between shear and extensional forces (Figure 3.30). They found that in the low-stress region before the deformation index was saturated, the extensional flow is much more efficient in deforming RBCs than the simple shear flow.

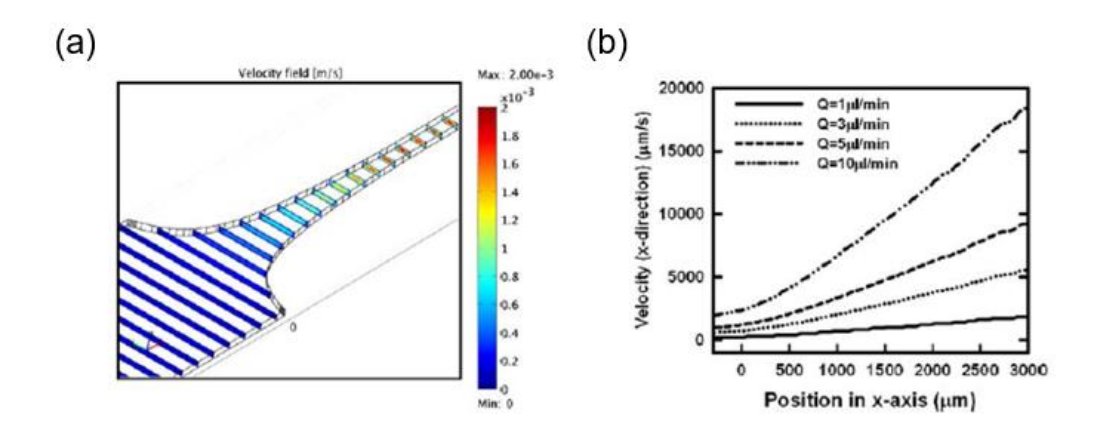


Figure 3.30 Hyperbolic converging microfluidic channel proposed by Lee et al. (a) Velocity field, flow rate $Q=1\mathrm{ul/min}$. (b) Velocity of the x-axis direction at the centerline of the channel. The slope of this graph implies the extensional rate, which is a constant. Copied from (Lee et al. 2009) Recently, Faustino et al. (Faustino et al. 2019) used a hyperbolic converging channel to generate a controlled homogeneous extensional flow field. They investigated the deformability of RBCs of end-stage kidney disease patients with or without diabetes. Observing the flow at the hyperbolic region, the RBCs did not show a tumbling and rolling motion, characteristics of shear-dominated RBC dynamics. Parallel investigations by Piergiovanni et al. (Piergiovanni et al. 2020) extended this methodology to nucleated cells, which are stiffer than RBCs. From FEM modelling and microfluidic experimentation (Figure 3.31), they established critical design-performance relationships. The straight and long hyperbolic channels are dominated by shear forces, leading to bullet-shaped cell deformation. The extensional forces are prevalent in the short hyperbolic channel so that cells perform elliptical deformation patterns. They confirm that the hyperbolic channel can be extended to deformability studies of nucleated cells.

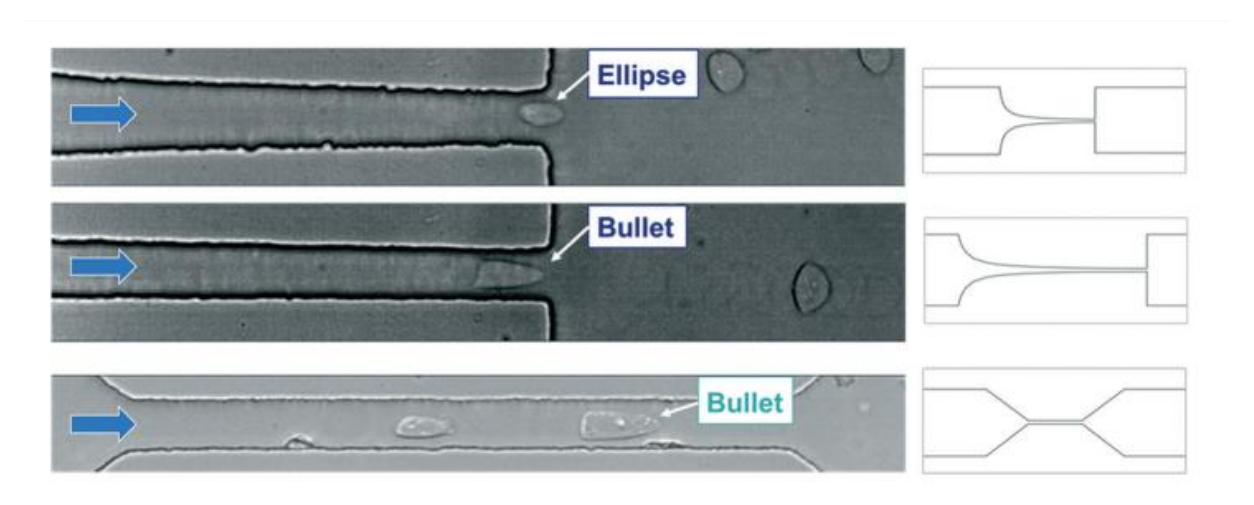


Figure 3.31 Images of two modes of deformation shapes occurring in different geometries. The top one is a short hyperbolic channel, the middle one is a long hyperbolic channel, and the last one is a straight channel. The extensional forces are prevalent in the short hyperbolic channel, causing cells to adopt elliptical deformation. Long and straight hyperbolic channels are primarily influenced by shear forces, resulting in bullet-shaped cell deformation. (Piergiovanni et al. 2020)

3.4.7 Fluid selection

Following analysis of hydrodynamic focusing principles and deformation-inducing fluidic characteristics, the appropriate suspension media requires consideration. For single-cell impedance spectroscopy introduced in **Chapter 5**, the hardware configuration (optimised electrode geometry) coupled with advanced software algorithms (Spencer and Morgan 2020) effectively compensates for the positional variation of cells within the microchannel, thereby eliminating the necessity for hydrodynamic focusing. For dielectric characterisation of nucleated cells rather than mechanical deformability assessment, media formulations inducing cellular deformation are intentionally excluded.

When using MIC for mechanical phenotyping, this system lacks an effective mechanism to eliminate the impact of particle position along the channel height, requiring hydrodynamic focusing to ensure reproducibility. To address this, the system used a sheathless viscoelastic focusing mechanism, using polyethylene oxide (PEO) or methylcellulose (MC). Typical concentration are 0.1% w/v PEO-DPBS and 0.5% w/v MC-DPBS and, both formulations achieve focusing. MC has a higher density and viscosity, enabling a higher deformation of cells at lower flow rates (Piergiovanni et al. 2020; Otto et al. 2015; Herbig et al. 2018). It magnifies the deformability alteration and improves discrimination between subpopulations. Therefore, in the deformability experiments presented in **Chapters 4 and 6**, 0.5%w/v MC-DPBS solution was used.

3.5 Cell Sorting

The sorting system is based on integrated membrane pumps to deflect fluids. This section describes the fundamental hydrodynamic principles governing sorting, with membrane deflection mechanics and laminar flow dynamics validated through COMSOL Multiphysics simulations.

As mentioned in **Chapter 2**, the optimal choice of sorter uses integrated membrane pumps. A membrane pump deflected by an external force injects a small amount of liquid into the main channel to induce alterations in the path of particles flowing in the channel. Membrane deflection theory quantitatively explains the displacement mechanism induced by the membrane pump. Controlled deformation of the elastomeric membrane generates transient pressure gradients that move particles along the channel width as they traverse the microfluidic channel, thereby enabling sorting. Simulations demonstrate how these fluidic perturbations achieve precise spatial control within the laminar flow regime of the main channel.

3.5.1 Membrane pump for local-flow control

Figure 3.32 shows the components of the on-chip membrane pumps. This concept of on-chip membrane pumps was proposed by Sakuma et al. (Sakuma et al. 2017) in 2017. In one MIC sorting chip, there are two membrane pump structures which are positioned on either side of the main channel. The membrane pump consists of a chamber containing the local flow and a thin membrane deflected by an applied force (Figure 3.32(a)). The sorting channel connects to the main channel containing the main flow, and under stable hydrodynamic conditions within the microfluidic chip, the local flow is stagnant due to balanced pressure gradients (Figure 3.32(b)).

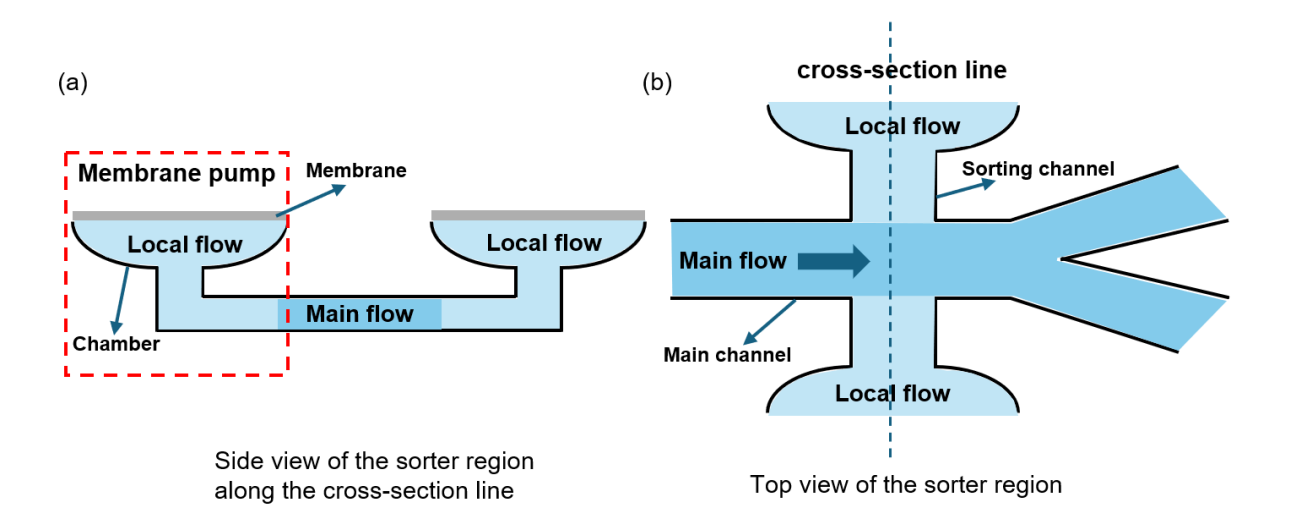


Figure 3.32 Schematic diagram of membrane pump when the sorter is inactivated. (a) Side view along the cross-section line shown in (b). In a stable inactivated state, the liquid flows inside the main channel and spreads to two outlets at the end. The two chambers covered by a thin membrane are filled with the local flow, which can be pumped into the main channel when the sorter is activated, but it is stagnant in the inactivated state. (b) Top view. The part connecting the main channel and the chamber is the sorting channel.

The sorting mechanism induces localised fluidic actuation within dedicated chambers to redirect flow trajectories in the main microchannel, thereby guiding target particles toward different outlets. **Figure 3.32** is a conceptual diagram of the sorter in the "Inactivated" state. The sorter is positioned downstream of the impedance detection region. Under stable hydrodynamic conditions, the main channel flow is laminar flow, distributing fluid symmetrically between two outlets without external pressure regulation. The two chambers are filled with liquid, and a thin membrane seals the chambers at the top.

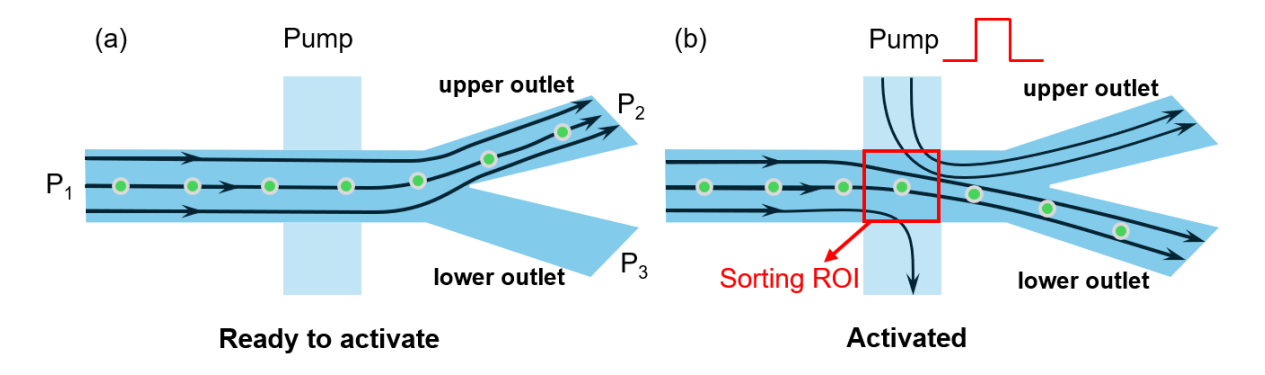


Figure 3.33 Schematic diagram of the pump showing how the sorting works (chambers and membranes are not shown in this diagram). (a) "Ready to activate" state. The pressure of the inlet (P_1) and two outlets $(P_2$ and $P_3)$ are controlled by the pressure pump. In this state, the particles in the main flow target the upper outlet. (b) "Activated" state. The red outlined region is sorting ROI. When the membrane covering the upper pump is triggered by a pulse, the local flow stored in the upper chamber is pumped into the main channel. The particles flow in the main flow, and when they enter the sorting ROI, their traces are changed to another outlet.

Although one MIC sorting chip has two membrane pumps as shown in **Figure 3.32**, a single pump is sufficient for binary sorting. The sorting sequence initiates through a two-stage activation protocol:

- 1. Ready to activate phase (**Figure 3.33(a)**): In this status, inlet pressure P_1 and outlet pressure P_2 and P_3 are configured to establish flow conditions that particles are hydrodynamic biased toward the upper outlet. Sorting chambers maintain static fluid equilibrium.
- 2. Activated phase (Figure 3.33(b)): The membrane pump is triggered by an external force controlled by a pulse in this state. No matter what external device is used, if the force it provides can deflect the membrane and generate a volumetric change in the local flow, the squeezed liquid finally enters the main channel, and the sorting works in sorting ROI. Particles are targeted to the opposite (lower) outlet.

3.5.2 Deflection of a circular membrane

For sorting membrane deflection is actuated via an externally applied force. This section discusses the deflection characteristics of a circular membrane.

Considering a circular isotropic membrane, the deflection is given (Wan 1999),

$$D = \frac{Eh^3}{12(1-u^2)} \tag{3.19}$$

where E is the elastic modulus, u is Poisson's ratio, and h is the thickness of the membrane. Figure 3.34 shows a schematic diagram of the deflection of a circular isotropic membrane. A central point load, F, is applied to create a blister deflection, w(r), where r is the distance from a

point on the membrane to the central point. The central deflection is $w_0 = w(r=0)$. A polynomial expansion can approximate the membrane stress, but the stress is equal-biaxial, and an average stress N is adopted. The radial and tangential stresses equal the average stress N, so $N_r = N_t = N$. The radius of the membrane is a.

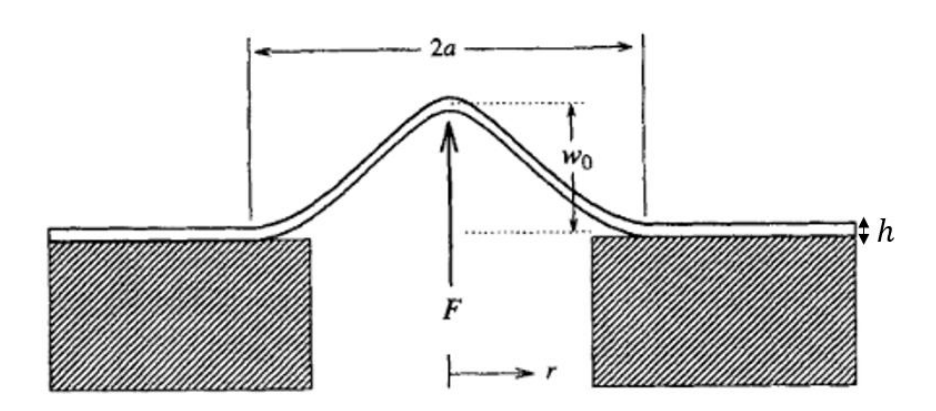


Figure 3.34 Schematic of a circular membrane deflection model. The radius of the circular membrane is "a", and the applied central point load is "F". "r" is the distance from a point on the membrane to the central point, and w_0 is the deflection displacement when r=0. Copied from Wan (Wan 1999).

At equilibrium, linear elasticity obeys the von Karman equations (Timoshenko and Woinowsky-Krieger 1959):

$$\frac{d}{dr}(N_r + N_t) + \frac{Eh}{2r}(\frac{dw}{dr})^2 = 0 {(3.20)}$$

$$Q_r + N_r \frac{dw}{dr} + \frac{F}{2\pi r} = 0 ag{3.21}$$

where the shear force is given by

$$Q_r = -D\left(\frac{d^3w}{dr^3} + \frac{1}{r}\frac{d^2w}{dr^2} - \frac{1}{r^2}\frac{dw}{dr}\right)$$
(3.22)

Combining these three equations gives:

$$\frac{d^3w}{dr^3} + \frac{1}{r}\frac{d^2w}{dr^2} - \frac{1}{r^2}\frac{dw}{dr} - \frac{N}{D}\frac{dw}{dr} = \frac{F}{2\pi r}$$
(3.23)

The boundary conditions are (i) w(r=a)=0, (ii) $\frac{dw}{dr}$ is continuous and equal to 0 when r=0 and r=a. Wan (Wan 1999) converted **equation 3.23** to a modified Bessel equation and for a special case where N is negligible (no radial and tangential stress), for a plate under pure bending, the deflection can be derived as (Wan 1999)

$$w = w_0 \left(1 - \left(\frac{r}{a} \right)^2 + \left(\frac{r}{a} \right)^2 \ln \left(\frac{r}{a} \right)^2 \right)$$
 (3.24)

where,

$$w_0 = \frac{3Fa^2(1 - u^2)}{4\pi Eh^3} \tag{3.25}$$

Thus, the maximum displacement of the centre point of the movable membrane is given by

$$w(r=0) = \frac{Fa^2}{16\pi D} \tag{3.26}$$

Under this condition, the volume change of local-flow C_v is calculated as (Sakuma et al. 2017):

$$C_v = \int_0^{2\pi} \int_0^a rw(r)drd\theta = \frac{Fa^4}{64D} = \frac{\pi a^2}{4}w(r=0)$$
 (3.27)

3.5.3 Simulation of circular membrane

Before building the sorting system, the deflection of the circular membrane was simulated to calculate its displacement.

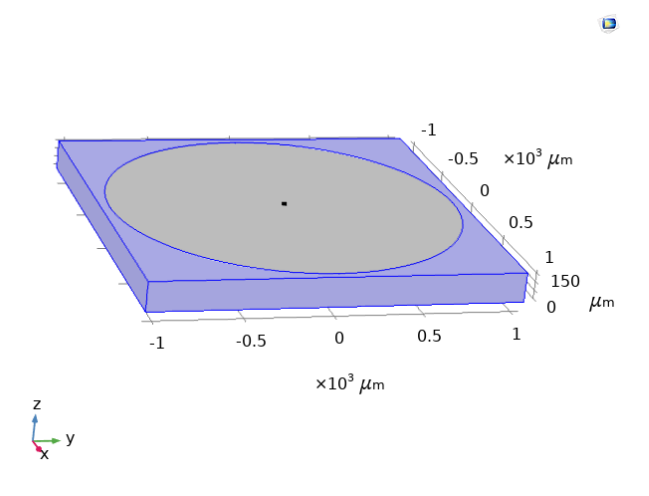


Figure 3.35 The 3D geometry model was created in COMSOL. The diameter of the circular membrane was 2mm, and the thickness was $170\mu m$, the same as the normal cover slip made from borasilicate with Young's modulus G = 64 Gpa; Poisson's ratio u = 0.2. The point load (F = 20 N) was applied at the central point of the memrbane to simplify the simulation. The blue region represents the polygon that is clamped and set to be "Fixed Constraint".

Figure 3.35 shows the geometry of the membrane model. The covers slips had a thickness of 170 μ m made from borosilicate (Young's modulus G: 64GPa; Poisson's ratio u: 0.2). The radius of the circular membrane (grey region) was a = 1mm. The modules "Solid Mechanics", and "Linear Elastic Material" were used in COMSOL. The membrane was clamped so that the polygon area around the membrane (blue region) was set to be "Fixed Constraint". The point load (F=20N) was applied to the centre point of the membrane to simplify the simulation.

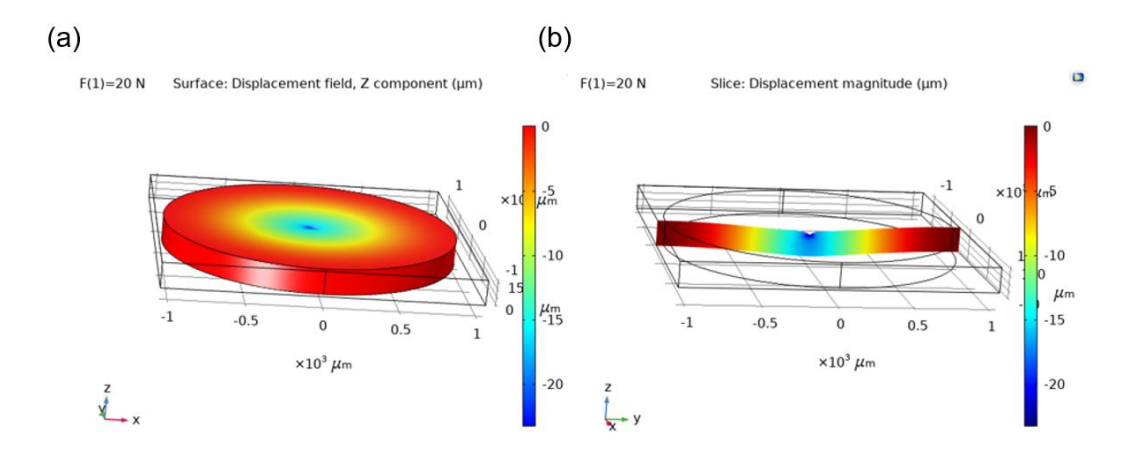


Figure 3.36 (a) The surface displacement and (b) the slice view of the displacement magnitude. The displacement at the central point of the membrane (r=0) is higher than other points on the same surface and the surface in direct contact with the point load exhibits maximum displacement magnitude which is around 23 μ m.

Figure 3.36(a) shows the surface displacement distribution of the membrane under applied load, while **Figure 3.36(b)** shows a corresponding cross-sectional displacement profile through the symmetry plane. The membrane surface in direct contact with the point load exhibits maximum displacement magnitude (~23μm), contrasting with a 30% reduction in displacement amplitude (~16μm) observed on the opposing surface. The volume change C_v with a 16μm displacement (calculated from **equation 3.27**) is around 12.6 nL, while the volume in the sorting chamber is 0.15 nL (the channel height is 30μm, width of sorting channel and main channel = 50 μm and 100 μm, see **Chapter 6**). Thus, the displacement is enough to deflect the main flow. This simulation of the relationship between the point load and displacement can be used to guide the choice of the piezoelectric actuator. The blocking force (the maximum output force) of the piezo actuator should be larger than the actual load force. Otherwise, it may result in failure. For the final choice of actuator, the blocking force was 360 N and the maximum displacement is 25.5 μm, thereby ensuring it meets both the volume of flow requirement and blocking force.

3.5.4 Simulation for fluid in the sorter

Complementary hydrodynamic simulations were conducted to quantify flow changes within the microchannel. This section details a study examining the effect of channel dimension on flow field characteristics, with particular emphasis on velocity profile distributions and streamline patterns.

The model implemented the "Laminar Flow" interface to solve the incompressible Navier-Stokes equations. The Reynolds number Re = 1, density $\rho = 1000 \text{ kg/m}^3$ with no-slip boundary conditions at channel walls.

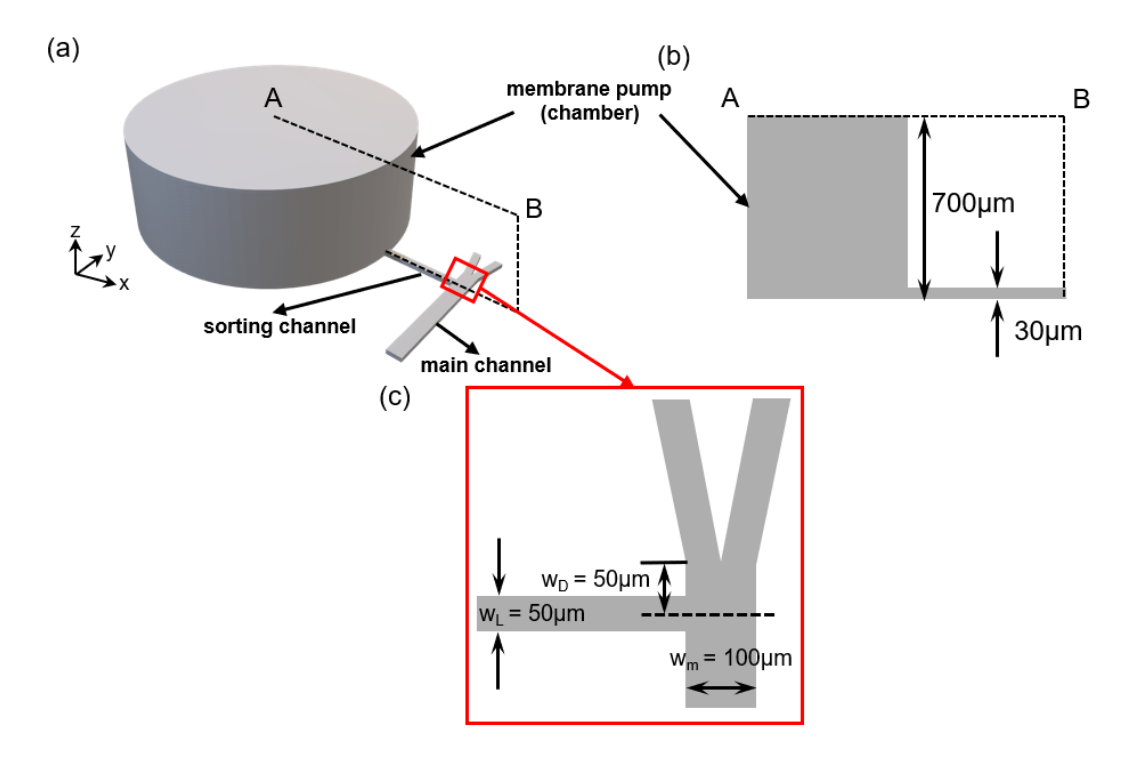


Figure 3.37 3D geometry model used for the fluidic simulation. (a) Whole microfluidic domain. To simplify the simulation, the contralateral chamber is neglected. (b) The dimension of the radial section AB. The overall height is 700 μ m, and the height of the main channel is 30 μ m. (c) The dimension of the sorting ROI. w_L is the width of the sorting channel; w_D is the distance between the outlet junction and the centre of the sorting channel; w_D is the width of the main channel.

The dimension of the model are shown in **Figure 3.37**, where a cylindrical chamber of a radius a_{pump} = 1mm acts as a single membrane pump. The main channel extends along the y-axis (**Figure 3.37(a)**) and is split into two equal outlets with a width of w_m = 100 µm. The sorting channel width is w_L = 50 µm, connecting the chamber to the main channel. The distance between the outlet junction and the centre of the sorting channel is w_D = 50 µm (**Figure 3.37(c)**). The height of the chamber is 700 µm, and the height of the main channel is 30 µm (**Figure 3.37(b)**). To simplify the simulation, the contralateral chamber is neglected.

The initial and boundary conditions are specified in **Figure 3.38**. The membrane velocity profile follows a rectangular pulse waveform with 2 ms pulse width (**Figure 3.38(b)**), mathematically defined as $v_{\text{mem}} = 0.001 \times rect1(t)$ [m/s]. The top surface of the chamber is set as the inlet boundary with a "Normal inflow velocity" condition. Pressure boundary conditions are configured to establish upper outlet flow bias: $P_{inlet} = 39.6$ kPa; $P_{o1} = 11$ kPa; $P_{o2} = P_{inlet} - P_{o1} = 28.6$ kPa; The boundary condition on the device wall is "No-slip". Because the pulse function is symmetrical with t = 2 ms (**Figure 3.38(b)**), the flow field states of the system are identical at time points with the same pulse magnitude within t < 2 ms and t > 2 ms. Thus, flow field solutions were analysed at three characteristic timepoints: t = 0, 1, 2 ms. The mid-plane cross-section (cut plan 1 in **Figure 3.38(a)**) along the main channel longitudinal axis serves as the primary analysis plane for streamline visualisation in subsequent discussions.

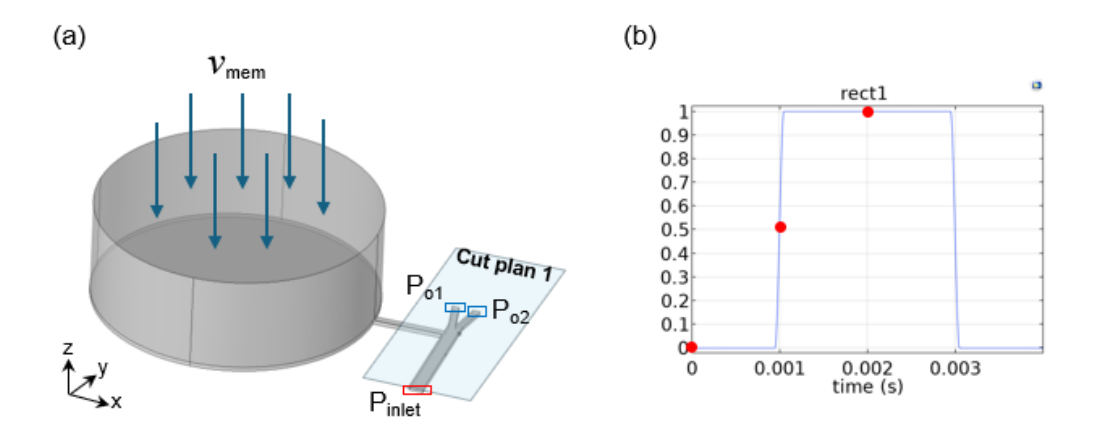


Figure 3.38 (a) The initial and applied conditions for the model. (b) The rectangular pulse generated an external velocity v_{mem} = 0.001× rect1(t)[m/s], which is set as a "Normal inflow velocity" condition in the inlet boundary (top surface of the chamber). Because the signal was symmetric about t=2ms, the fluidic changes at t = 0ms, t = 1ms, and t = 2ms were focused.

The finite element mesh configuration used physical-controlled meshing with "Normal" element size parameters. Numerical analysis used a stationary solver coupled with a parametric sweep across t = 0-4 ms, giving 0.5 ms temporal increments. Simulations were executed on the Iridis 5 HPC cluster of the University of Southampton, requiring 4 hours of computational time for complete numerical solutions.

Figure 3.39 illustrates the velocity magnitude distribution and streamline patterns in cut plane 1. Under quiescent membrane conditions (t = 0ms), streamlines showed preferential flow routing through the upper outlet (left-hand side outlet in **Figure 3.39**, maintaining nomenclature consistency with **Figures 3.32 and 3.33**. The same applies to the other outlet, referred to as the lower outlet.). Because the outlet was narrow, the velocity magnitude was higher than upstream pre-bifurcation values.

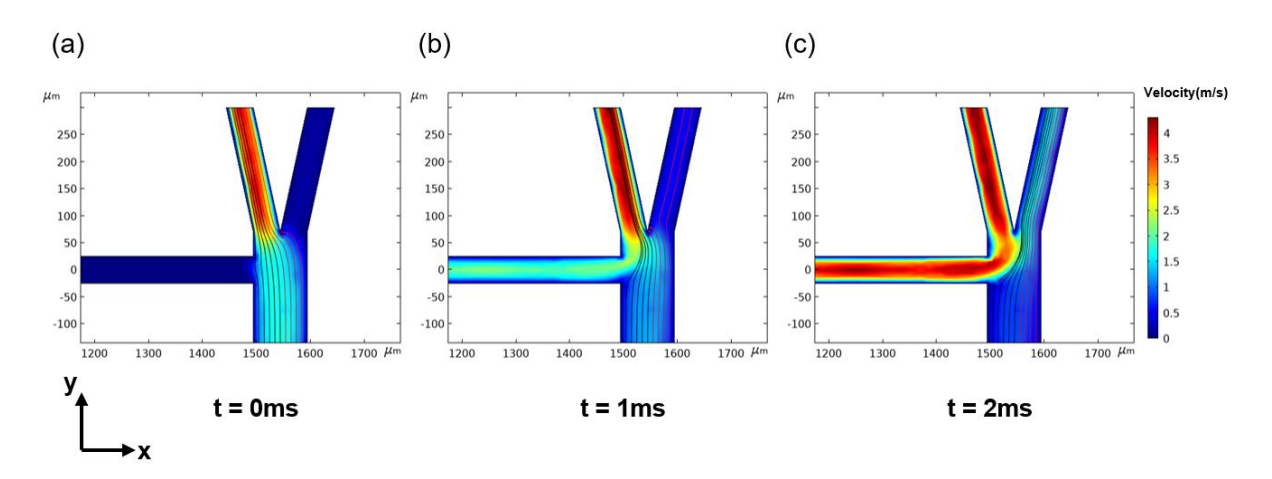


Figure 3.39 Numerical characterisation of the fluidic velocity field and path of the streamlines originating at the main channel when an external force pulse is applied at different time points: (a) t = 0ms; (b) t = 1ms; (c) t = 2ms.

The hydrodynamic sorting mechanism works in distinct actuation phases. At t = 1ms, v_{mem} is at half the maximum value, the local flow diverts a portion of the main flow into the lower outlet,

while some fluid continues to flow toward the upper outlet. At peak actuation (t = 2ms) when v_{mem} attains maximum amplitude, membrane deflection culminates in maximal fluid displacement, driving high-velocity local flow injection into the main channel. The streamlines in the main channel show that all the flowing fluid is compressed and redirected by the local flow toward the designated lower outlet, thereby enabling binary particle sorting.

A subsequent simulation investigated channel geometry modifications while maintaining operational parameters. All initial conditions remained unchanged ($v_{mem} = 0.001 \times rect1(t)$ [m/s]; $P_{inlet} = 39.6$ kPa; $P_{o1} = 11$ kPa; $P_{o2} = P_{inlet} - P_{o1} = 28.6$ kPa) except for the distance between the outlet junction and the centre of sorting channel w_D . w_D was increased from 50 μ m to 100 μ m and 150 μ m.

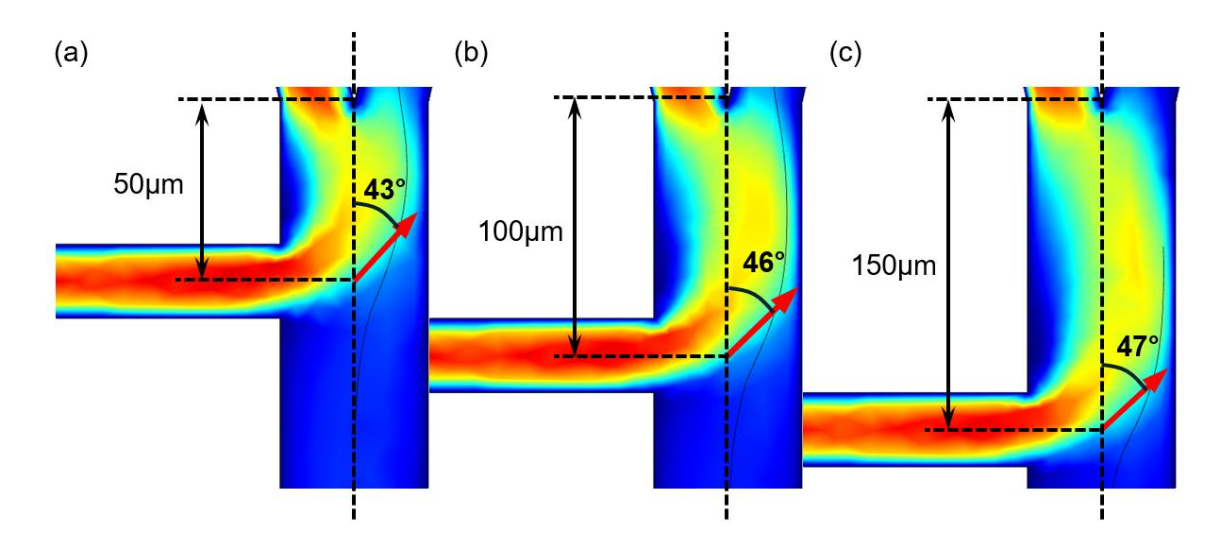


Figure 3.40 Simulations when w_D was set to (a) $50\mu m$ (b) $100\mu m$ (c) $150\mu m$ at t=2ms. The red arrows indicated the tangential direction of the centre streamline at the middle of the channel, demonstrating the magnitude of the fluid deflection angle within the main channel. For a changing w_D , there is no significant difference on the positional interference concluded by the angular perturbations.

As shown in **Figure 3.40**, the velocity magnitude distribution and streamline patterns in Cut plane 1 at t = 2 ms (corresponding to maximal membrane deflection and v_{mem} actuation) demonstrate disturbance of the injected liquid to the main flow within the main channel. Tangential vectors (red arrows) to the streamlines at this junction reveal flow angular deviation relative to the main channel axis, where the deflection angle magnitude exhibits negligible dependence on w_D variations up to 150 μ m. This limited angular perturbation, lower than 10%, confirms minimal positional interference on sorting performance within the tested range.

The main channel width was to w_m = 40 µm while maintaining other parameters. Figure 3.41 confirms maintained flow orientation toward the upper outlet at the "Ready to activate" state. However, intermediate actuation (t = 1ms, when the half value of v_{mem} is applied), induced vortex formation within the main channel, resulting in abrupt velocity gradients between the input local flow and primary stream. This hydrodynamic instability causes unintended flow reversal (Figure 3.41(b) and (c), red arrows).

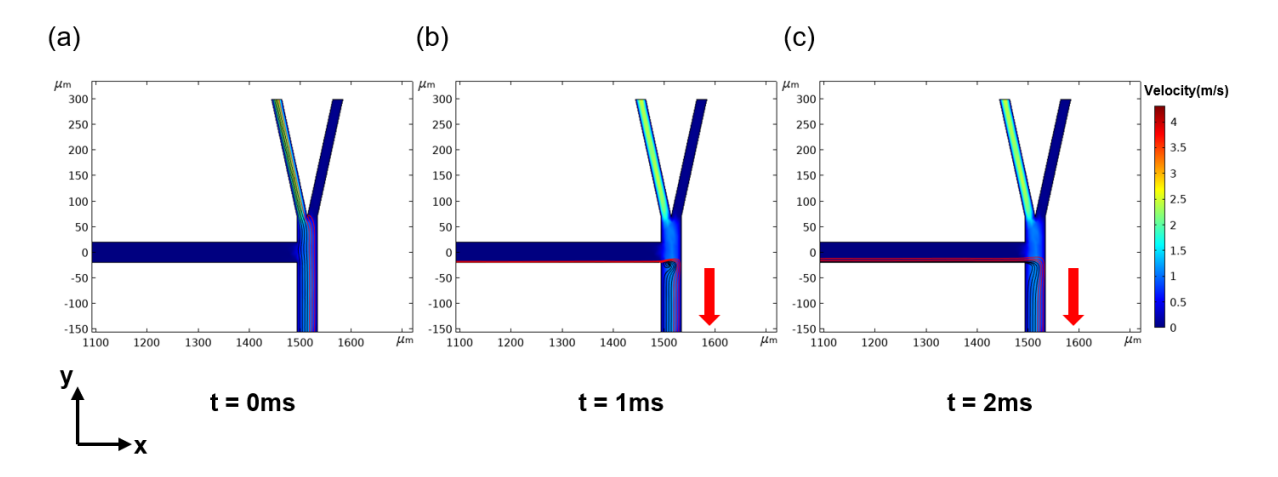


Figure 3.41 Simulation after changing w_m from 100 μ m to 40 μ m at (a) t = 0ms; (b) t = 1ms; (c) t = 2ms. The v_{mem} was too high to achieve successful sorting. The main flow changes its direction, as shown by red arrows.

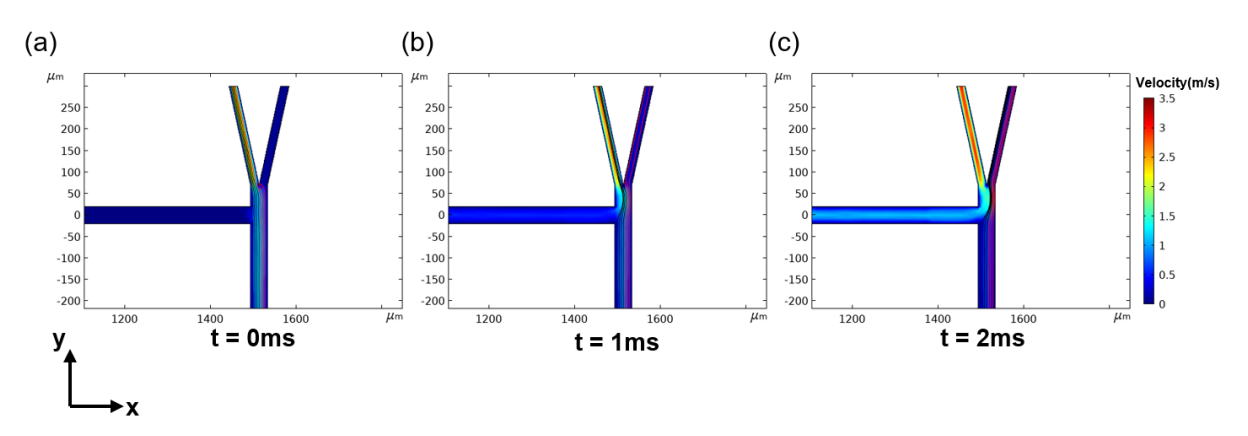


Figure 3.42 Numerical characterisation of the fluidic velocity field and path of the streamlines originating at the main channel when an external force pulse is applied at different time points after decreasing the magnitude of v_{mem} from 0.001 to 0.0002 m/s at (a) t = 0ms; (b) t = 1ms; (c) t = 2ms.

Membrane actuation velocity v_{mem} was reduced as follows: 0.0008, 0.0006, 0.0004 and 0.0002 m/s. Successful particle sorting required a fivefold reduction in actuation magnitude, from 0.001 to 0.0002 m/s, as evidenced in **Figure 3.42**. It implies that the narrow main channel does not require the same amount of membrane deflection as used for sorting in the wide main channel.

3.6 Discussion

This chapter describes the theoretical foundations and computational methodologies used in the thesis. Dielectric theory and numerical models for single-cell spectroscopy were investigated. A comprehensive analysis of microfluidic operational principles and viscoelastic fluid dynamics pertinent to cellular deformability quantification was conducted.

The mechanical deflection theory governing circular membrane actuators in the sorting system was developed, complemented by COMSOL simulations that showed transient hydrodynamic during active sorting operations. Empirical validation of these theoretical frameworks across three distinct experimental subprojects is detailed in subsequent chapters: **Chapter 4** - Electro-

Chapter 3

Optical deformability MIC system; **Chapter 5** - Single-cell spectroscopy of nucleated cells; and **Chapter 6** - Single-cell sorting based on MIC.

Chapter 4 Electro-Optical Deformability MIC system

4.1 Introduction

In section 2.2.1, the mechanical properties of cells were introduced, and the common microfluidic methods for measuring cell deformability were discussed in **section 2.2.2**. Generally, cell deformability helps to study cellular processes and cell-related diseases as well as to identify new therapeutic targets. The most extensive research currently focuses on the relationship between cell deformability changes and cancerous states. It is reported that the stiffness of cancer cells implies metastatic potential because those cells can experience an epithelialmesenchymal transition, characterised by various biochemical and cytoskeletal changes that allow it to sustain mobility and an invasive state (Byun et al. 2013). Alibert et al. (Alibert, Goud, and Manneville 2017) summarised the stiffness difference between cancer cells and normal cells by reviewing the experimental studies that compared the mechanics of these two types of cells. It concluded that cancer cells are generally softer compared to normal cells (Figure 4.1). Although solid tumours tend to be stiffer overall (which can be detected through palpation), at the single-cell level, cancer cells typically exhibit lower stiffness and greater deformability. However, in some rare cases, certain cancer cells may exhibit higher stiffness than normal cells (Zhang et al. 2002). Overall, the stiffness of cells, reflected by the deformability in practical experiments, is of interest to investigate cancer diagnosis and treatment.

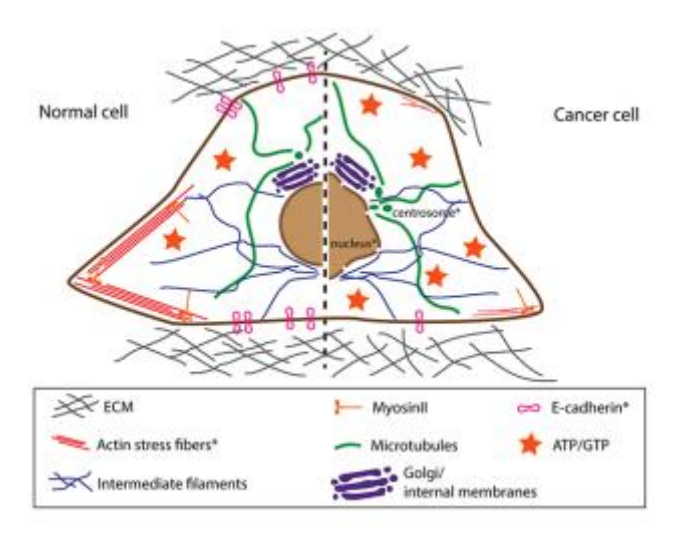


Figure 4.1 Cancerous cells have differences in rheological behaviours. Actin stress fibres contribute to cell deformability. Cancerous cells have less dense and less organised fibres compared with normal cells. Adapt from (Alibert, Goud, and Manneville 2017).

This chapter introduces the Electro-Optical deformability MIC system. This deformability cytometer can simultaneously measure the optical and electrical shape change of single cells in a viscoelastic shear flow. The system used HL60 cells, a suspending leukaemia cell line, as a cellular model to evaluate their deformability with/without different treatments. It demonstrated

an excellent correlation between the two methods and presented a feasible triggering mechanism that will be used in cell sorting. The content is presented as follows: system overview, experiment setup, correlation between optical and electrical measurements, comparison between optical and electrical deformability distributions and last, the optical-electrical deformability results for cells with different treatments.

4.2 System Overview

4.2.1 Electrodes configuration and electrical deformability

The electrode configurations were designed by Dr. Junyu Chen (Chen et al. 2024). In general, a microfluidic chip contains an array of micro-electrodes that measure the shape of the cell along two different axes.

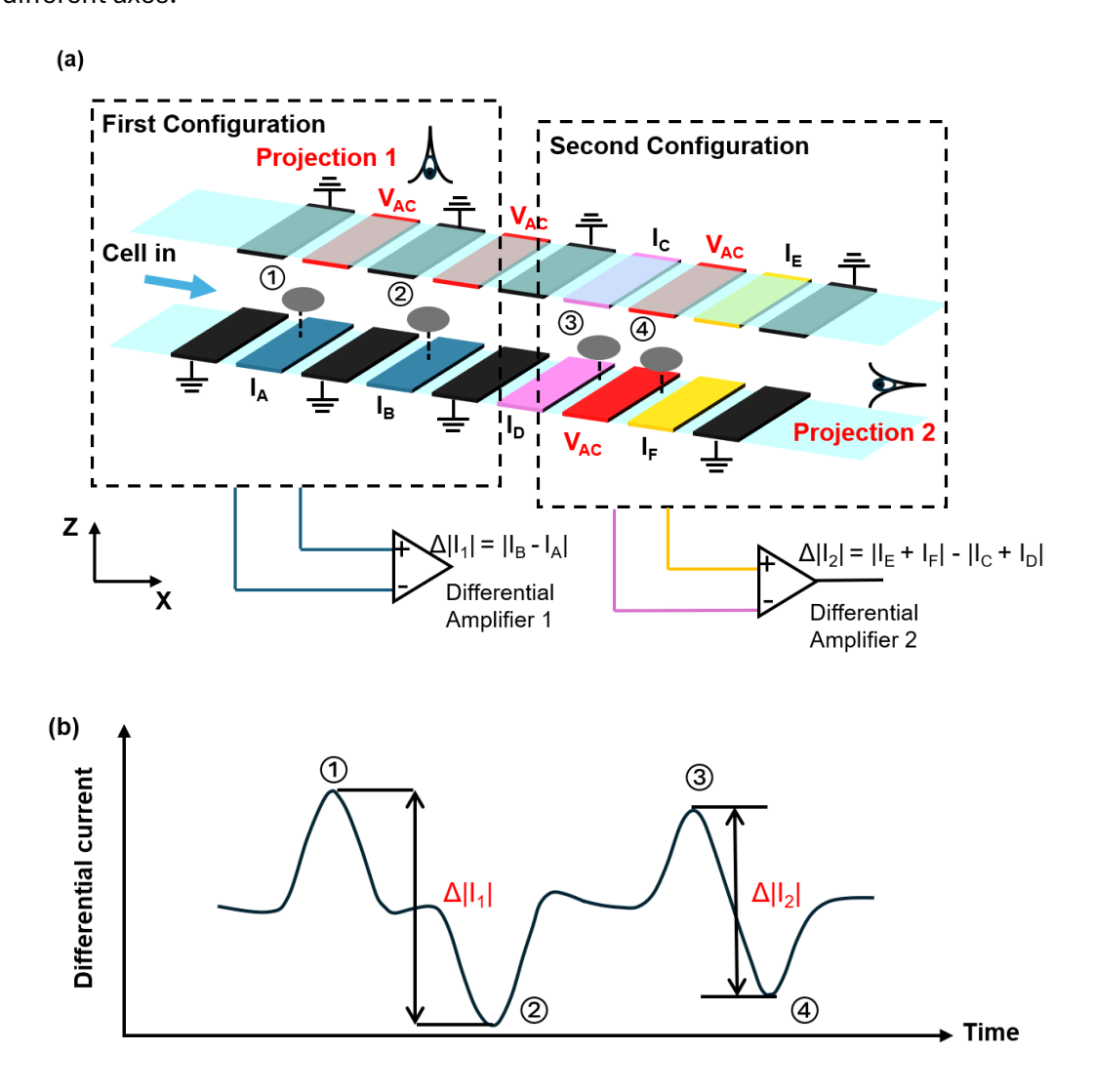


Figure 4.2 Electrode configurations and the calculation of the electrical deformability. (a) Two configurations of electrodes and deformed cells pass through the channel from position 1 to 4. The differential current generated from the first set is $\Delta |I_1|$, and the second set is $\Delta |I_2|$. (b) The waveform of the output differential current. The final output current is the sum of $\Delta |I_2|$.

Nine pairs of facing electrodes are integrated into the microchannel ($40\mu m \times 30\mu m$), and these electrodes can be divided into two configurations (**Figure 4.2(a**)). When a cell passes along it generates a differential current waveform consisting of two consecutive anti-symmetric double Gaussians (**Figure 4.2(b**)). The main part of the first configuration is two pairs of vertical voltage-sensing electrodes, which generate an electric field from top to bottom (**Figure 4.3(a**)). When a cell flows through the channel from position ① to ②, the maximum amplitude of the waveform is I_B and I_A (**Figure 4.2(b**)), and the differential current for this first configuration is $\Delta |I_1| = |I_B - I_A|$. The second configuration consists of two coplanar sets at the top and bottom walls of the channel, creating an electric field along the flow direction (**Figure 4.3(b**), along the x-axis). When a cell passes through position ③ to ④, the differential current is $\Delta |I_2| = |(I_E + I_F) - (I_C + I_D)|$ (**Figure 4.2(b**)). Finally, the generated waveform is as shown in **Figure 4.2(b**), which is the sum of $\Delta |I_1|$ and $\Delta |I_2|$.

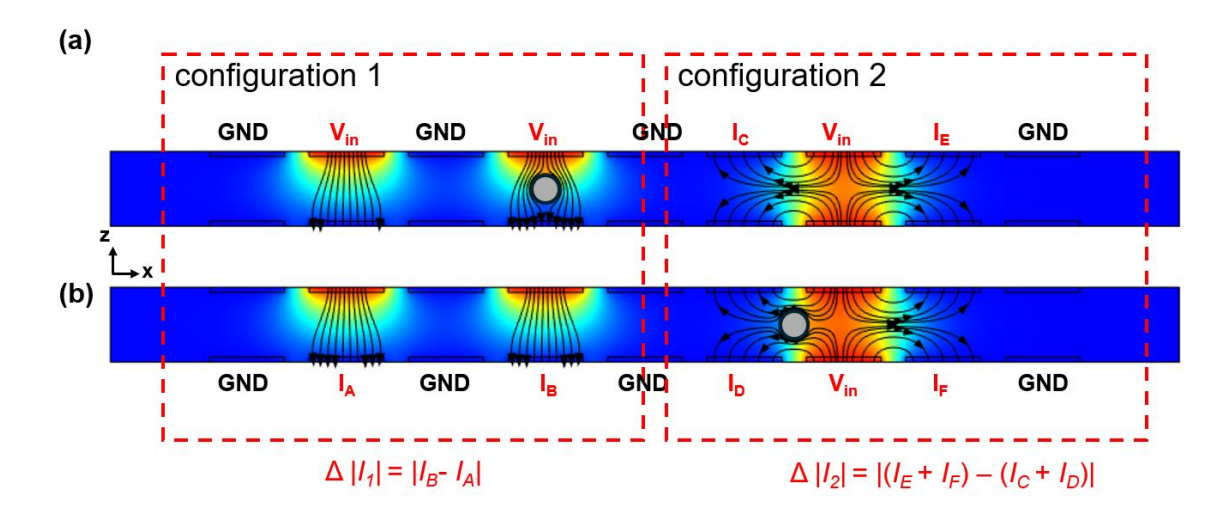


Figure 4.3 2D simulation of the electrode configurations. Applied voltage V_{in} is 1V at frequency 500kHz, and the channel dimension is 30 μ m high and 430 μ m long. The permittivity of the suspension media is $80\varepsilon_0$ and the conductivity is 1.6 S/m. The particle has a permittivity $2.5\varepsilon_0$ and conductivity 10^{-11} S/m with a diameter of 10μ m. Electrical potential and current density streamlines when the particle is in configuration (a) 1 and (b) 2.

Data processing of the impedance signal is based on a convolution filter algorithm. The normalised convolution templates, designed according to the signal waveform, are multiplied by the raw data stream. The magnitude (peak) of the impedance is extracted. The results include the timeline of the data recording period, the impedance real and imaginary parts with the transit time of each event, and the triggering signal.

The impedance on different frequency windows can probe different features of cells. At low frequencies (<1MHz), cells are electrically insulating, this feature is usually used to determine cell size. AC voltage at 500kHz is applied so that the impedance ($\Delta |I_1|$ and $\Delta |I_2|$) is a function of particle cross-section when observed from projections 1 and 2 (**Figure 4.2(a**)). In other words, these signals measure the shape of the object along the x-y and y-z plane (refer to the cartesian coordinate axis in **Figure 4.4**). Thus, the electrical deformability (**ED**) is the ratio of the impedance

(current) from the first and second electrode configurations: $\frac{\Delta |I_1|}{\Delta |I_2|}$. The design of the microchannel gradually contracts from a wide channel (width is 300mm) to a narrow one (width is 40mm) with increasing shear stress on cells generated by the viscoelastic fluid explained in **section 3.4.7**. Thus, the wide part of the channel is called the "pre-detection region", and the impedance and image detection part is called the "detection region" (**Figure 4.4**). Table 4.1 summarises the possible values of **ED** for undeformed and deformed cells.

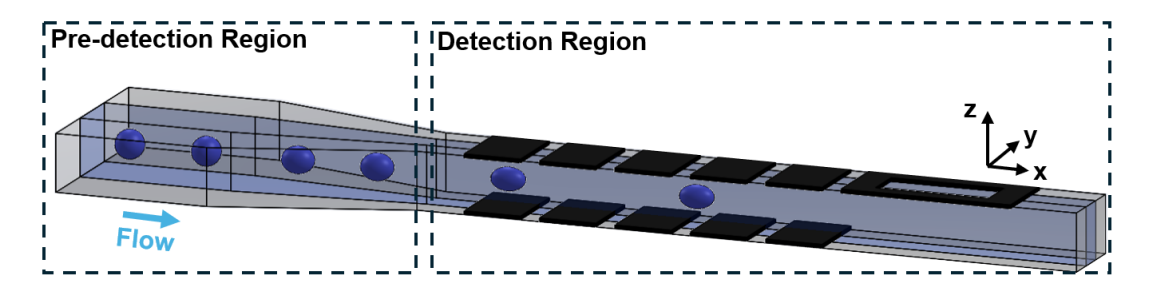
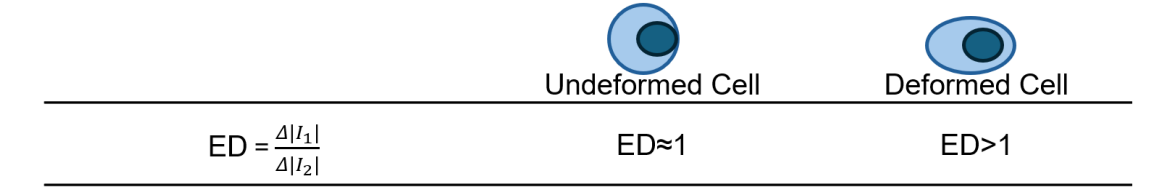


Figure 4.4 Illustration of how a cell is deformed when it flows from pre-detection to detection regions of the microchannel. To simplify the diagram, GND electrodes are not shown here. The dark blue region in the centre of the channel, corresponding to the central region that will be mentioned in **section 4.4.2**. The focusing plan induced by the viscoelastic flow in this case is parallel to the x-y plan and located at the centre of the channel height (z-axis).

Table 4.1 Definition of electrical deformability (**ED**) and the range of **ED** values for cells in undeformed and deformed states.



When cells flow in the channel, from the pre-detection to the detection region, the shear stress increases gradually, and cells are elongated along the flow direction (x-axis). Thus, cells in the pre-detection region are spherical particles whose sizes in projections 1 and 2 are the same, so the **ED** is around 1; cells in the detection region have a bigger size in projection 1 than in projection 2 so the **ED** is greater than 1. Polystyrene beads were used to calibrate the deformability. They are solid particles with fixed diameter and dielectric properties, meaning their projections in the two directions and the low-frequency impedance are the same. Their **ED** should be 1.

4.2.2 Image acquisition and processing and optical deformability

The second part of the system measures the optical deformability (**OD**) of cells. There are two crucial stages in optical measurement: image acquisition, which is controlled by the triggering mechanism, and the image processing algorithm. A homemade bright-field microscope system was built up at the top of the MIC board. As shown in **Figure 4.5**, when deformed cells are in the

"detection region" and their corresponding impedance is generated, synchronised optical images of them are captured by triggering a high-speed LED, which projects an image onto a low-cost CMOS camera (MQ003CG-CM, XIMEA). This system uses a variable time delay in the trigger. The triggering mechanism is a real-time data processing implemented by the microcontroller (MCU, Teensy 4.0, PJRC). The circuit connection is shown in **Figure 4.5(a)**. The impedance signal is first demodulated with a lock-in amplifier (HF2LI, Zurich Instruments) before the digitised signal is sent to the MCU. The MCU determines the velocity of the cell and calculates the time point at which it arrives at the image capture window. At this point, the output current signal of the MCU is amplified by the LED driver and then used to trigger an LED (CBT-90-B-L11, Luminus), illuminating the image capture zone and projecting the cell outline onto the camera which is set to video recording mode (100fps). Thus, each frame contains an image of a cell, synchronising to the electrical impedance signal.

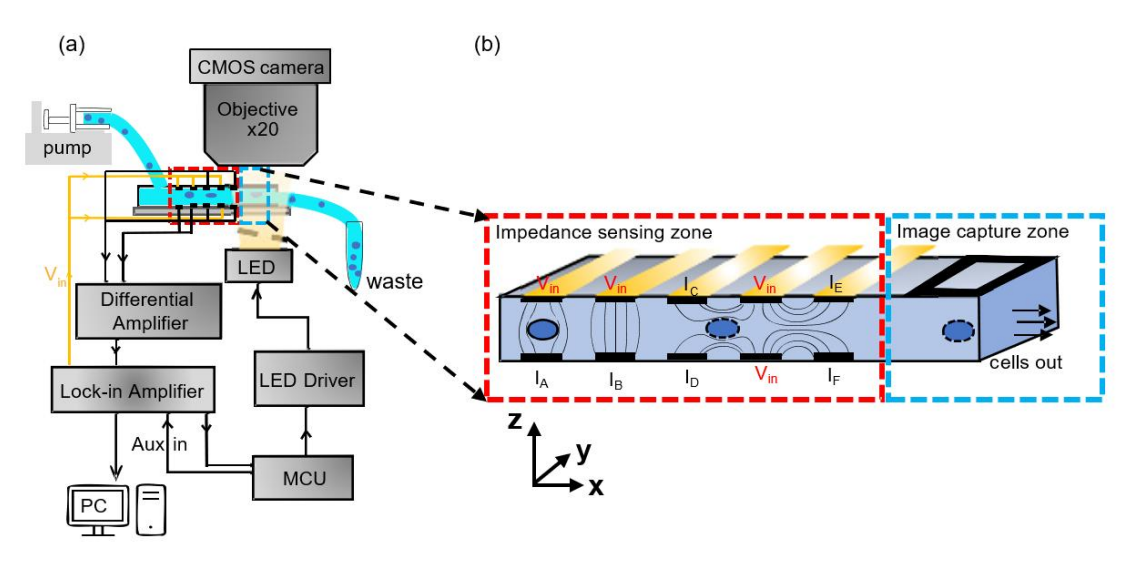


Figure 4.5 System overview. Cells suspended in a viscoelastic fluid are pumped through the "detection region" of the channel ($40\mu m \times 30\mu m$) where they deform and become elongated. The electrodes are connected to amplifiers and a lock-in to extract the impedance signals. The lock-in also provides a trigger signal. (b) The detection region is divided into two parts: the electrical impedance sensing zone and the optical image capture zone. The two electrode configurations measure the vertical ($\Delta |I_1|$) and horizontal ($\Delta |I_2|$) impedance of the cell. An image is focused onto a simple CMOS camera with a X20 objective.

4.2.2.1 Triggering principle

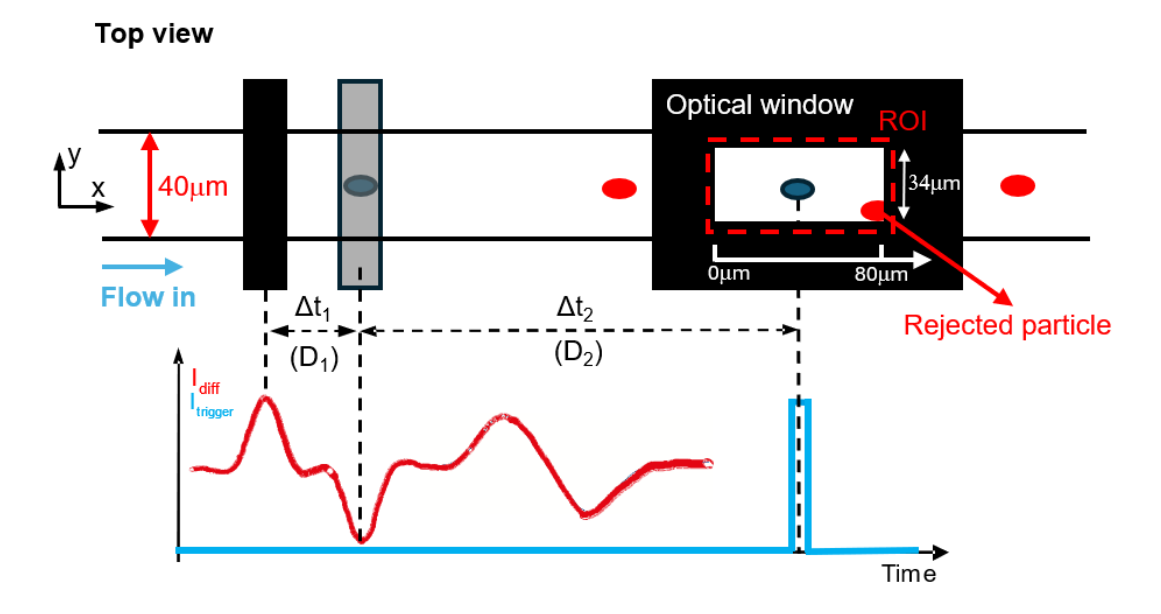


Figure 4.6 Diagram showing the principle of the triggering mechanism. The impedance (differential current) of the first configuration is used to calculate the velocity of the particle, obtained from the ratio of the distance between the impedance peak and valley (D_1) and the transit time (Δt_1) obtained from the impedance signal. The predicted time to trigger Δt_2 is then calculated with known distance D_2 and the trigger pulse generated to drive the LED. The red rectangle defines the ROI (34µm wide, 80µm long) of the optical image capture zone. Only two pairs of electrodes in the first configuration are shown in the diagram because the other set is not used for triggering.

The triggering principle does not use a simple threshold trigger but uses the time at which a cell arrives at the imaging zone by calculating its velocity. The MCU samples the impedance signal of the first configuration via an ADC at a sample rate of 87ksps. To ensure that the collected impedance data is sufficiently smooth for peak detection, an IIR filter was applied after the ADC. Particles flowing in the "detection region" have a steady velocity because the fluid in the channel can be considered laminar flow, and the velocity of laminar flow follows a stable parabolic distribution. The data stream is processed by a peak-valley detection algorithm to determine the transit time Δt_1 . As **Figure 4.6** shows, the peak and valley of the impedance signal correspond to the centre of the two pairs of electrodes (D_1 = 80mm), allowing the velocity to be calculated from:

$$v = \frac{D_1}{\Delta t_1} \tag{4.1}$$

The distance to the centre of the optical window D_2 is known so that the transit time Δt_2 that LED will be triggered is given by:

$$\Delta t_2 = \frac{D_2}{v} \tag{4.2}$$

The peak-valley detection is a second-order differential identification algorithm. The sampled data stream is expressed as:

$$F_d = [d_1, d_2, d_3, ..., d_n]$$
 (4.3)

The first differential operation is:

$$Diff_i = d_{i+1} - d_i \ (1 \le i < n)$$
 (4.4)

As the amplitude does not matter, the possible values of $Diff_i$ are set to 1 or -1 according to the sign:

$$sign(Diff_i) = \begin{cases} 1, & if \ Diff_i > 0 \\ 0, & if \ Diff_i = 0 \\ -1, & if \ Diff_i < 0 \end{cases}$$

$$(4.5)$$

for position i, whose $sign(Diff_i) = 0$, meaning $d_{i+1} = d_i$. A possible circumstance is if "i" is the peak or valley position, the differential of $sign(Diff_i)$ will be the same as the non-peak or non-valley position. To solve this, $sign(Diff_i) = 0$ can be classified into 1 and -1 with an additional condition:

$$\begin{cases} -1, & if \ Diff_i = 0 \ and \ Diff_{i-1} < 0 \\ 1, & if \ Diff_i = 0 \ and \ Diff_{i-1} > 0 \end{cases}$$
 (4.6)

Then, the differential of $sign(Diff_i)$ is processed. There are only two possible values, -2 and 2. The position of -2 is the peak, and 2 is the valley. **Figure 4.7** summarises a flow chart of the algorithm.

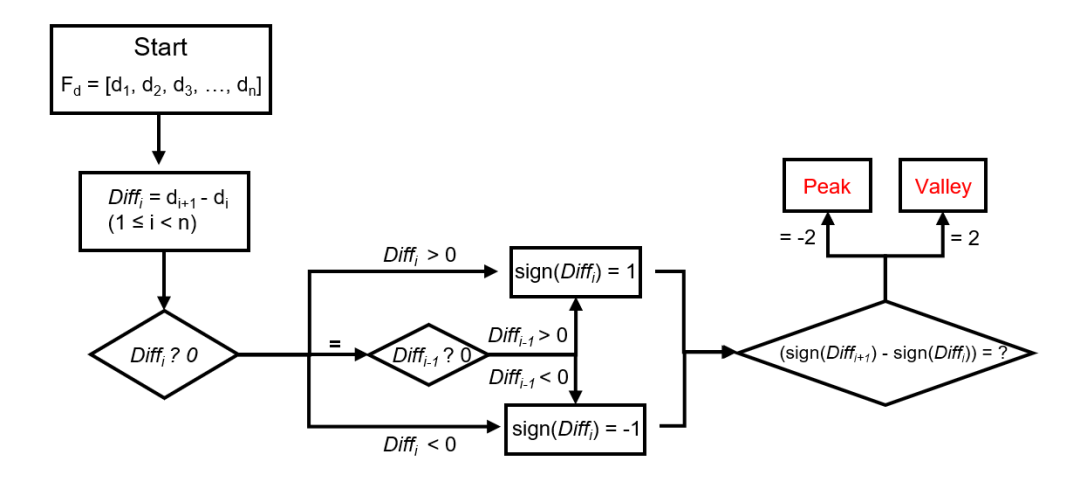
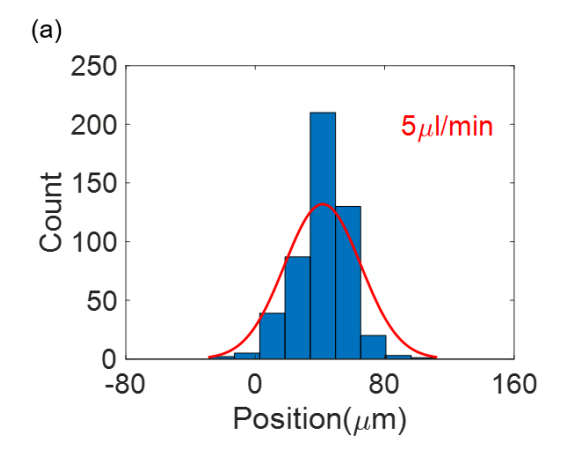


Figure 4.7 The flow chart of the peak-valley detection algorithm. The data is processed by differencing operation twice, and the results of each differencing are binarised. Finally, the values of 2 or -2 in the results are used to determine the peaks and valleys of the original signal.

Ideally, the MCU should illuminate the particle in the centre of the ROI, but a small random offset in position occurs due to latency in the MCU.



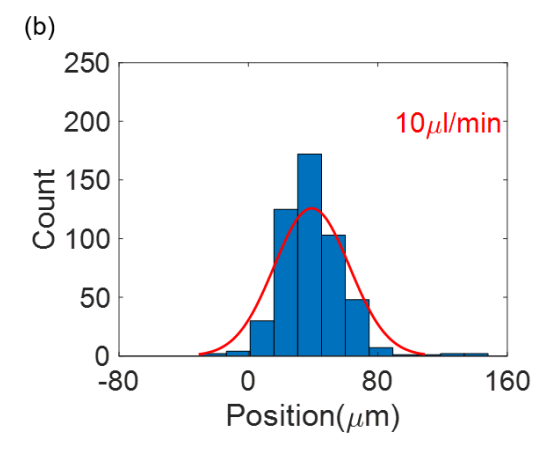


Figure 4.8 Histogram of experimental cell position illuminated by the LED at (a) 5 and (b) 10 μ L/min flow rates. Data for 500 cells for each plot. The x-axis labelled "Position" corresponds to the x coordinate within the optical window shown in Figure 4.6.

To assess the algorithm, the position information of cells was extracted. The cells have their position coordinates determined by the transit time analysed from the impedance signal. The dimension of the ROI (**Figure 4.6**) is 80µm long and 34µm wide. The cell position along the flow direction (x-axis) is of interest so their position ranges from 0~80µm if they are inside the ROI. **Figure 4.8** shows experimental data of one sample. It demonstrates that the camera can capture the vast majority of the cells (within 0-80µm). At 5μ L/min and 10μ L/min, the position distribution was fitted to a normal distribution: N~(μ = 41.7, σ = 23.6) and N~(μ = 39.1, σ = 23.3), respectively. The peaks (μ) are close to the centre of the ROI (+40mm), which means that most of the triggers are accurate, and similar standard derivation (σ) indicates the triggering mechanism is stable.

The strategy for triggering signals differs from other reported systems. Impedance-based triggering has been previously demonstrated (Liang et al. 2021), where an electrical signal from a cell crossing an electrode array was used to trigger a camera that recorded 15 frames at 2,000 frames per second with a 50µs exposure time. Another imaging system based on LED illumination relied on a threshold value to trigger (Bansal et al. 2022). These methods collected a series of images for one cell at a high frame rate, meaning a massive amount of data was processed. As mentioned above, this triggering system uses the individual velocity of each cell to determine the LED trigger timing. Accurate position prediction eliminates the need for continuous imaging, reducing the frame rate and enhancing the efficiency of image post-processing.

Although the camera has a low frame rate (100fps), motion blur is eliminated by using a short illumination pulse generated by a MOSFET driver that provides the required high current to the LED (Wilson et al. 2014; Bansal et al. 2022). To freeze the motion of cells which are in the flow, the total camera exposure time was decreased to the order of microseconds. Herein, we set the LED pulse time to 2 µs rather than adjusting the camera exposure time. For 5µL/min flow rate, the

maximum velocity of cells in the flow is 0.144 m/s and the flowing distance within 2 μ s is 0.288 μ m. For 10 μ L/min flow rate, this mapping length is 0.576 μ m and 0.864 μ m for 15 μ L/min. The typical average diameter of cells is 12 μ m, which means the blur edge is up to about 7.2% of the diameter. This is acceptable for the processing algorithm to recognise particles from the images.

4.2.2.2 Image processing

Post image processing was performed using custom scripts in MATLAB. **Figure 4.9** shows a flow chart of the image processing.

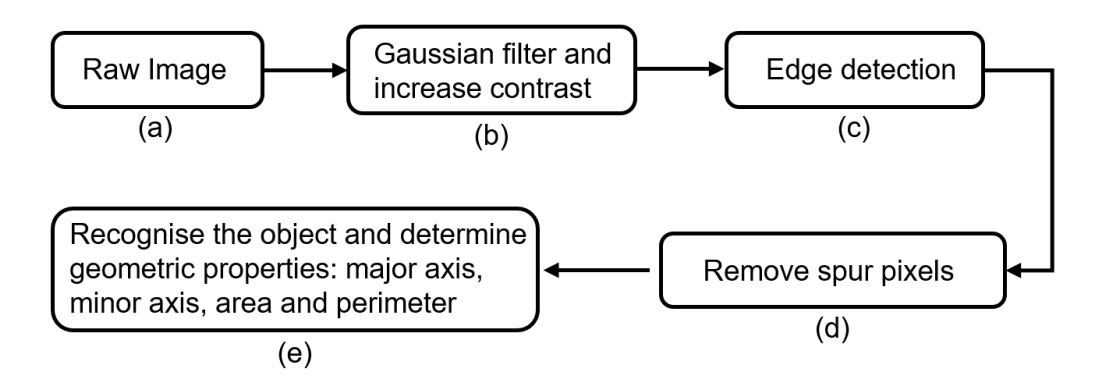


Figure 4.9 The flow chart of image processing. (a) - (e) corresponds to the label number of the processed result image at each stage.

There are four stages to process a raw image. Due to the limited number and size of pixels (648 \times 488, 7.4 μ m \times 7.4 μ m), the image quality is not high. Moreover, cells are transparent, which makes it hard to recognise the object from the background. Thus, the algorithm is designed to improve the contrast between cells and the background and extract information on the target particle. The following Figures **4.10-4.14** show an example of the procedure.

Stage 1: Gaussian filter and adjust contrast

It is apparent in the raw image (a) that the background noise is high. The first step is to use a Gaussian filter to smooth the ROI to reduce interference from textures and fine details in edge detection and feature extraction in the next stage, making recognition more robust. Increasing the contrast makes the edges clearer. If this stage fails, the edge detection will not find the enclosed outline of the particle, and the object will be missed.

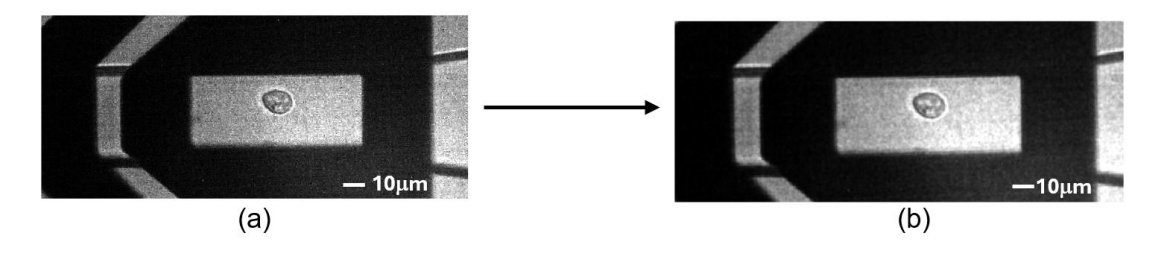


Figure 4.10 Raw image (a) and the resulting image (b) after processing by a Gaussian filter and increasing contrast. The image is blurrier than the raw image because the filter removed noise and smoothed the edges.

The key part of the code in MATLAB is:

Stage 2: Edge detection

The edge detection algorithm finds the region where pixel intensity (brightness or colour) changes significantly. These changes often correspond to the edges of objects in the image. A threshold value is first determined to extract significant edges. There are many different methods, and simple ones are gradient-based methods, i.e. Sobel Operator, Prewitt Operator and Roberts Cross Operator. However, the choice should be based on the characteristics of the image. In this case, the particle edge in image (b) has a smooth grayscale transition, so it needs a more comprehensive method, the Canny method. Unlike other methods, it applies two different thresholds to distinguish strong and weak edges, including weak edges in the output only if they are connected to strong edges. The resulting (c) is a binary image whose pixel values are 0 or 1.

The code is:

```
thre = graythresh(imgD); % Get the threshold

BW_filter1 = edge(imgD, 'canny', thre*0.8) % Edge detection function
```

Note that the threshold used in the function requires multiple manual attempts to determine a proper value. If the threshold is not suitable, the output edge of the particle will not be enclosed, which is eliminated by the following stage and no particle is recognised.

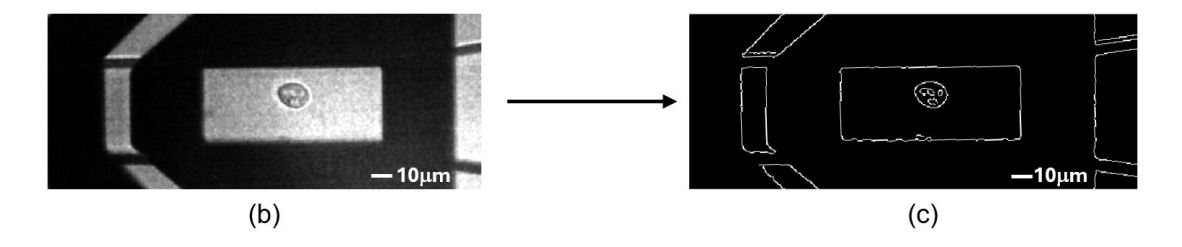


Figure 4.11 Image (b) in the last stage and the resulting image (c) after being processed by the edge detection function.

Stage 3: Remove spur pixels

The image has been converted to a binary one in which the value of white is 1, and the value of black is 0. In (c), there are many objects with enclosed edges. This stage removes as many irrelevant pixels as possible. A morphological operation on binary is applied first, to eliminate spurred pixels around the edge. If the enclosed edge has spurred pixels, they can influence the assessment of the major or minor axis in the last stage, leading to inaccurate optical deformability. For example, here is how the code processes spurred pixels:

0000		0000
0000		0000
0010	becomes	0000
0100		0100
1100		1100

Figure 4.12 Example of eliminating spur pixels using the morphological operation.

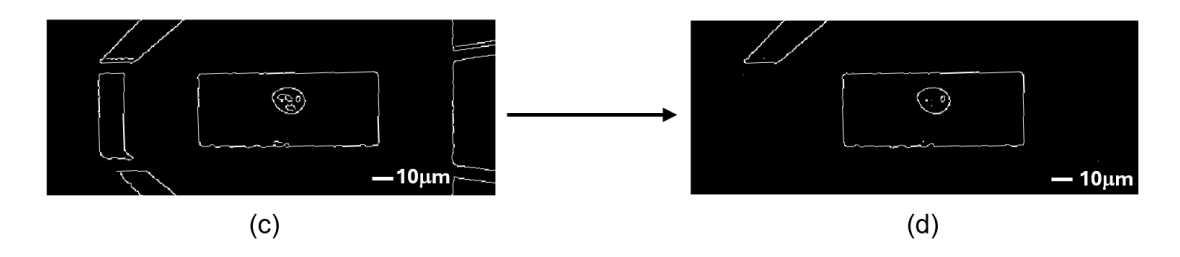


Figure 4.13 Image (c) from **Figure 4.11** and the resulting image (d) after applying the morphological operation to eliminate spurred pixels.

The code is:

```
BW_filter2 = bwmorph(BW_filter1,'spur',inf);
```

Stage 4: Extract target particle

In this stage, the first step is to remove the connected components with more than a specific number of pixels (replaced by 0) to ensure that only the target object is left. As shown in (d), the rectangle around the particle is the edge of the ROI, which has a specific length so that it can be removed. Then, fill the object which has an enclosed edge using the "imfll" function. Finally the geometric properties of a filled object (Image (e)) can be extracted using the function called "regionprops" in MATLAB.

The key code is given by:

```
BW_filter3 = filterLarge(BW_filter2,400);

BW_filled = imfill(BW_filter3,'holes');

BW_filled = bwareaopen(BW_filled,400);

stats = regionprops('table',BW_filled,'Area','BoundingBox','Centroid',...,'MajorAxisLength','MinorAxisLength','Perimeter');
```

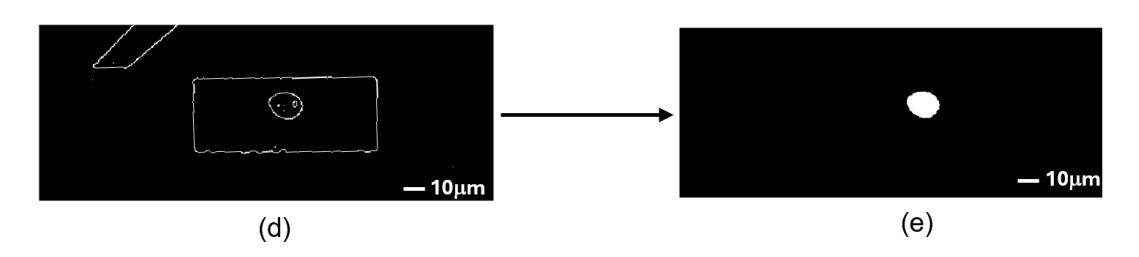


Figure 4.14 Image (d) in Figure 4.13 and its resulting image (e) after extracting the target particle.

The "regionprops" function evaluates properties such as area, centroid, major and minor axis for each object in an image. It identifies distinct objects in binary images using 8-connected neighbourhoods for 2D images. The properties that are used are defined as follows:

Area is calculated from the actual number of pixels in the region and returned as a scalar.

Centroid is the centre of mass of the region, returned as a 1-by-2 vector. The first element of Centroid is the horizontal coordinator and the second is the vertical coordinator.

Major (minor) axis length is the length in pixels of the major (minor) axis of the ellipse that has the same normalised second central moments as the region, returned as a scalar.

As **Figure 4.15** shows, the edge of the contour, major axis and minor axis are recognised by the algorithm.

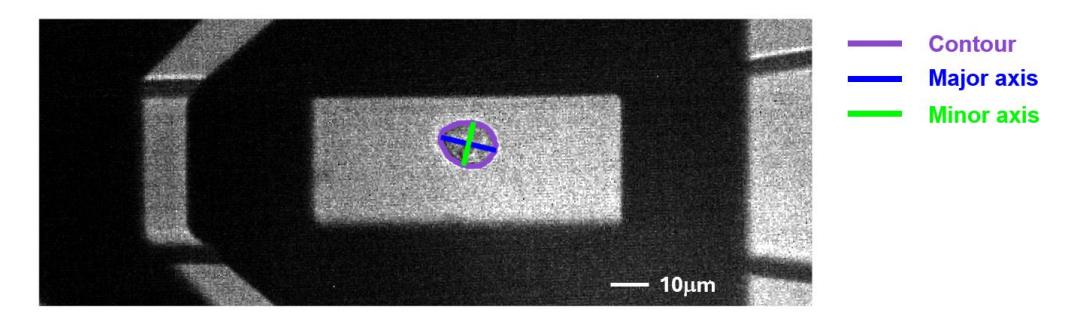
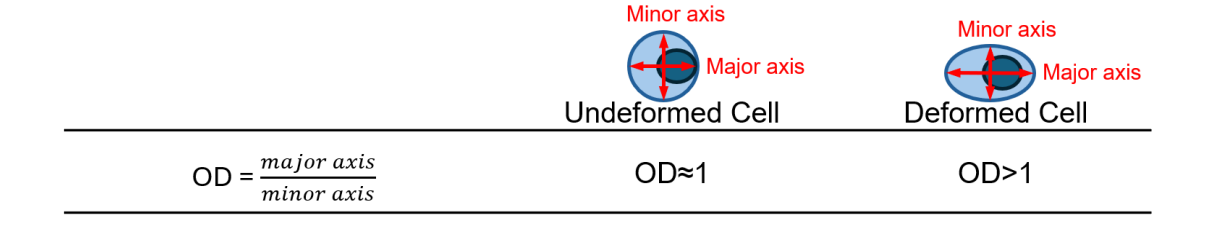


Figure 4.15 The cell contour, major axis and minor axis extracted by the MATLAB image processing script. The contour is determined by the edge detection algorithm; major and minor axis are determined with the "regionprops" function.

The optical deformability (**OD**) is defined as the ratio of major axis length to minor axis length: **OD** $= \frac{major \ axis}{minor \ axis}.$ The possible values of **OD** are summarised in **Table 4.2**.

Table 4.2 Definition of electrical deformability (**OD**) and cases for cells in different states.



It is worth noting that other methods for recognising the target particles were also tested. For example, image opening and closing operations were tried. Opening operation is a process in which erosion is applied first, and then a dilation operation is performed; closing is a process in which the dilation process is performed first, followed by an erosion operation. Opening is used to remove small objects from the foreground, whereas closing is used to remove small holes in the foreground. After obtaining a binary image, these operations can be applied. Compared to the final chosen process, this method can address the shortcoming of losing the target object due to failed edge detection. However, opening and closing operations need structuring elements with

fixed shapes, such as diamond, disk, and octagonal shapes. Thus, it would change the outline of the particles, making the major and minor axis lengths inaccurate, which is unacceptable.

The overall accuracy of the image processing pipeline is about 53%. Different days with slightly different illumination conditions may influence the accuracy.

4.2.3 Electro-Optical data matching and system calibration

To correlate two datasets captured from different systems without complicated synchronised settings, matching the corresponding **OD** and **ED** is crucial. The camera is set to video recording mode (100fps), and the LED is illuminated when triggered. Thus, only bright frames contain particles. The number of dark frames between two consecutive bright frames can be used to calculate the time interval between two adjacent bright frames. The timeline of impedance data is known, and the trigger signal matches its corresponding impedance. Thus, as long as the start time of the impedance timeline is aligned with the first bright frame in the video, data synchronisation can be achieved.

Coincidence in this system has three aspects: the impedance signal, trigger signal and image detection. The coincidence of impedance data is very low. For example, the impedance detection region dimension is $350\times30\times40(\mu\text{m})$, and at a typical cell concentration of $5\times10^5/\text{mL}$, the Poisson distribution $P(k) = \lambda^k e^{-\lambda}/k!$ shows that the probability of two coincident particles is 2%. Therefore, the cell concentration was set to $1\times10^5/\text{mL}$ where the probability of coincidence is nearly zero. The next possible occurrence of coincidence is the trigger signal generated by the microcontroller. With the sample rate of the ADC, the triggering algorithm can detect as many cells as the number of impedance signals. Even though a rare coincidence happens, the trigger system can still generate separate trigger signals. For example, **Figure 4.16** shows two impedance signals overlapping with the time interval between them only 1.53 ms, but two consecutive trigger signals were generated separately.

Practically, the coincidence rate is dominated by the frame rate of the camera. The frame rate was set to 100fps; if the interval between two adjacent cells is less than 10 ms, the exposure time will be too long to generate separate images, and image coincidence occurs. A set of images was analysed at a flow rate of 5μ L/min to determine the coincidence rate. This gave a coincidence rate of around 2% (1.9% for 53 frames with two cells from a total of 2844). Increasing the flow rate would lead to a higher coincidence rate, so values between 5, 10 and 15 μ L/min were used.

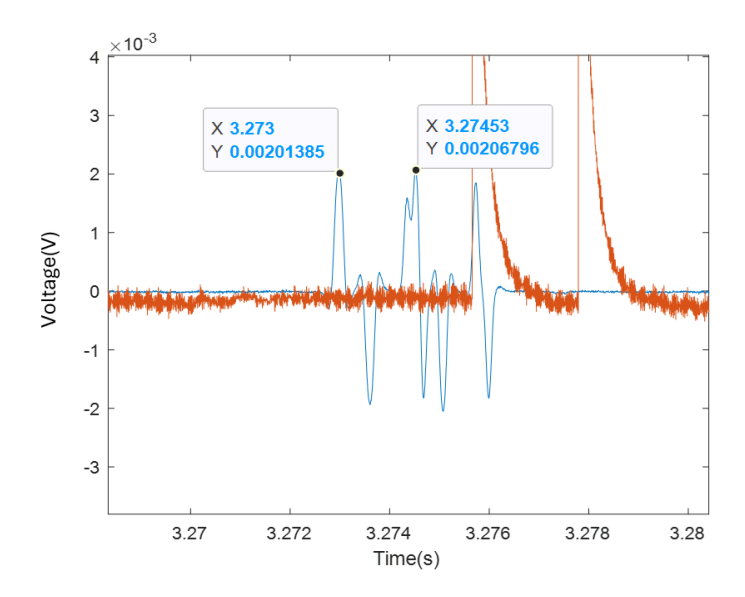


Figure 4.16 Example of impedance (blue line) coincidence with the corresponding trigger signal (brown). The time interval between these two particular events is 1.53 ms.

As mentioned above, the polystyrene beads were used as calibration particles because they have fixed size, deformability and dielectric properties. For **ED**, the cell impedance signal of the first and second configuration should be normalised against that of beads because it can eliminate any drift in the impedance system. Practically, the mean value of the bead population is used to normalise. The normalisation of **ED** is expressed as:

Normalised **ED** =
$$\frac{\Delta |I_{1(cell)}|/mean(\Delta |I_{1(bead)}|)}{\Delta |I_{2(cell)}|/mean(\Delta |I_{2(bead)}|)}$$
(4.7)

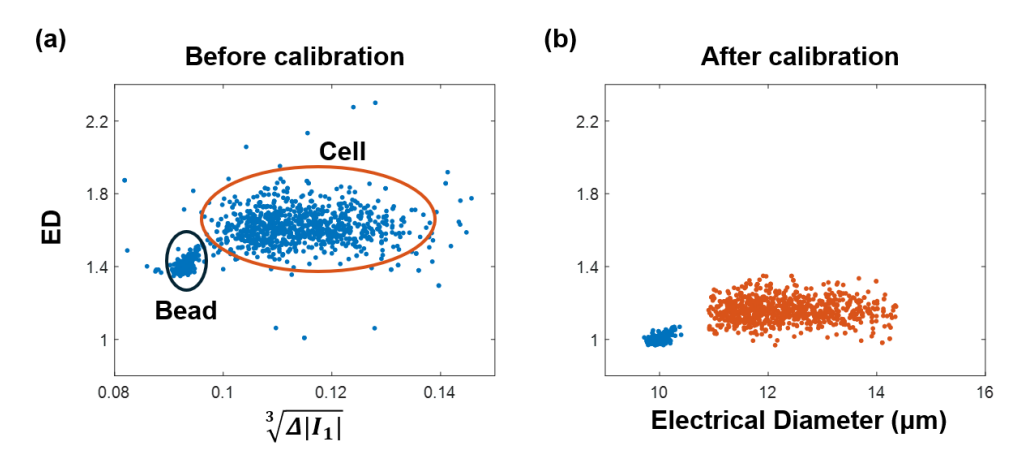


Figure 4.17 (a) The scatter plot of $\sqrt[3]{\Delta|I_1|}$ versus **ED** for untreated cells at 5 mL/min before calibration. (b) The scatter plot of Electrical Diameter for those cells after calibration.

Figure 4.17 (a) and (b) shows a scatter plot of ED for untreated cells at 5 μ L/min before and after calibration. The x-axis is the electrical radius of the particle. In this system, 10 μ m diameter beads are used and the typical diameter of cells is 12 μ m, so beads and cells can be gated along the x-axis. After gating, the mean value of $\Delta |I_1(\text{bead})|$ and $\Delta |I_2(\text{bead})|$ for beads is calculated, with

 $\Delta |I_{1}(\text{cell})|$ and $\Delta |I_{1}(\text{cell})|$ normalised using **equation 4.7**. After calibration, the mean **ED** of beads should be 1, and deformed cells > 1.

In addition to calibration for **ED**, **OD** also needs to be normalised. The optical diameter is defined as the average of major axis and minor axis: $\frac{major\ axis + minor\ axis}{2}$ in pixels. As for **ED**, before calibration, the **OD** for beads is not 1, so it needs to be normalised. The **OD** of cells also needs to be calibrated using the mean value of the beads. **Figure 4.18** shows a scatter plot of beads and cells after gating and calibration.

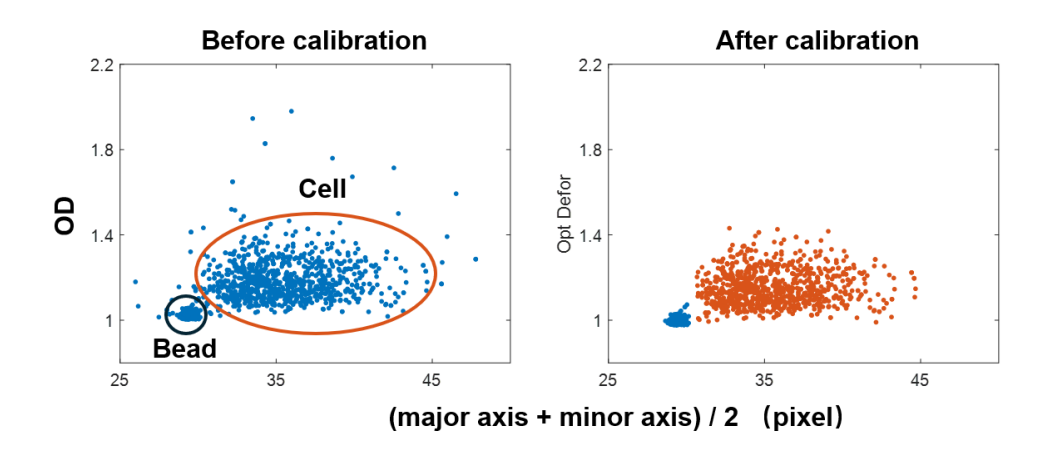


Figure 4.18 Scatter plot of optical diameter versus **OD** for untreated cells at 5 μ L/min before and after calibration. The mean **OD** of the gated bead before calibration was 1.03 and after calibration was 1.0; the mean **OD** of the gated cell before calibration was 1.19 and after calibration was 1.15.

Finally, the electrical and optical diameter of cells needs to be calibrated because they have absolute dimensions. For electrical diameter, normalised $\sqrt[3]{\Delta|I_1|}$ is scaled by the mean of $\sqrt[3]{\Delta|I_1(bead)|}$ and set to "10 (µm)". For optical diameter, the major and minor axis of the beads are calculated in pixels, to determine their absolute value. The physical dimensions of the chip are then used to scale the real size of the beads.

4.3 Experiment Setup

4.3.1 Experiment procedure

Cells were suspended in a viscoelastic fluid and loaded in a 1mL syringe (Disposable syringe with Luer-Lok Tips, 309628, BD), flowing along the "detection region" (see **Figure 4.4**), where shear stress deformed them. The flow rate was set to 5, 10 and 15 μ L/min, controlled by a high-accuracy pump (Pump 11 Pico Plus, Harvard Apparatus). The outlet was placed directly on a clean petri dish to collect waste without affecting the fluid pressure in the microchannel or causing flow rate instability.

A 0.5%(w/v) methylcellulose-DPBS buffer was used to suspend cells. 200 mL of 0.5%(w/v) MC-DPBS solution was made as follows:

After heating 70 mL of DPBS in a clean beaker to 80°C, 1 g of MC powder was added and stirred gently to disperse. 130 mL DPBS at room temperature was added to the mixture with constant stirring to avoid clumping or aggregation. The MC mixture was hydrated as the temperature decreased and became a jelly. After the solution had cooled to room temperature, the mixture was stored at a 4°C fridge to hydrate the MC and avoid bacterial growth.

Before measurement, all buffers were filtered through a 0.22 μ m filter to avoid chip blockage. The chips were cleaned with 1M sodium hydroxide solution at a low flow rate (typically 5 μ L/min) for about 10 minutes before the experiment. After washing, the channel was flushed with deionised water (DI water). After treatment, cells were resuspended by the centrifuge (Centrifuge 5418, Eppendorf) at 100 rcf for 5min. Then, remove the supernatant and add MC-DPBS buffer. Finally, the calibration polystyrene beads (10 μ m, Sigma Aldrich) were added to the sample. For each experiment group, measurements were recorded after the flow had stabilised for around 2 minutes.

As mentioned in <u>section 4.2.3</u>, the key point in this combined system to synchronise two different datasets was to align the start time of the impedance timeline with the first bright frame in the video. The order of recording data from the two systems was essential to achieve this. The impedance system first recorded the data, including the real and imaginary parts of impedance and the triggering signal produced by the MCU that connected to the Auxiliary port in the Lock-in. When the MCU circuit was not powered, the auxiliary channel had no trigger signal. Then, the power of the optical trigger circuit was turned on so that the first trigger signal in the recorded MATLAB file corresponded to the first illuminated frame.

4.3.2 HL60 cell culture

HL60 is a human cell line originating from the peripheral blood lymphocytes of a 36-year-old woman diagnosed with acute promyelocytic leukaemia. It was among the first human myeloid leukaemia cell lines successfully established as a continuous suspension culture, overcoming previous challenges in maintaining such cells in long-term culture. HL60 is a suspension cell line with a round shape and some clustering. It is widely used to study cellular mechanical properties because it is easy to culture and has a constant 10-14mm diameter. Apart from this, many studies (Urbanska et al. 2020; Otto et al. 2015; Xavier et al. 2016) have proven that it is simple to change the physical properties of HL60 cells with chemical treatments that alter their deformability. HL60 can double every 24 hours and must be within the concentration of $1 \times 10^5 \sim 1 \times 10^6$ cells/mL. Thus, they must be split every 48 hours and resuspended to a concentration of 2×10^5 cells/mL.

HL60 cells were grown in RPMI 1640 + Glutamax (Gibco) media with 10% (or 20%) Fetal Bovine Serum (FBS, Gibco), 1% Penicillin-Streptomycin (Sigma-Aldrich) in a humidified incubator at 37°C and 5% CO₂. Choosing 10% FBS or 20% FBS depends on the stage of the cells. If it is just thawed from the liquid nitrogen, a medium with 20% FBS should be used because cells in this state need more nourishment to recover. For the routine culture, 10% FBS is enough to maintain cells normal state.

Cells were frozen in liquid nitrogen to prevent cell death and maintain long-term viability. The cryopreservation solution was made of 10% DMSO with 90% (v/v) FBS. When thawing them, the solution must be quickly removed from the culture by centrifugation after bathing in a 37°C water bath. Then, resuspend cells in the culture media with 20% FBS for around 2 weeks until they had resumed viability.

4.3.3 Cell treatment

This section includes the cell treatments regarding altering the deformability of HL60 cells. To test the feasibility of the system, the deformability cellular model should have a wide range of variations. Herein, Cytochalasin D (CytoD) and Latrunculin B (LatB) were used to perturb the cytoskeleton, reducing the stiffness of the cells and leading to higher deformability. Glutaraldehyde was used to crosslink proteins, especially in the cell membrane, which fixed cells and led to cells in an undeformed state.

4.3.3.1 Cytochalasin D and Latrunculin B

As <u>section 4.1</u> mentioned, actin stress fibre is one of the key components that directly impact cell stiffness (Alibert, Goud, and Manneville 2017). It conveys intracellular traction and contraction forces to the extracellular matrix to maintain cell structure and tone. Thus, measuring stiffness provides a direct indication of the physical state of the actin cytoskeleton. The mechanical properties of the filament system in a cell are determined by the intrinsic characteristics of individual actin filaments and their organisation into networks and bundles (Wakatsuki et al. 2001). In short, changes in actin filament dynamics reflect the degree of cell deformability. The actin cytoskeleton is a highly dynamic structure, with its fundamental unit, monomeric actin or G-actin, undergoing constant polymerises and depolymerises. The produced polymer is known as filamentous or F-actin (Ketelaar et al. 2012). Cytochalasin D is a class of fungal metabolites known as a kind of inhibitor of actin dynamics via multiple mechanisms (Shoji et al. 2012). A well-known way is the barbed-end capping mechanism. This inhibition occurs by binding to the growing ends of F-actin, blocking the addition of monomeric actin (G-actin) at these sites (Casella, Flanagan, and Lin 1981) (Figure 4.19). This process would lead to a destabilisation

of the cell actin cortex (Otto et al. 2015). Long actin filaments would be disrupted and replaced by large focal aggregates of F-actin (**Figure 4.20**).

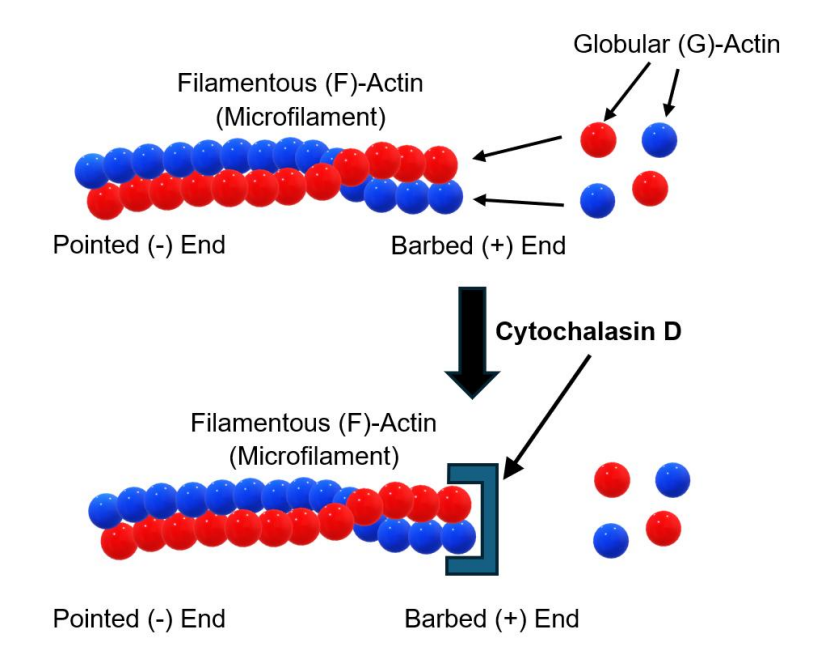


Figure 4.19 The diagram of the barbed end capping mechanism of Cytochalasin D (CytoD) that inhibits the polymerisation of F-actin.

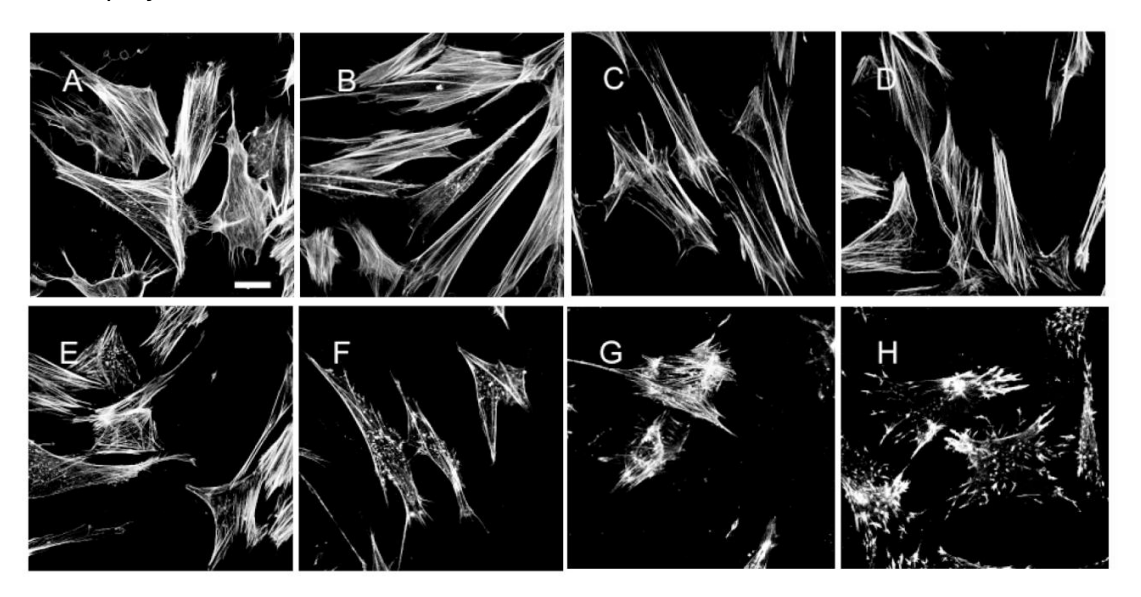


Figure 4.20 The microscope images of changes in the organisation of the actin cytoskeleton at various concentrations of CytoD. The cells were incubated with 0.1% DMSO (A, control), 200pM (B), 900 pM (C), 4 nM (D), 20 nM (E), 90 nM (F), 400 nM (G) and 2μM (H) for 30 minutes. At a CytoD concentration of 2 μM, almost all the long actin filaments were disrupted and replaced by large focal aggregates of F-actin. Scale bar: 50μm. The image is adapted from (Wakatsuki et al. 2001). Latrunculin B (LatB) are architecturally marine compounds isolated from the RED Sea sponge *Latrunculia magnifica* (Spector et al. 1989). It is also an inhibitor of actin dynamics that disrupt the cytoskeleton. Unlike CytoD, LatB has a different mechanism of action. It affects the polymerisation of pure actin in a manner consistent with the formation of a 1:1 molar complex with G-actin (Spector et al. 1989; Coué et al. 1987). Because filamentous formation requires monomers to bind to the barbed end continuously, this process is interrupted by LatB binding

with G-actin (**Figure 4.21**). In conclusion, CytoD inhibits F-actin to prevent it from elongation, while LatB binds with G-actin to avoid it from polymerisation.

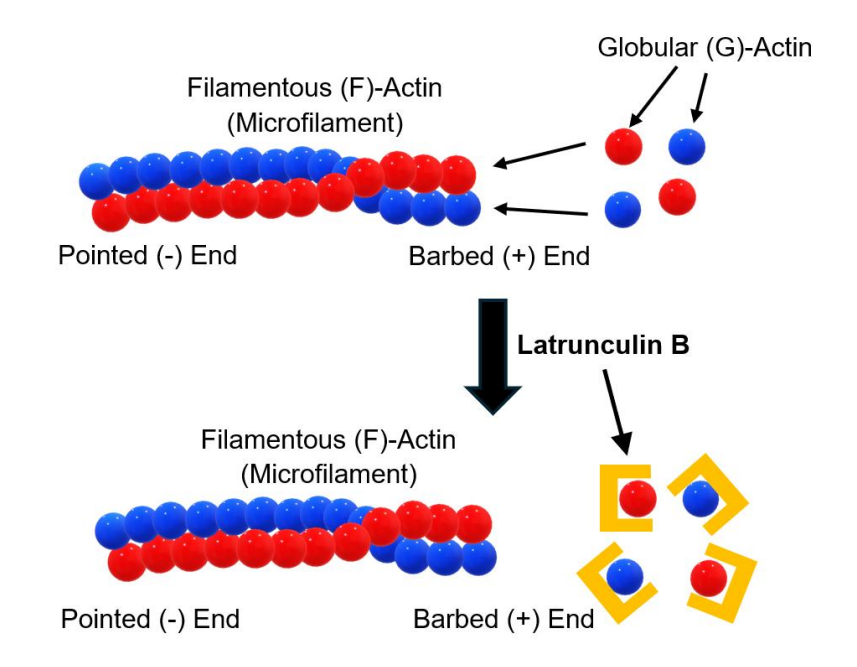


Figure 4.21 The diagram of the capping mechanism of Latrunculin B (LatB) that inhibits G-actin.

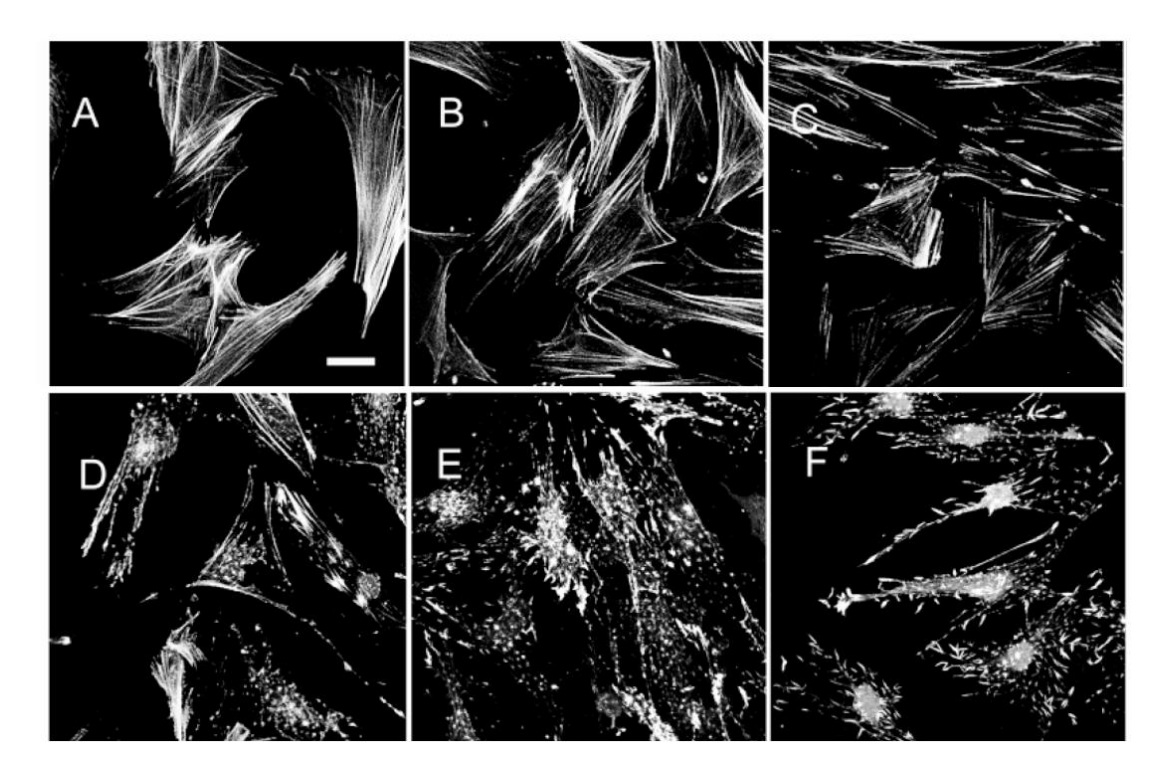


Figure 4.22 The microscope images of changes in the organisation of the actin cytoskeleton at various concentrations of LatB. The cells were incubated with 10 nM (A), 40 nM (B), 160 nM (C), 630 nM (D), 2 μ M (E), 10 μ M (F) for 30 minutes. At a LatB concentration of 2 μ M, almost all the long actin filaments were disrupted and replaced by large focal aggregates of F-actin. Scale bar: 50 μ m. The image is adapted from (Wakatsuki et al. 2001).

HL60 cells are treated with CytoD (Sigma Aldrich) and LatB (Sigma Aldrich). HL60 cells in 1ml volume at a concentration of 1×10^5 cells/ml were resuspended in 0.5%(w/v) MC-DPBS solution. CytoD and LatB were added to the cell suspension to a concentration of 1μ M and 25nM,

respectively. Stock solutions of CytoD and LatB were made in DMSO. The stock solutions were prepared using a stepwise dilution method to achieve more accurate volume measurements. This stock was diluted to ensure the same concentration of DMSO in each group of cells, which is 0.5% (v/v). CytoD and its untreated control group (DMSO exposed) were kept at 37°C in an incubator for 10 minutes; LatB and its untreated control group were kept for 30 minutes. After incubation, the samples were directly loaded into the syringe for measurement because those drugs are reversible (Stevenson and Begg 1994).

4.3.3.2 Glutaraldehyde

Glutaraldehyde (GA) is commonly used to fix cells for electron microscopy and other structural studies because it crosslinks proteins, preserving cellular structures. Cells fixed by GA have been a crucial cellular model to study cell mechanical properties (Abay et al. 2019; Reinhart and Singh 1990). According to Zeng et al. (Zeng et al. 2013), GA at the lowest concentrations (0.001-0.005, 0.01-0.05, and 0.01-0.1% v/v) can fully fix surface granules, stress fibres, the cell cortex, and internal cell structures within 20 minutes. It was found that this crosslinking reaction is concentration-sensitive (Guzniczak et al. 2020). The higher the concentration, the stronger the fixation effect and the less deformability until the deformability decreases to a stable value close to a rigid spherical particle. Moreover, GA fixation can also be used to vary the dielectric parameters of cells (Salahi, Honrado, et al. 2022), and this effect is explored in **Chapter 5**.

To fix HL60 cells with GA, cells were harvested at 5×10⁵ cells/mL and suspended in DPBS. Five different groups of cells were processed in pure DPBS with varying concentrations of GA-DPBS solutions (0, 0.0001%, 0.001%, 0.01% and 0.1% v/v) and kept at room temperature for 30 minutes. After incubation, cells were centrifuged and resuspended in 0.5% w/v MC-DPBS solution before deformability measurements.

4.4 Results

4.4.1 Correlation between electrical and optical techniques

Figures 4.23 (a) and (b) show scatter plots of **ED** and **OD** vs electrical and optical diameter for beads (blue dots) and cells (red dots) at a flow rate of 5μ l/min. As mentioned in section 4.2.3, the electrical diameter was calculated from the cube root of the $\Delta |I_1|$ measured from the first electrode configuration, calibrated with the 10 μ m beads. This electrode configuration accurately measured particle volume and was less influenced by shape change, as proved by Dr Junyu Chen (Chen et al. 2024). The optical diameter was calculated as described above $\left(\frac{major\ axis+minor\ axis}{2}\right)$, again referenced to the calibration beads. The two plots show that as anticipated, the cells

deformed due to the shear flow but that the beads did not and had a mean deformability of 1.0, just like rigid and spherical particles.

The Normal distribution of **Figure 4.23 (a) and (b)** are $N_{ED} \sim (1.167 \pm 0.06)$ and $N_{OD} \sim (1.156 \pm 0.08)$. From the fitting curves of the histogram, the **OD** distribution is more dispersed with a higher variance.

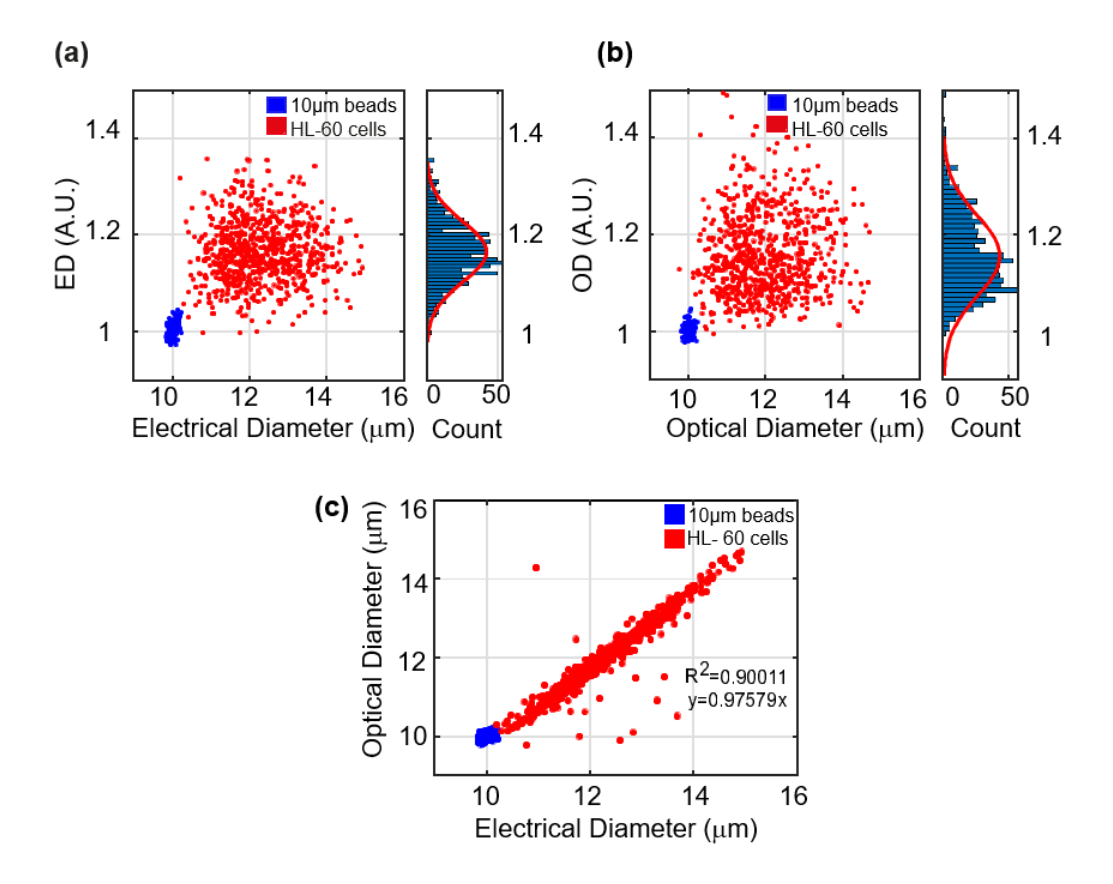


Figure 4.23 Correlation between electrical and optical properties of untreated HL60 cells and beads at a flow rate of 5 μ L/min. (a) and (b) are scatter plots of Electrical and Optical Diameter versus ED and OD, together with histograms of deformability. 10 μ m polystyrene beads were used as calibration particles for both size and deformability. (c) Scatter plot of electrical diameter versus optical diameter, with a fitted straight line y=0.98x, R²>0.90.

Figure 4.23 (c) shows a plot of the correlation between the electrical diameter and optical diameter after system calibration using known-sized solid particles as described in section 4.2.3. Beads (blue dots) are gathered at the point ($10\mu m$, $10\mu m$), which satisfies the actual dimension of the beads. Most of the cells (red dots) are located along the fitted straight line y = 0.98x with varying diameters ($R^2 > 0.9$). Some points deviate from the straight line due to incorrect matching of electrical and optical data. That may be because of the coincidence of events in the same photo. Since the probability of this coincidence occurring in practice was extremely low, no additional code was used to handle this circumstance. Therefore, each photo was assumed to contain only one particle to simplify image processing. Only the object with the smallest x-axis position was selected for images containing multiple particles. Thus, this may result in the particle matching an incorrect impedance signal.

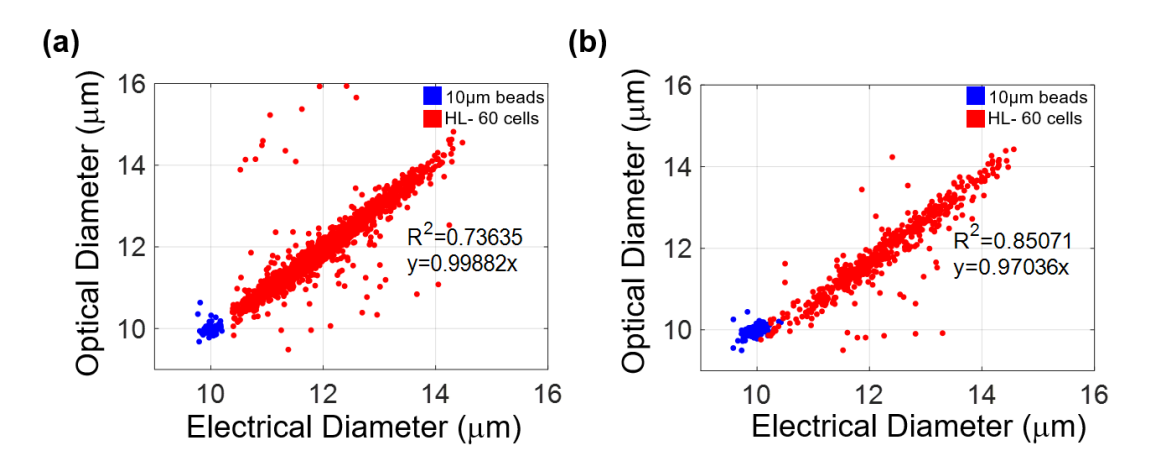


Figure 4.24 Correlation of electrical and optical diameter for untreated HL60 cells at (a) 10 μ L/min and (b) 15 μ L/min. Data was obtained for the same day as the correlation plot in **Figure 5.6 (c)** but at different flow rates.

Figure 4.24 shows the correlation scatter plots of electrical and optical diameter for untreated HL60 cells at 10 and 15 μ L/min flow rates, consistent with the 5 μ L/min flow rate result. Similar to Figure 4.23 (c), cells are distributed along the fitted straight line with high R². The subpopulation of beads is highly condensed at (10 μ m, 10 μ m).

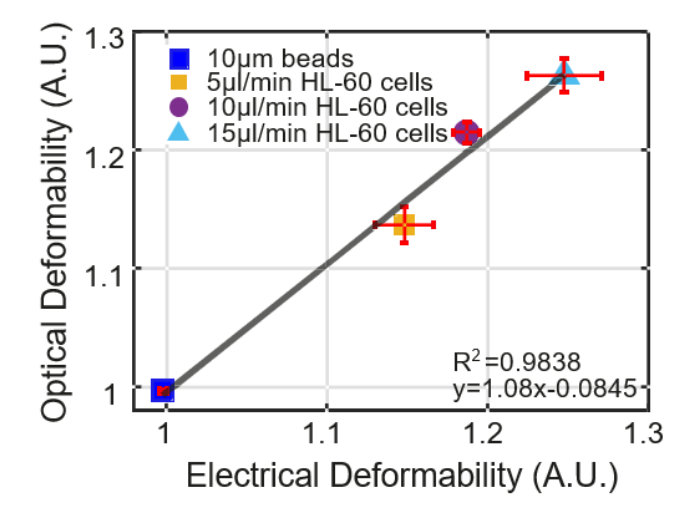


Figure 4.25 Correlation between the mean \pm SD value of ED vs OD for beads and untreated HL60 cells at different flow rates (5, 10, and 15 μ L/min) for three repeats.

Figure 4.25 shows the correlation ($R^2 > 0.9$) between the mean \pm SD value of **ED** and **OD** for beads and untreated HL60 cells at three different flow rates (5, 10, and 15 μ L/min) from three repeated experiments. As flow increases, cells are exposed to a higher shear stress, leading to a higher deformability. The trend is linear (y = 1.08x - 0.0845) again, with excellent correlation between the two techniques. The values of each point are summarised in **Table 4.3**.

Table 4.3 The mean ± SD value of **ED** and **OD** plotted in **Figure 4.25**.

•	bead	5 μL/min	10 μL/min	15 μL/min
ED	1.00±0.0023	1.15±0.0182	1.19±0.0084	1.25±0.0229

|--|

Moreover, Figure 4.26 presents the example images demonstrating the deformation of the cell in the flow at 10 μ L/min flow rate and that this deformation depends on the chemical treatment: 10 μ m bead, Untreated cell, GA fixed cell (0.1% v/v), and CytoD treated cell. From visual observation, the GA-treated cell was as round as the bead because its membrane proteins had been fixed, and its undeformed state was maintained. The deformability is close to the value of the rigid spherical polystyrene bead, which is around 1. The untreated cell in the detection region was deformed by the shear stress, and the cell exposed to CytoD was much softer than that, with the highest deformability among these example cells.

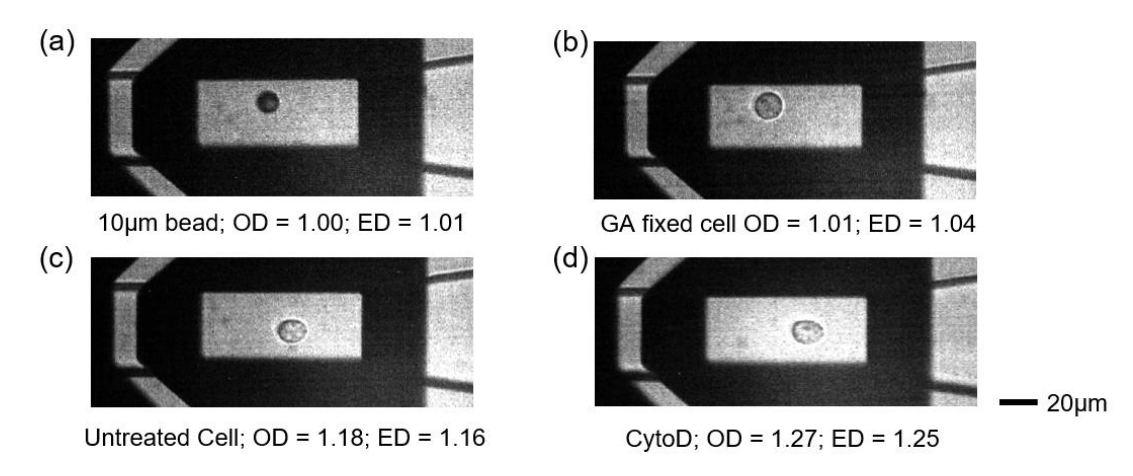


Figure 4.26 Example images of a single HL60 cell deforming in the channel at a 10 μ L/min flow rate.

The correlation between the two methods for different treatments was also evaluated by plotting OD vs ED. Figure 4.27 shows this plot of untreated, GA fixed, and CytoD treated cells. Each data point is the mean \pm SD of several hundred cells (**Table 4.5**) with three biological repeats. Similar to **Figure 4.25**, **ED** and **OD** have an excellent correlation ($R^2 = 0.99$). Because GA treatment is concentration-sensitive, data from two concentrations were presented with distinct values. A higher concentration (0.1% v/v) led to lower deformability, close to 1, and a lower concentration (0.001% v/v) resulted in higher deformability but was still less than that of untreated cells. Details are provided in the **section 4.4.4**.

The values of mean \pm SD in **Figure 4.27** are summarised in **Table 4.4.** Together with **Table 4.3**, when the deformability is around or below 1.2, the numerical difference between **OD** and **ED** is tiny. As the deformability grows, especially when it is larger than 1.2, the numerical value of **OD** is significantly greater than that of **ED**.

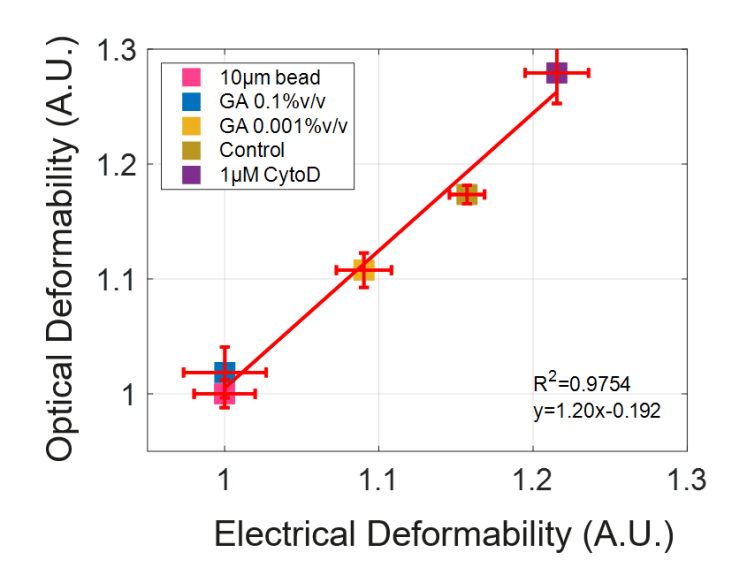


Figure 4.27 Correlation between the ED and OD for HL60 cells (Untreated, GA fixed and CytoD treated) with 10 μ m rigid spherical beads at a 10 μ L/min flow rate. Data is the mean \pm SD of three biological repeats (n = 3). The correlation between the two methods is given by the solid line (R² = 0.98).

Table 4.4 The mean ± SD value of **ED** and **OD** plotted in **Figure 4.27**.

	bead	GA 0.1%	GA 0.001%	Untreated	CytoD
ED	1.00±0.0198	1.00±0.0268	1.09±0.0179	1.16±0.0114	1.22±0.0206
OD	1.00±0.0121	1.02±0.0221	1.11±0.0150	1.17±0.0079	1.28±0.0267

Table 4.5 The number of cells used in Figure 4.27 and Table 4.4.

Cell Number	Repeat 1	Repeat 2	Repeat 3
Fixed 0.1%	421	486	504
Fixed 0.001%	422	487	511
Untreated	1045	835	675
CytoD	530	513	726

4.4.2 Deformability distribution between optical and electrical measurements

As mentioned in the last section, the value of **OD** tends to be larger than **ED** when the deformability exceeds 1.2. Besides, a comparison of the histograms in **Figures 4.28 (a) and (b)** shows that the distribution of **OD** has a higher variance than **ED**. HL60 cells were treated with CytoD and LatB to explore the reason for this. This trend was related to the y-position in which cells are located when illuminated in the ROI.

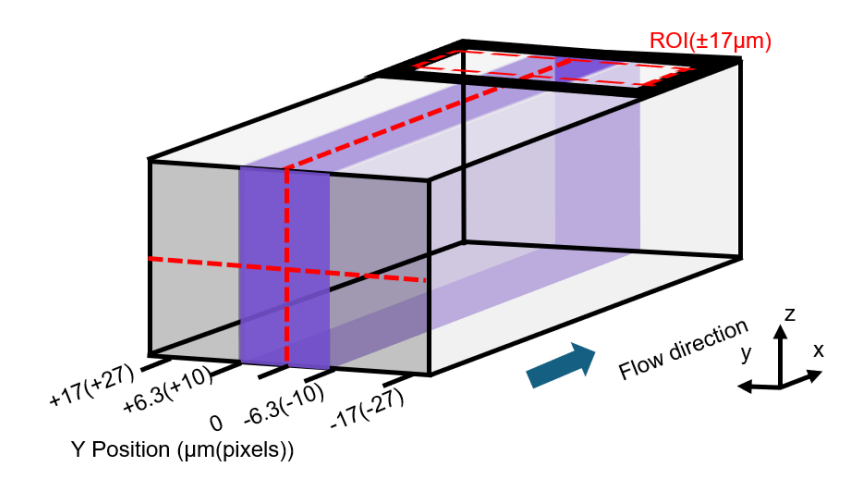


Figure 4.28 Schematic diagram showing channel cross section and dimensions. The shaded box (-6.3 μ m to +6.3 μ m) defines the ROI within which cells were measured. Those near the walls were discarded.

The channel can be divided into three parts along the y-axis, as **Figure 4.28** shows. Taking the midpoint of the channel in the y-direction as the zero point. A boundary corresponding to ± 10 pixels on either side of the channel centre line (approximately $\pm 6.3 \mu m$) was defined as the central region (purple).

Figure 4.29 shows the comparison between **OD** and **ED** for HL60 cells treated with CytoD and LatB, demonstrating how cell deformation depends on lateral position in the channel. The top row shows **OD** scatter data for untreated and treated cells, while the bottom row shows the scatter plot of **ED**. The data was plotted as a function of Y-position across the channel width. The data show that treated cells have a higher deformability than untreated cells, consistent with previous reports (Urbanska et al. 2020; Guzniczak et al. 2020). It is known that the viscoelastic fluid focuses particles into the central region (along the y-axis) (Del Giudice 2019; Serhatlioglu et al. 2019; Chen et al. 2024), significantly reducing variation in the impedance signals along the z-axis because of the removal of position dependence (Spencer and Morgan 2011). However, the data in **Figure 4.29** also shows that the deformability is influenced by the position of the cell across the channel width. Unlike the **ED**, the scatter plot of **OD** has a parabolic shape and different treatments result in varying degrees of curve bending, with LatB showing the most significant curvature.

Chapter 4

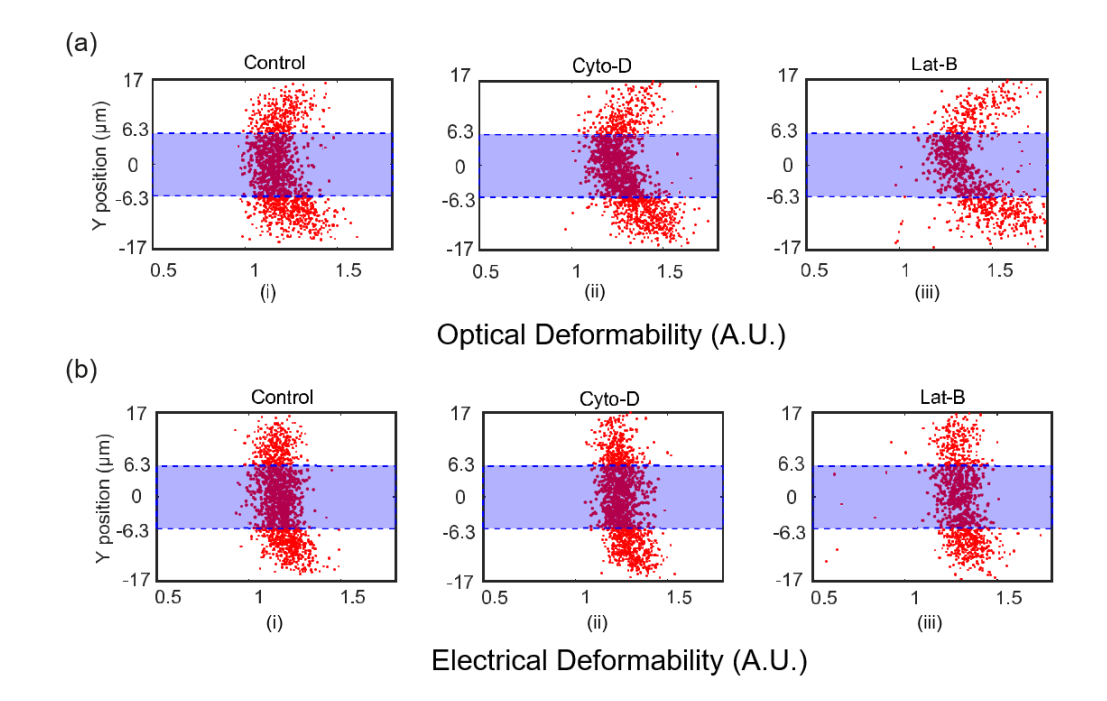


Figure 4.29 Comparison between (a) **OD** and (b) **ED** for HL60 cells treated with CytoD and LatB demonstrating how cell deformation depends on lateral position in the channel at a 10 μ L/min flow rate.

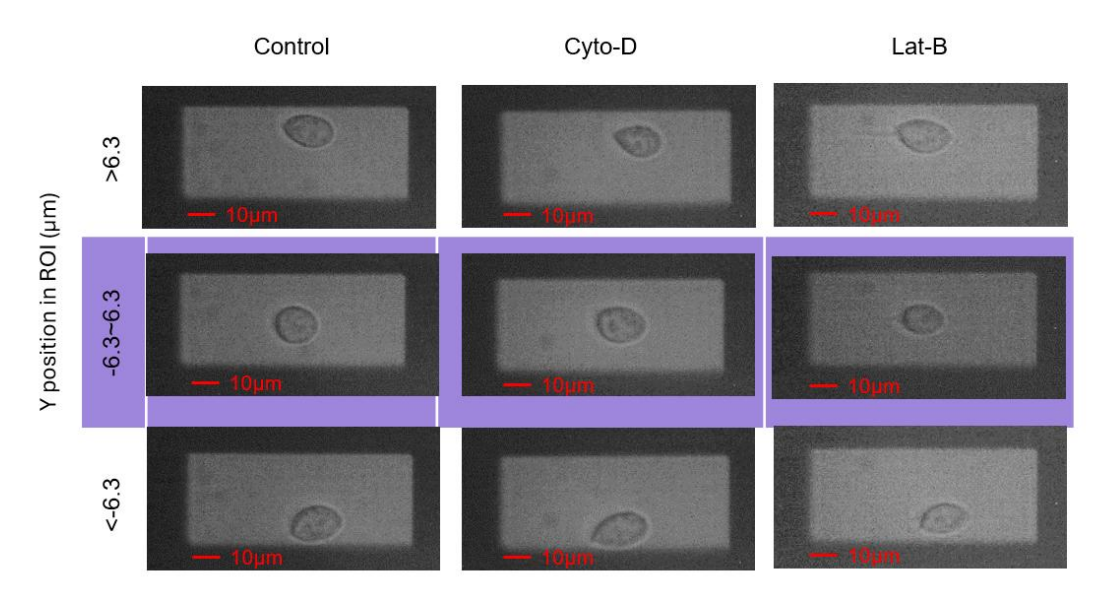


Figure 4.30 Images of cells located at different Y-position in the ROI (-17 μ m to +17 μ m) and different treatments. Cells are treated with 1 μ M CytoD and 25nM LatB.

Figure 4.30 shows representative images of the three different populations of cells at three different regions in the optical ROI (refer to **Figure 4.28**): two regions near the channel wall and the central region. In **Figure 4.30**, the top and bottom row images show that the cells near the channel wall are deformed into teardrop shapes with a small tail, presumably due to unbalanced shear forces near the wall. 2D image processing of these cells which includes the shape of the tail, and tends to skew the long axis measurement of the cell and, therefore the mean **OD**. Thus, these cells have a higher **OD** than those flowing close to the centreline. This distortion in the cell

shape is reflected in the scatter plots of **Figure 4.29**, which has a parabolic shape because cells closest to the wall deform the most and are found at the extremes of the parabola.

The optical data can be contrasted with the **ED**, which appears independent of the Y-position. The asymmetric teardrop shape has a minor influence on the electrical impedance as it blocks minimal current, so the measured **ED** is far less dependent on the Y-position of the cells in the channel (**Figure 4.29 (b)**).

4.4.3 Optical-electrical deformability measurements for HL60 cells with disrupting cytoskeleton

This section compares the two methods investigated by post-processing the data to eliminate the slower-moving cells near the channel walls, demonstrating an excellent correlation between the **ED** and **OD**.

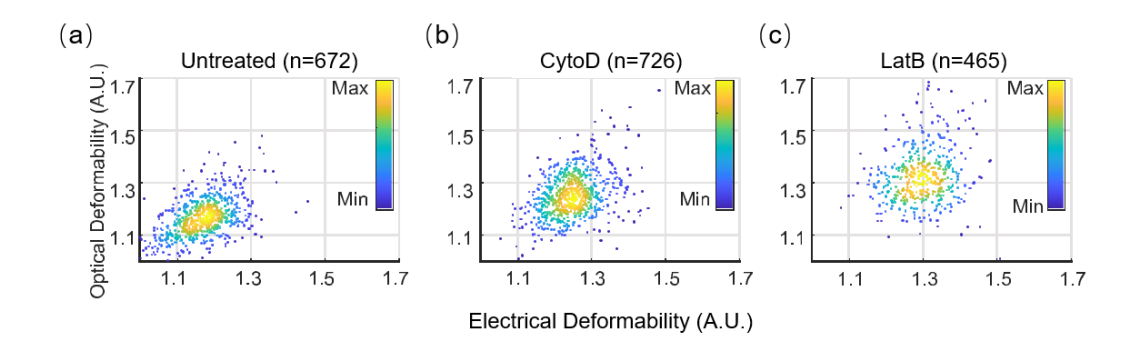


Figure 4.31 Scatter plots of **ED** v.s. **OD** for (a) untreated HL60 cells and treated with (b) CytoD and (c) LatB at a 10 μ L/min flow rate. The results are filtered according to the Y-position in the channel to exclude cells close to the channel walls, i.e. outside the shaded region in **Figure 4.29**.

Figure 4.31 presents the scatter plots of **ED** versus **OD** for untreated HL60 cells and those treated with CytoD and LatB. These plots are from the data sets that have been further filtered from the data in the previous **Figure 4.29**. The filtering is based on the Y-position of cells within the channel, and those in the central region are plotted. As expected, untreated cells have the lowest deformability, whilst the LatB-treated cells have the largest deformability. The correlation between the two techniques is excellent. For CytoD and LatB groups, it can be observed that the deformability of the central point in the population is over 1.2, and the x-coordinate values are approximately equal to the y-coordinate values, which is an optimisation of **Figure 4.27**. The numbers of cells in the plots are 672 out of 1430 (47%) untreated cells, 726 out of 1511 (48%) CytoD-treated cells and 465 out of 1095 (42%) out of LatB-treated cells.

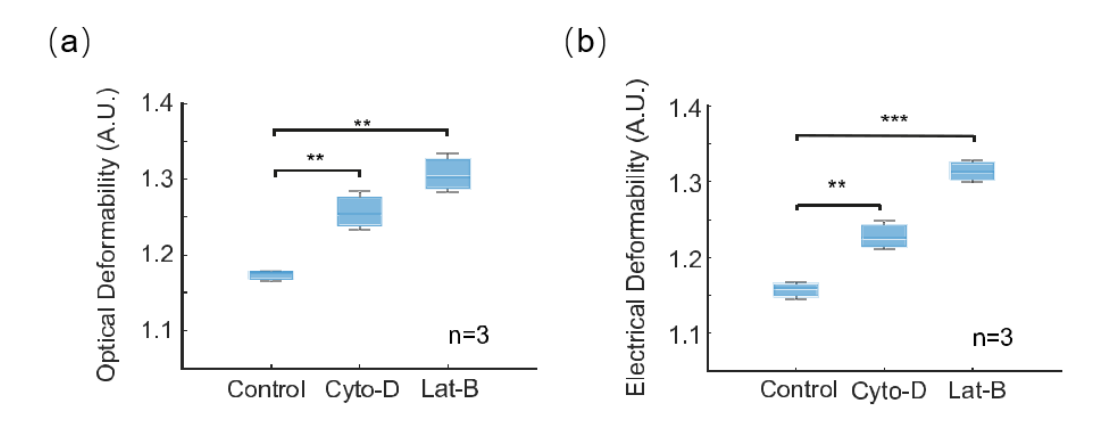


Figure 4.32 Box charts of (a) **ED** and (b) **OD** (n = 3). Data are mean \pm SD. The statistic analysis is the student t-test, ** p \leq 0.001, *** p \leq 0.001, compared with the untreated group. The flow rate is 10 μ L/min.

Figure 4.32 (a) and (b) show OD and ED (mean \pm SD) data for HL60 cells treated with CytoD and LatB after being filtered by the Y-position. These biological repeated data were statistically analysed by the student's t-test, and it proves that CytoD and LatB alter cell deformability significantly. Besides, compared with untreated cells, the data of treated cells shows that deformability determined by impedance is equivalent to the optical method. For example, at a flow rate of 10 μ L/min, the ED of untreated cells = 1.16 \pm 0.011, compared with OD = 1.18 \pm 0.008. Other data for this figure is summarised in Tables 4.6 and 4.7.

Table 4.6 The mean \pm SD value of **OD** for untreated and treated HL60 cells for three repeats at 10μ L/min in **Figure 4.32(a)**.

OD	Repeat 1	Repeat 2	Repeat 3	mean±SD
Untreated	1.18	1.18	1.16	1.17±0.0079
CytoD	1.23	1.28	1.25	1.26±0.0252
LatB	1.30	1.28	1.33	1.31±0.0259

Table 4.7 The mean \pm SD value of **ED** for untreated and treated HL60 cells for three repeats at 10μ L/min in **Figure 4.32(b)**.

ED	Repeat 1	Repeat 2	Repeat 3	mean±SD
Untreated	1.15	1.16	1.17	1.16±0.0114
CytoD	1.21	1.23	1.25	1.23±0.0186
LatB	1.31	1.33	1.30	1.31±0.0149

From the results in this section, it can be concluded that the electrical method is less influenced by the Y-position of cells, and it can be as accurate as the conventional optical methods. If the electrical system is less sensitive than the optical one, the mean of electrical deformability would not as the same as the mean of optical deformability of cells flowing along the central region in the channel. In summary, the data shows that the population **ED** is as accurate as it should be, which means the sensitivity of the electrical system is enough to differentiate cell phenotypes according to deformability.

4.4.4 Optical-electrical deformability measurements for fixed HL60 cells

As a final set of experiments, the performance of this electro-optical deformability cytometer was evaluated using HL60 cells treated with different concentrations of glutaraldehyde (GA), which crosslinks the cell proteins, making them stiffer. Fully crosslinked cells have a deformability similar to solid beads, close to 1.

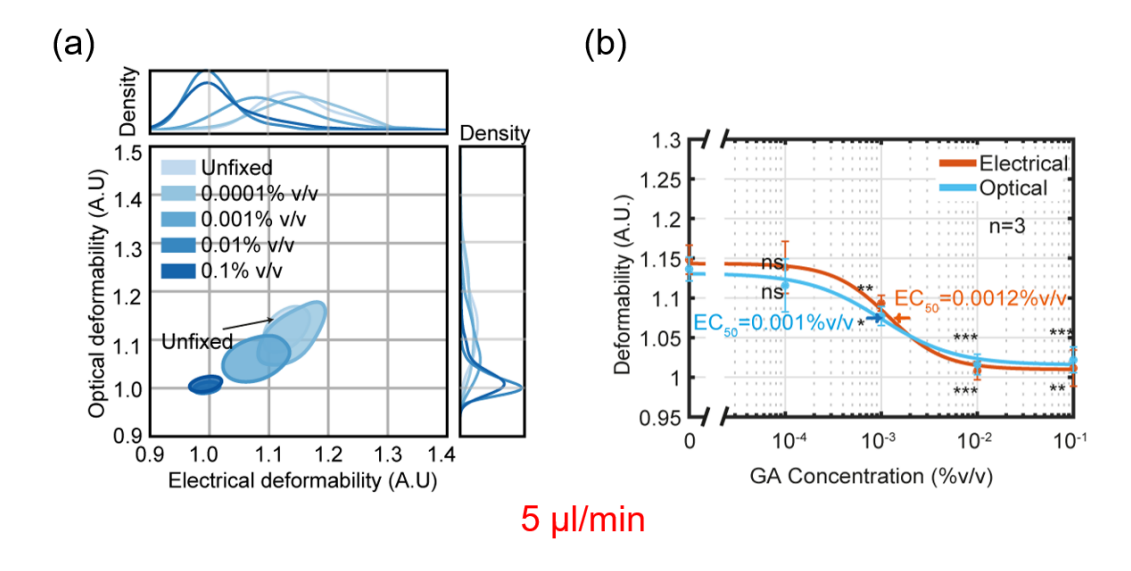


Figure 4.33 (a) The contour plots of **ED** vs **OD** for HL60 cells treated with different concentrations of GA at a flow rate of 5 μ L/min. (b) Dose-response curves of **ED** and **OD** for three repeated experiments at a flow rate of 5 μ L/min (n = 3). P- values are relative to the unfixed group, where *** p ≤ 0.001, ** p ≤ 0.05 and ns is not significant.

Figure 4.33 (a) shows ED versus OD as a function of GA concentration plotted as 50% contour plots at a flow rate of 5 μ L/min, including cell count histograms. ED and OD have a consistent growing trend when the concentration is decreasing. The lowest concentration, 0.0001% v/v, would not affect cells because the contour at this concentration overlaps that of unfixed cells. The higher concentrations (0.01% and 0.1% v/v) can fix cells to the greatest extent, causing their deformation to reach the level of rigid spherical beads close to 1. The middle concentration (0.001% v/v) deformability is between the values of lowest and higher, slightly overlapping with the higher groups.

The dose-response curves of **ED** and **OD** are presented in **Figure 4.33 (b)**. They are fitted to the Hill equation, which is given by (Gadagkar and Call 2015):

$$y = \beta_1 + \frac{\beta_2 - \beta_1}{1 + \frac{x}{(\beta_3)^{\beta_4}}} \tag{4.8}$$

where y is the response (deformability), vector x is the concentrations, $\beta = [\beta_1, \beta_2, \beta_3, \beta_4]$ is the fitting parameters: β_1 is the response when the concentration (dose) is zero (minimum asymptote), β_2 is the stable response for infinite concentration (maximum asymptote), β_3 is the effective concentration (EC_{50}) at the half-maximum response, and β_4 is the maximum curvature value of the curve (Hill slope). The mean \pm SD values (n = 3) of deformability at different concentrations were input into a custom MATLAB script, which was used to fit the equation and derive the half-maximum concentration (EC_{50}) of GA. The electrical and optical EC_{50} are 0.0012% and 0.001%, respectively, and the P-values shown in the plots are relative to the unfixed group (*** p \leq 0.001, * p \leq 0.05, and ns is not significant). The values of **Figure 4.33 (b)** are summarised in **Tables 4.8 and 4.9**.

Table 4.8 The mean \pm SD value of **ED** for unfixed and fixed HL60 cells for three repeats at 5μ L/min in **Figure 4.33(b)**.

ED (5 μL/min)	Repeat 1	Repeat 2	Repeat 3	mean±SD
Unfixed	1.15	1.17	1.13	1.15±0.0182
GA 0.0001%	1.11	1.17	1.14	1.14±0.0329
GA 0.001%	1.10	1.10	1.08	1.09±0.0098
GA 0.01%	1.01	1.02	1.00	1.01±0.0115
GA 0.1%	1.01	1.04	1.00	1.01±0.0228

Table 4.9 The mean \pm SD value of **OD** for unfixed and fixed HL60 cells for three repeats at 5μ l/min in **Figure 4.33(b)**.

OD (5 μL/min)	Repeat 1	Repeat 2	Repeat 3	mean±SD
Untreated	1.15	1.14	1.12	1.14±0.0150
GA 0.0001%	1.08	1.15	1.12	1.12±0.0333
GA 0.001%	1.09	1.08	1.06	1.08±0.0120
GA 0.01%	1.02	1.03	1.00	1.02±0.0130
GA 0.1%	1.02	1.04	1.01	1.02±0.0162

The demonstrations were also conducted at higher flow rates: 10 and 15 μ L/min. For the contour plots (**Figure 4.34**), the unfixed and lowest concentration (0.0001% v/v) subpopulations are moving up along both the x and y axes as expected because a higher flow rate leads to a higher deformability. The deformability of the middle concentration (0.001% v/v) population also grows but is still located between the higher and lowest concentrations. Contours of cells fixed with higher concentrations of GA (0.01% and 0.1% v/v) remain at point (1, 1), although the flow rate increases. This unchanged deformability means cells were fully crosslinked and would not be deformed even though the shear stress increased.

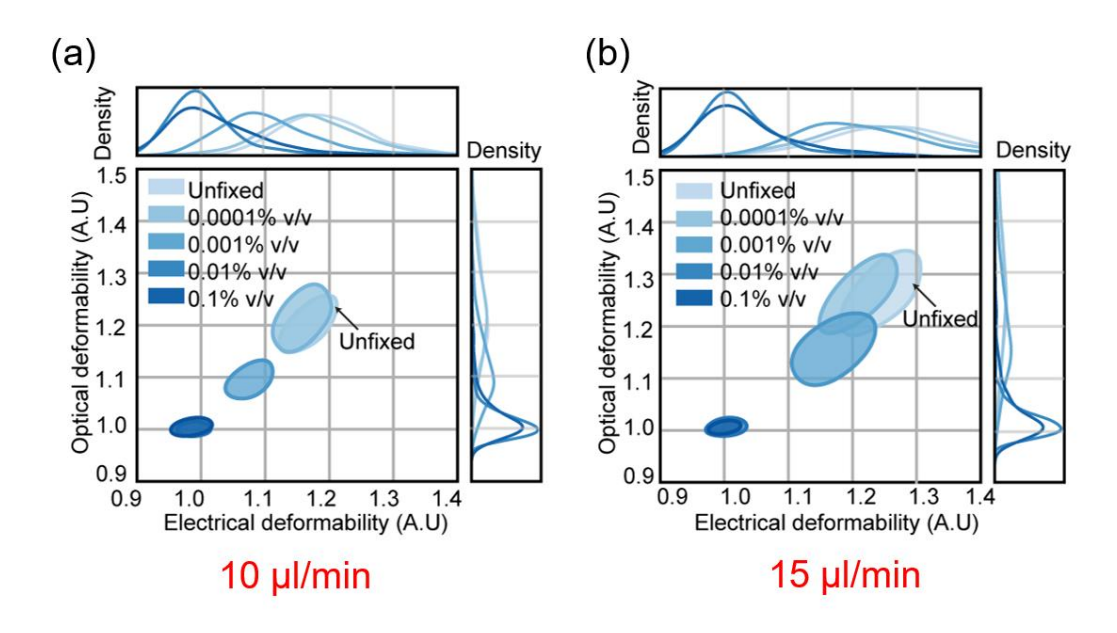


Figure 4.34 The contour plots of **ED** vs **OD** for HL60 cells treated with different concentrations of GA at flow rates of (a)10 μ L/min and (b) 15 μ L/min.

Figure 4.35 (a) and (b) are the dose-response curves of **ED** and **OD** at flow rates of 10 and 15 μL/min for three biological repeats, respectively. Consistent with the 5 μL/min curve, **ED** and **OD** have no significant change in the GA concentration of 0.0001% v/v, and the fitting curves remain stable. Then, they drop as the concentration increases to around 0.0005%, finally reaching a minimum asymptote at 0.01% and 0.1% v/v concentrations. The p-values of these concentrations are significant, with *** $p \le 0.001$ and ** $p \le 0.01$. The output EC₅₀ of two different techniques at 10 and 15 μl/min are similar to those at 5 μL/min (**ED**: 0.001% v/v at 10 μL/min and 0.0013% v/v at 15 μL/min; **OD**: 0.00097% v/v at 10 μL/min and 0.0011% v/v at 15 μL/min). The EC₅₀ values are similar to those reported elsewhere (Guzniczak et al. 2020).

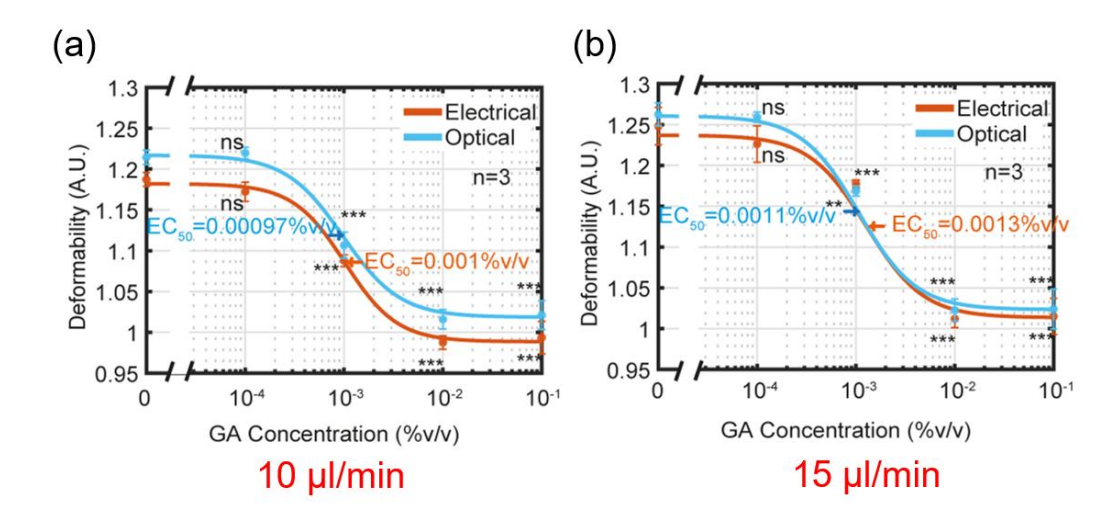


Figure 4.35 Dose-response curves of **ED** and **OD** for three repeated experiments (n = 3) at flow rates (a) 10 and (b) 15 μ L/min. P- values are relative to the unfixed group, where *** p ≤ 0.001, ** p ≤ 0.05 and ns stands for not significant.

4.5 Discussion

This chapter described the experimental results of a developed electro-optical deformability cytometer. The system determined the correlation between electrical and optical deformability and provided a feasible triggering mechanism for subsequent sorter development. It used simple shear flow to deform cells in the microchannel, and the electrical deformability of particles was determined by the impedance generated from two different configurations of electrodes. To obtain optical deformability, the device uses a simple and inexpensive CMOS camera to capture images of particles at a throughput of a few tens of cells per second. As a cell moves down a channel from the undeformed to the deformed region, the electrical impedance signal is used to trigger a high-intensity LED, which projects an image of a particle onto the camera. Compared to other reported triggering methods (Liang et al. 2021; Bansal et al. 2022), this system did not adopt a threshold value to trigger. It calculated the velocity of each event and allocated a custom expected time to determine the trigger signal. The electrical deformability is defined as the ratio of the electrical impedance measured along two different orthogonal axes, and the optical deformability is defined as the ratio of the major and minor axes from the image post-processed by MATLAB.

The correlation between these two methods was assessed using HL60 cells treated with/without chemicals as cellular models. The drugs that disrupt the cytoskeleton, cytochalasin D (CytoD) and latrunculin B (LatB), were used to soften cells to extend the value range of deformability. Glutaraldehyde, a type of cell fixative, can crosslink proteins of cells and make them stiff, decreasing the deformability to approximately 1.

The scatter plots of electrical and optical diameters presented an excellent correlation at three different flow rates. Cells were located on a line passing through the origin with an approximate slope of 1, while beads were gathered at the point (10 μ m, 10 μ m). The electrical and optical deformability error bar charts also showed a good correlation. However, when the deformability is greater than 1.2, the optical deformability has a higher variance than the electrical deformability. This was caused by the cells different Y-position of the channel. The system does not use a hydrodynamic sheath flow but relies on the viscoelastic fluid to partially focus cells into a plane in the centre of the channel. Although this simplifies the system, some particles close to the channel wall are asymmetrically distorted, leading to errors in the optical images. This leads to a positional dependence in the scatter data, which can be corrected by post-processing by excluding all cells that flow close to the channel walls. Interestingly, the electrical deformability appears to be much less affected by the position of the cells in the channel.

Finally, GA fixed cells at different concentrations were demonstrated using this system to validate the correlation between these two techniques. The effective concentration derived from the dose-response curve is similar to the report elsewhere (Guzniczak et al. 2020). In conclusion, this system is simple, and the correlation between electrical and optical deformability is exceptionally high.

Chapter 5 Single-cell Spectroscopy of Nucleated Cell

5.1 Introduction

The electrical or dielectric properties of cells are important label-free measurement indicators in addition to their mechanical properties. Sections 2.2.3 and 2.2.4 introduced the dielectric parameters of cells that are of research interest and presented how the measurement methods were developed. In summary, MIC was usually used to measure cells at two or at most three discrete frequencies and discriminated subpopulations by the value of the impedance signal, for example, amplitude, phase, and/or electrical opacity (the ratio of high to low-frequency impedance). However, this limited range of measurements is insufficient to determine the intrinsic parameters of each single cell because it requires fitting frequency-dependent impedance set to a set of Debye relaxations (Morgan and Green 2003) with the help of multi-shell models. Studies focused on measuring the membrane and cytoplasm parameters. They usually used enucleated cells, such as red blood cells and ghost cells as cellular models because they were easy to obtain and model, so the single-shell model was adopted. Even when measuring nucleated cells, the fitted shell models also used the single-shell one rather than the double-shell model to simplify the process of fitting, which overlooks the contribution of the nucleus to the model. Moreover, the limited detection frequency range also needs to be extended because, for nucleated mammalian cells suspended in physiological saline, the frequency should be up to >500MHz to fully characterise the electrical properties. The MATLAB calculations of the singleshell model and double-shell model in electrolytes with different conductivities were compared in section 3.2.4, implying that low-conductivity solutions can help distinguish cells with different membrane and cytoplasm parameters.

This chapter describes an improved single-cell spectroscopy system capable of high-speed multi-frequency characterisation of nucleated cells. In order to extract the dielectric properties of each individual cell, single-cell spectra were fitted to the double-shell model by post-processing the data. Throughput is around 250 cells/s, and the system performance was demonstrated by measuring the intrinsic dielectric properties of different nucleated cells. The content is organised in the following order: system overview, experiment setup and finally, the experimental results.

5.2 System Overview

5.2.1 Electrode configuration

Building on Dr. Daniel Spencer's previous work (Spencer and Morgan 2020), this system was improved to measure nucleated cells by extending the detection frequency range to 550MHz (instead of the original 50MHz) and an algorithm was developed to fit the frequency-dependent spectra to the double-shell model rather than the single-shell. Dielectric theory and simulations are described in **Chapter 3**, and the method of relating the measured current to the frequency-dependent impedance spectra is described in **section 5.2.2**. The system performance was demonstrated by measuring the intrinsic properties (diameter: d, membrane capacitance: C_{mem} , cytoplasm conductivity: σ_{cyt}) of different cells in two different saline conductivities (1.6 S/m conductivity and 0.32 S/m conductivity).

The electrode arrangement in this part differs from the deformability MIC system mentioned in Chapter 4 and Chapter 6. Cells used in this system are suspended in NaCl of different molarities. However, cells suspended in saline move through the channel with a random distribution along the vertical direction of the channel, which can lead to errors in the measured impedance of offcentre particles (Spencer and Morgan 2011). To solve this problem, the system uses encoded electrodes as shown in Figure 5.1. The array consists of eight pairs of voltage-sensing electrodes and three pairs of ground electrodes to minimise the leakage current and eliminate off-centre errors (Spencer and Morgan 2020). The voltage electrodes are divided into two groups with a 180-degree phase difference. The sensing pairs are also divided into two sets (dark blue and purple in Figure 5.1(a)), and they are connected to a differential amplifier to provide an output differential current. Ideally, the waveform of the output signal should be like Figure 5.1(b), a central symmetric form with peaks and valleys. The position of peaks and valleys corresponds to position ① to ②, which are at the center of electrodes.

The output signal from each frequency channel is processed to filter out the background noise and extract the impedance signals and transit time of each event with convolution filters. First, fifty normalised convolution templates with different transit times are generated according to the electrode encoding, channel dimension and the flow rate used in the experiments (**Figure 5.1(c)**). Then, they are multiplied by the raw data stream within a fixed size of window. Taking one waveform of an event as an example, the largest value among these fifty convolution results is the matched impedance value of this event, and the transit time is also determined. That data is saved for further analysis.

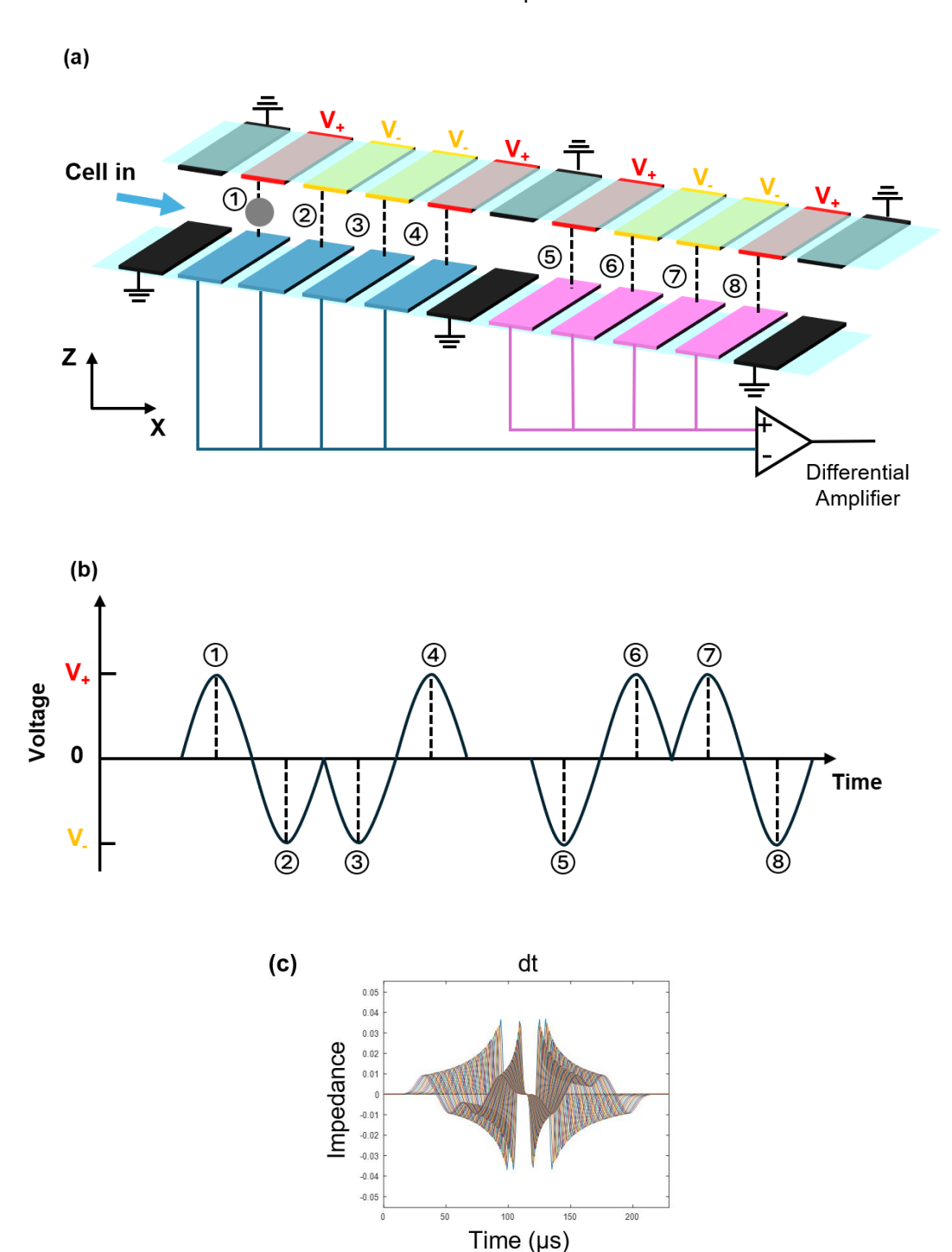


Figure 5.1 (a) The electrode configuration of this single-cell spectroscopy. Cells suspended in the saline with different conductivities pass through the channel from position 1 to 8 (centre position of electrodes) at a flow rate of $\textcircled{30\mu L/min}$. AC voltage V_+ and V_- have inverted phases and were applied to some electrodes. Their parallel electrodes were sensing ones and output the differential current. (b) The ideal output waveform for a single event. It is a central symmetric form with peaks and valleys that matches the position 1 to 8 at (a). (c) Convolution template generated according to the electrode encoding, channel dimension and the flow rate used in the experiments. Fifty normalised templates are multiplied to the raw data stream within a fixed size of window and the maximum result is the matched impedance of this event.

5.2.2 Measurement principles and data processing

After learning about the electrode configuration, this section describes the measurement process, principles and data processing. As **Figure 5.2** shows, a cell suspension was pumped into the microchannel (40µm×30µm) at a flow rate of 30mL/min. AC voltages with inverted phases at discrete frequencies were generated by a Lock-in Amplifier (UHFLI, Zurich Instruments) and amplified by a custom electronic circuit (designed by Dr Daniel Spencer). The voltages were applied to a top set of electrodes. The custom electronic circuit differentiated the current measured from the bottom electrodes, and then the signal was demodulated with a lock-in followed by post-processing.

A cell transited through the channel produces a bipolar Gaussian differential signal (**Figure 5.1(b)**), with amplitude corresponding to the cell impedance at the specified frequency. In order to measure the complete frequency spectrum of cells, data at discrete frequencies were obtained using two different methods. In the first, the impedance of a population mean was measured using an eighteen-frequency sweep. A 1mL sample loaded into a syringe was pumped through the chip and measured at 18 different frequencies ranging from low (250kHz) to high (550MHz) (250kHz, 398kHz, 631kHz, 1MHz, 1.58MMz, 2.51MHz, 3.98MHz, 6.31MHz, 10MHz, 15.8MHz, 25.1MHz, 39.8MHz, 63.1MHz, 100MHz, 158MHz, 251MHz, 398MHz, 550MHz), with the data recorded for 30 seconds at each frequency. The data at these 18 frequencies corresponds to the mean impedance of the cell population at each frequency point. This method is referred to as the "population-mean" method. The second method involved collecting eight frequencies simultaneously for many single cells (251kHz, 761kHz, 2.31MHz, 6.99MHz, 21.2Mhz, 64.1MHz, 194.3MHz, 575MHz). The data was recorded for around 2 minutes. This method is referred to as the "single-cell" method. The differential current from both methods was gated and calibrated

using polystyrene beads. The frequency spectrum consisting of discrete frequency data is fitted to the double-shell model, to obtain single cell dielectric parameters.

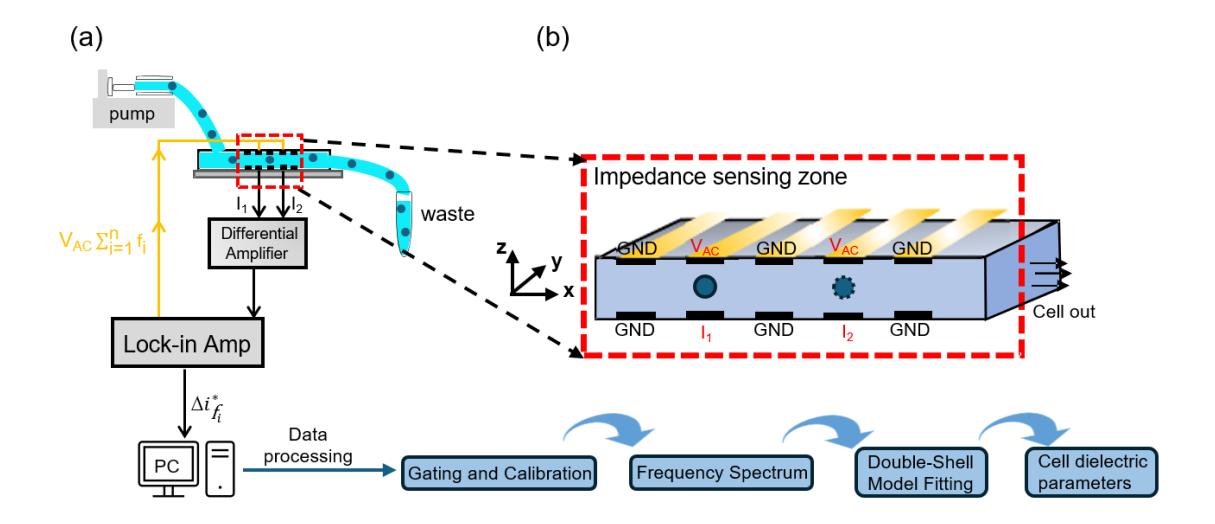


Figure 5.2 System conceptional overview and measurement principle. (a) Cells suspended in saline flow along the microchannel ($40\mu m \times 30\mu m$) where electrodes measure the impedance at discrete frequencies ranging from 250kHz to 550MHz. After Gating and calibration, the frequency spectrum was fitted to the double-shell model to give cell diameter d, membrane capacitance (C_{mem}) and cytoplasm conductivity (σ_{cyt}). (b) To simplify the diagram, not all electrodes are shown here. The detailed wiring scheme is shown in **Figure 5.1 (a)**.

5.2.2.1 Complex permittivity and differential current measurement

Ideally, the current in the empty channel should remain constant regardless of frequency. However, the actual device consists of many circuit elements, resulting in a non-linear impedance of the empty cell. Polystyrene beads of known size and dielectric properties are used as internal calibration particles to overcome these non-linearities (Spencer and Morgan 2020; Haandbæk et al. 2016).

The impedance of a mixture consisting of a spherical cell dispersed in a suspending media is given by (Spencer and Morgan 2020):

$$Z_{mix}^* = \frac{1}{j\omega\varepsilon_{mix}^*\kappa} \tag{5.1}$$

where κ is a constant depending on the electrode and gap dimensions. The differential complex current of the mixture is (Spencer and Morgan 2020):

$$\Delta i_{cell}^* = \frac{VS^*(\omega)}{Z_{med}^*} - \frac{VS^*(\omega)}{Z_{mix}^*} = j\omega\kappa VS^*(\omega)(\varepsilon_{med}^* - \varepsilon_{mix(cell)}^*)$$
 (5.2)

where V is the applied voltage, and $S^*(\omega)$ is a complex system transfer function assumed to be 1 because the system has no nonuniformity. Thus, the ratio of a cell and a bead differential current is given by:

$$\frac{\Delta i_{cell}^*}{\Delta i_{bead}^*} = \frac{\varepsilon_{med}^* - \varepsilon_{mix(cell)}^*}{\varepsilon_{med}^* - \varepsilon_{mix(bead)}^*}$$
(5.3)

After combining equation 3.7 in section 3.2.2 and equation 5.3, the ratio becomes:

$$\frac{\Delta i_{cell}^*}{\Delta i_{bead}^*} = \frac{\varphi_{cell} f_{CM(cell)}^* \left(\varphi_{bead} f_{CM(bead)}^* - 1 \right)}{\varphi_{bead} f_{CM(bead)}^* \left(\varphi_{cell} f_{CM(cell)}^* - 1 \right)}$$
(5.4)

When volume fractions are small (φ <0.01), the **equation 5.4** can be simplified to:

$$\frac{\Delta i_{cell}^*}{\Delta i_{bead}^*} = \frac{\varphi_{cell} f_{CM(cell)}^*}{\varphi_{bead} f_{CM(bead)}^*}$$
(5.5)

Because $\varphi_{bead}/\varphi_{cell} = r_{bead}^3/r_{cell}^3$, the Clausius-Mossotti factor can be expressed as:

$$f_{CM(cell)}^* = \frac{r_{bead}^3}{r_{cell}^3} f_{CM(bead)}^* \times \frac{\Delta i_{cell}^*}{\Delta i_{bead}^*}$$
 (5.6)

Equations 5.6 and 3.8 in section 3.2.2 are two different expressions of the same parameter, $f^*_{CM(cell)}$. The equations show that the dielectric spectrum of the cell can be determined from the experimentally measured differential currents (Δi^*_{cell} and Δi^*_{bead}) provided the frequency-dependent dielectric properties of the beads (r_{bead} and $f^*_{CM(bead)}$) are known according to:

$$f_{CM(cell)}^* \frac{r_{bead}^3}{r_{cell}^3} = f_{CM(bead)}^* \times \frac{\Delta i_{cell}^*}{\Delta i_{bead}^*}$$
 (5.7)

The impedance signals give the differential current for the bead and cell (right-hand side of equation 5.7), if the radius and dielectric properties of the bead are known. Thus, from equation 5.7, the unknown dielectric parameters of the cell $f_{CM(cell)}^*$ can be determined. The left-hand side of equation 5.7 is the spectrum used to analyse. Herein, r_{cell} and $f_{CM(cell)}^*$ are unknown and expressed by the shell model with adjustable intrinsic parameters ($\varepsilon_1 \sim \varepsilon_4$, $\sigma_1 \sim \sigma_4$) and cell radius (see section 3.2.3). Equation 5.7 is called normalised $f_{CM(cell)}^*$. Note that the wanted cell

membrane capacitance C_{mem} , cytoplasm conductivity σ_{cyt} , and cell diameter d evaluated in the experimental section correspond to $C_1(C_1 = \varepsilon_1/d_1)$, σ_2 , and $2r_{cell}$ in the shell model shown in **Figure 3.2** in section 3.2.3.

5.2.2.2 Gating and calibration

Cells behave as insulators at low frequencies, so cell dimension dominates the measurement. At higher frequencies, dielectric properties influence the spectrum, especially the membrane capacitance and cytoplasm conductivity. In order to measure the complete dielectric properties of nucleated cells, a system that can extend the frequency bandwidth up to hundreds of MHz is demanded. Detailed illustrations were presented in section 3.2.

Two frequencies were collected simultaneously for each data point for the population-mean method. One was fixed to 18MHz as a reference to gate beads and cells, and another frequency was swept from 250kHz to 550MHz. For the method that measured single-cell, eight simultaneous frequencies were applied. The frequencies were spaced logarithmically apart in the window 250kHz to 575MHz.

Gating and calibration with beads were done from the phase scatter plots (**Figure 5.3**). For the population-mean method, 18MHz is used as a reference frequency because beads and cells are highly distinct in phase (the ratio of imaginary and real part). For the single-cell method, the phase at 7MHz was used.

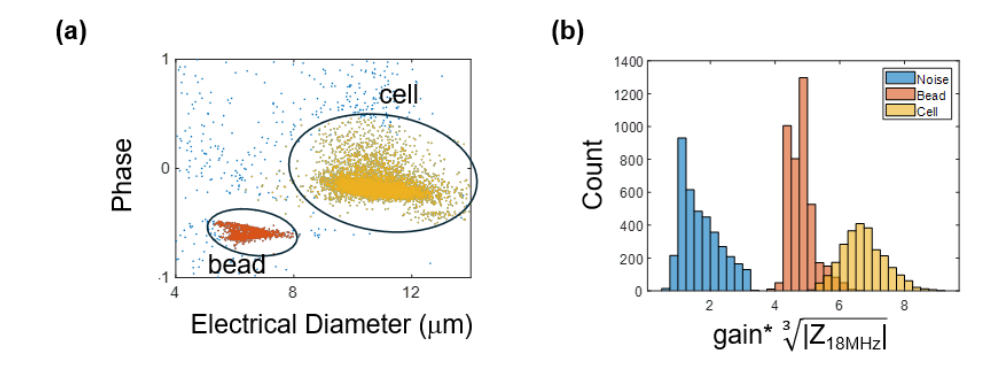


Figure 5.3 (a) An example impedance phase scatter plot of beads and cells used in the "gating and calibration" step. For the population mean method, this is the plot at reference frequency 18MHz; for the single-cell method, this is the plot at around 7MHz. This plot is used to gate beads and cells. (b)Histogram of gain* $\sqrt[3]{|Z_{18MHz}|}$ at 18MHz. The noise, beads and cells are gated as blue, red and yellow subpopulations. The population mean square ratio of noise impedance to the particle impedance is SNR.

The SNR (signal-noise-ratio) in the system is defined as the mean square ratio of the baseline impedance noise to the particle impedance. Consider data of untreated HL60 cells collected simultaneously at two frequencies (18MHz and 15.9MHz, where 18MHz is the fixed reference

frequency for gating beads and cells) in a low conductivity media (0.32 S/m). After gating the noise, beads and cells subpopulations (**Figure 5.3(b)**), the SNRs of beads and cells were calculated as follows:

$$SNR_{bead} = 10 \times log_{10} \left(\frac{mean \, square(beads)}{mean \, square(noise)} \right) = 10 \times log_{10} \left(\frac{23.4}{3.3} \right) = 8.5 \, dB$$
 (5.8)

$$SNR_{cell} = 10 \times log_{10} \left(\frac{mean \, square(cells)}{mean \, square(noise)} \right) = 10 \times log_{10} \left(\frac{45.9}{3.3} \right) = 11.4 \, dB$$
 (5.9)

The typical values of SNR for high (1.6 S/m) and low (0.32 S/m) media conductivity mentioned in the <u>section 3.2.4.1</u> are calculated in this way.

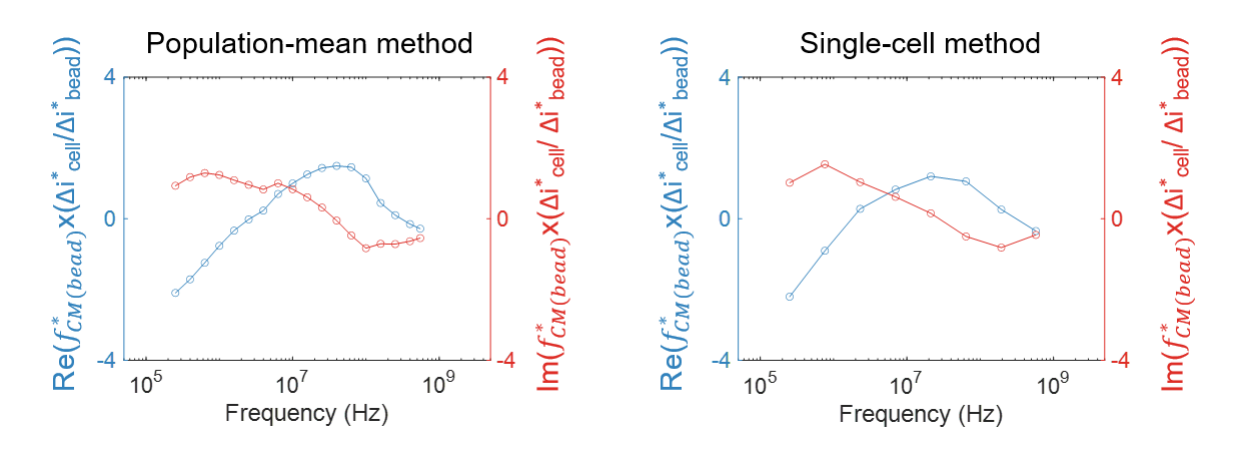


Figure 5.4 Example normalised $f_{CM(cell)}^*$ spectrum of untreated HL60 cells from two different methods: (a) population mean method and (b) single-cell method, in 0.32 S/m conductivity saline. Blue circles and lines represent the real part, and red represents the imaginary part. For further analysis, see the results in **section 5.4**.

As shown in **Figure 5.4**, this is the spectrum of normalised $f_{CM(cell)}^*$ (right-hand side of **equation 5.7**) obtained from two different methods. The population-mean method can provide more frequency points to generate the spectrum of the mean value of the cell populations. However, compared to single-cell spectra, it cannot be used to analyse the properties of individual cells so that has lower measurement resolution.

Finally, both methods need their normalised $f_{CM(cell)}^*$ (spectra like **Figure 5.4**) to be fitted to the shell model by using custom MATLAB scripts.

5.2.2.3 Model fitting

The double-shell model fitting was implemented in MATLAB with a function called "patternsearch". The fit determines cell size, the volume ratio of nucleus to cell, and dielectric

parameters, such as permittivity and conductivity of cell membrane, cytoplasm, nuclear envelope, and nucleoplasm.

The "patternsearch" function is usually used to solve optimisation problems, and it is designed for those where the objective function is not smooth, continuous or differentiable. It establishes the fitting curve based on the allocated starting values of dielectric parameters and adjusts the fitting within the boundaries of the parameter sets. The outcoming cell diameter d, membrane capacitance C_{mem} and cytoplasm conductivity σ_{cyt} are mainly discussed in **section 5.4**.

Table 5.1 is the parameter setting for running the "pattern search" function. The initial values of parameters are given by vector \mathbf{x}_0 , and the lower boundary vector is \mathbf{b}_{l} , the upper boundary vector is \mathbf{b}_{l} . Herein, we fixed the cell membrane conductivity σ_1 to 10^{-10} S/m because it can be ignored. The membrane and nuclear envelope thickness were set to 5 and 20nm, respectively. The suspending media permittivity was fixed to $80\varepsilon_0$, bead permittivity was $2.5\varepsilon_0$, and conductivity was 0.57 mS/m.

Table 5.1 An example of initial values and set range for cell parameters when running the "pattern search" function in MATLAB.

Cell parameter	Initial value [x₀]	Set range [b _l b _u]
Volume ratio of cell and bead	13.8 (5µm diameter bead), 5.6 (7µm diameter bead)	5~25 (5µm diameter bead), 2.6~8.6 (7µm diameter bead),
Volume ratio of nucleus and cell	0.6	0.3~0.8
Cell membrane permittivity (\mathcal{E}_1)	7 ε ₀	2~15ε₀
Cytoplasm conductivity (σ_2)	0.015 S/m	0.001~0.4 S/m
Cytoplasm permittivity (\mathcal{E}_2)	90ε ₀	40~160ε₀
Nuclear envelope conductivity (σ_3)	0.003 S/m	10 ⁻⁴ ~10 ⁻² S/m
Nuclear envelope permittivity (\mathcal{E}_3)	30ε ₀	1~200ε₀
Nucleoplasm conductivity (σ_4)	1.8 S/m	0.1~2 S/m
Nucleoplasm permittivity ($\mathcal{E}_{\scriptscriptstyle{4}}$)	70ε ₀	20~150ε₀

To test the performance of the fitting code, a set of data points (left-hand side of **equation 5.7**) with known cells and beads parameters was generated. Then, this dataset is fed to the program

to see if the output is close to what it is supposed to be. As shown in **Figure 5.5**, this is the plot of a generated dataset of normalised $f_{CM(cell)}^*$ (solid dots) and the fitting curve after running the "patternsearch" program in MATLAB. The real (blue) and imaginary (red) parts of the fitting outcome are in good agreement with the input data points from 100kHz to 1GHz.

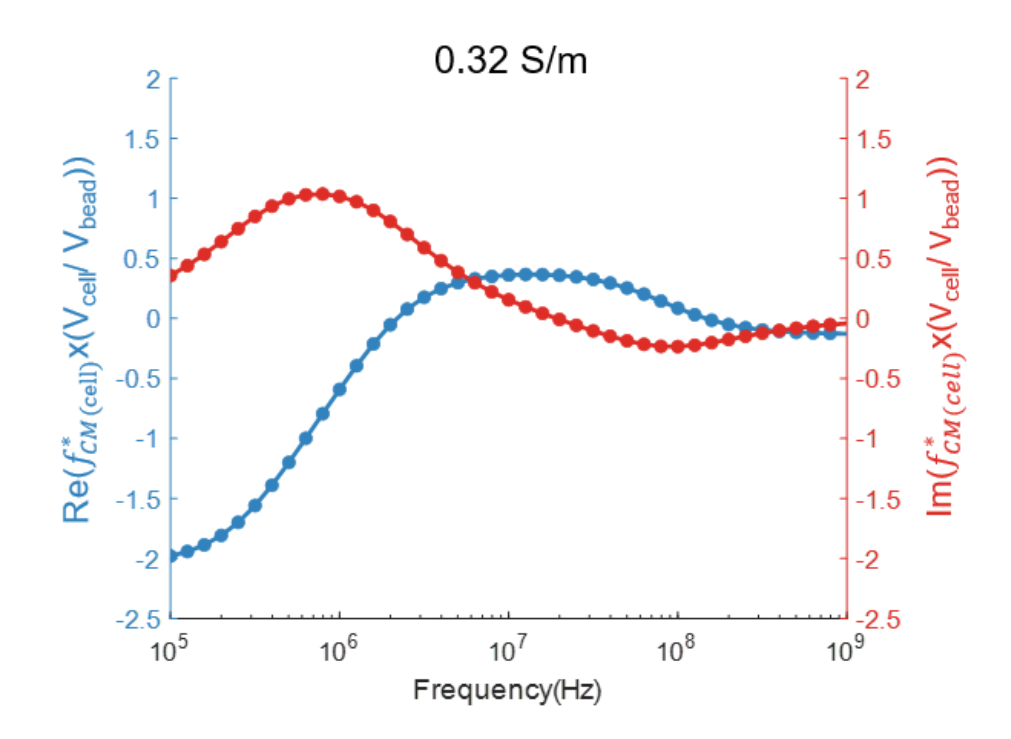


Figure 5.5 A generated data set of normalised $f_{CM(cell)}^*$ (solid dots) and its fitting curve in 0.32 S/m conductivity media with the double-shell model at the frequency range of 100kHz to 1GHz. Blue is for the real part, and red is for the imaginary.

Table 5.2 The setting dielectric parameters of the generated dataset in **Figure 5.5** and the output results from the "pattern search" fitting program.

	Diameter d (µm)	C_{mem} (mF/m ²)	σ₁ (S/m)	$oldsymbol{arepsilon}_2$	$\sigma_{cyt}(S/m)$
Dataset	12.00	12.39	3.14 × 10 ⁻⁵	60.0ε₀	0.30
Fitting	11.97	12.18	3.14 × 10 ⁻⁵	44.1ε₀	0.28

Table 5.2 summarises the numerical result of the input parameters and fitting results. As the double-shell model simulation in **Chapter 3** shows, compared to dielectric parameters of the nucleus, the variation of the cell membrane and cytoplasm parameters highly influences the $f_{CM(cell)}^*$ spectrum in low conductivity saline. Thus, the analysis focuses on cell diameter d, membrane capacitance C_{mem} and cytoplasm conductivity σ_{cyt} in 0.32 S/m saline. Membrane conductivity σ_1 is fixed to a very low value of 3.14 × 10⁻⁵ S/m, and cytoplasm permittivity ε_2 is free, although it can be ignored. In the best-fit case, output d, C_{mem} and σ_{cyt} have a 0.25%, 1.7% and 6.7% error rate, respectively, which is acceptable.

A critical metric for assessing the accuracy of fitted parameters is the confidence interval (CI). The method used to evaluate the CI of the fitting implemented by the "patternsearch" function in MATLAB is bootstrap. This is an approach used in nonlinear fitting to compute the CI. The concept involves resampling the elements in the residual set $\{r_i^*\}$, difference between measured and fitted, given by

$$r_i^* = (f_{CM}^*)_{i(measure)} - (f_{CM}^*)_{i(fitted)}$$
 (5.10)

"i" stands for the i^{th} frequency of the measurement. The new set of residuals $\{r_{i(resample)}^*\}$ is generated by resampling the r_i^* with a replacement, which means randomly generating a new set of n ($i \in 0 \sim n$) residuals, where each of n frequencies is one of the original residuals chosen with equal probability. Typically, some of the original residuals r_i^* can be chosen more than once, while some cannot be chosen at all.

The resample residual $r_{i(resample)}^*$ is then added to its corresponding fitted response $(f_{CM}^*)_{i(fitted)}$, producing a new bootstrap dataset $\{(f_{CM}^*)_{i(bootstrap)}\}$, given by

$$(f_{CM}^*)_{i(bootstrap)} = (f_{CM}^*)_{i(fitted)} + r_{i(resample)}^*$$
(5.11)

The $\{(f_{CM}^*)_{i(bootstrap)}\}$ dataset is treated as an independent replicate experiment and fit it to the model to calculate new estimates of model parameters and obtain new values of d, C_{mem} and σ_{cyt} . For each cell group, 1,000 new bootstrap datasets of the 18 or 8 frequencies spectrum for "population-mean" method and "single-cell" method were generated and fitted to the "patternsearch" function 1,000 times. The initial values of the fitting parameters were set to the best-fit output. The 95% CI of d, C_{mem} and σ_{cyt} are in the tables in **section 5.4**.

5.3 Cell Treatment and Media Preparation

Two different cell lines were used in this part of the experiment: HL60 and THP-1 cells. They are all cells from leukaemia but have different differentiation abilities. The culture method and properties of HL60 cells were introduced in detail in **Chapter 4**, so they are not elaborated on in this section. This section focuses on introducing THP-1 cells and their differentiated macrophages M0 cells.

5.3.1 THP-1 cells and macrophages

THP-1 cells are seen as a reliable model of monocytes that can differentiate into macrophages (Gatto et al. 2017), and classifying differentiated macrophages from monocytes is essential for studying immune processes and diseases. Monocytes migrate to the site of inflammation where their differentiated macrophages recognise, engulf and digest pathogens. Macrophages play a role in regulating immune and inflammatory responses by producing and releasing various soluble mediators, including radicals like superoxide anions (O_2^-) , cytokines such as tumour necrosis factor-α (TNF-α), and eicosanoids such as prostaglandin E2 (PGE2) (Schwende et al. 1996; Lewis and McGee 1992). These biological active agents are also known to modulate cell differentiation and proliferation. Phorbol 12-myristate 13- acetate (PMA) is a stimuli commonly used to induce macrophages differentiation in monocytic cell lines because it can activate protein kinase C (PKC) (Daigneault et al. 2010), triggering downstream signal pathways which regulate the expression of genes involved in macrophage-specific markers, such as CD11b, CD14 and CD36, promoting macrophage-like characteristics, e.g. increased cytoplasmic volume and adhesion. The regular assessment method of differentiated macrophages is to use flow cytometry after fluorescent staining of cell surface markers. However, capturing the complete spectrum of macrophage activation using molecular markers from a single signalling pathway is often not feasible because macrophage phenotypes are dynamic and depend on specific stimuli. Additionally, endpoint fluorescent staining assays are unsuitable for downstream studies in the same set of cells within a sample (Gordonov et al. 2016). Thus, single-cell label-free analysis is of interest because it does not rely on definitive markers of a particular signalling mechanism (Pavillon et al. 2018).

Protocols for differentiating THP-1 cells vary widely depending on cell status and operations. PMA concentration ranges from 100ng-400ng/ml with treatment durations varying from 1 to 5 days which may be followed by 1 day rest or not (Starr et al. 2018; Daigneault et al. 2010; Aldo et al. 2013; Baxter et al. 2020; Mohd Yasin et al. 2022). In this work, THP-1 was differentiated into a macrophage (M0) by exposure to PMA (200ng/ml) for 48h followed by washing and resuspending.

The protocol of THP-1 cell culture is the same as that of HL60 cells mentioned in **Chapter 4**. The cells were grown in RPMI 1640 + Glutamax (Gibco) media, 10% Fetal Bovine Serum (FBS, Gibco), and 1% Penicillin-Streptomycin (Sigma Aldrich) in a humidified incubator at 37°C and 5% CO₂.

5.3.2 Media preparation

As mentioned above, two different conductivity saline solutions were used. The first is normal physiological saline at 1.6 S/m (0.9% w/v) with an osmolarity of 280 to 300mOsm, and the second type is low-conductivity saline. The physiological saline was first diluted with deionised water at

a ratio of 1:5 so that the media conductivity decreased to 0.32 S/m. Then, D-mannitol was added to adjust the osmolarity to the range of 280 to 300 mOsm. Before using, all the solutions were filtered through a 0.22 µm filter.

5.3.3 HL60 cells fixation and treatment with cytochalasin D

Similar to cell treatment in **Chapter 4**, GA-DPBS solution at a concentration of 1% v/v was added to a 1ml suspension of cells in DPBS. The sample was kept at room temperature for 30 minutes and then resuspended in saline (0.32 S/m or 1.6 S/m conductivity). Cytochalasin D (CytoD) was used to disrupt cells cytoskeletons. Stock solutions of CytoD were dissolved in DMSO and added to 1ml cell sample with 0.32 S/m or 1.6 S/m saline media to adjust the concentration to $10\mu M$. After incubating the cells at $37^{\circ}C$ incubator for 10 minutes, the sample was kept in room temperature for around 1 minute so that the conductivity of media returned the correct value. The untreated group was added to the same amount of DMSO and also kept at $37^{\circ}C$ for 10 minutes, following the same process as the treated group.

5.3.4 THP-1 cells differentiation into macrophages

THP-1 differentiation was achieved by adding PMA (Sigma Aldrich, P1585) into the cells suspended in culture media, followed by incubation at 37°C and 5% CO2 for 48h (Figure 6.1). THP-1 cells were harvested at a concentration of 5×10⁵/ml and resuspended in fresh culture media. Stock PMA dissolved in DMSO was added to adjust the concentration to 200ng/ml. The untreated THP-1 group was added to the same amount of DMSO as a control. Then, two different cell suspensions were both moved to 6-well flasks and placed into an incubator at 37°C and 5% CO2. After 48h, the differentiated macrophages (M0) bathed in a thin layer of TrypLE Express (Gibco) were placed in the incubator for 10 minutes and then resuspended in culture media without PMA at 5×10⁵/ml, awaiting further measurement. The control group was also resuspended in culture media at the same concentration. Another control group was set to prove that the cell dissociation reagents TrypLE did not affect cell measurement. After harvesting THP-1 cells, they were resuspended in TrypLE and treated for 10 minutes in the incubator. When the measurements were started, samples were resuspended in 0.32 S/m conductivity saline with polystyrene beads. In conclusion, as **Figure 5.6** shows, there are three groups of cells:

- ① THP-1: THP-1 cells in culture media with DMSO
- ② M0: M0 cells differentiated from THP-1 cells treated with PMA
- ③ THP-1 + TrypLE: Harvested THP-1 cells from group ① treated with TrypLE

Figure 5.7 shows images of THP-1 and M0 cells in culture media. THP-1 cells float and have regular round shapes, while M0 cells attach to the flask bottom and have a spreading morphology.

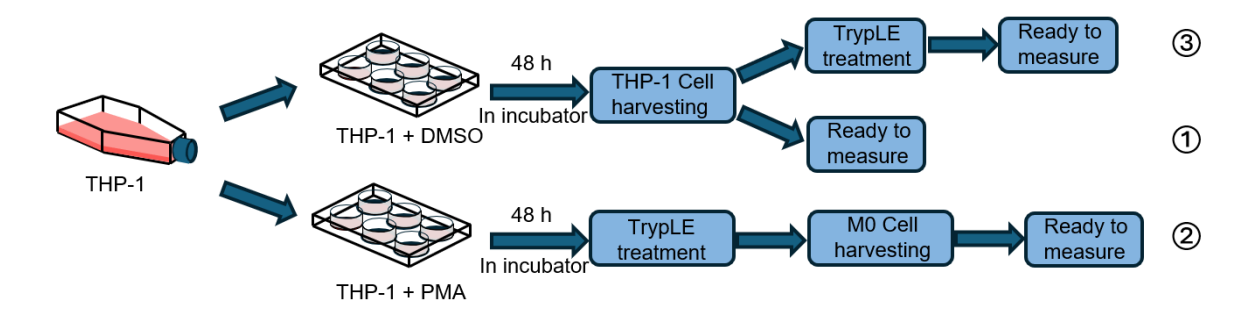


Figure 5.6 The procedure of THP-1 differentiation treatment. Three different groups awaiting to suspend in the measurement media: ① - THP-1 cells in culture media with DMSO; ② - M0 cells differentiated from THP-1 cells treated with PMA in culture media; ③ - Harvested THP-1 cells treated with TrypLE than moved in culture media.

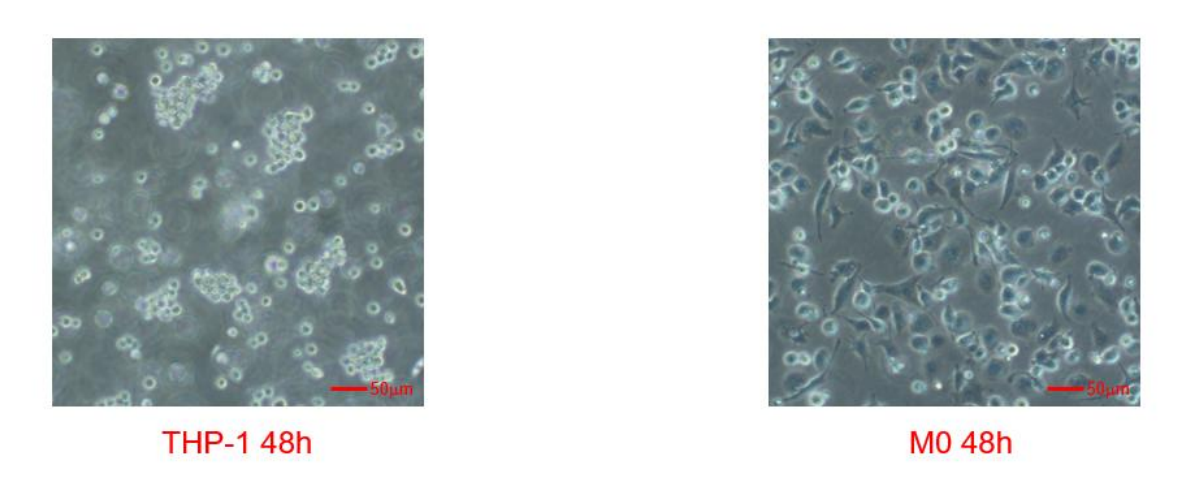


Figure 5.7 Images of THP-1 and M0 cells at 48h in the culture media before harvesting. THP-1 cells have regular round shapes and float in the flask, while M0 cells attach to the flask bottom and have a spreading morphology.

5.4 Results

5.4.1 Mean dielectric properties and influence of suspending media conductivity

This section illustrates results that were measured from the population mean method mentioned in section 5.2.2. Data was collected using two frequencies: a fixed reference frequency of 18MHz and a second frequency that was swept between 250kHz and 550MHz at 18 discrete frequencies spaced logarithmically apart. Figure 6.3 shows examples of frequency spectra for a population of HL60 cells (control (solid dots) and fixed with GA (unfilled circles)). They are the values of the normalised $f_{CM(cell)}^*$ at each frequency and represents the average for cell populations. The data was determined using equation 5.7 scaled by the ratio of the volume of cells to beads, along with a double-shell model best-fit curve for the real (blue) and imaginary (red) parts of the spectrum. The cell diameter d, membrane capacitance C_{mem} , and cytoplasm conductivity σ_{cyt} were extracted from the fit described in section 5.2.2.3.

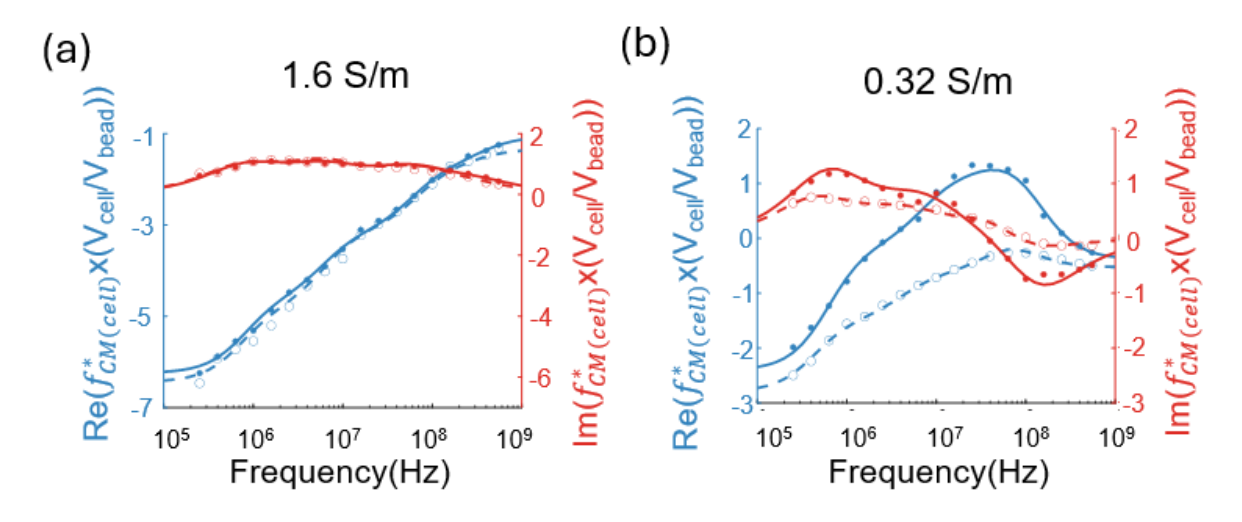


Figure 5.8 Plots of the normalised Clausius Mossotti factor (real and imaginary parts) for HL60 cells in control (solid lines with dots) and fixed group (dashed lines with unfilled circles) suspending in (a) high conductivity saline: 1.6 S/m with 5mm diameter beads and (b) low conductivity saline: 0.32 S/m with 7 mm diameter beads.

Figure 5.8 shows that the spectra curves of control and fixed groups in physiological saline are close and difficult to identify, while the difference is more evident in 0.32 S/m saline. Table 5.3 summarises the fit results for unfixed and fixed cells suspended in saline at 0.32 S/m (R² > 0.98) and 1.6 S/m (R² > 0.90). For physiological saline, cell diameters for fixed and unfixed were similar, around 12mm. The two key dielectric parameters (C_{mem} and σ_{cyt}) were also close (C_{mem} : 11.07 mF/m² vs 11.52 mF/m², σ_{cyt} : 0.31 S/m vs 0.33 S/m). In the lower conductivity media, there were slight differences between unfixed and fixed cell diameter while C_{mem} and σ_{cyt} decreased after glutaraldehyde exposure (C_{mem} : 9.14 mF/m² reducing to 6.32 mF/m²; σ_{cyt} : 0.33 S/m reducing to 0.07 S/m). This conclusion was consistent with previous literature showing that C_{mem} and σ_{cyt} of RBCs (no nucleus) decreased after fixing (Cheung, Gawad, and Renaud 2005; Salahi, Honrado, et al. 2022; Gagnon et al. 2008; Lavi, Crivellari, and Gagnon 2022).

As mentioned, GA can react with proteins and cross-link the cell membrane to make the cell stiffer and decrease membrane capacitance. Apart from that, proteins and other biomolecules in the cytoplasm are also influenced by GA. They would form a stable cross-linked network (e.g. gel) that restricts the free diffusion of ions within the cytoplasm, reducing conductivity.

Table 5.3 Fitting results for unfixed and fixed HL60 cells in different conductivity saline shown in **Figure 5.8** with confidence interval (CI).

		Diameter (d, mm)	Membrane capacitance (C_{mem} , mF/m²)	Cytoplasm conductivity (σ _{cyt} , S/m)
1.6 S/m	Untreated	11.6,	11.07,	0.31,

	CI = [11.54, 11.64]	CI = [10.00,12.01]	CI = [0.28, 0.34]
Fixed	11.7,	11.52,	0.33,
	CI = [11.61,11.77]	CI = [9.68, 13.10]	CI = [0.28, 0.37]
Untreated	12.0,	9.14,	0.33,
	CI = [11.74, 12.27]	CI = [8.48, 10.28]	CI = [0.25, 0.37]
Fixed	12.6,	6.32,	0.074,
	CI = [12.51, 12.75]	CI = [5.63, 6.96]	CI = [0.073, 0.081]
	Untreated	Fixed	Fixed

HL60 cells were also treated with CytoD, a chemical that disrupts the cytoskeleton, changing the mechanical properties of cells, and this was discussed in **Chapter 4**. However, it remains unclear how the dielectric parameters alter. The most common way is to measure the electrical opacity of cells. Opacity is used to qualitatively assess cell electrical property at some specific frequencies without deriving the parameter values. It results from the ratio of impedance magnitude at a mid-range frequency over low frequency, probing membrane electrical properties. Our previous work used high-conductivity media (MC-DPBS, 1.6 S/m) to measure CytoD-exposed HL60 cells, which shows a non-significant change in electrical opacity (**Figure 5.9**) (Chen et al. 2024). In this work, the experiment was optimised by using 0.32 S/m saline.

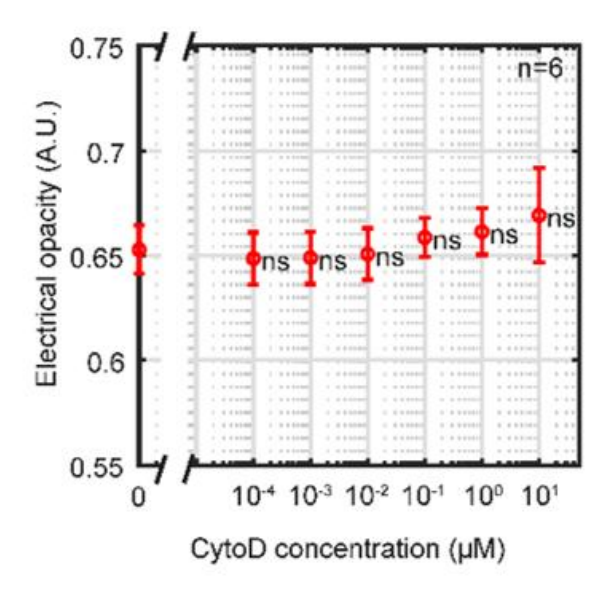


Figure 5.9 The dose-response plot of CytoD-treated HL60 cells for opacity. Adapted from (Chen et al. 2024).

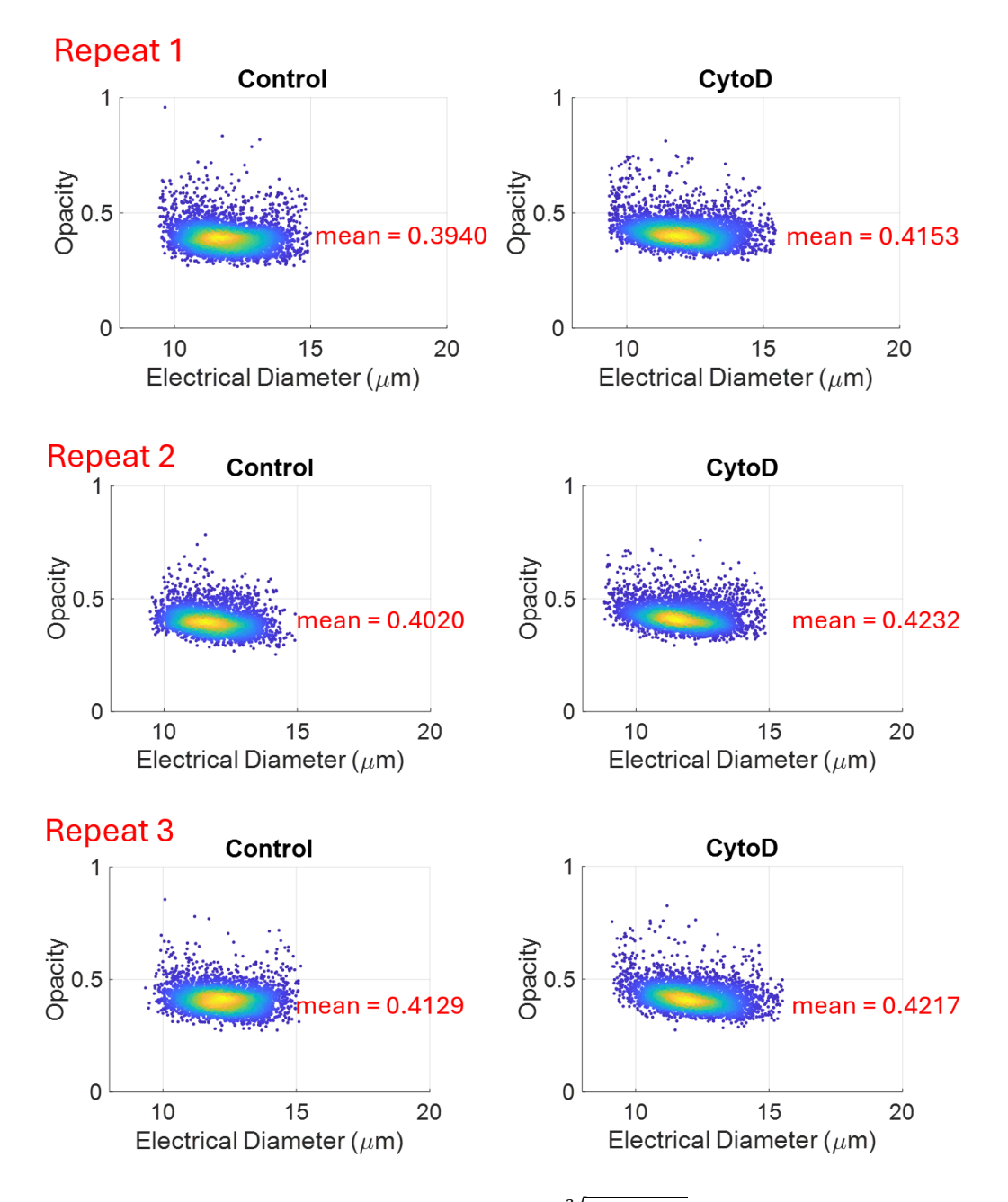


Figure 5.10 Scatter plot of electrical diameter $(gain * \sqrt[3]{|Z_{150kHz}|})$ versus opacity $(|Z_{3MHz}|/|Z_{150kHz}|)$ for untreated and CytoD-exposed HL60 cells measured in 0.32 S/m saline. Data were repeated three times. The means of the populations show that the opacity had a slight change.

As **Figure 5.10** shows, in low-conductivity media, CytoD-treated cells have a higher opacity constantly for three repeated examinations. **Figure 5.11** is the error bar chart of opacity for three repeat experiments, which presents a significant change (*, $p \le 0.05$). It indicates that cell membrane capacitance is supposed to decrease (Chen et al. 2024). The population mean spectra were also obtained with the same opacity assessment sample.

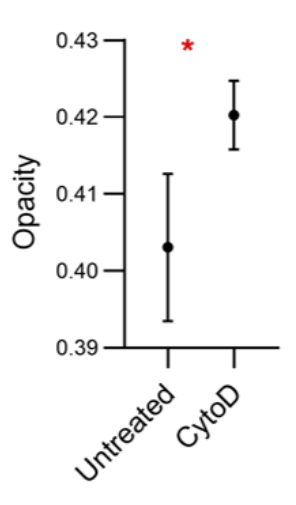


Figure 5.11 Error bar chart of opacity for untreated and CytoD-treated cells (n=3). Data was statistically analysed by students' t-test (*, $p \le 0.05$).

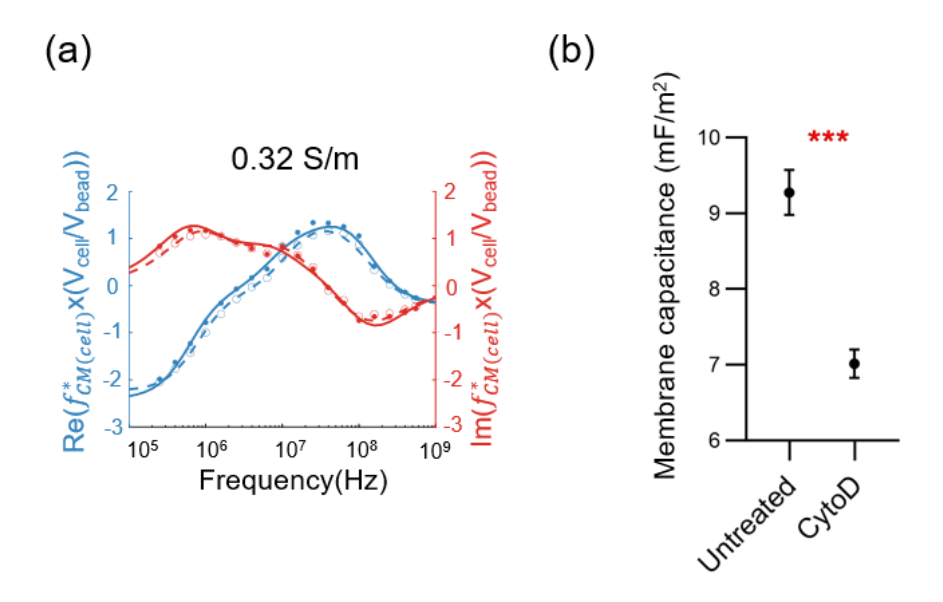


Figure 5.12 (a) Normalised Clausius Mossotti factor spectra (real and imaginary parts) for untreated (solid lines with dots) and CytoD-treated group of HL60 cells (dashed lines with unfilled circles) suspending in 0.32 S/m conductivity saline. (b) Mean and S.D. of C_{mem} for untreated and CytoD-treated cells demonstrated a significant change (***, p<0.005).

An example of the data set and its fitted normalised Clausius Mossotti factor spectra are shown in **Figure 5.12** (a). The best fits using the double-shell model (solid and dotted lines) are summarised in **Table 5.4**. C_{mem} is reduced after treatment, but σ_{cyt} remains unchanged. This alteration is expected because CytoD would only disassemble the actin filaments in the cytoskeleton, which alters membrane properties. However, the cells will remain viable, so the cytoplasm keeps the same conductivity. The results summarised in Figure 6.7 (b) demonstrate a statistically significant difference. The membrane capacitance $C_{mem} = 9.27 \pm 0.30$ mF/m² for the untreated group and 7.01±0.19 mF/m² for the CytoD group.

Table 5.4 Fit results of untreated and CytoD-treated HL60 cells shown in **Figure 5.12(a)** with confidence interval (CI).

		Diameter (d, mm)	Membrane capacitance (C_{mem} , mF/m²)	Cytoplasm conductivity (σ _{cyt} , S/m)
0.32 S/m	Untreated	12.0,	9.14,	0.33,
		CI = [11.74, 12.27]	CI = [8.48, 10.28]	CI = [0.25, 0.37]
	CytoD	11.7,	7.11,	0.33,
		CI = [11.56, 11.90]	CI = [6.54, 7.78]	CI = [0.32, 0.40]

Several studies have examined membrane capacitance using different methods. Jaffe and Voldman (Jaffe and Voldman 2018) used a Dielectrophoresis spring system to measure a hundred cells treated by CytoD and demonstrated a small but significant difference in cell polarizability. Liu et al. (Liu et al. 2020) used a constriction channel to measure cell electrical properties and concluded that treated cells had a higher membrane capacitance. However, the method applies significant stress on a cell, changing its shape and potentially influencing the membrane capacitance (Meacham et al. 2018).

This section shows that suspending cells in a lower conductivity electrolyte increases the sensitivity of the system, allowing small changes in cell electrical properties to be determined by the population-mean method.

5.4.2 Single-cell spectroscopy for fixed HL60 cells

The single-cell spectra method is easier to operate than the population-mean method because the impedance was measured by applying eight simultaneous frequencies spaced logarithmically apart on the window 250kHz to 575MHz. This method saves time in data collection and reduces the amount of samples used. Most importantly, the dielectric properties of individual cells can be determined to improve the resolution of phenotypical analysis.

The experiments started with a suspension sample of HL60 cells consisting of a 50/50 mixture of normal and GA fixed, along with reference beads, measured in 0.32 S/m or 1.6 S/m saline.

Notably, when gating beads and cells, the distinction of phase subpopulation for the mixture sample at different frequencies in 0.32 and 1.6 S/m conductivity saline is not similar. In **Figure 5.13**, the top row consists of scatter plots of phase in low-conductivity saline. Two subpopulations start to present at 760kHz and remain at 575MHz. However, in physiological saline, the mixture has one population at 760kHz and is separated into two at 575MHz.

Chapter 5

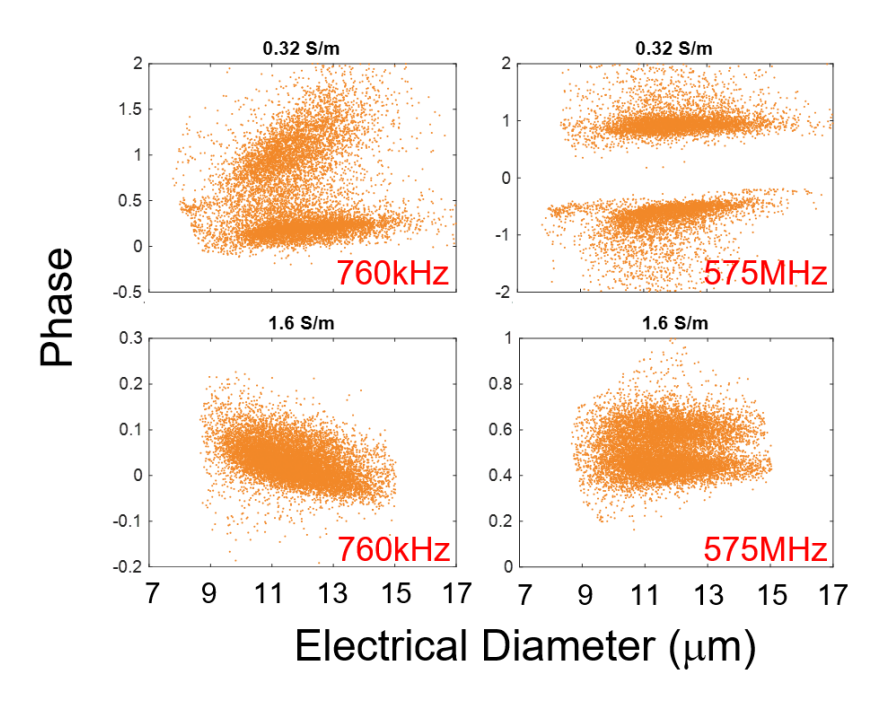


Figure 5.13 Scatter plot of electrical diameter versus phase at different frequencies (left column: 760kHz; right column: 575MHz) for mixture samples (50%/50% normal and fixed cells) suspended in different conductivity media (top row: 0.32 S/m; bottom row: 1.6 S/m). The subpopulations of the mixture can be discriminated in low-conductivity saline at very low frequency (750kHz) but are difficult to distinct in high-conductivity saline even at high frequencies (575MHz).

Each single-cell spectrum was then normalised against the mean bead impedance and fitted to the double-shell model described in **section 5.2.2.3**.

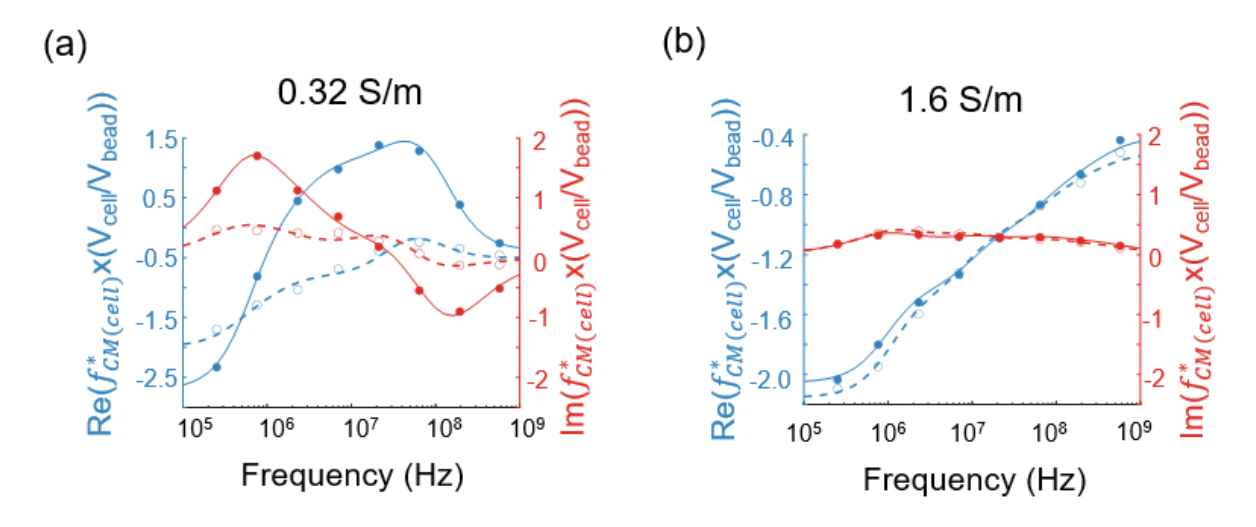


Figure 5.14 Examples of normalised $f^*_{CM(cell)}$ (blue: real part, red: imaginary part) for untreated (solid lines with dots) and fixed cells (dashed lines with unfilled circles) measured in saline of conductivity (a) 0.32 S/m and (b) 1.6 S/m, respectively.

Table 5.5 Fitting results for untreated and fixed single-cells in 0.32 S/m and 1.6 S/m saline (**Figure 5.14**), with confidence interval (CI).

		Diameter (<i>d</i> , mm)	Membrane capacitance (C _{mem} , mF/m²)	Cytoplasm conductivity (σ_{cyt} , S/m)
	Untreated	12.5,	10.31,	0.24,
0.32	Untreated	CI = [12.32, 12.66]	CI = [9.74, 10.99]	CI = [0.20, 0.26]
S/m	Fixed	11.3,	6.26,	0.077,
		CI = [10.89, 11.62]	CI = [4.55, 10.65]	CI = [0.055, 0.078]
	Untreated	11.4,	10.23,	0.36,
1.6 S/m		CI = [11.37, 11.48]	CI = [9.52,11.39]	CI = [0.30, 0.42]
	Fixed	11.6,	9.26,	0.43,
		CI = [11.55, 11.64]	CI = [8.83, 9.92]	CI = [0.38, 0.48]

Figure 5.14 shows examples of single-cell spectra for cells in the two different conductivities. Similar to the population mean data (Figure 5.8), the change in the normalised $f_{CM(cell)}^*$ for the untreated and fixed cells in 0.32 S/m saline is very clear. However, this difference is barely visible for cells suspended in physiological saline. The fitting results from Figure 5.14 are summarised in Table 5.5. In low-conductivity media, C_{mem} and σ_{cyt} decrease significantly after fixation.

Then, the spectrum for 1,000 individual cells of each type was fitted to the double-shell model, and the results are shown in the scatter plots and histogram in **Figures 5.15 and 5.16**.

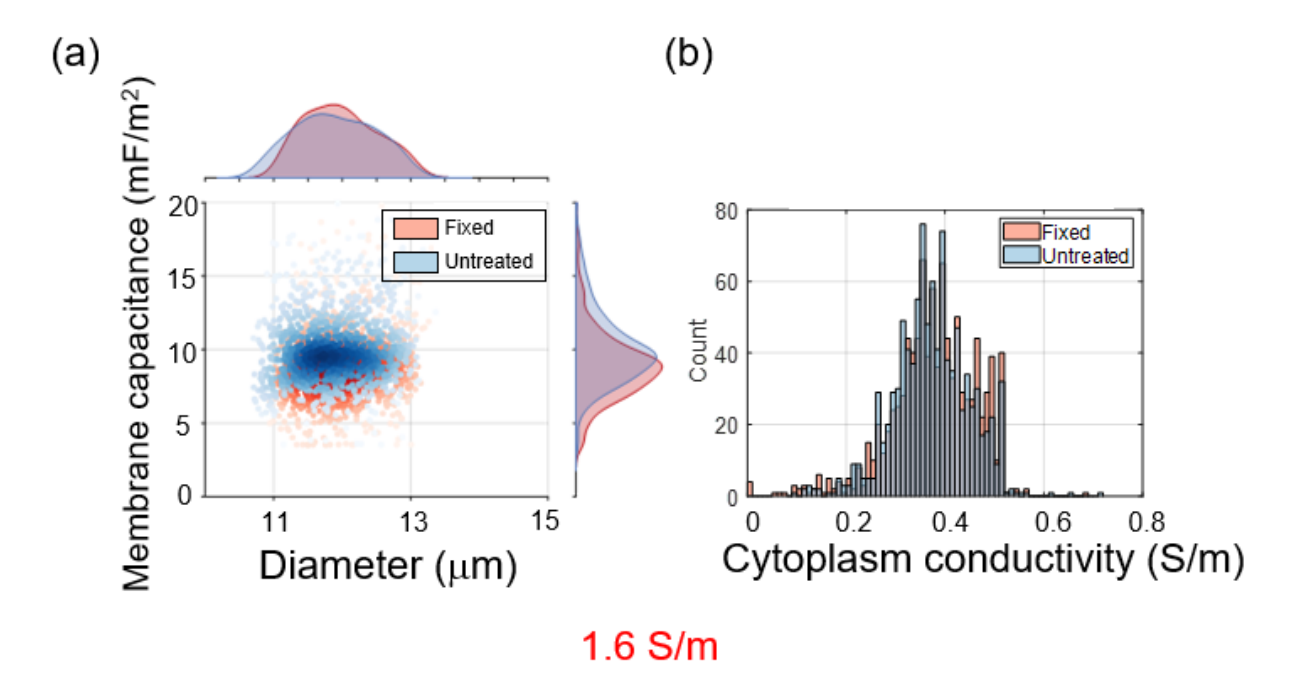


Figure 5.15 Single-cell fitting results in physiological saline. (a) Scatter plot (d vs C_{mem}) for 1000 individual untreated (blue) and fixed (red) HL60 cells. (b) Histogram of σ_{cyt} . Mean \pm SD are summarised in **Table 5.6.**

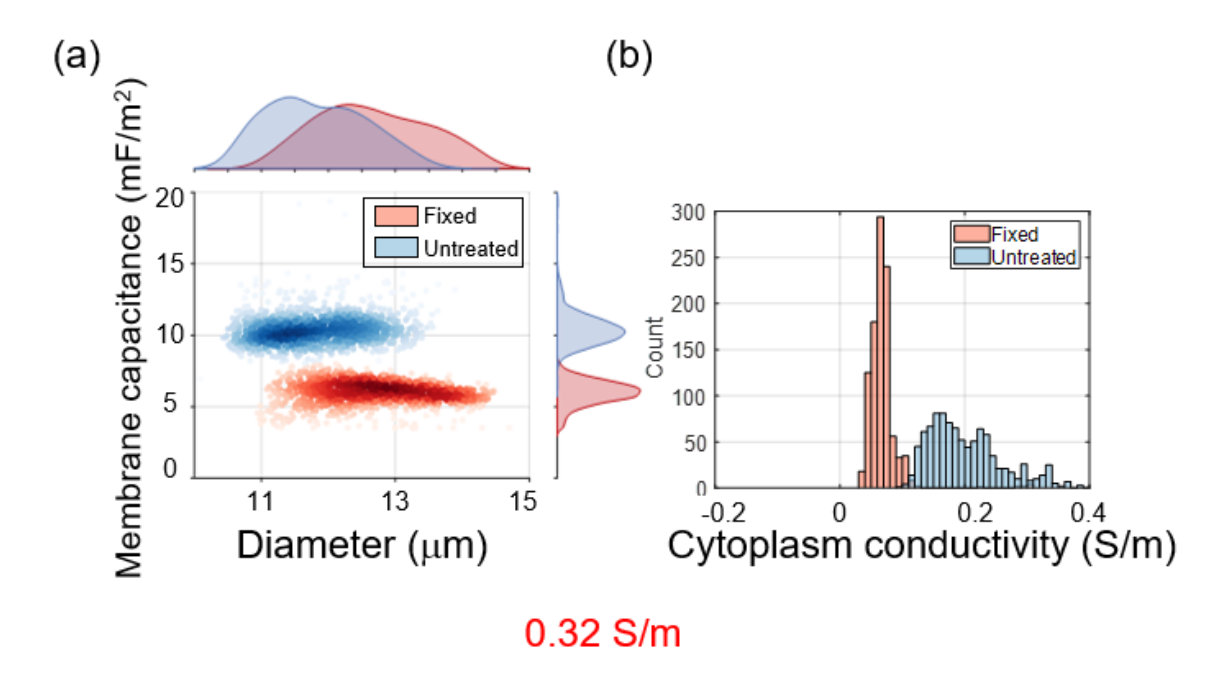


Figure 5.16 Single-cell fitting results in 0.32 S/m conductivity saline. (a) Scatter plot (d vs C_{mem}) for 1000 individual untreated (blue) and fixed (red) HL60 cells. (b) Histogram of σ_{cyt} . Mean \pm SD are summarised in **Table 5.6.**

In physiological saline, the subpopulations in **Figure 6.10** overlap in d, C_{mem} and σ_{cyt} , making it impossible to discriminate untreated and fixed cells. However, for the lower of the two suspending conductivities (**Figure 6.11**), the cell distribution has a low coefficient of variance, with clear separation in size and dielectric properties. The fixed cells have lower C_{mem} and σ_{cyt} compared with the population mean.

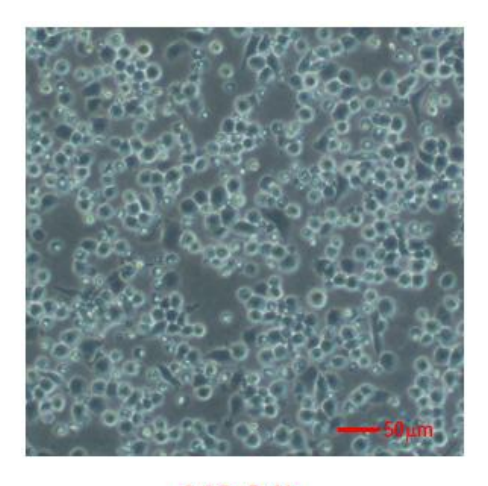
Table 5.6 Single-cell fitting results (mean \pm SD) for untreated and fixed cells in two different conductivity saline (**Figures 5.15 and 5.16**). CV stands for coefficient of variation.

		Diameter (d, mm)	Membrane capacitance $(C_{mem}, mF/m^2)$	Cytoplasm conductivity (σ _{cyt} , S/m)
0.32 S/m	Untreated	11.8±0.7, CV = 0.06	10.47±1.26, CV = 0.12	0.22±0.10, CV = 0.45
0.32 5/111	Fixed	12.6±0.8, CV = 0.06	6.02±0.84, CV = 0.14	0.07±0.03, CV = 0.43
1.6 S/m	Untreated	11.9±0.6, CV = 0.05	10.64±3.68, CV = 0.35	0.37±0.08, CV = 0.22
	Fixed	12.0±0.5, CV = 0.04	9.15±3.20, CV = 0.35	0.38±0.09, CV = 0.24

However, in **Table 5.6**, the values of C_{mem} and σ_{cyt} are slightly different compared to the results in **Table 5.3**. That may be because the limited set of frequency data reduces the accuracy of the fits, although it does not influence the ability to classify different cellular subpopulations.

5.4.3 Single-cell spectroscopy for differentiation into macrophages

After examining the single-cell spectroscopy with untreated and fixed HL60 cells, the system proved that the low-conductivity suspending media can enhance the performance of classifying cell phenotypes. This section will focus on experiments characterising THP-1 and its differentiated macrophages (M0) using single-cell spectroscopy. As mentioned in **section 5.3.1**, the protocol of THP-1 differentiation varies significantly in the treatment time. To determine if 24h or 48h is the best treatment duration, a measurement after 24h was conducted first.



M0 24h

Figure 5.17 An image of M0 cells in the culture media at 24h before harvesting. Cells adhere to the bottom without many protrusions around the membrane.

From the image shown in **Figure 5.17**, cells started to adhere to the bottom of the culture flask, but there were not as many protrusions around the cell membrane compared with the 48h-treated M0 observed in **Figure 5.7**. The data points in **Figure 5.18** are the mean value of single-

cell data for 24h treatment before fitting to the double-shell model. The spectra of different groups are nearly overlapped and difficult to discriminate. However, the 48h treatment results are entirely different (**Figure 5.19**).

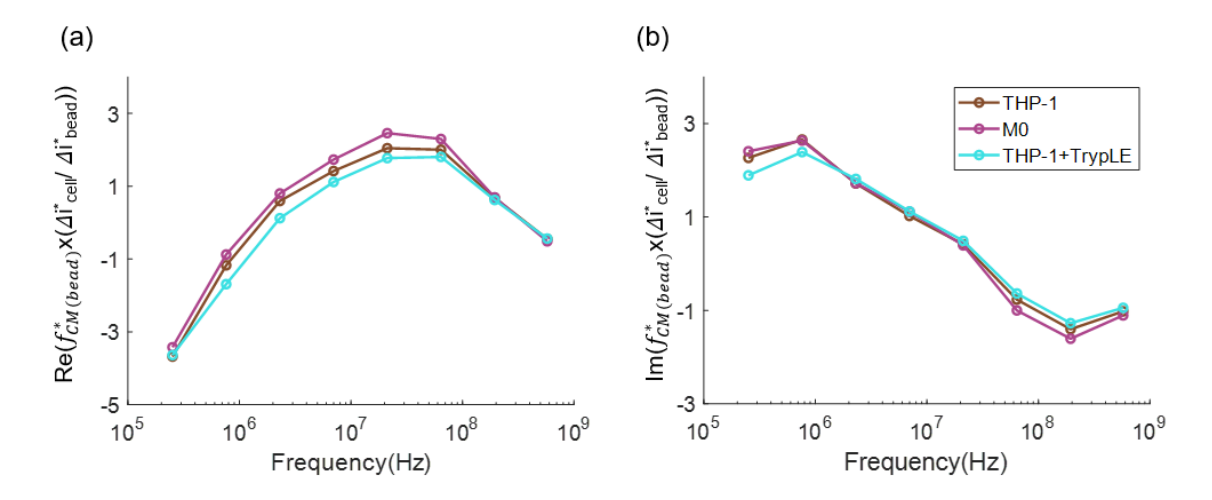


Figure 5.18 The mean value of single-cell normalised $f_{CM(cell)}^*$ for three different groups in (a) real part and (b) imaginary part after 24h treatment. The three groups are nearly overlapped.

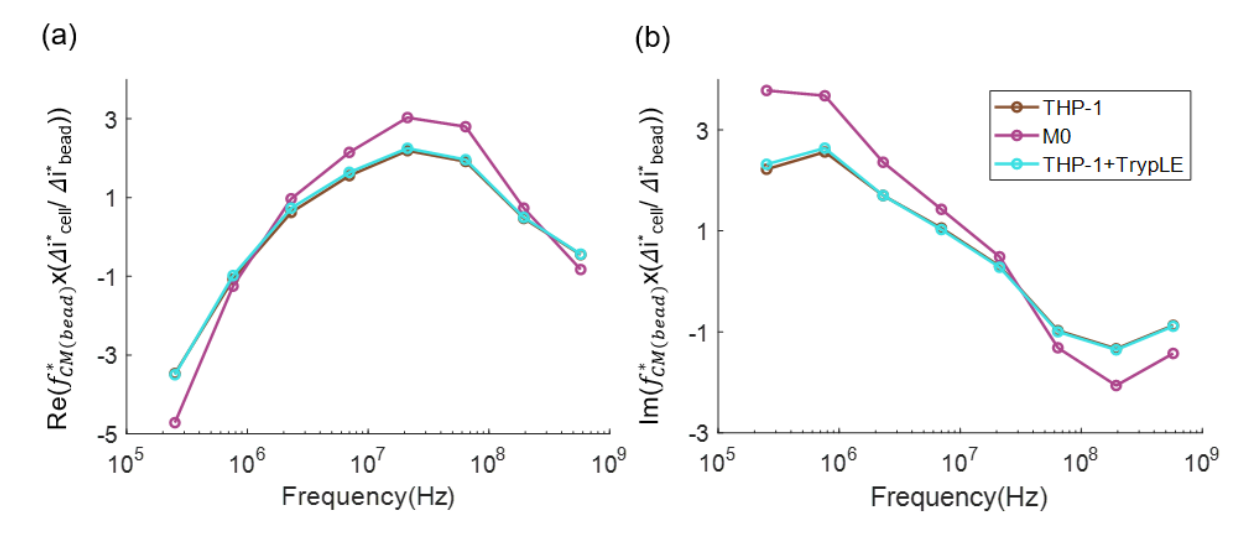


Figure 5.19 The mean value of single-cell normalised $f_{CM(cell)}^*$ for three different groups in (a) real part and (b) imaginary part after 48h treatment. THP-1 and THP-1 + TrypLE groups overlap but data of M0 cells are significantly different from them.

The curves for THP-1 and THP-1+TrypLE groups overlap, meaning that the dissociation enzyme TrypLE cannot influence the membrane properties of cells. The spectra of M0 cells are significantly different between the other two control groups over the range of 250kHz to 575MHz, indicating the alteration of cell properties. Thus, the following fitting results will focus on 48h treatment for THP-1 and M0 cell groups.

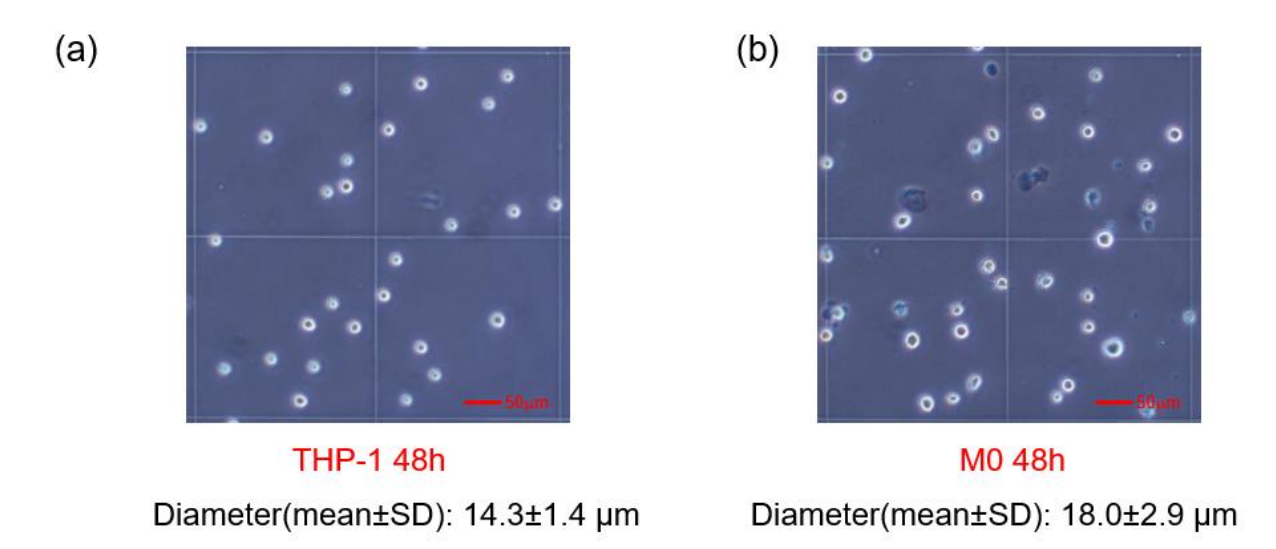


Figure 5.20 (a) and (b) are images of cells dyed with Trypan blue after harvesting from the plates and ready to be measured. The average diameter (mean±SD) of 30 THP-1 cells is 14.3±1.4mm and 18.0±2.9mm for 30 M0 cells.

Before measuring, cells were dyed with Trypan blue and then observed under an inverted microscope. Cell size was measured manually according to the images of THP-1 and M0 cells (**Figure 5.20**). The average diameter of 30 THP-1 cells was 14.3±1.4mm, and of M0 cells was 18.0±2.9mm. As expected, M0 cells were enlarged after differentiation.

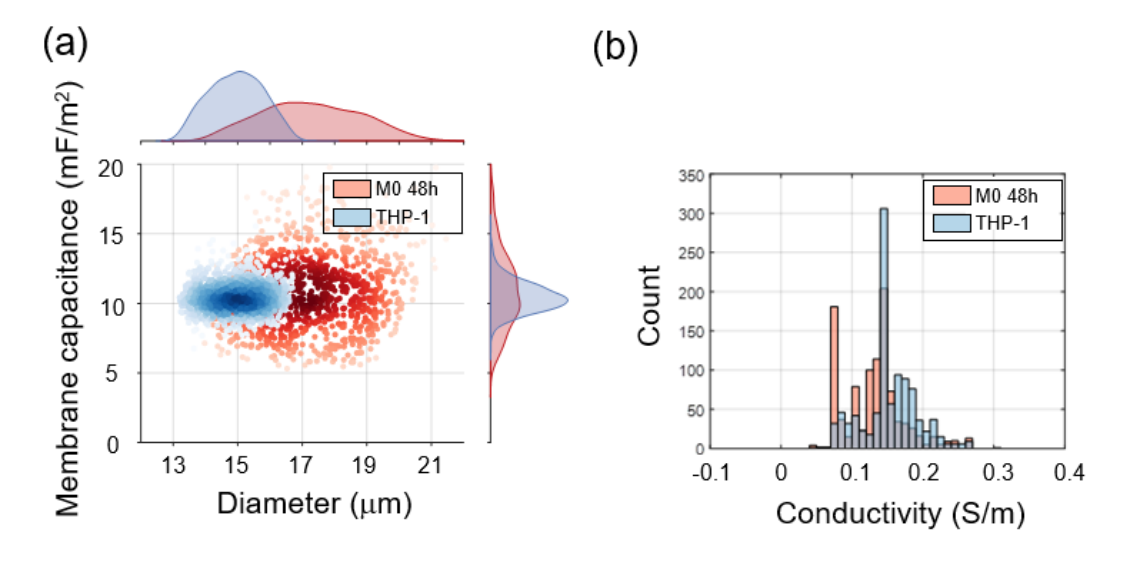


Figure 5.21 Single-cell fitting results of THP-1 cells differentiated into macrophages (M0) following 48h exposure to PMA in low conductivity saline (0.32 S/m). (a) Scatter plots (d vs C_{mem}) of 1,000 individual THP-1 cells (blue) and M0 cells (red). (b) Histogram of σ_{cyt} for two different cell subpopulations.

Figure 5.21 (a) shows a scatter plot of diameter (*d*) vs C_{mem} for the THP-1 and M0 populations. M0 cells have a larger and broader size range and are more dispersed along the x and y-axis. **Figure 5.21 (b)** shows a histogram of σ_{cyt} , showing that the two groups have a similar range but differ in their mean value.

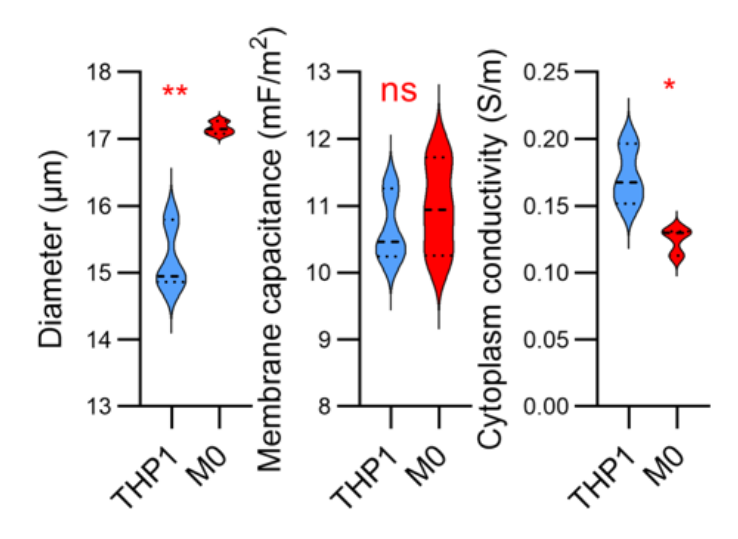


Figure 5.22 Statistical analysis of d, C_{mem} and σ_{cyt} for three repeat experiments with student's t-test (*, p≤0.05; **, p≤0.01; ns, not significant).

Figure 5.22 shows data for three repeats with statistical analysis using the student's t-test. There is a significant difference in cell diameter (**, p \leq 0.01), accompanied by a change in cytoplasm conductivity (*, p \leq 0.05), but no significant change in membrane capacitance. The plots show that the THP-1 cells have two populations with different membrane capacitance and cytoplasm conductivity. The differentiated M0 cells have a tighter size and cytoplasm conductivity distribution, with a broad spread in membrane capacitance. These results differ from the work of Soe et al. (Soe, Spiller, and Noh 2022), who used Dielectrophoresis (DEP) to characterise macrophage phenotypes and reported that the membrane capacitance of THP-1 monocytes and M0 cells were different (11.1 and 12.8 mF/m²), but these values were determined from a single DEP cross-over frequency measurement in very low conductivity media.

5.5 Discussion

This chapter mainly demonstrates the dielectric parameters of cells with the impedance spectroscope. There are two different ways to measure: one is using the population-mean spectra, which is from an eighteen frequencies sweep, to fit the double-shell model and then obtain the fitted cell diameter and dielectric properties; another method is using single-cell eight simultaneous frequencies spectra to fit the model and outcome the parameters. To get a more complete frequency-dependent spectrum of single nucleated cells at high throughput, the bandwidth was extended up to 550MHz. Also, the single-shell fitting model was replaced by the double-shell model, which is more reasonable to describe the construction of nucleated cells.

The measurement was also optimised by the choice of electrolyte. This work shows that lower conductivity media (0.32 S/m) significantly improves the resolution and sensitivity of the system, making it possible to discriminate untreated from treated cells. This finding was determined by the population-mean measurement with HL60 cells treated with GA and CytoD. Fitting to the

double-shell model at 0.32 S/m showed that the membrane capacitance of untreated cells is around 10 mF/m², which is smaller than the values that other studies reported. For example, Wang et al. (Wang et al. 2017) summarised that the membrane capacitance of cancer cell lines is around 20 mF/m²; Wang et al. demonstrated that the result of untreated HL60 cells is around 17.5 mF/m² (Wang, Becker, and Gascoyne 2002). That may be because previous studies used the single-shell model to fit the nucleated cells, which results in an inaccurate description of the cell dielectric properties.

Moreover, the population-mean method can discriminate treated cells from untreated cells and provide a correct alteration trend of dielectric parameters in low-conductivity media. The membrane capacitance of cross-linked cells was 30% less than untreated cells in saline. The reduction in cytoplasm conductivity was greater, demonstrating a decrease in ion concentration in the non-viable cells. Cells treated with CytoD had a significantly reduced membrane capacitance but unchanged cytoplasm conductivity because cells were kept alive, and the ion transport function of proteins on the cell membrane was unaffected. These differences could not be observed in cells suspended in physiological saline.

Finally, single-cell measurements of nucleated cells were made by applying eight simultaneous frequencies. Compared with the population mean method, this method can collect data with less time and less sample volume in high throughput. In 0.32S/m saline, untreated and fixed cells could be easily discriminated through changes in membrane capacitance and cytoplasm conductivity, consistent with the data for the mean population method. However, the values are slightly different because the number of data points is less than the population-mean method, reducing the accuracy of the fits. For example, in 0.32 S/m media, the membrane capacitance of untreated cell derived from population mean method is 9.14 mF/m², whereas the value derived from the single cell method is 10.31 mF/m². For a more detailed comparison, please refer to **Table** 5.3 and Table 5.5). To further prove the feasibility of the system, THP-1 monocytes and their differentiated M0 cells were tested. The fitting results demonstrate moderate changes in size and cytoplasm conductivity, with a higher variance in the membrane capacitance. Kawai et al. (Kawai et al. 2020) reported that the membrane capacitance of THP-1 cells is 11 mF/m², which is still slightly higher than the experimental results from this work. Most assessments of macrophages using impedance cytometry remain analysing the implicit parameters, such as phase and opacity (Salahi, Rane, et al. 2022; Torres - Castro et al. 2023), without presenting the dielectric parameters directly. The single-cell spectroscopy in this thesis fills this gap and gives a perspective of characterising monocytes and differentiated macrophages and even different types of activated macrophages in immune system studies.

Chapter 6 Single-cell Sorting System Based on deformability MIC

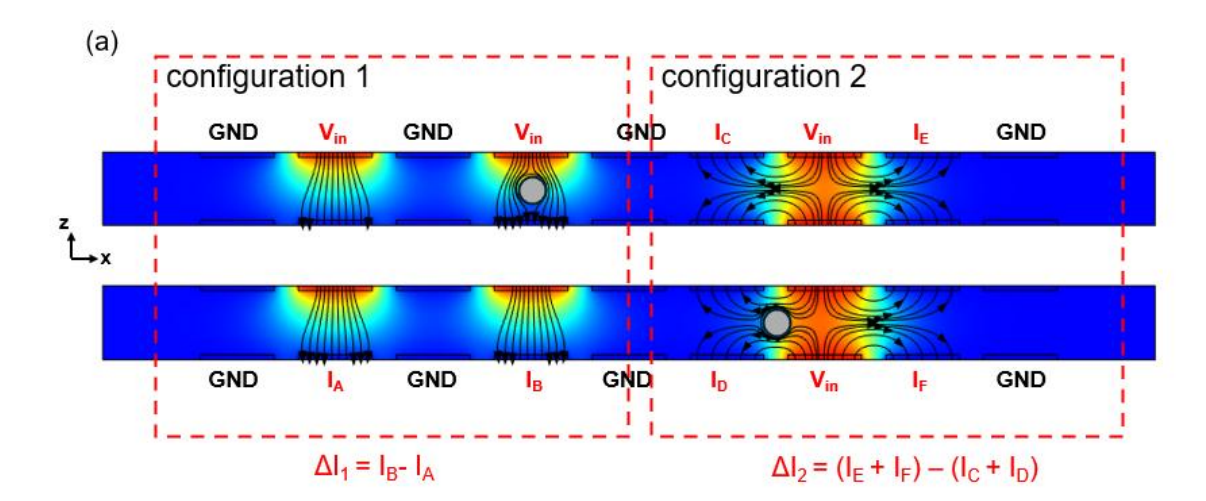
6.1 Introduction

Chapter 2 described different microfluidic cell sorting systems but and showed that most sorting systems were based on analysis of optical images of cells or fluorescence assessment (Nitta et al. 2018; Nawaz et al. 2020; Li et al. 2019). This chapter describes a novel sorting system with membrane displacement pumps placed downstream of the detection area, demonstrating proof of principle real-time deformability identification and enrichment of fixed and unfixed HL60 cells.

6.2 Sorting System

6.2.1 Electrode configuration

As mentioned in **Chapter 4**, the electrode arrangement for deformability MIC consists of two configurations as shown in **Figure 6.1 (a)**. The electrical deformability is defined as the ratio of impedance from configuration 1 to configuration 2 $(\Delta |I_1|/\Delta |I_2|)$. From the differential current plots calculated in the COMSOL simulation (**Figure 6.1 (b)**), there appears a system bias in the output waveform, where the baseline current is not at zero on the y-axis (y = 0.0165).



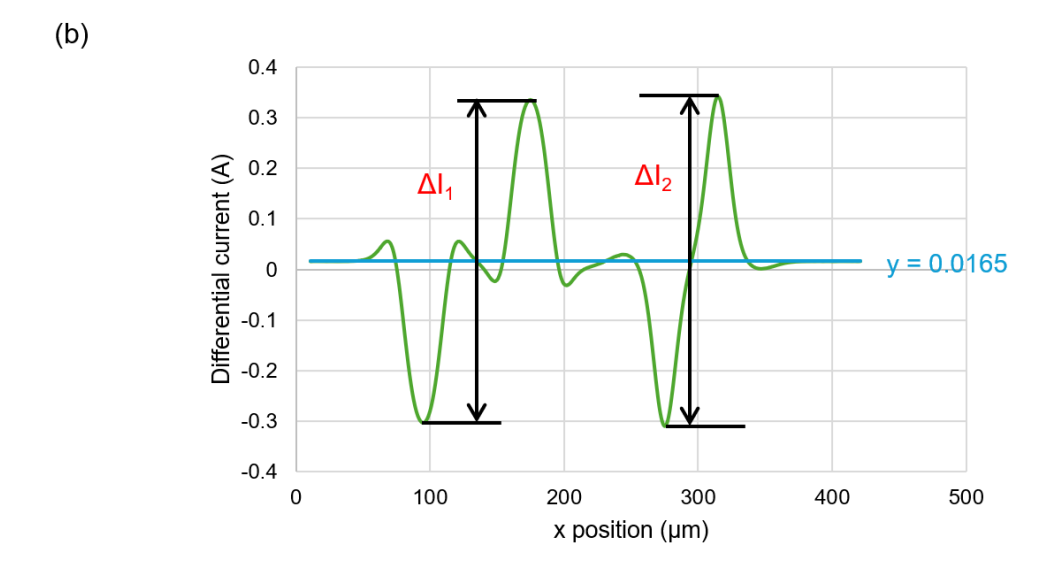


Figure 6.1 2D simulation of the electrode configuration introduced in **Chapter 4**. Applied voltage V_{in} is 1V at frequency 500kHz, and the channel dimension is 30µm high and 430µm long. The permittivity of the suspension media is $80\varepsilon_0$ and the conductivity is 1.6 S/m. The particle has a permittivity $2.5\varepsilon_0$ and conductivity 10^{-11} S/m with a diameter of 10μ m. (a) Electrical potential and current density streamlines when the particle is in configuration 1 and 2. (b) Output differential current plotted as a function of the particle position when it moves from x=11 to x=421. Only the real part of the current is presented because at low frequency the imaginary part is extremely small. ΔI_1 and ΔI_2 are the current of configuration 1 and configuration 2.

Under ideal conditions, the signal baseline should be zero. This is because in an empty channel containing conductive solution, the current generated by the two pairs of "voltage-sensing" electrodes should be equal to each other, and the differential current should be zero. However, in this simulation case, there are two different differential electrode configurations, and they are not physically isolated, so the different electric fields may interfere with each other, which leads to a non-zero baseline current. To mitigate this, two optimisations for the electrode arrangement were used as shown in Figure 6.2. The first is to insert one more pair of ground electrodes between configuration 1 and 2. This isolates the current interference between configurations 1 and 2. The second is to change the connection of V_{in} (1 V @ 500kHz) in configuration 1 so that one V_{in} is applied to the top electrode and the second V_{in} to the bottom. Figure 6.2 (a) shows the electrical potential of the optimised electrode configuration, calculated from the 2D simulation using the "Electric Current" interface. For the simulation boundary conditions, material constitutive relations and meshing parameters, remain unchanged from the simulation in Figure 6.1. Figure 6.2 (b) shows that the inclusion of the central ground electrode reduces the offset current to almost zero, with y = 0.0005. This three-orders-of-magnitude reduction in baseline drift validates the new electrode configuration.

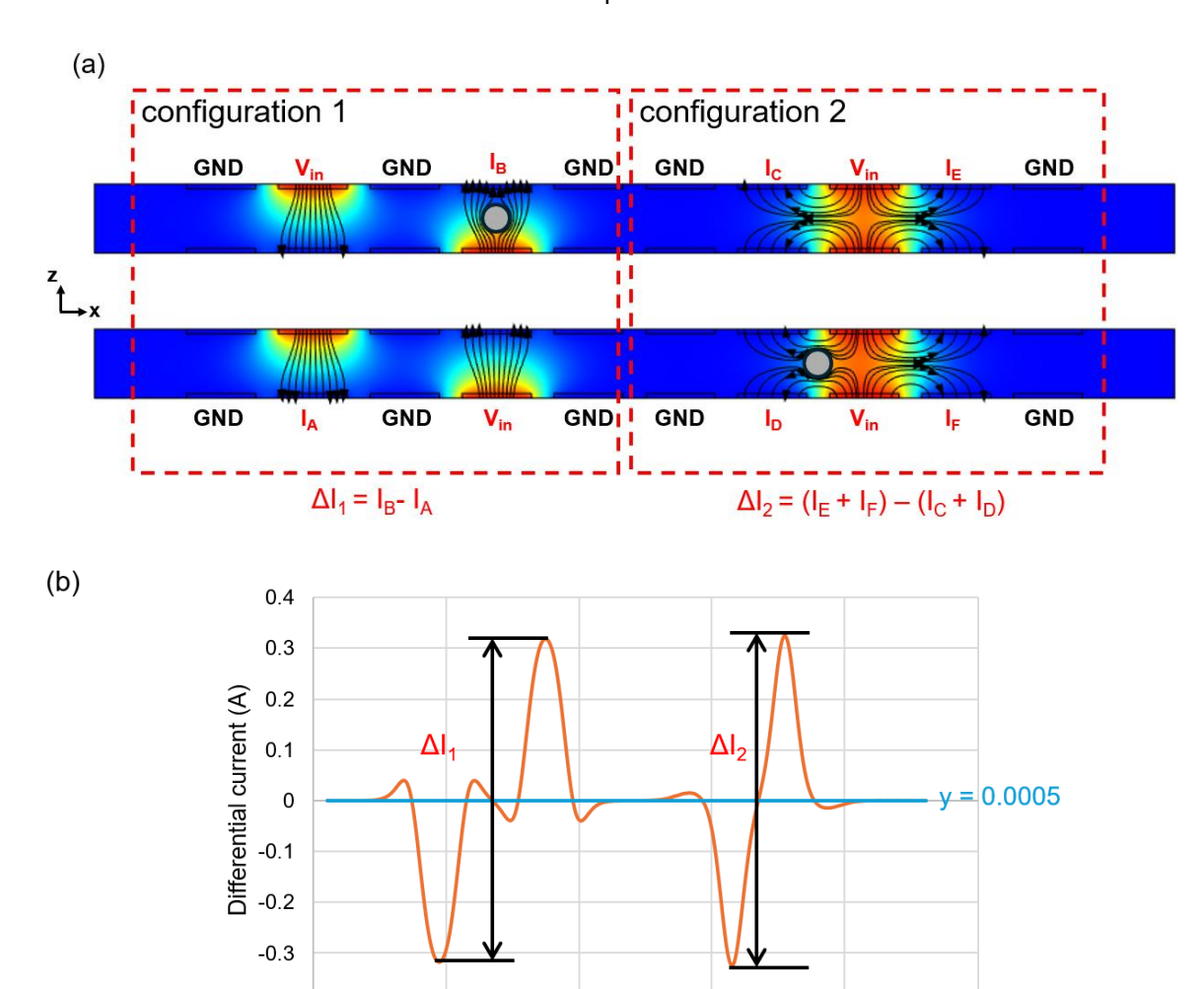


Figure 6.2 2D COMSOL simulation of the optimised electrode configuration used in this chapter. (a) Electrical potential and current density streamlines when the particle is placed in the configuration 1 and 2. (b) The output differential current plotted as a function of the particle position when it flows from x=11 to x=461. Only the real part of the current is plotted because at low frequency the imaginary part is extremely small. ΔI_1 and ΔI_2 are the current of configuration 1 and configuration 2. The figure shows that the offset is close to zero.

x position (µm)

200

300

400

500

100

6.2.2 System setup

The working principle of the membrane-pump sorter was described in section 3.5. This section describes the implementation of the sorting system. Figure 6.3 is a schematic illustration of the sorting system. In Figure 6.3(a), the pressure pump (Elevflow, OB1) regulates the pressure of the inlet ③ and two outlets ① ② in the microchannel, with the pressures controlled to direct the particle passing through the impedance detection region ($40\mu m \times 30 \mu m$) towards the upper outlet ① during the "Ready to activate" state. A typical set of pressure values is: $P_3 = 400 \text{ mbar}$, $P_2 = 168 \text{ mbar}$, $P_1 = 12 \text{ mbar}$. A custom inverted fluorescence microscopy system was constructed for real-time observation and video recording of the sorting. The excitation source is a green LED (M530L2, Throlab), and the emitted fluorescence captured with a 20× objective, with spectral separation via a dichroic mirror and optical filters. A CMOS camera (MQ003CG-CM, XIMEA) was

used to capture images. An white light mounted atop the device stage was used for bright-field observation. The differential impedance signals are collected by a lock-in amplifier (HF2LI, Zurich Instruments), with subsequent digitisation performed by a microcontroller (MCU, Teensy 4.0, PJRC). The MCU implements a real-time peak detection algorithm to extract $\Delta |I_1|$, $\Delta |I_2|$ and particle velocity, to calculate the predicted transit time for the trigger signal. This signal is routed to a pulse-generation circuit that produces rectangular voltage waveforms. This pulse is amplified by a power amplifier (9200, Tabor Electronics) with a gain = 15 before driving a piezoelectric actuator (PK3JUP1, Throlab) integrated on top of the membrane pump (**Figure 6.3(b)**). The actuator assembly is positioned downstream of the impedance detection region, ensuring precise temporal synchronisation between particle detection and sorting actuation.

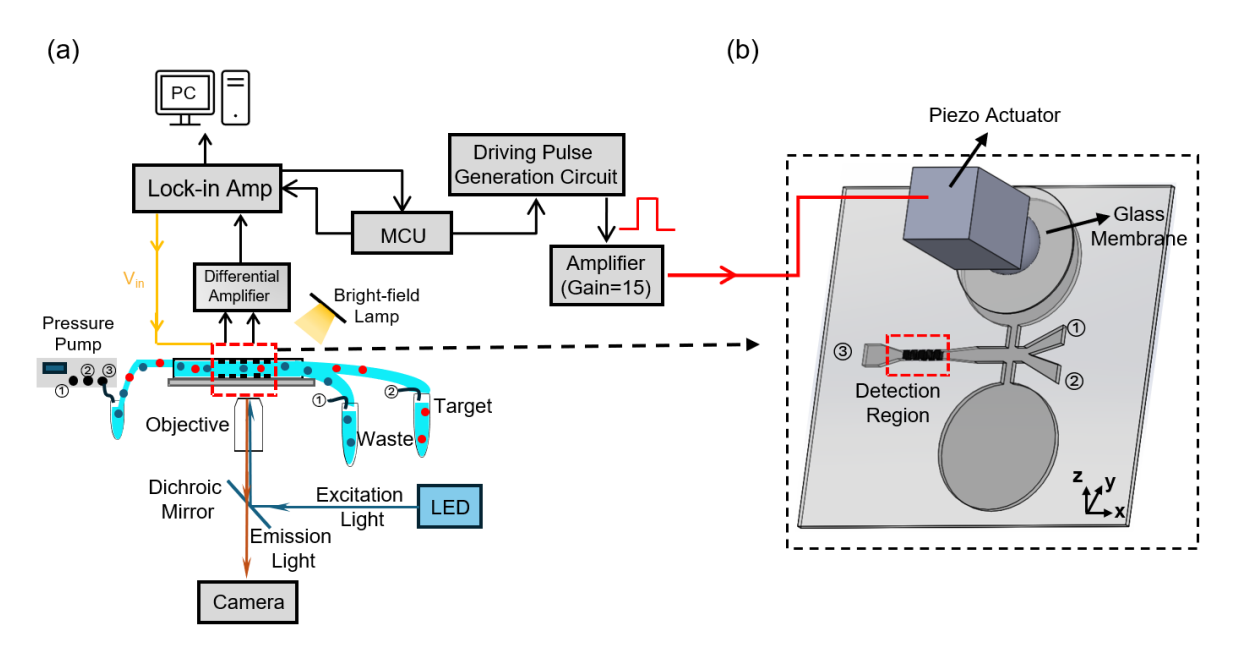


Figure 6.3 Schematic illustration of the sorting system. (a) Pressure pump regulates the pressure of the inlet @ and two outlets, @ and @, directing particles toward outlet @ during the "Ready to activate" state. The impedance signals from the detection region are collected by the lock-in amplifier and sent to the MCU to be processed in real-time. MCU generated trigger signals drive a pulsed voltage circuit, which is subsequently amplified by a voltage amplifier (gain factor = 15) to meet the operational requirements of the piezo actuator. The customised optical pathway of fluorescence detection consists of an LED that generates excitation light, a dichroic mirror for spectral separation, an objective, and a camera to capture the emission images at 250 fps. (b) Illustration of the sorting chip. The membrane-pump sorter is downstream of the impedance detection region $(40\mu m \times 30\mu m)$ on the chip. Grounded electrodes are omitted. The piezo actuator is controlled by the impedance measurement, and it provides an external force to deflect the membrane.

The triggering mechanism and peak detection algorithm were described in **Chapter 4**. The following subsections elaborate on other three critical system components: an optimised triggering algorithm to solve event conflicts, a pulse generation circuit, and the design of piezo actuator assembly.

6.2.2.1 Real-time triggering algorithm to solve conflicts

The operational principle of the triggering mechanism was described **in Chapter 4**. In summary, the MCU predicts the particle transit time between the impedance detection region and image capture region by calculating the velocity of each individual particle. Initial experiments used beads of different sizes so that in addition to calculating transit time, a threshold impedance was also applied to differentiate 6µm and 10µm beads. Because the membrane pump required a large amount of space, the main channel length was extended. Thus, the time interval between the impedance signal and the trigger pulse increased. The single-threaded algorithm described in **Chapter 4** was first used. When a particle entered the detection region, it generated an impedance signal. The signal was sent to the ADC on MCU, and a transit time delay was calculated to output the pulse. During this time delay, if there was a new particle entering the detection region, its impedance would not be sampled by ADC because the execution was stuck by the single thread. This results in signal conflicts, reducing the sorting efficiency. This was optimised by modifying the MCU control algorithm. A sorting triggering mechanism was optimised using a multi-thread algorithm, and the time sequence limitation of detection and triggering signal caused by the single-thread algorithm was solved.

Figure 6.4(a) shows an example impedance signal (blue) and threshold (orange) used to differentiate $6\mu m$ and $10~\mu m$ beads. To implement sorting the impedance signal was first amplified and added to an offset to adjust the peak-to-peak amplitude within the range of 3.3~V (input voltage limitation of MCU) through the lock-in, with MCU signals taken from the lock-in auxiliary output port. Impedance amplitudes exceeding the established threshold were attributed to the $10~\mu m$ microbeads, whereas sub-threshold measurements corresponded to $6~\mu m$ particles.

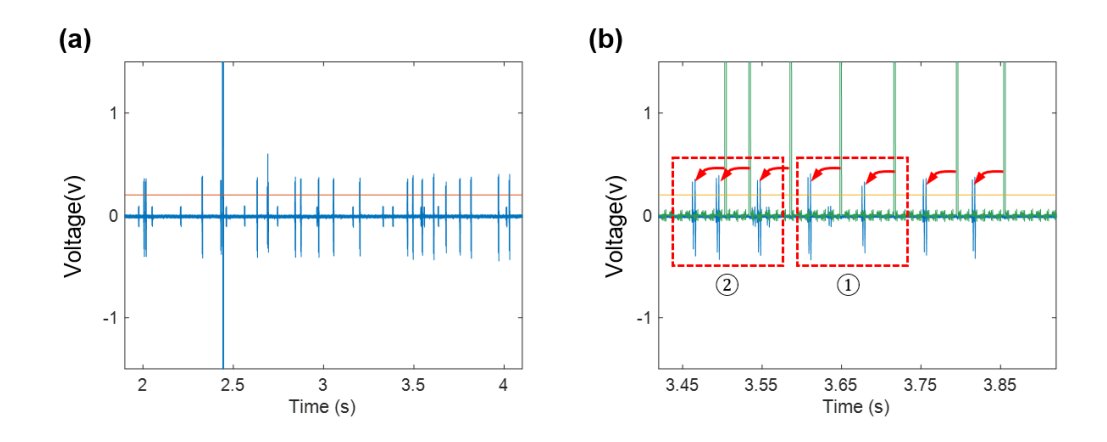


Figure 6.4 Impedance signals from 6µm and 10 µm beads. (a) Impedance signals (blue) transmitted from the lock-in auxiliary output port to the MCU and the threshold (orange) for triggering. (b) Synchronised impedance-pulse (blue-green) correlation depicting two operational scenarios:

① Normal sequencing - trigger pulses immediately follow respective impedance signatures while preceding subsequent detection events. ② Temporal conflict - delayed pulse generation overlaps with successive impedance occurrences. Red arrows denote correspondence of matched impedance-pulse signals.

Figure 6.4(b) shows the impedance signal (blue line) and the corresponding trigger pulse (green line, red arrow). There are two different operational scenarios: ① Normal sequencing – a trigger pulse is created immediately follow an impedance signal. In this case, the MCU executes a four-stage signal conditioning via: analogue-to-digital-conversion (ADC), peak detection, transit time calculation and generation of the digital signals that are then sent to the pulse generating circuit. Scenario ② corresponds to a temporal conflict. Under such temporal constraints, adjacent impedance events have insufficient temporal separation, and the existing algorithm is unable to generate synchronous trigger pulses within the required actuation window. This was optimised by using parallel threads in the MCU. **Figure 6.5 (a) and (b)** show scenarios ① and ② from **Figure 6.4(b)** respectively. τ_d is the time delay between a matched impedance-pulse signal. Note that τ_d includes the calculated particle transit time and an offset to compensate for the program execution delay. Before algorithm optimisation, the trigger pulse in the red dashed rectangle in **Figure 6.5(b)** would fail because the input from the second impedance signal would block the pulse generation.

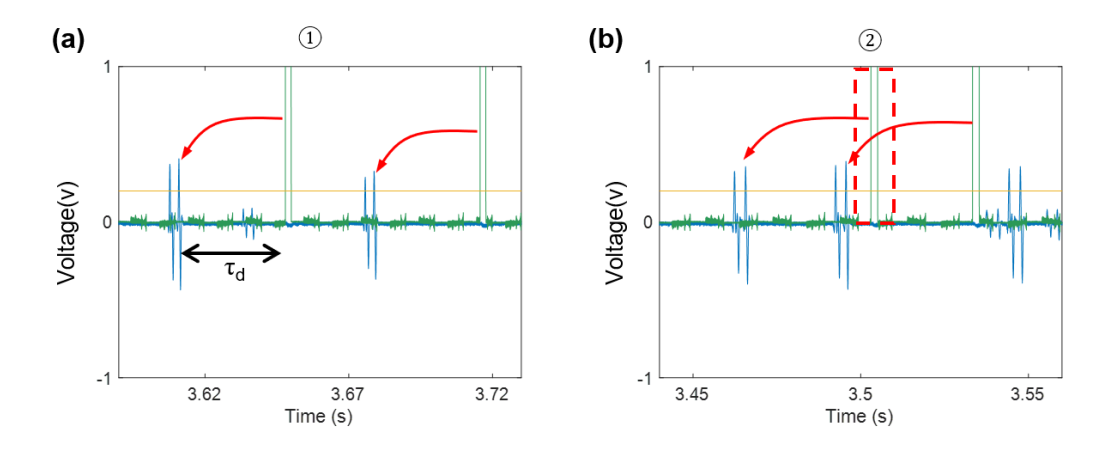


Figure 6.5 Detailed plots of impedance-pulse signals in two different scenarios mentioned in **Figure 6.4(b)**. (a) Scenarios ① and (b) Scenarios ②. The time interval between the impedance and trigger pulse is denoted " τ_d " which includes the calculated particle transit time and an offset to compensate for the program execution delay.

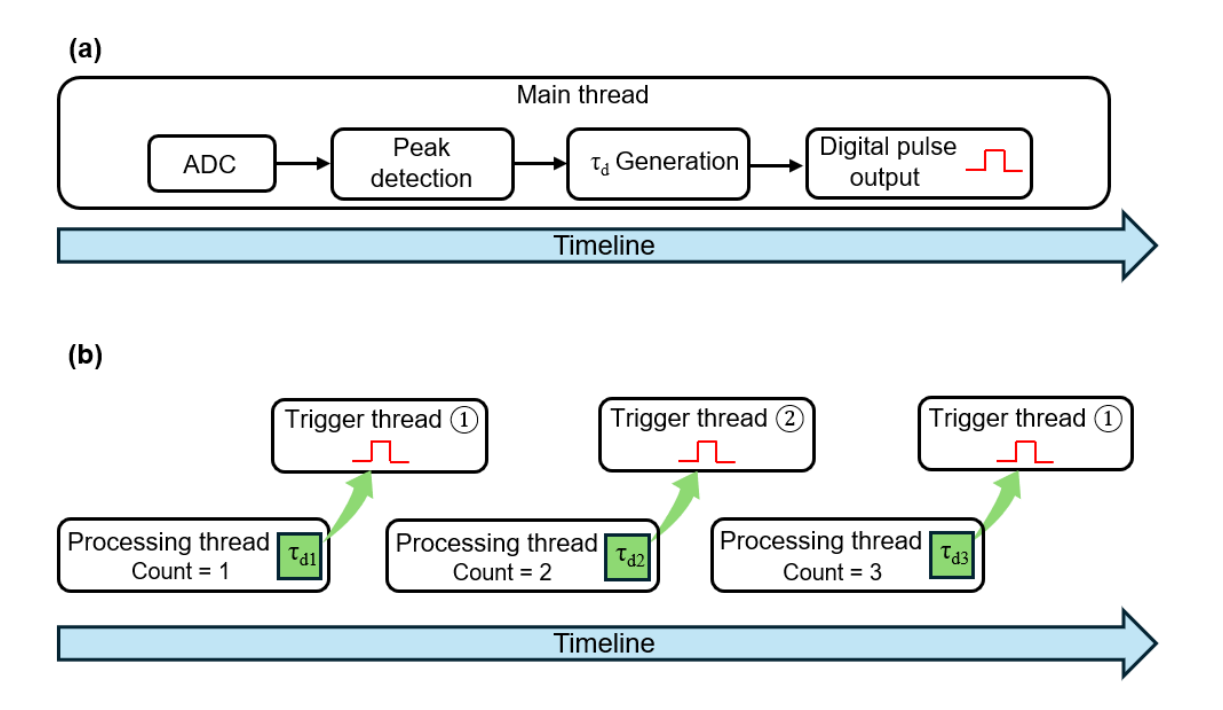


Figure 6.6 (a) Program execution timeline before optimisation. The program has one thread, and the order of execution is ADC, peak detection, τ_d generation and finally digital pulse output. These processes are in serial. (b) Optimised program execution timeline. There are three parallel threads: Processing thread, Trigger thread ① and Trigger thread ②. The processing thread achieves ADC, peak detection and generating τ_d . An event counter is used in this thread to index the impedance signal. Trigger thread ① and ② monitor the parity of parameter "count" and output of τ_d . Once the generated τ_d is detected by the trigger thread, and the parameter count is an odd number, trigger thread ① produces a digital pulse. Conversely, trigger thread ② produces the pulse when parameter count is an even number.

Figure 6.6 compare the previous MCU program and the optimised program. Figure 6.6(a) shows the sequential processes including ADC, peak detection, τ_d generation and finally digital pulse output. Following τ_d acquisition, the main thread initiates a latency period precisely equivalent to τ_d , awaiting trigger pulse generation. From the ADC stage to pulse generation stage, the main process serves is for one impedance event, which a waste of computational resource. The MCU supports multithreading by adding a library "TeensyThreads.h" to the program in Arduino IDE, enabling concurrent execution to solve the temporal conflicts. Figure 6.6(b) shows the execution timeline of the optimised program. There are three parallel threads in the program: a processing thread and two trigger threads. The processing thread includes ADC, peak detection and τ_d generation. A parameter "count" chronologically indexes the impedance signal. Trigger thread ① and ② monitor τ_d generation and the parity of parameter "count". If there is a τ_d with an odd "count", trigger thread ① generates the digital pulse. Conversely, trigger thread ② produces the digital pulse when "count" is an even number. The trigger threads operate independently of the processing thread, allowing the processing thread to handle more input impedance signals within the same timeframe. Additionally, indexing the two alternating trigger threads ensures the correct order of the generated digital pulses.

6.2.2.2 Driving pulse circuit

Precise control of the piezoelectric membrane pump actuator requires stable pulse generation with programmable waveform characteristics. The driving circuit architecture integrates three critical stages: analogue amplification, digital modulation, and power amplification (**Figure 6.7**). A 3.3 V DC signal from the MCU undergoes initial amplification through an operational amplifier (TL081CP, Texas Instruments) with gain adjusted via feedback potentiometer ($R_f = 250\Omega$). Subsequently, MCU-generated digital pulse signals modulate the amplified analogue output to create rectangular waveforms using a reed relay (SIL12-1A72-71D, MEDER electronic Inc.). Finally, a commercial power amplifier conditions the modulated signals to achieve the requisite voltage/current levels for reliable actuator operation. Due to the high voltage requirement (100V) of the piezo actuator, this multi-stage circuit design ensures operational safety by allowing the final power amplifier stage to remain disconnected during initial signal testing, thereby significantly reducing the risk of accidents caused by high-voltage conditions.

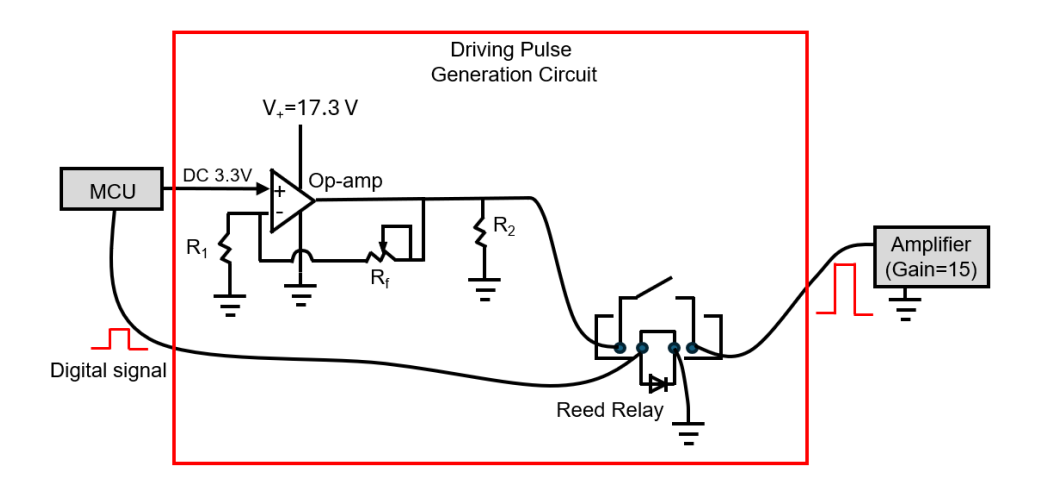


Figure 6.7 Custom circuit for generating driving pulses. 3.3V DC voltage from the MCU is amplified via an operational amplifier (op-amp), with gain adjustable by potentiometer resistance (R_f =250 Ω). The digitalised MCU output pulses control the electromagnetic switch of the reed relay, generating rectangular waveforms with desired triggering patterns. Finally, the output pulse is sent to a commercial amplifier with a gain of 15. R_f = 100 Ω , R_2 = 22k Ω .

Figure 6.8 shows the output pulse of the pulse generation circuit before the power amplifier. **Figure 6.8(a)** shows representative waveforms of an impedance signal (blue) and its synchronised trigger pulse (brown). These data were acquired through the lock-in amplifier. As mentioned in **section 6.2.2.1**, the peak-to-peak magnitude of the blue line signal is adjusted to a range within 3.3V to facilitate simplified real-time processing in MCU.

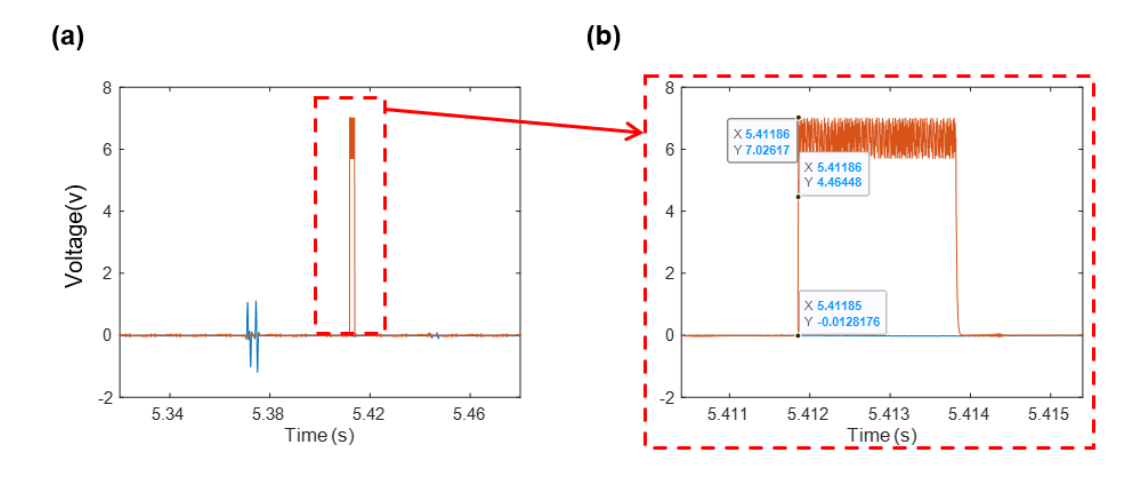


Figure 6.8 Generated pulse before being amplified by the power amplifier. (a) An impedance signal (blue) and its synchronised trigger pulse (brown). (b) Details for the triggering signal. During low-level MCU digital signals ($t < 5.41185 \, s$), the reed relay maintains an open (Voltage = 0V) state. Upon transitioning to a high-level signal, magnetically induced current activates the reed relay, resulting in switch closure to conduct the output amplified voltage from operational amplifier. The level transition demonstrates a 10 μs switching delay (from $t = 5.41185 \, to \, t = 5.41186 \, s$).

Figure 6.8(b) shows the shape of the trigger signal. For a low-level digital output from the MCU, the reed relay maintains its open configuration (Voltage = 0 V). Transition to high-level digital output switches on the reed relay, passing the amplified voltage of the op-amp. Temporal analysis reveals a 10 μ s switching delay (t = 5.41185 s to t = 5.41186 s), with output voltage transitioning from 0 V to 6.7 V root-mean-square (RMS) as measured by an oscilloscope, confirming system tolerance within acceptable parameters.

6.2.2.3 Piezo actuator assembly

The piezo actuator assembly drives the external actuation of the membrane pump. Precise alignment ($\pm 2\mu m$ tolerance) between the actuator and pump membrane is achieved using locating holes. Additionally, the actuator assembly design must eliminate mechanical damping and provides a preload to the actuator, ensuring that the subtle displacement is transmitted to the on-chip membrane, which is achieved by inserting a spring screw on top of the actuator. Details are shown in **Figure 6.11**.

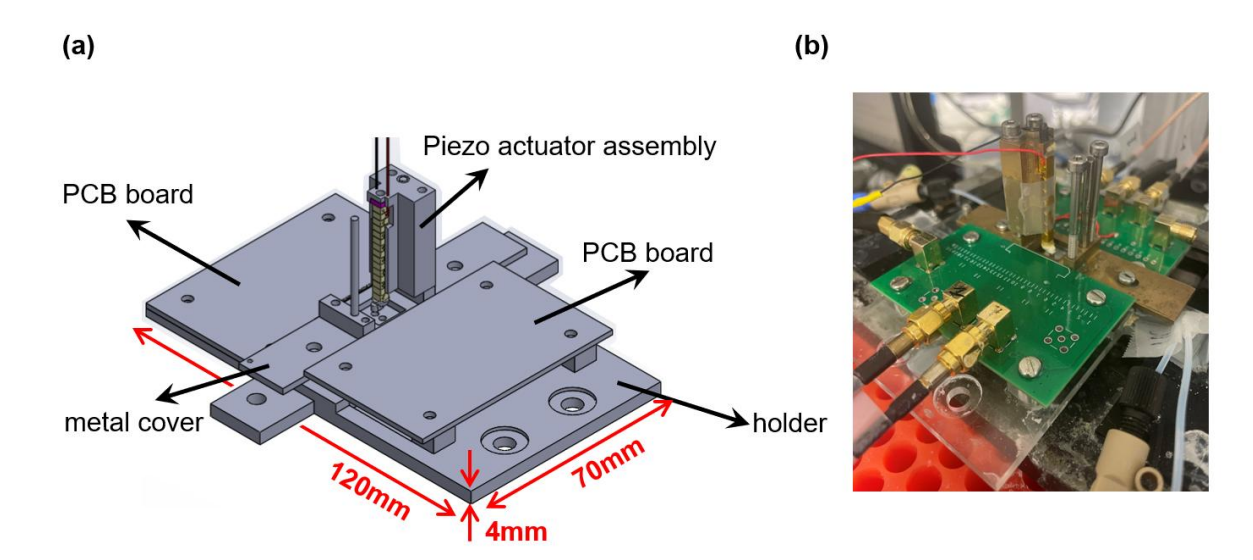


Figure 6.9 Piezo actuator assembly integrated into the impedance cytometry system. (a) CAD model of the system. The microfluidic impedance chip (omitted) is placed in the plastic holder and mechanically secured via a metal cover to maintain leak-free fluidic connections. The top and bottom PCB boards are fixed to the holder to ensure electrical continuity. The piezo actuator assembly is integrated on the metal cover and aligned precisely with the membrane pump of the impedance chip by using locating holes. (b) Photograph of the sorting system.

An overview of the piezo actuator assembly integrated in the impedance cytometry system is presented in **Figure 6.9** generated using SolidWorks. The microfluidic impedance chip is placed in the holder and mechanically secured via a metal cover with screws, maintaining no-leak fluidic connections. The top and bottom PCBs are mounted to the holder to ensure electronic connections with electrode pads of the impedance chip. The piezo actuator assembly is integrated on the metal cover with locating holes to achieve a precise alignment. **Figure 6.9(b)** is the photograph of the sorting system.

Figure 6.10 presents the CAD modules of the holder and PCB components. The central slot houses the impedance chip, with four precisely aligned circular ports serving as fluidic inlet/outlets. The spring connector (FSI-120-03-G-S, Samtec) maintains electrical continuity between the PCB and the electrode pads of the chip, achieving high SNR acquisition in impedance measurements.

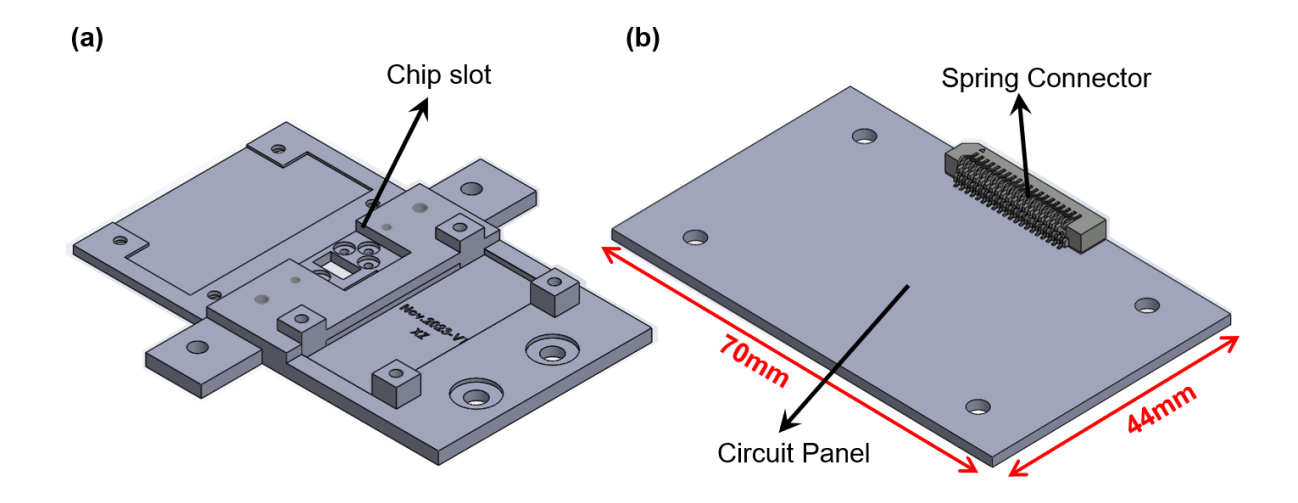


Figure 6.10 (a) CAD module of the holder. The centre rectangular slot is used to place the impedance chip and enable fluidic connections. (b) PCB geometry design. The spring connector on it is to connect the electrode pads of the impedance chip and send the signal to the lock-in amplifier via the PCB circuit.

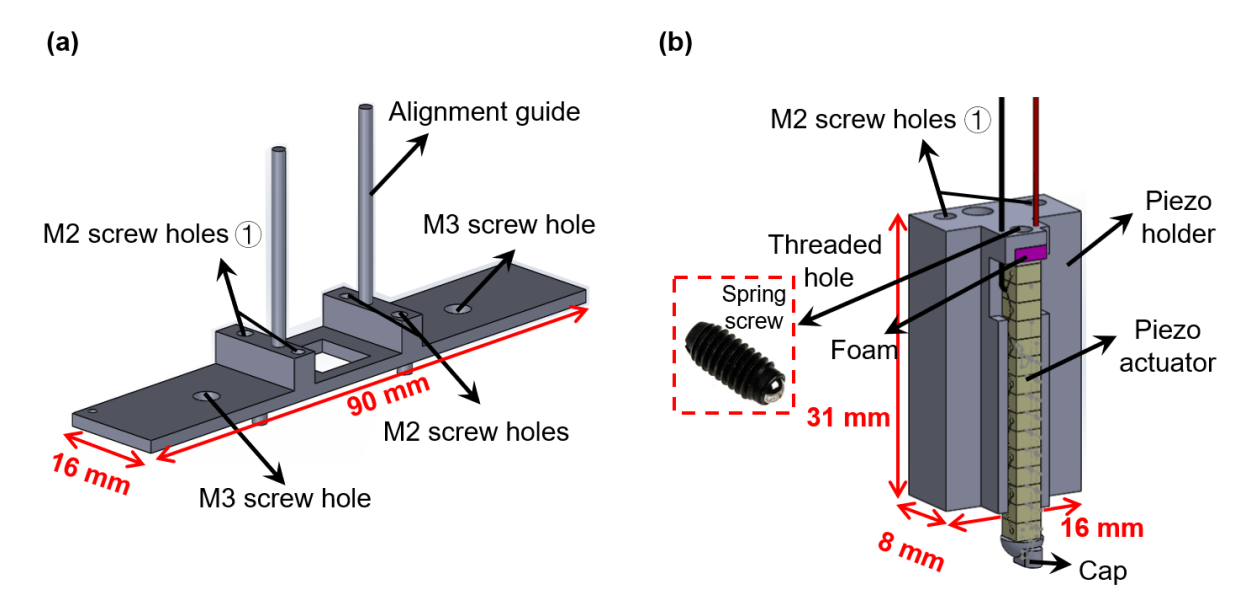


Figure 6.11 (a) Detailed illustration of metal cover. Two rods are used as alignment guides and secure the piezo actuator assembly while maintaining precise vertical positioning of the actuator cap over the membrane pump. M3 screws mechanically couple the cover to the holder; M2 screws rigidly fix the actuator assembly. (b) Detailed illustration of piezo actuator assembly. It comprises a brass holder with a precision-machined slot for actuator housing. On top of the holder, there is a threaded hole for the spring screw to fix the actuator. The spring screw provides a preload for the actuator and the spring inside eliminates damping. Between the actuator and the spring screw, a small piece of foam is added as a buffer, preventing surface damage to the actuator caused by the spring screw. The cap is fitted to the hemispherical end and its flat underside is glued to a ball bearing (not shown) that touches the surface of the chip.

Figure 6.11(a) shows the metal cover which incorporates dual alignment rods that precisely constrain the piezo actuator assembly, ensuring vertical positioning accuracy of ±2 mm for the actuator cap (glued to a 1.5mm diameter ball bearing) relative to the on-chip membrane pump. M3 screws mechanically couple the cover to the holder, while M2 screws rigidly fix the actuator assembly through holes at position ①.

Figure 6.11(b) shows the piezo actuator sub-assembly, comprising a brass holder with machined slots for actuator housing. The preload and elimination of mechanical damping were achieved by using a spring screw to fix the actuator in the holder with a piece of foam between the actuator and the spring screw to prevent damage.

6.2.3 Sorting chip design and fabrication

Critical to the functionality of this system is the integration of the membrane pump-based sorting mechanism within the microfluidic architecture. This section describes the design and fabrication processes of the pump sorter.

6.2.3.1 Prototype design

The prototype microfluidic architecture was experimentally validated before including electrodes within the microchannel. This design is shown in **Figure 6.12**.

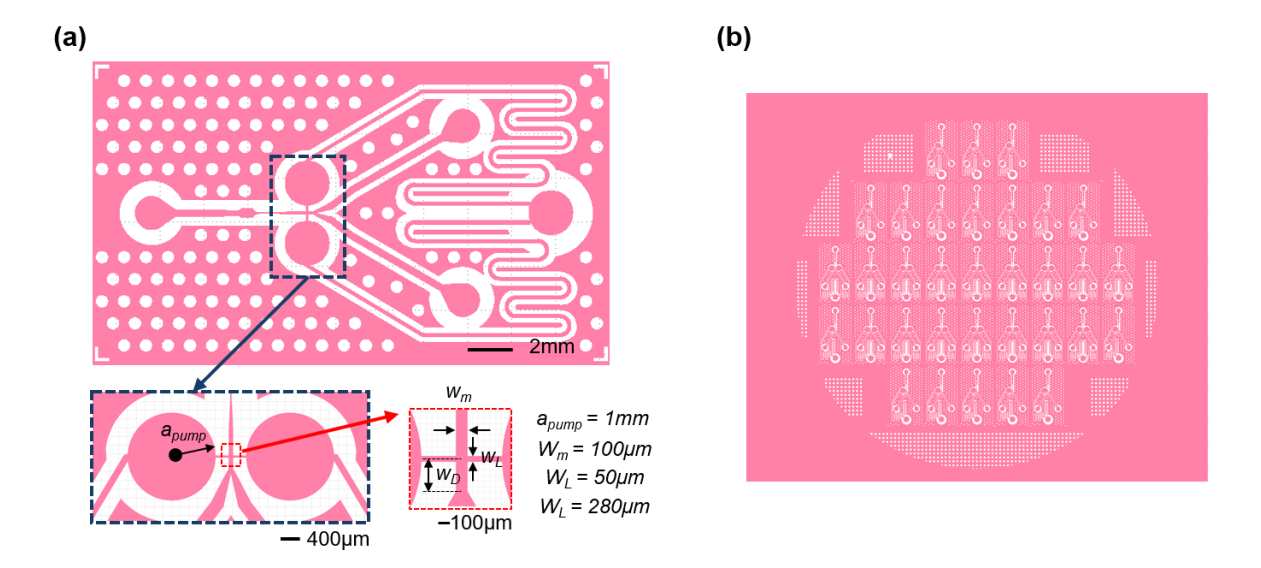


Figure 6.12 The design of the sorting chip without electrodes. (a) The features in pink define the fluidic layer. Dimensions of the sorter: radius of the chamber $a_{pump} = 1$ mm, main channel width $w_m = 100 \mu m$, sorting channel width $w_L = 50 \mu m$, distance between the centre of the sorting channel and the outlet junction is $w_D = 280 \mu m$. These dimensions are the same as used for the simulation in **section 3.6**, with the exception of w_D , which has no effect on sorting performance. The serpentine microchannels provide sufficient flow resistance, preventing local flowback. (b) Wafer layout.

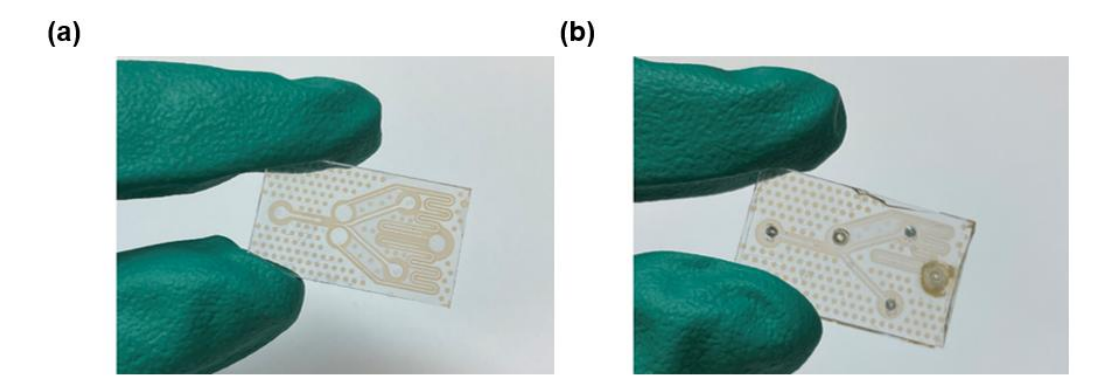


Figure 6.13 Photograph of the chips. There are two different designs, (a) one has dual membrane pumps and (b) the other one has single membrane pump.

Experiments with prototype chips were performed using polystyrene beads suspended in 0.5% w/v methylcellulose (MC) solution. Images of chips are shown in Figure 6.13. Two distinct design configurations were developed: a dual-membrane-pump and a single-membrane-pump. Optical tracking was used to plot the trajectories of beads in the main channel. Bead movement when using the single-membrane-pump is shown in Figure 6.14. The trace in Figure 6.14(d) shows that the bead was deflected by the local flow, but the bead returned to its original path. The dual-membrane pump design did not show this unexpected situation, see section 6.3.1. Additionally, given the high costs associated with mask fabrication, the single-pump configuration was excluded from the revised mask design to maximise wafer mask space utilisation efficiency and mitigate experimental failure risks.

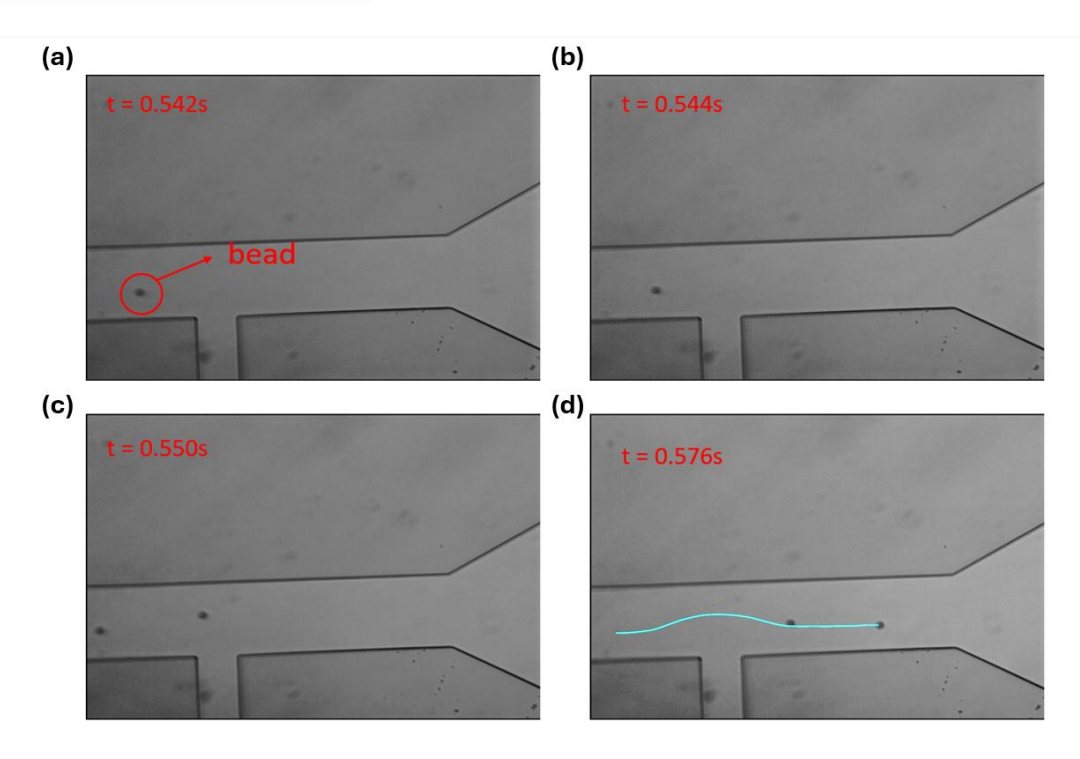


Figure 6.14 The frames of bead movement using a single-pump prototype sorting chip. (a-c) Specific frames of the bead position. The blue line in (d) is the trace of the bead from t = 0.542 s and t = 0.576 s. It is clear to see that after a subtle deflection, the beads returned to its original path when using the single-pump chip.

6.2.3.2 Final design

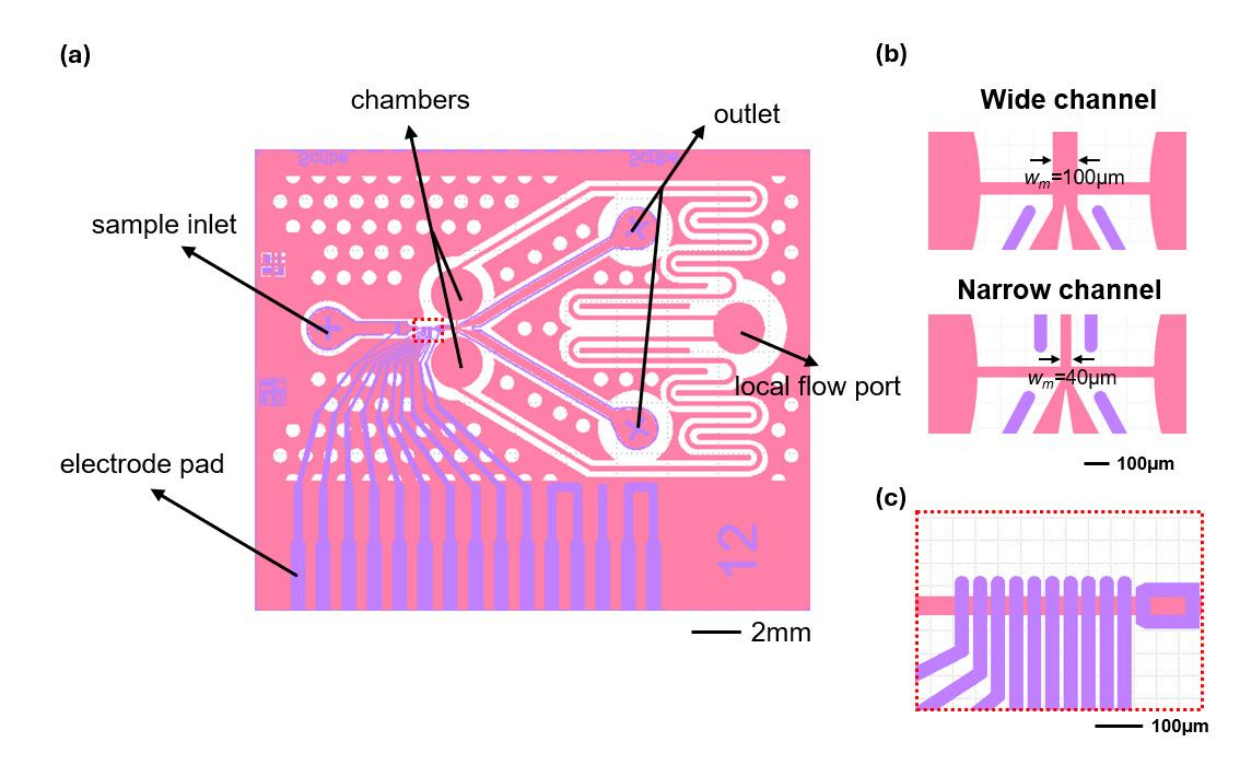


Figure 6.15 (a) Mask design of the final version of the chips. This version integrated the electrodes (purple region). The features in pink are fluidic regions. (b) There are two different designs with the main channel width w_m = 100µm (wide channel) and w_m = 40µm (narrow channel). The distance between the centre of the sorting channel and the outlet junction w_D was shorten to 80µm because the simulation in **Chapter 3** shows w_D has no significant influence on the sorting performance. (c) The electrode array consists of 10 electrodes 30µm in width and 10µm gap.

Following validation of the sorting mechanism, the electrode array was integrated into a final chip design (**Figure 6.15(c**)). The array consists of 10 electrodes with an optical detection region. The width of electrodes are 30µm and the gap 10µm. As shown in **Figure 6.15(a**), the serpentine microchannels around the outlets connect the local flow ports with the membrane pump chambers, providing pre-packaging flow before the chips are installed into the holder. The processes of pre-filling the chamber via the local flow port is described in **Figure 6.17**.

The electrode pads are connected to the spring connectors to ensure electrical continuity. In one wafer mask design, there are two different designs with the main channel width $w_m = 100 \mu m$ (wide channel) and $w_m = 40 \mu m$ (narrow channel).

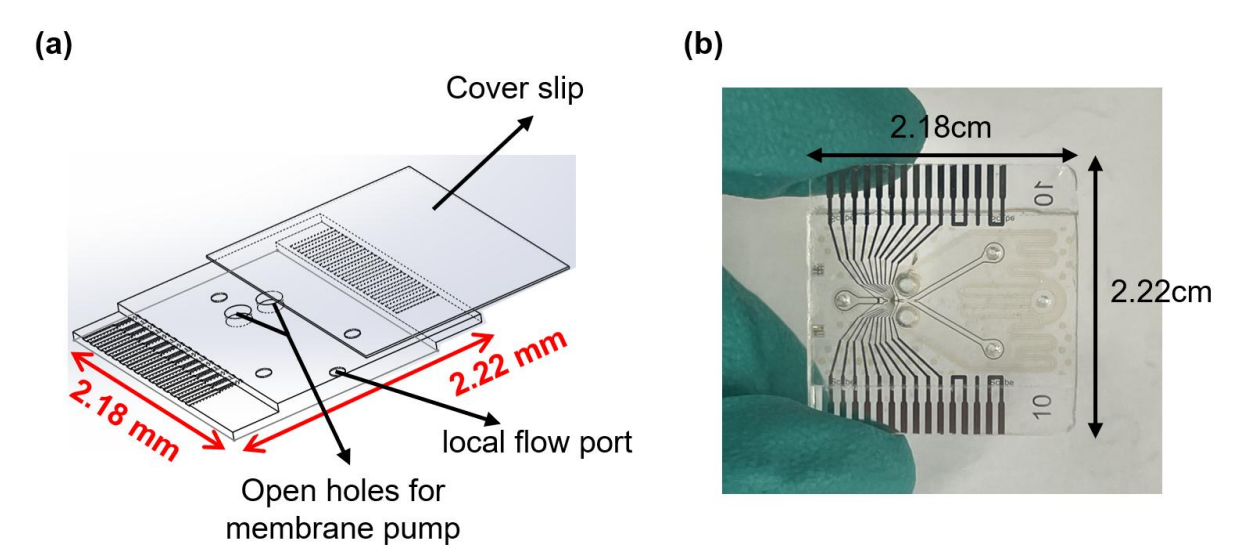


Figure 6.16 (a) Schematic of the MIC sorting chips with internal microchannel networks and electrode arrays omitted. Two holes are drilled in the pump chamber with a laser cutter. A 170 μ m thick cover slip was bonded to the glass sealing the holes and producing the deformable membrane. The inlet/outlet ports and local flow port are drilled on the reverse surface of the chip. (b) Image of a chip.

Figure 6.16(a) shows the final MIC sorting chip. Two holes on top of the membrane chambers were drilled by a laser cutter and a 170 μm thick cover slip was bonded to the underlying glass to act as the deformable membrane. On the reverse side of the chip, inlet/outlet and local flow ports were drilled and interconnected to the fluidic pipelines. The local flow port was integrated with a normally closed valve to ensure no leak during the experiments. Figure 6.16(b) shows the final version of the sorting chip with dimensions of 2.18×2.22cm.

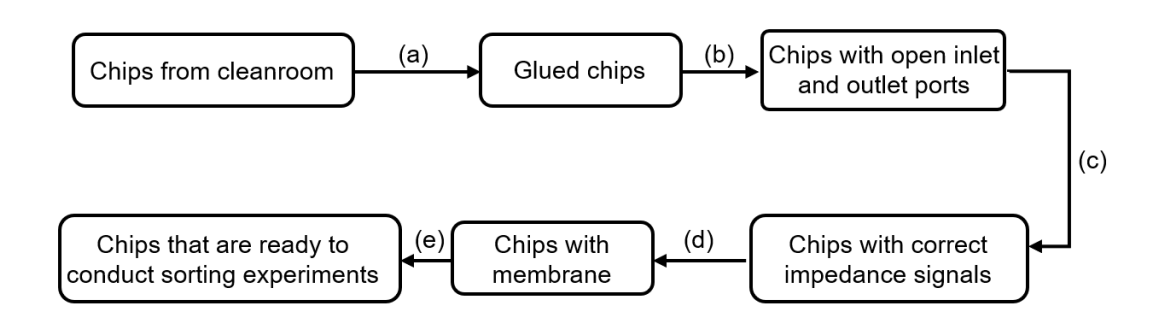


Figure 6.17 The flow chart of post-processing chips after fabrication in the cleanrooms. Details are described in the text.

Figure 6.17 shows a flow chart of the post-processing for cleanroom fabricated chips.

(a) Chip gluing

After fabrication, the chips were glued with vacuum-assisted capillary filling of thermosetting epoxy adhesive (EPO-TEK 301, EPOXY TECHNOLOGY)

(b) Holes drilling

The glued chips are placed in the laser cutter (Mini 18, Epilog Laser) to drill holes for inlet/outlet and local flow ports.

(c) Chip cleaning

After mounting in the holder, the electrodes were cleaned by flushing 2-4 mL of 4M NaOH solution at 20 µL/min.

(d) Glass membrane bonding

After cleaning, holes were made in the glass for the pump membranes, allowing the chambers to be filled with liquid and ensuring no air between the cover slip membrane. Coverslips were bonded with UV adhesive (NOA81, Norland Products) and exposed to UV for 15 mins.

(e) Local flow loading

The chips need priming with liquid before use. To do this a chip was placed in a petri dish containing PBS, with the liquid level only covering the local flow port, while all other ports remain exposed to air. The petri dish and chip were placed in a vacuum desiccator, creating a pressure difference, causing the PBS from the petri dish to be drawn into the membrane pump. The chip was then installed into the holder, and the piezo actuator assembly was mounted.

When making holes for the membrane pumps, if they are not aligned perfectly, the piezo actuator may not target the centre of the membrane pump and the deflection of the membrane may be reduced. Misalignment may break the main channel, because the distance between the main channel and the membrane pump is only $350 \, \mu m$.

When coating the UV adhesive on the surface, particular attention must be devoted to preventing capillary wicking along the perimeter of microfluidic orifices. Otherwise, after curing, the main channel is blocked, and the chip becomes unusable.

6.3 Experiment Setup

The experiments include two stages, bead sorting based on size and cell sorting based on deformability using low frequency impedance signals (500kHz).

6.3.1 Sample preparation

The first stage experiment aimed to sort 6μm (CAT No: 19111-2, Fluoresbrite® PC red microspheres (525/565), Polyscience Inc.) from 10μm (FluoSpheres Polystyrene Microspheres, orange fluorescent (540/560), Thermo Fisher) fluorescent beads. The samples were suspended in viscoelastic methylcellulose-DPBS media (MC-DPBS, 0.5%w/v). Untreated and fixed HL60 cells were used as cellular deformability models. The GA concentration was set to 1% v/v. The cell concentration was adjusted to 2.5×10⁵ cells/mL, suspended in 0.5%w/v MC. All samples were loaded into 1.5mL Eppendorf tubes.

6.3.2 Sorting process

To begin the sorting, the chip was fixed in the chip holder. The actuator assembly was carefully mounted on the guide rod of the metal cover and fixed with two M3 screws. During installation the ball bearing at the actuator base was brought into light contact with the membrane surface without misalignment. Before pumping the sample, the main channel was flushed with DI water to remove debris. The inlet was connected to the tube containing the sample, and two outlets connected to 1.5mL Eppendorf tubes. Then three ports were pressurised and the pressures adjusted to flow all the particles into the "upper outlet" (see Chapter 3 Figure 3.33), defined as the "Ready to activate" state.

Once the high-voltage amplifier was switched on, the sorting system entered the "Activated" state. Sorting efficiency of beads was determined using video of particle trajectories, whereas the cell mixture was assessed the by counting cells using a commercial flow cytometer (Attune NxT, ThermoFisher). The fluorescent bead experiments did not require consideration of the dead volume, which is the volume of liquid that flowed from the upper outlet when the system was in "Ready to activate" state. In the cell experiments, this dead volume consisted of both untreated and fixed cells and may cause inaccurate results in the flow cytometry test. To solve this problem, the pipe connected to the upper outlet was cut as short as possible. After operating in the "Activated" state for 15 minutes, the upper outlet suspension in the Eppendorf tube was removed, and the effluent used for assessment.

6.4 Sorting Evaluation Result

6.4.1 Fluorescence beads test

Chips with two different channel widths (40 μ m and 100 μ m) were tested, together with pulse widths of 2ms, 1.5ms and 1ms. The piezo actuator driving voltage was set to 100 V, delivering the maximum displacement of 100 μ m. The throughput of the system was around 13 particles/s and samples with two different ratios of the beads were measured.

Counting of different beads was done by image analysis. Fluorescent images in the dark field were converted to binary images with pixel values of 0 or 1. By evaluating the sum of pixel values in the ROI of the upper or lower outlet, the bead size and number was determined.

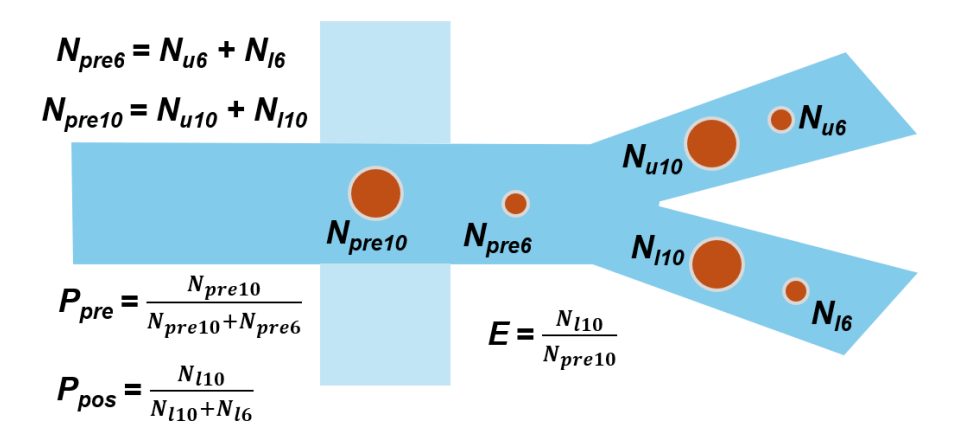


Figure 6.18 Definition of the efficiency and purity used to evaluate the system performance. E is the efficiency; P_{pre} and P_{pos} are pre-sorting and post-sorting purity. N_{pre6} and N_{pre10} are the numbers of 6 μ m and 10 μ m beads before sorting, respectively. N_{u6} and N_{u10} are 6 μ m and 10 μ m beads directed to the upper outlet; N_{l6} and N_{l10} are 6 μ m and 10 μ m beads directed to the lower outlet.

The sorting efficiency and purity were used to quantify the performance of the system, as in **Figure 6.18**. The purity (P) is defined as $P = \frac{N_i}{N_{sum}}$. N_i is the number of sorted beads (10µm), and N_{sum} is the total number of beads. Therefore, the pre-sorting purity (P_{pre}) is calculated from the ratio of the total number of 10µm beads directed to upper and lower outlets (N_{pre10}) to the total number of 6 µm and 10µm beads directed to upper and lower outlets ($N_{pre10}+N_{pre6}$). The post-sorting purity (P_{pos}) is the ratio of the number of beads (10µm) that were correctly sorted (N_{l10}) to the total number of 6µm and 10µm beads that were directed to the lower outlet ($N_{l10}+N_{l6}$). The sorting efficiency (E) is defined as the ratio of the number of correctly sorted beads (N_{l10}) to the total number of beads (N_{pre10}). Note that N_{pre6} and N_{pre10} were obtained by calculating the sum of wanted beads: $N_{pre6} = N_{l6} + N_{u6}$; $N_{pre10} = N_{l10} + N_{u10}$.

Tests were initially conducted using the wide channel sorting chips. The pressure and bead concentration was the same in each trial. The performance of the sorter was tested using different ratios of 10 μ m and 6 μ m beads and varying the pulse width of the driving voltage of the piezo actuator. The ratios N_{pre10} : N_{pre6} were 3:2 and 2:3: one example with target particles (10 μ m bead) greater than non-target particles (6 μ m bead), and the other where target particles fewer than non-target particles. The pulse width of the driving voltage was set to 1 ms, 1.5 ms and 2 ms. The voltage magnitude remained the maximum at 100 V.

Due to the significant difference in the impedance magnitude (real part 500kHz) of the beads (see **Figure 6.4**), the trigger for the sorter was determined simply by recognising if the first peak of the event exceeded a threshold.

Data from the experiments is shown in **Figure 6.19**, and summarised in **Table 6.1**. In both experimental groups with different N_{pre10} to N_{pre6} ratios, the sample purity showed a significant improvement, increasing from approximately 60% and 40% pre-sorting to around 97% post-sorting, respectively.

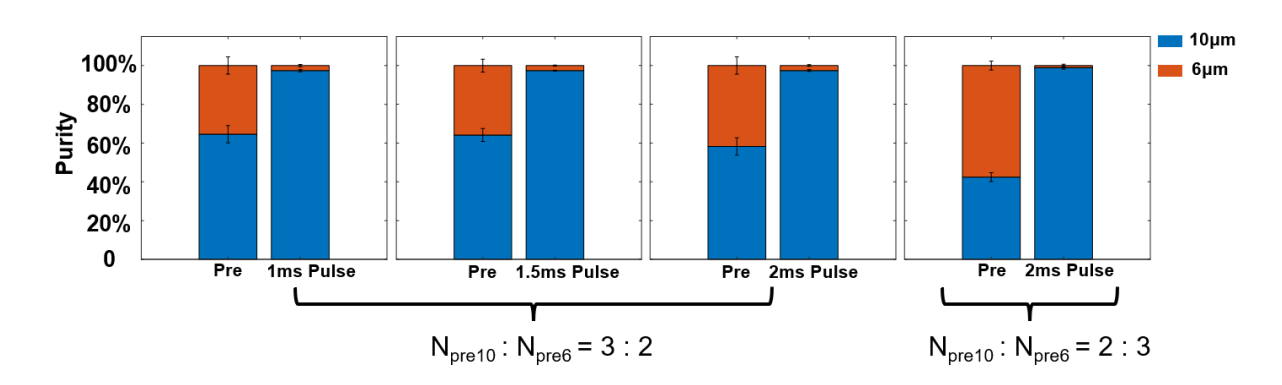


Figure 6.19 Wide channel purity for two different N_{pre10} to N_{pre6} ratios with different pulse widths of actuator driving signal. The purity increased from around 60% (N_{pre10} : N_{pre6} =3:2) and 40% (N_{pre10} : N_{pre6} =2:3) to approximate 97%. Data are summarised in **Table 6.1.**

Table 6.1 Purity of $10\mu m$ beads with two different ratios of N_{pre10} to N_{pre6} and different pulse widths. The data was plotted in **Figure 6.18**.

Purity (10µm bead)				Repeat 1	Repeat 2	Repeat 3	mean±SD
N _{pre10} : N _{pre6}	3:2	1ms pulse	Pre-sorting	61%	64%	70%	64%±4.5%
			Post-sorting	97%	97%	98%	97%±0.6%
		1.5ms pulse	Pre-sorting	61%	67%	64%	64%±3.3%
			Post-sorting	97%	98%	97%	97%±0.3%
		2ms pulse	Pre-sorting	62%	60%	53%	58%±4.5%
			Post-sorting	97%	0.97%	98%	97%±0.5%
	2:3	2ms pulse	Pre-sorting	42%	41%	45%	42%±2.3%
			Post-sorting	99%	98%	99%	99%±0.7%

Changing the driving pulse width had no obvious effect on the post-sorting purity. This demonstrated that the algorithm accurately identified bead size and gave precise timing predictions, so that the 10 μ m target beads were deviated within the sorting region while the 6 μ m beads remained unaffected. As a result, particles successfully flowing through the lower outlet were almost exclusively 10 μ m beads. The pulse width modulates the magnitude of the sorting force exerted on beads within the sorting region and determines whether their deviation from the original trajectory is sufficient to reach the lower outlet. This parameter directly impacts separation efficiency (**Figure 6.20**).

Chapter 6

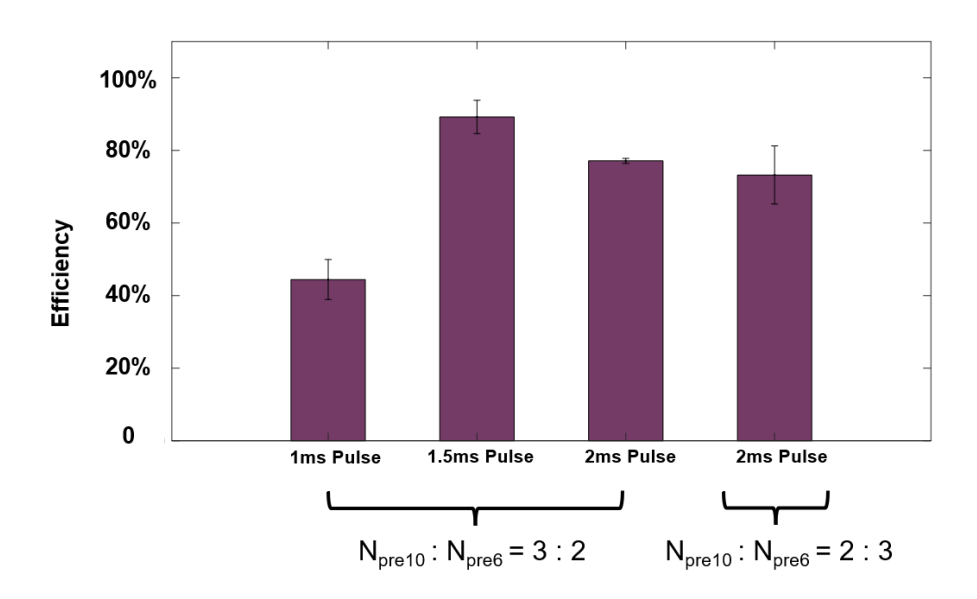


Figure 6.20 Sorting efficiency ($E = N_{l10}/N_{pre10}$) of the 10µm beads under different conditions including two distinct N_{pre10} to N_{pre6} ratios (3:2 and 2:3) and different pulse width. It was achieved above 70% by using 1.5 ms and 2 ms pulse width, while under the 1 ms pulse width condition, the sorting efficiency showed a significant drop, falling below 50%. The data is summarised in **Table 6.2.**

Table 6.2 Sorting efficiency for $10\mu m$ beads with two different ratios of N_{pre10} to N_{pre6} and different pulse widths. The data is plotted in **Figure 6.19**.

Efficiency (10µm bead)			Repeat 1	Repeat 2	Repeat 3	mean±SD
N _{pre10} :N _{pre6}		1ms pulse	43%	40%	51%	44%±5.5%
	3:2	1.5m pulse	84%	92%	92%	89%±4.6%
		2ms pulse	77%	77%	78%	77%±0.7%
	2:3	2ms pulse	64%	78%	78%	73%±8.0%

Figure 6.20 and Table 6.2 show that the efficiency of sorting was correlated with the driving pulse width. When the pulse width was set to 1.5 ms and 2 ms, the sorting efficiency was above 70%. In contrast, if the pulse width was 1 ms, the efficiency decreased to less than 50%. This occurs because the 1 ms pulse results in insufficient duration of the actuator to maintain its maximum displacement position. Consequently, the pressure generated by the membrane exerts only a short-time influence on the local flow, ultimately reducing the volume of local flow deflected from the sorting channel. This limitation prevents any changed in particle trajectories within the main channel.

Narrow channel MIC sorting chips were also tested. For the conditions of N_{pre10} : N_{pre6} = 2:3 and a driving voltage pulse width of 2 ms, the sorting purity increased from 38.7%±1.4% to 98.6%±0.4%

(mean±SD) as **Figure 6.21** shows. The data of the three repeats was summarised in **Table 6.3**. The sorting efficiency was 71.9%±2.5%.

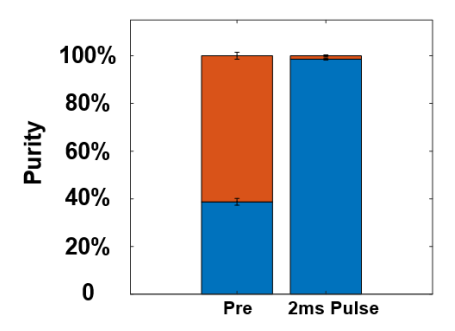


Figure 6.21 Narrow channel purity when N_{pre10} to N_{pre6} ratio was 2:3 with the pulse widths of the actuator driving signal 2 ms. The values are summarised in **Table 6.3**.

Table 6.3 The purity for 10 μ m beads with the ratio of N_{pre10} to N_{pre6} 3:2 and 2 ms pulse widths. The data was plotted in **Figure 6.21**.

Purity (10µm bead)			Repeat 1	Repeat 2	Repeat 3	mean±SD
N _{pre10} :N _{pre6} =2:3	nulse	Pre-sorting	40%	39%	37%	39%±1.4%
принимания		Post-sorting	98%	99%	99%	99%±0.4%

Figure 6.22 shows images fluorescent 10 μ m bead having been triggered successfully and flowing toward the lower outlet in a narrow channel chip. Due to the low frame rate of the camera, a high-speed 10 μ m bead appears as a bright streak rather. At t=4 ms, the bead was triggered to deflect it towards the lower outlet and its velocity decreased. At t=32 ms, a 6 μ m bead started to appear in the image as a darker streak, and at t=36 ms, it entered the upper outlet without being sorted.

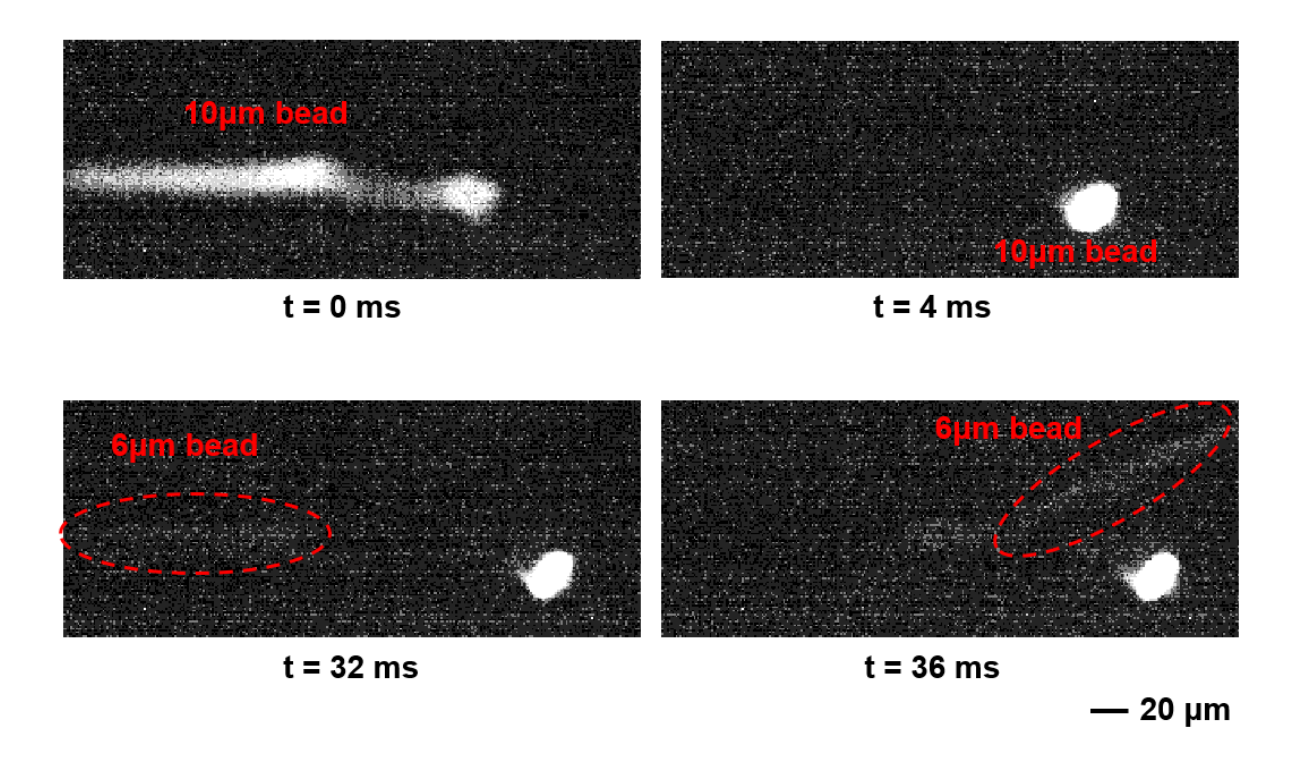


Figure 6.22 Example images of a sorting a $10\mu m$ bead towards the lower outlet. At t=32 ms, a $6\mu m$ bead entered the channel without being sorted. The system applied the 2ms pulse width driving voltage.

In summary, the fluorescent bead tests demonstrated efficient sorting with at a throughput of 13 particles/s, the post-sorting purity of around 97%.

6.4.2 Cell deformability sorting

The second experiment involved sorting based on cell deformability. HL60 cells with or without GA treatment were measured using a narrow channel MIC chip. The performance of the algorithm for Real-time electrical deformability (Real-time ED) sorting was evaluated. Real-time ED was used to characterise the mechanical properties of cells. Compared to offline analysis, real-time data processing requires immediate action, so that time-consuming convolution with complex templates is impractical. A Finite Impulse Response (FIR) filter was used as an alternative to enhance or suppress specific frequency components through a weighted moving average of input signals, and accomplish signal de-noising in real-time. The raw impedance (real part at 500kHz) was sent to the MCU and sampled by the ADC, then prior to peak detection, the data stream was filtered by a custom FIR. The FIR results for 10 µm beads, untreated HL60 cells and fixed cell are shown in Figure 6.23. As for the raw impedance data, the output has two peaks (pk1 and pk2) from electrode configuration 1 and 2. The Real-time ED is defined as the ratio of peak 1 to peak 2 so for a 10µm bead. The values of peak 1 and peak 2 detected by the algorithm were 0.55 and 0.35, so that the Real-time ED was 1.59 (Figure 6.23(a)). A fixed cell with pk1, pk2, and Real-time ED values of 0.54, 0.34, and 1.61, respectively, closely resembles a bead (Figure 6.23(c)). In contrast, an untreated cell has a higher Real-time ED (2.37) with pk1 and pk2 values of 0.46 and 0.19 (Figure

6.23(b)). This is consistent with the optical and electrical deformability analysis of untreated and fixed cells in **Chapter 4**. Rigid spherical particles have lower Real-time ED values compared to softer ones, such as untreated cells.

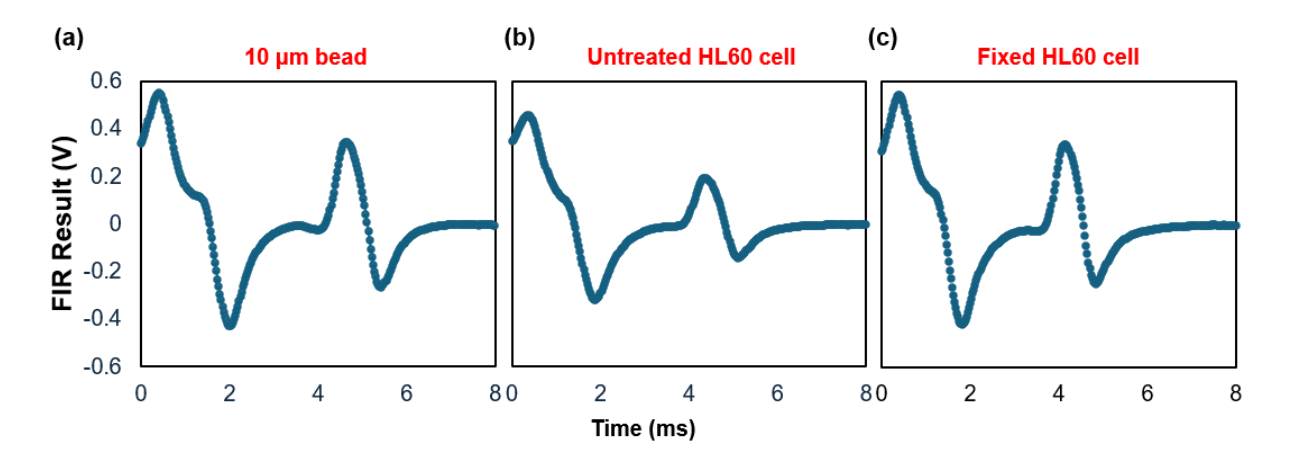


Figure 6.23 Signal output from the MCU serial port after the raw impedance signal was filtered by a custom FIR for (a) $10\mu m$ bead, (b) untreated HL60 cell, (c) fixed HL60 cell. Each signal has two peaks, from electrode configuration 1 and 2. The peak detection results from the MCU were: (a) pk1 is 0.55, pk2 is 0.35, real-time ED is 1.59; (b) pk1 is 0.46, pk2 is 0.19, real-time ED is 2.37; (c) pk1 is 0.54, pk2 is 0.34, real-time ED is 1.61.

Before sorting untreated and fixed cells, a uniform suspension of 10 µm plain beads was measured to set the threshold for the Real-time ED. As **Figure 6.24** shows, pk1, pk2 and Real-time ED of beads were collected from the MCU via the serial output port, then the data was post-processed. First, the main population of the beads in the scatter plot of pk1 versus real-time ED was gated as shown in **Figure 6.24(a)**. Then, the mean Real-time ED was calculated to a threshold. In this example, the threshold was 1.68.

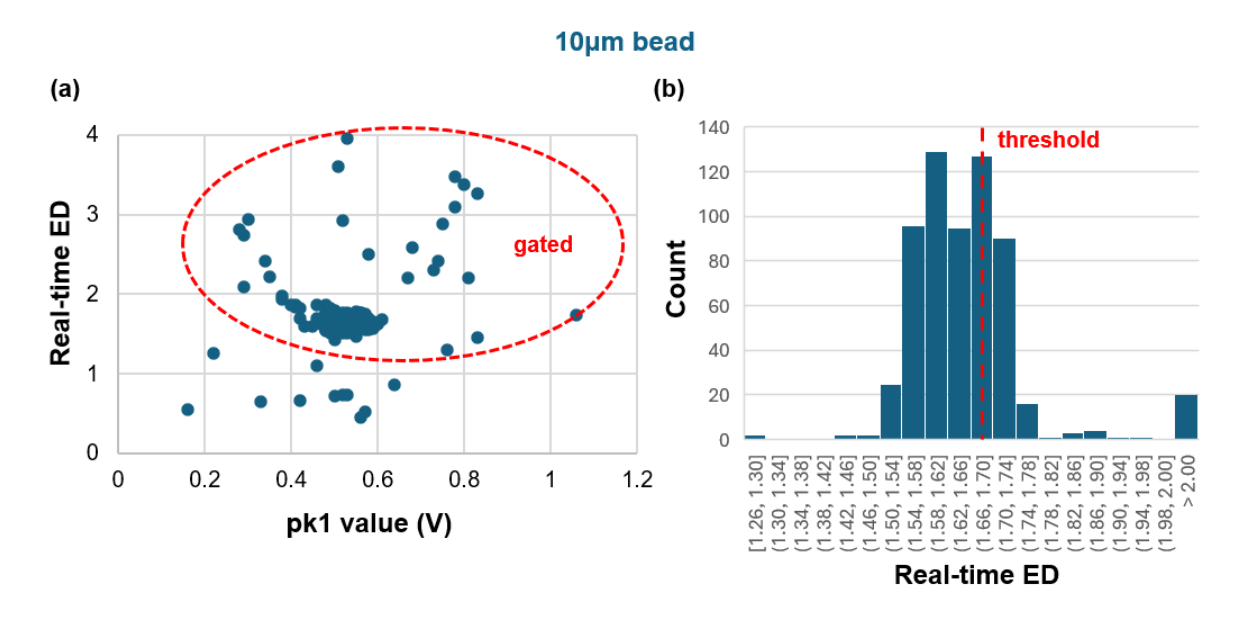


Figure 6.24 Real-time ED evaluation of beads used to set a threshold for sorting. (a) Scatter plot of pk1 versus Real-time ED. Cells in the red circle were gated (614 beads) to do further analysis. (b) The Real-time ED distribution of gated beads. Threshold (dashed red line) is the mean Real-time ED value of the gated beads (1.68), with 78% of beads exhibiting a lower Real-time ED than 1.68.

Figure 6.24(b) shows a histogram of the Real-time ED of gated beads. The red dashed line is the threshold. 78% of gated beads had a Real-time ED less than 1.68. It indicates that if the interested events have a Real-time ED less than the threshold, the MCU algorithm that calculates Real-time ED has a 78% detection efficiency. To assess the threshold for cells, a suspension of untreated and fixed HL60 cells were measured. Figure 6.25 is a scatter plot of pk1 versus Real-time ED for untreated cells, with the bead data in Figure 6.24(a) superimposed. For the same threshold, if the discrimination criterion was set to "Real-time ED that above threshold", 95% of gated events could be identified correctly by the Real-time ED detection algorithm. (936-53/936=5%)

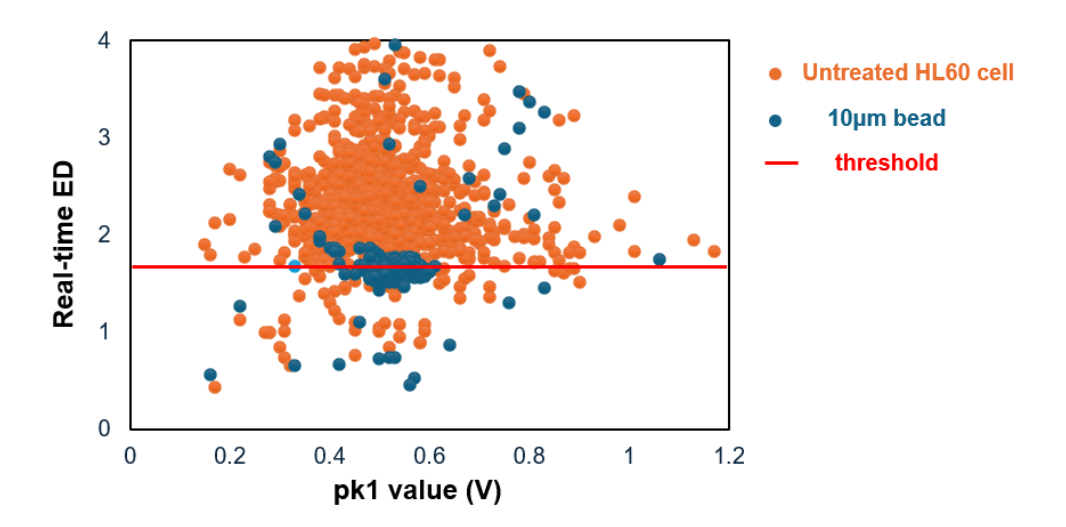


Figure 6.25 Scatter plot of pk1 versus Real-time ED for untreated cells (orange dots). The bead population (dark blue dots) in **Figure 6.21(a)** overlaps. The red line is the threshold obtained from the beads assessment in **Figure 6.21**.

Figure 6.26 shows a scatter plot of pk1 versus Real-time ED for fixed cells collected from the serial output port, with the untreated cells in **Figure 6.25** superimposed. From the dose-response plots shown in **section 4.4.4**, GA at concentrations higher than 0.1% v/v can stabilise cell deformability to a plateau value, matching the deformability of rigid spherical beads. Therefore, when cells were treated with 1% v/v GA, the real-time ED should align with that of the beads. The fixed cell population exhibits a broader distribution along both x- and y-axes compared to beads, with a broader y-axis distribution propagating errors in the algorithmic determination of real-time ED values for fixed cells.

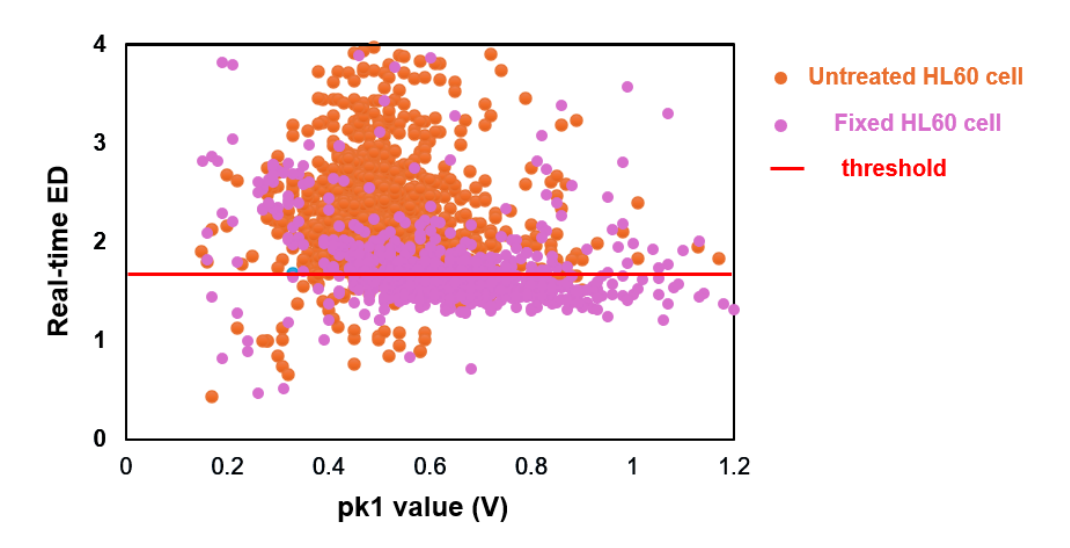


Figure 6.26 Scatter plot of pk1 versus Real-time ED for fixed cells (pink dots). The untreated cell population (orange dots) in **Figure 6.23(a)** overlaps. The red line is the threshold obtained from the beads assessment in **Figure 6.22.**

Figure 6.27 shows a histogram of the Real-time ED for fixed cells - the y-axis data of Figure 6.26. The total number of fixed cells is 843, and the number of fixed cells with Real-time ED less than the threshold is 491, meaning that 58% of fixed cells were recognised by the real-time algorithm. Returning to Figure 6.26, it is clear that increasing the threshold enhances the detection efficiency of the algorithm for fixed cells, but for a sorting an untreated/fixed cell mixture, it would lead to mis-incorporation of untreated cells into the target population, thereby compromising sorting purity.

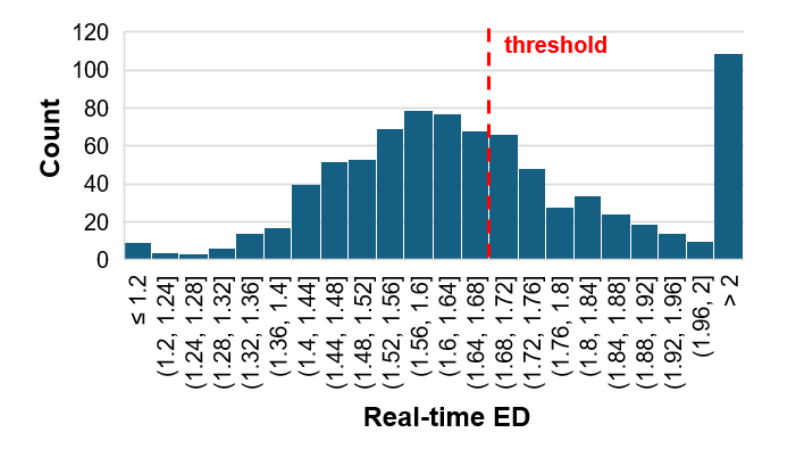


Figure 6.27 The distribution of Real-time ED for gated fixed cells shown in **Figure 6.26**. The discrimination criterion was set to "Real-time ED that below threshold". 58% of fixed cells were identified by this condition.

Figure 6.28 shows example images of a bead in the "Ready to activate" state. The frame rate of the CMOS camera was set to 500 fps, the maximum value that this camera can achieve without frame dropping. Rapidly moving beads in the image field manifest as temporal smearing artifact.

For better presentation, a false colour bead was placed on top of the images. The particles in this state were all directed to the upper outlet.

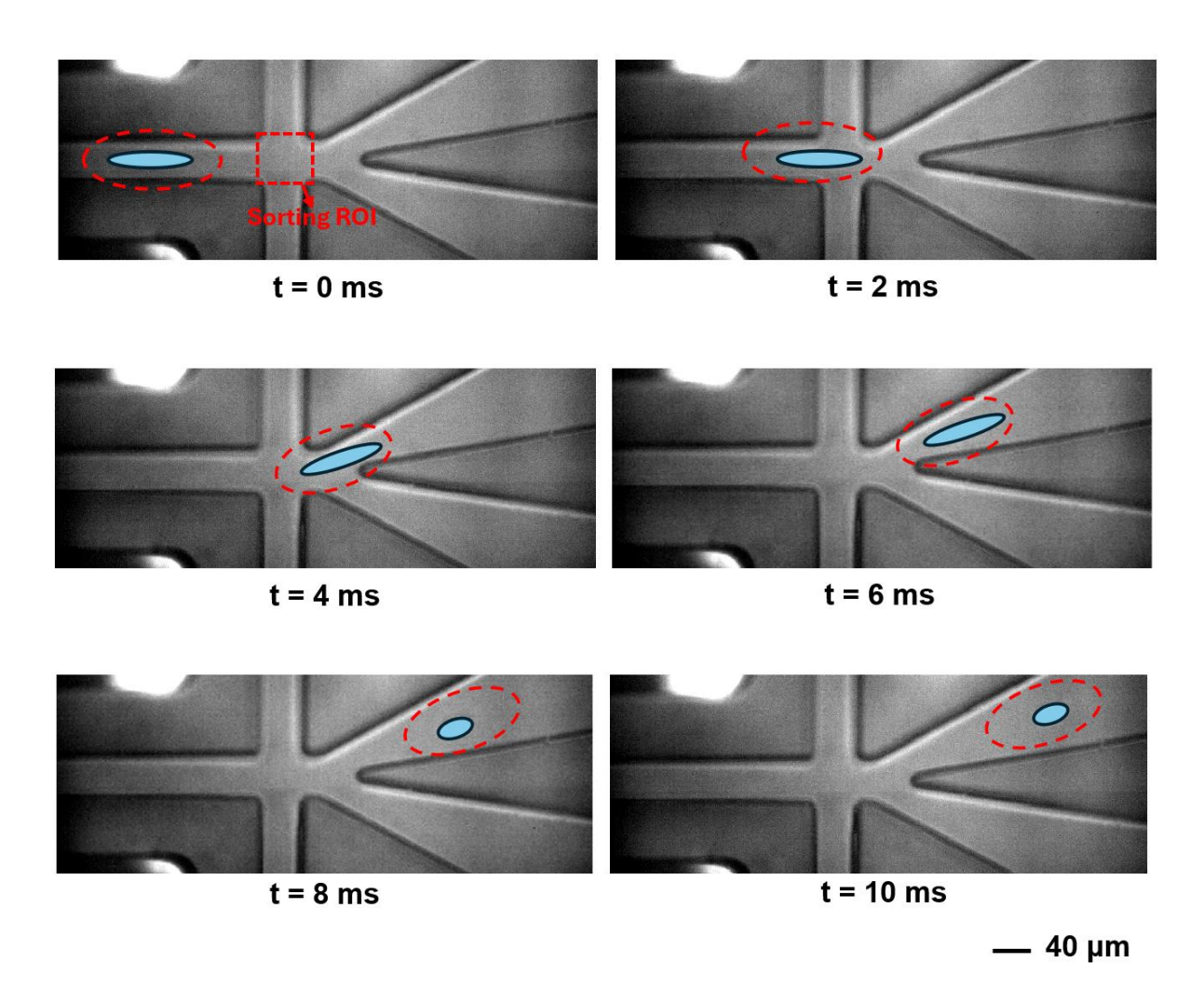
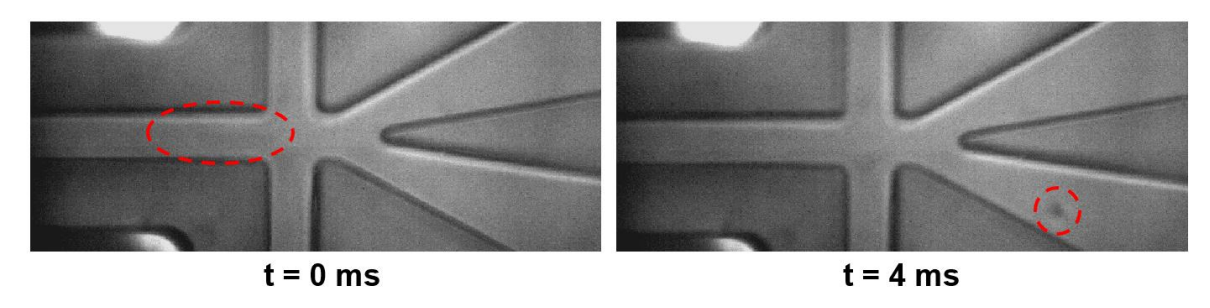


Figure 6.28 Images of an example bead in "Ready to activate" state. The bead is circled with the red dashed lines and directed to the upper outlet.

Figure 6.29 shows images of two different beads with different velocities. Due to the low frame rate of the camera, the complete trajectory of bead displacement was not recorded. At t = 0 ms, bead 1 and bead 2 approach the sorting ROI (shown in **Figure 6.28**). After 4 ms and 6 ms respectively, bead 1 and bead 2 were shown in the lower outlet, meaning successful sorting was achieved.

(a) Bead 1



(b) Bead 2

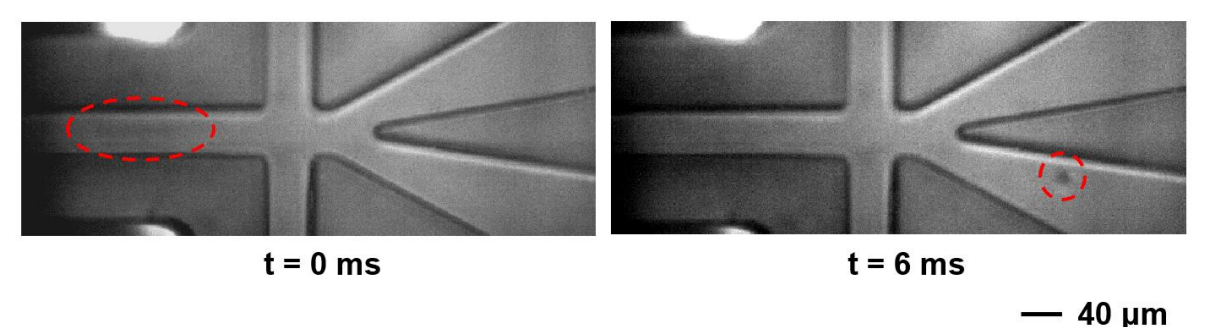
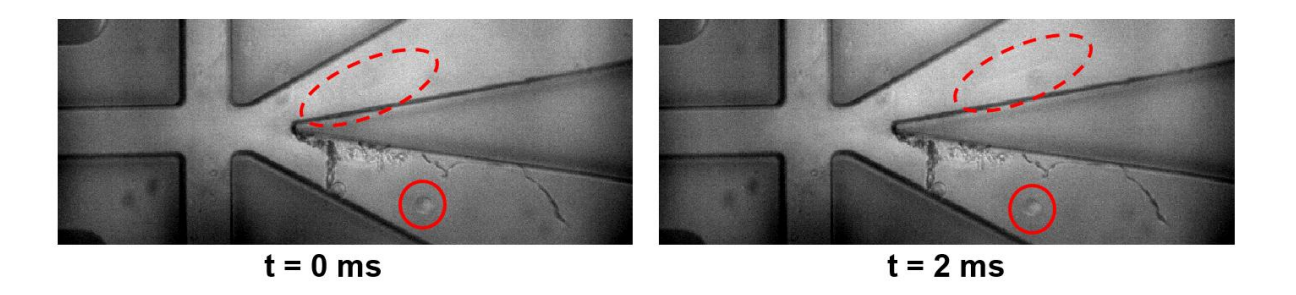


Figure 6.29 Beads in "Activated" state. (a) and (b) are two example beads with different velocities. At t = 0 ms, beads were approaching the sorting ROI and successfully being sorted at t = 4 ms and 6 ms respectively.

After estimating the Real-time ED from the serial output port of the MCU for beads (with reference to set the threshold), the untreated/fixed cell mixture was measured. This time, pre-sorting and post-sorting purity were examined with a flow cytometer. The sorted cells were the fixed cells because they had a more consistent Real-time ED compared with untreated cells. The discrimination criterion was "Real-time ED less than threshold", meaning that the fixed cells should be sorted to the lower outlet. During operation of the microfluidic chip, the predominant flow is directed to the upper outlet, while target cells move to the lower outlet. The upper outlet liquid was collected to test because it took significantly less time to harvest a high yield of sorted cells, and the pre-sorting and post-sorting purity of untreated live cells were focused on downstream analysis.

Figure 6.30 shows example images of cell sorting. Compared with polystyrene beads, cells are more transparent under the same illumination conditions. Additionally, cells directed to the upper outlet had higher velocities, making them more difficult to observe. Nevertheless, untreated cells (circled with dashed red line) move with the main fluid toward the upper outlet, while a fixed cell (circled with solid red line) was sorted into the lower outlet.



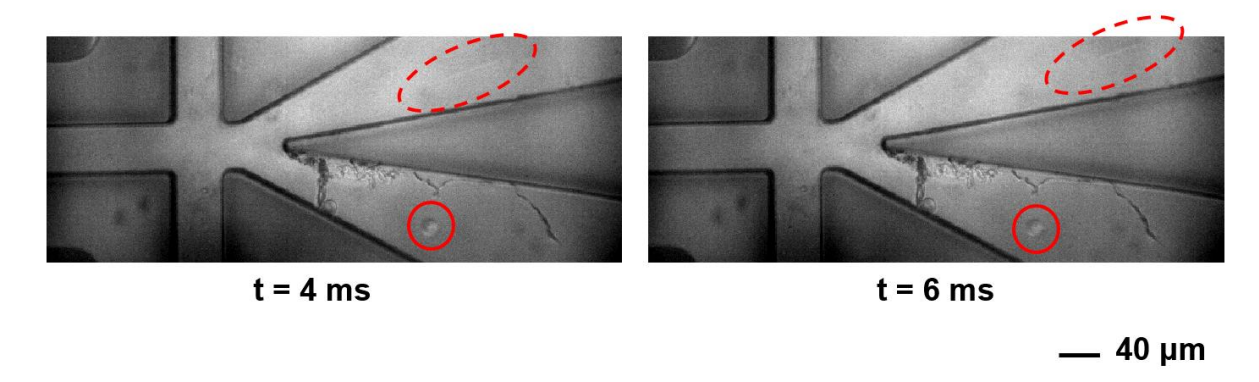


Figure 6.30 Images of an example sorting scenario that an untreated live cell (circled with dashed red line) is directed toward the upper outlet with high velocity, and a subsequent fixed cell (circled with solid red line) is sorted to the lower outlet. The cells are successfully sorted based in deformability.

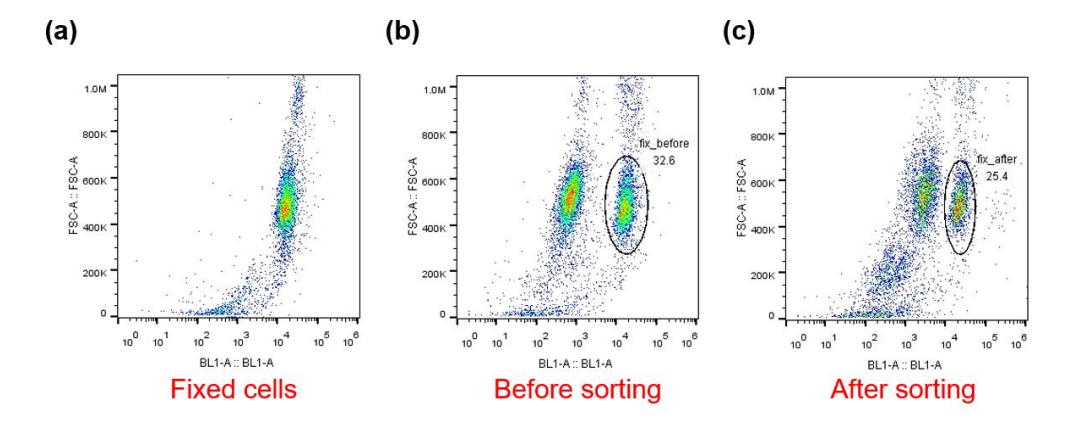


Figure 6.31 Results of commercial flow cytometer test. (a) The Forward scatter (FSC) in BL1-A channel of the fixed cells sample. The single population represented fixed cells. (b) The FSC in BL1-A channel of the untreated and fixed cell mixture before sorting. The circled subpopulation is fixed cells by comparing with (a). The percentage of this population is 32.6%. (c) The FSC in BL1-A channel of the upper outlet suspension after sorting. The percentage of fixed cells is decreased to 25.4%.

Finally, **Figure 6.30** shows the result from a commercial flow cytometer. A sample containing only fixed cells was measured as the control group (**Figure 6.30(a)**). The untreated and fixed cells mixture was measured before sorting, and the percentage of fixed cells was around 33% (**Figure 6.30(b)**). After sorting for 45 minutes (excluding a 15-minute dead volume purge), the suspension from the upper outlet was measured again and the percentage of fixed cells was decreased to 25%.

6.5 Discussion

This chapter illustrated the operational principle of a deformability MIC sorting system with the experimental results of bead and cell sorting. The system successfully integrated the sheath-less shear flow deformability MIC with an active particle sorter showing that fluorescence beads could be sorted with 97% post-sorting purity and > 70% sorting efficiency. Cell experiments with

untreated and fixed HL60 cells were used to remove fixed cells, lowering the proportion from 32% to 25%.

Both new software and hardware were developed and the system optimised by changing the electrode configuration to minimise the current offset and to facilitate real-time impedance processing. In the MCU program, the application of multiple threading solved temporal conflicts, increasing the trigger pulse rate. A reliable post-processing procedure for microfluidic chips was developed, enabling the integration of membrane pumps onto pre-fabricated MIC chips. The mechanical design of the system was optimised, enabling the external actuator that induces deflection in the membrane to be precisely aligned with the membrane pump within a confined space while achieving micrometre-level displacement transmission.

This sorting system showed a moderate sorting performance with beads but not for a cell mixture because the former experiments used a simple classification criterion: the peak values of the first configuration. However, cell sorting based on real-time electrical deformability was less efficient. The distributions in values for different subcellular populations was high, with substantial overlap, making it difficult to define a suitable threshold for discrimination. In the future, this limitation could be addressed by integrating neural networks to perform more comprehensive analysis of real-time impedance signals. By extracting additional parameters, such as the transit time, to characterise cells with varying deformability, classification efficiency could be significantly improved.

Chapter 7 Conclusions and Future Work

This thesis has described label-free methods for single-cell biophysical analysis and sorting based on the MIC technique. Cellular mechanical properties (e.g. deformability) and dielectric parameters (e.g. membrane capacitance and cytoplasm conductivity) were characterised using different designs of MIC. Proof of principle sorting was achieved by integrating a pump-sorter into the MIC. This chapter summarises the achievements and provides potential working directions for developing improved MIC systems for label-free single-cell biophysical analysis and sorting.

The deformability of cells was first analysed by MIC (**Chapter 4**). A novel electro-optical deformability system was developed to characterise the mechanical properties of single cells at a high speed using shear flow without contacting the microchannel. The electrical deformability was obtained from the shape change along two different axes measured by sets of integrated microelectrodes. Optical deformability was derived from single-cell contour in the optical images. This system synchronised the impedance signal of a cell with its optical image enabling comparison of the electrical and optical deformability. The key technique in this system is the LED triggering mechanism. Unlike traditional triggering that relies on fixed thresholds, this system calculated the velocity of each individual cell and assigned its predicted transit time when it appeared in the image detection region to trigger an LED. This approach significantly reduces the amount of image data requiring processing, thereby simplifying the optical analysis.

HL60 cells were treated with glutaraldehyde, cytochalasin D and latrunculin B. These chemicals alter the cytoskeleton of cells by different principles, leading to different deformability. Glutaraldehyde crosslinks proteins in the membrane so that the cells are fixed as rigid spheres which cannot be deformed by shear forces, and the deformability should be 1. Cytochalasin D and latrunculin B cause cytoskeleton disruption and prevent the assembly of actin filaments by different mechanisms. Cells become softer and more deformable, resulting in higher deformability compared with rigid spheres. Experiments show a very high correlation between both deformability methods and prove the feasibility of deformability MIC. The optical deformability was observed to be influenced by the position of the cells across the channel width. Due to the use of viscoelastic fluid, cells were partially focused into a plane in the centre of the channel. Although this simplified the system, it meant that some cells close to the channel wall were asymmetrically distorted, leading to errors in the optical images. This results in a positional dependence in the scatter data, which can be corrected by post-processing, excluding cells that flow close to the channel wall. Unlike optical deformability, electrical deformability appears to be much less affected by the position of the cells in the channel, which is also a convincing reason to use MIC for measuring deformability.

One possible future direction for deformability MIC is applying this for real-word clinical diagnostic. For example, there is solid evidence that the stiffness of cancer cells and immune cells reflects antitumour immune responses (Mittelheisser et al. 2024; Wang and Kelley 2025). Real-time optical deformability cytometry has been used to analyse the biomechanical differences in tissue (Soteriou et al. 2023). Inflammatory changes in colon tissue can be determined by this solid tissue biopsy method. This demonstrates the potential use of deformability cytometry as a rapid test for cancer diagnosis.

This thesis also explored single-cell dielectric analysis to determine the membrane capacitance and cytoplasm conductivity of individual cells (**Chapter 5**). The system utilised different electrode configurations to measure the impedance over a broad frequency range of up to 575MHz at a high throughput. This enabled a more comprehensive analysis of the dielectric spectrum of a nucleated cell, which cannot be achieved by previous studies. The frequency spectrum data was analysed with the double-shell model which includes the contribution of the nucleus to the equivalent dielectric properties.

Two different methods were used to obtain the impedance-frequency spectrum. One is the population mean method, which measures the mean impedance of a population of cells at 18 different frequencies from 250kHz to 550MHz to generate the Clausius Mossotti factor spectrum. The data at each frequency point was collected one by one. This method derived the dielectric parameters of cell subpopulations. A second method measured single cells where 8 frequencies between 250kHz and 575MHz were applied simultaneously to generate individual spectra at high throughput.

An interesting finding is that the low conductivity suspending media (0.32 S/m) enhances the ability to discriminate the dielectric parameters of control cells and treated cells. Experiments using HL60 cells fixed with glutaraldehyde or treated with cytochalasin D were conducted. Fixed cells have a significantly lower membrane capacitance and cytoplasm conductivity compared to unfixed cells when measured in the low conductivity media, while this difference cannot be measured in physiological saline (1.6 S/m). Both the population mean method with 18 frequencies and the single-cell method with 8 frequencies reported the same trend. Cells treated with cytochalasin D were also examined in low conductivity media, and a subtle decrease in the membrane capacitance after treatment was noted. This was not observed in previous MIC studies using high conductivity media.

The single-cell method was also used to measure dielectric parameter changes between THP-1 cells and those differentiated into M0 macrophages. The results showed an enlarged size and decreased cytoplasm conductivity of M0 cells after differentiation, indicating the possible use of this method in the study of immune processes and diseases.

Future work could test other cellular models to explore the dielectric changes behind the biological alterations. For example, in CAR-T (Chimeric Antigen Receptors-T cell) therapy, the final step is selecting the modified CAR-T cells with the desired target expression capability. Cells with different levels of immune expression have varying amounts of antibodies on their membrane surface, which could alter the membrane capacitance and could be detected by MIC (Honrado et al. 2021). In addition, the MIC can use multi-parameters to characterise cell mechanics and dielectrics simultaneously and provide a more comprehensive understanding of single-cell biophysical properties. The technique needs to embrace new technologies, such as artificial intelligence and machine learning to improve the efficiency of distinguishing cellular heterogeneity rather than being limited to measuring biophysical properties. Sometimes, direct characteristics of the impedance signal, such as peak value and signal width, may be overlooked by manual analysis. Al methods, which learn from large datasets, may be able to identify these differences.

The last part of this thesis is the single-cell sorting system. Studies of single-cell biophysical analysis in **Chapters 4 and 5** demonstrated cell phenotype discrimination. However, in some cases, identifying and isolating rare cells is critical for clinical applications. For example, CTCs (Circulating Tumour Cells) are tumour cells shed from primary or metastatic lesions of solid tumours into the bloodstream. These cells act as critical indicators of cancer metastasis and serve as targets in liquid biopsy, offering non-invasive screening, real-time treatment response monitoring and prognostic evaluation. However, the concentration of CTCs in blood is extremely low, hindering the detection and analysis. Thus, single-cell sorting is necessary to enrich the cells before further analysis. Integrating an efficient sorter in the downstream region of the MIC chip is important but the selection of a sorter should consider chip dimensions, fabrication cost, production cycle and the ease of integration into the mechanical design of the existing device. Due to the high cost of fabricating, the on-chip membrane pump was chosen as the optimal solution for the sorter. The sorter integrates membrane pumps directly into the MIC chip structure with the membrane on top of the pump actuated by an external piezoelectric actuator.

The implementation of the sorting system requires consideration of various software and hardware design and optimisation. The triggering mechanism was transferred from the electro-optical deformability MIC system but had optimisations. With an optimised multi-threads algorithm, the time sequence limitation of detection and triggering signal caused by the single thread algorithm was solved, thereby improving detection efficiency. In addition, the mechanical design of the piezo actuator assembly was carefully considered to ensure proper alignment between the actuator and on-chip membrane pump, as well as to manage the micro-level displacement convened to induce the membrane deflection. The proposed MIC sorting system was evaluated with microbeads and mixed cells experiments. The results showed a good sorting

performance that the throughput was achieved to around 13 particles/s and the post-sorting purity of the beads was up to 97% with above 70% efficiency. However, the work on cell mixture sorting was limited by the real-time deformability decision from raw impedance data, and the evaluation showed a decrease in the proportion of unwanted cells in the suspension after separation, from 37% to 25%, which is not a significant separation.

Future work on this sorting system looks to improve the throughput and simplify the experiment setup. There are many steps to prepare a sorting chip before conducting an experiment. The membrane pump is filled with liquid by degassing before being clamped on the chip holder which can lead to small fibres or dust entering the channel. Frequently disassembling the chip increases the possibility of damage therefore automating the pre-filling of the membrane pump should reduce these issues and improve the experimental process. In addition, the real-time detection algorithm could be optimised using machine learning to enhance the signal differences between different cellular subpopulations. Performing complex convolution operations to filter the single in real time increases execution time, resulting in missing the trigger timing. However, extracting the peaks of the impedance signal does not meet the requirements for identification. Machine learning methods could provide new perspectives for detecting the difference in raw signals. Indeed, machine learning has been integrated with label-free single-cell biophysical detection (Nitta et al. 2018; Kobak and Berens 2019), which can be applied to the MIC real-time sorting in the future.

The MIC sorting system also has many potential improvements and application prospects. For example, the sorted single cells can be used to prepare single-cell genome sequencing, which is a process to reveal the genetic heterogeneity behind phenotypes. It is even possible to integrate the early-stage cell preparation for single-cell sequencing into the microfluidic separation system, such as allocating barcodes to single cells within droplets. Furthermore, the immune therapies, such as CAR-T, requires isolating the modified cells with the same expression capability for subsequent amplification and then injected into the patient body. If the amplification step is directly integrated after the sorting system, it can prevent the target cells from contacting with the open environment, thereby increasing their quantity in a more stable environment and helping to generate target immune cells with higher purity.

In summary, single-cell biophysical analysis and sorting systems based on microfluidic impedance cytometry (MIC) were described. Biophysical properties, including deformability and dielectric parameters, were determined by MIC with different electrode configurations. An optical system was coupled with the MIC to measure the optical and electrical deformability of single cells, exhibiting an excellent correlation between optical and electrical deformability. A novel impedance spectroscopic method with a broad frequency range was used to determine the membrane capacitance and cytoplasm conductivity and uncover subtle dielectric changes in

Chapter 7

cells treated with different chemicals. Finally, on-chip membrane pumps were integrated with MIC, and the sorting performance was evaluated. MIC is a label-free technique for assessing cellular phenotypes with different biophysical properties and achieving single-cell sorting, which can be applied to clinical rapid diagnosis and promote the point of care field.

Reference

- Abay, Asena, Greta Simionato, Revaz Chachanidze, Anna Bogdanova, Laura Hertz, Paola Bianchi, Emile Van den Akker, Marieke von Lindern, Marc Leonetti, and Giampaolo Minetti. 2019. 'Glutaraldehyde–a subtle tool in the investigation of healthy and pathologic red blood cells', *Frontiers in physiology*, 10: 514.
- Adamo, Andrea, Armon Sharei, Luigi Adamo, ByungKun Lee, Shirley Mao, and Klavs F Jensen. 2012. 'Microfluidics-based assessment of cell deformability', *Analytical chemistry*, 84: 6438-43.
- Aldo, P. B., V. Craveiro, S. Guller, and G. Mor. 2013. 'Effect of culture conditions on the phenotype of THP-1 monocyte cell line', *Am J Reprod Immunol*, 70: 80-6.
- Alibert, C., B. Goud, and J. B. Manneville. 2017. 'Are cancer cells really softer than normal cells?', *Biol Cell*, 109: 167-89.
- An, Jaemin, Jangwon Lee, Sang Ho Lee, Jungyul Park, and Byungkyu Kim. 2009. 'Separation of malignant human breast cancer epithelial cells from healthy epithelial cells using an advanced dielectrophoresis-activated cell sorter (DACS)', *Analytical and bioanalytical chemistry*, 394: 801-09.
- Armistead, Fern J, Julia Gala De Pablo, Hermes Gadêlha, Sally A Peyman, and Stephen D Evans. 2019. 'Cells under stress: an inertial-shear microfluidic determination of cell behavior', *Biophysical journal*, 116: 1127-35.
- Arnold, WM, and U Zimmermann. 1982a. 'Rotating-field-induced rotation and measurement of the membrane capacitance of single mesophyll cells of Avena sativa', *Zeitschrift für Naturforschung C*, 37: 908-15.
- Arnold, WM, and U Zimmermann. 1982b. 'Rotation of an isolated cell in a rotating electric field', *Naturwissenschaften*, 69: 297-98.
- Arnold, WM, and U Zimmermann. 1988. 'Electro-rotation: development of a technique for dielectric measurements on individual cells and particles', *Journal of Electrostatics*, 21: 151-91.
- Augustsson, Per, Cecilia Magnusson, Maria Nordin, Hans Lilja, and Thomas Laurell. 2012. 'Microfluidic, label-free enrichment of prostate cancer cells in blood based on acoustophoresis', *Analytical chemistry*, 84: 7954-62.
- Azubuike, Udochi F, and Kandice Tanner. 2023. 'Biophysical determinants of cancer organotropism', *Trends in cancer*, 9: 188-97.
- Bae, Y. B., H. K. Jang, T. H. Shin, G. Phukan, T. T. Tran, G. Lee, W. R. Hwang, and J. M. Kim. 2016. 'Microfluidic assessment of mechanical cell damage by extensional stress', *Lab Chip*, 16: 96-103.
- Bansal, Ishita, Shamibrota K. Roy, Kaushik Basu, and Prosenjit Sen. 2022. "Flash imaging for microfluidics." In 2022 IEEE International Conference on Emerging Electronics (ICEE), 1-3.
- Bao, Ning, Gayani C Kodippili, Katie M Giger, Velia M Fowler, Philip S Low, and Chang Lu. 2011. 'Single-cell electrical lysis of erythrocytes detects deficiencies in the cytoskeletal protein network', *Lab on a Chip*, 11: 3053-56.
- Baxter, E. W., A. E. Graham, N. A. Re, I. M. Carr, J. I. Robinson, S. L. Mackie, and A. W. Morgan. 2020. 'Standardized protocols for differentiation of THP-1 cells to macrophages with distinct M(IFNgamma+LPS), M(IL-4) and M(IL-10) phenotypes', *J Immunol Methods*, 478: 112721.

- Belotti, Yuri, Serenella Tolomeo, Michael J Conneely, Tianjun Huang, Stephen J McKenna, Ghulam Nabi, and David McGloin. 2019. 'High-throughput, time-resolved mechanical phenotyping of prostate cancer cells', *Scientific reports*, 9: 5742.
- Bland, David Russell. 2016. The theory of linear viscoelasticity (Courier Dover Publications).
- Bonner, WA, HR Hulett, RG Sweet, and LA Herzenberg. 1972. 'Fluorescence activated cell sorting', *Review of Scientific Instruments*, 43: 404-09.
- Bufi, Nathalie, Michael Saitakis, Stéphanie Dogniaux, Oscar Buschinger, Armelle Bohineust, Alain Richert, Mathieu Maurin, Claire Hivroz, and Atef Asnacios. 2015. 'Human primary immune cells exhibit distinct mechanical properties that are modified by inflammation', *Biophysical journal*, 108: 2181-90.
- Buryk-Iggers, Stephanie, Jennifer Kieda, and Scott SH Tsai. 2019. 'Diamagnetic droplet microfluidics applied to single-cell sorting', *AIP Advances*, 9.
- Byun, Sangwon, Sungmin Son, Dario Amodei, Nathan Cermak, Josephine Shaw, Joon Ho Kang, Vivian C Hecht, Monte M Winslow, Tyler Jacks, and Parag Mallick. 2013. 'Characterizing deformability and surface friction of cancer cells', *Proceedings of the National Academy of Sciences*, 110: 7580-85.
- Casella, James F, Michael D Flanagan, and Shin Lin. 1981. 'Cytochalasin D inhibits actin polymerization and induces depolymerization of actin filaments formed during platelet shape change', *Nature*, 293: 302-05.
- Chai, H., Y. Feng, J. Zhu, X. Meng, F. Liang, J. Bai, and W. Wang. 2023. 'Evaluating the Accuracy of Impedance Flow Cytometry with Cell-Sized Liposomes', *ACS Sens*, 8: 2681-90.
- Chen, C. H., S. H. Cho, F. Tsai, A. Erten, and Y. H. Lo. 2009. 'Microfluidic cell sorter with integrated piezoelectric actuator', *Biomed Microdevices*, 11: 1223-31.
- Chen, J., X. Zou, D. C. Spencer, and H. Morgan. 2024. 'Single-cell electro-mechanical shear flow deformability cytometry', *Microsyst Nanoeng*, 10: 173.
- Chen, Jian, Yi Zheng, Qingyuan Tan, Ehsan Shojaei-Baghini, Yan Liang Zhang, Jason Li, Preethy Prasad, Lidan You, Xiao Yu Wu, and Yu Sun. 2011. 'Classification of cell types using a microfluidic device for mechanical and electrical measurement on single cells', *Lab on a Chip*, 11: 3174-81.
- Cheung, K., S. Gawad, and P. Renaud. 2005. 'Impedance spectroscopy flow cytometry: on-chip label-free cell differentiation', *Cytometry A*, 65: 124-32.
- Chiu, Tzu-Keng, Yang Zhao, Deyong Chen, Chia-Hsun Hsieh, Ke Wang, Wen-Pin Chou, Chia-Jung Liao, Hsin-Yao Wang, Beiyuan Fan, Junbo Wang, Jian Chen, and Min-Hsien Wu. 2017. 'A low-sample-loss microfluidic system for the quantification of size-independent cellular electrical property—Its demonstration for the identification and characterization of circulating tumour cells (CTCs)', Sensors and Actuators B: Chemical, 246: 29-37.
- Choi, G., R. Nouri, L. Zarzar, and W. Guan. 2020. 'Microfluidic deformability-activated sorting of single particles', *Microsyst Nanoeng*, 6: 11.
- Coué, Martine, Stephen L Brenner, Ilan Spector, and Edward D Korn. 1987. 'Inhibition of actin polymerization by latrunculin A', *FEBS letters*, 213: 316-18.
- Coulter, Wallace H. 1956. "High speed automatic blood cell counter and cell size analyzer." In *Proceedings of the National Electronics Conference*, 1034.
- Crowley, Timothy A, and Vincent Pizziconi. 2005. 'Isolation of plasma from whole blood using planar microfilters for lab-on-a-chip applications', *Lab on a Chip*, 5: 922-29.
- Daigneault, M., J. A. Preston, H. M. Marriott, M. K. Whyte, and D. H. Dockrell. 2010. 'The identification of markers of macrophage differentiation in PMA-stimulated THP-1 cells and monocyte-derived macrophages', *PLoS One*, 5: e8668.

- Davis, John A, David W Inglis, Keith J Morton, David A Lawrence, Lotien R Huang, Stephen Y Chou, James C Sturm, and Robert H Austin. 2006. 'Deterministic hydrodynamics: taking blood apart', *Proceedings of the National Academy of Sciences*, 103: 14779-84.
- Del Giudice, Francesco. 2019. 'Viscoelastic focusing of polydisperse particle suspensions in a straight circular microchannel', *Microfluidics and Nanofluidics*, 23: 95.
- Di Carlo, Dino. 2009. 'Inertial microfluidics', Lab on a Chip, 9: 3038-46.
- Di Carlo, Dino, Jon F Edd, Katherine J Humphry, Howard A Stone, and Mehmet Toner. 2009. 'Particle segregation and dynamics in confined flows', *Physical Review Letters*, 102: 094503.
- Di Carlo, Dino, Daniel Irimia, Ronald G Tompkins, and Mehmet Toner. 2007. 'Continuous inertial focusing, ordering, and separation of particles in microchannels', *Proceedings of the National Academy of Sciences*, 104: 18892-97.
- Ding, Xiaoyun, Zhangli Peng, Sz-Chin Steven Lin, Michela Geri, Sixing Li, Peng Li, Yuchao Chen, Ming Dao, Subra Suresh, and Tony Jun Huang. 2014. 'Cell separation using tilted-angle standing surface acoustic waves', *Proceedings of the National Academy of Sciences*, 111: 12992-97.
- Du, E., S. Ha, M. Diez-Silva, M. Dao, S. Suresh, and A. P. Chandrakasan. 2013. 'Electric impedance microflow cytometry for characterization of cell disease states', *Lab Chip*, 13: 3903-09.
- Dulińska, Ida, Marta Targosz, Wojciech Strojny, Małgorzata Lekka, Paweł Czuba, Walentyna Balwierz, and Marek Szymoński. 2006. 'Stiffness of normal and pathological erythrocytes studied by means of atomic force microscopy', *Journal of biochemical and biophysical methods*, 66: 1-11.
- Duncan, L, H Shelmerdine, MP Hughes, HM Coley, Y Hübner, and FH Labeed. 2007. 'Dielectrophoretic analysis of changes in cytoplasmic ion levels due to ion channel blocker action reveals underlying differences between drug-sensitive and multidrug-resistant leukaemic cells', *Physics in Medicine & Biology*, 53: N1.
- Evans, Heather M, Enkhtuul Surenjav, Craig Priest, Stephan Herminghaus, Ralf Seemann, and Thomas Pfohl. 2009. 'In situ formation, manipulation, and imaging of droplet-encapsulated fibrin networks', *Lab on a Chip*, 9: 1933-41.
- Fabry, Ben, Geoffrey N Maksym, James P Butler, Michael Glogauer, Daniel Navajas, and Jeffrey J Fredberg. 2001. 'Scaling the microrheology of living cells', *Physical Review Letters*, 87: 148102.
- Fan, Xiaoyun, Chunping Jia, Jun Yang, Gang Li, Hongju Mao, Qinghui Jin, and Jianlong Zhao. 2015. 'A microfluidic chip integrated with a high-density PDMS-based microfiltration membrane for rapid isolation and detection of circulating tumor cells', *Biosensors and Bioelectronics*, 71: 380-86.
- Faustino, V., R. O. Rodrigues, D. Pinho, E. Costa, A. Santos-Silva, V. Miranda, J. S. Amaral, and R. Lima. 2019. 'A Microfluidic Deformability Assessment of Pathological Red Blood Cells Flowing in a Hyperbolic Converging Microchannel', *Micromachines (Basel)*, 10.
- Feng, Y., H. Chai, W. He, F. Liang, Z. Cheng, and W. Wang. 2022. 'Impedance-Enabled Camera-Free Intrinsic Mechanical Cytometry', *Small Methods*, 6: e2200325.
- Feng, Y., Z. Cheng, H. Chai, W. He, L. Huang, and W. Wang. 2022. 'Neural network-enhanced real-time impedance flow cytometry for single-cell intrinsic characterization', *Lab Chip*, 22: 240-49.
- Feng, Y., J. Zhu, H. Chai, W. He, L. Huang, and W. Wang. 2023. 'Impedance-Based Multimodal Electrical-Mechanical Intrinsic Flow Cytometry', *Small*, 19: e2303416.
- Fiedler, Stefan, Stephen G Shirley, Thomas Schnelle, and Günter Fuhr. 1998. 'Dielectrophoretic sorting of particles and cells in a microsystem', *Analytical chemistry*, 70: 1909-15.

- Fong, Erika J, Amanda C Johnston, Timothy Notton, Seung-Yong Jung, Klint A Rose, Leor S Weinberger, and Maxim Shusteff. 2014. 'Acoustic focusing with engineered node locations for high-performance microfluidic particle separation', *Analyst*, 139: 1192-200.
- Fuchs, Stefanie, Sofia Johansson, Anders Ø Tjell, Gabriel Werr, Torsten Mayr, and Maria Tenje. 2021. 'In-line analysis of organ-on-chip systems with sensors: integration, fabrication, challenges, and potential', ACS Biomaterials Science & Engineering, 7: 2926-48.
- Gadagkar, Sudhindra R, and Gerald B Call. 2015. 'Computational tools for fitting the Hill equation to dose–response curves', *Journal of Pharmacological and Toxicological methods*, 71: 68-76.
- Gagnon, Z., J. Gordon, S. Sengupta, and H. C. Chang. 2008. 'Bovine red blood cell starvation age discrimination through a glutaraldehyde-amplified dielectrophoretic approach with buffer selection and membrane cross-linking', *Electrophoresis*, 29: 2272-9.
- Galie, P. A., P. C. Georges, and P. A. Janmey. 2022. 'How do cells stiffen?', *Biochem J*, 479: 1825-42.
- Gatto, F., R. Cagliani, T. Catelani, D. Guarnieri, M. Moglianetti, P. P. Pompa, and G. Bardi. 2017. 'PMA-Induced THP-1 Macrophage Differentiation is Not Impaired by Citrate-Coated Platinum Nanoparticles', *Nanomaterials (Basel)*, 7: 332.
- Gawad, Shady, Laurent Schild, and PH Renaud. 2001. 'Micromachined impedance spectroscopy flow cytometer for cell analysis and particle sizing', *Lab on a Chip*, 1: 76-82.
- Gerum, Richard, Elham Mirzahossein, Mar Eroles, Jennifer Elsterer, Astrid Mainka, Andreas Bauer, Selina Sonntag, Alexander Winterl, Johannes Bartl, and Lena Fischer. 2022. 'Viscoelastic properties of suspended cells measured with shear flow deformation cytometry', elife, 11: e78823.
- Giddings, J Calvin. 1985. 'A system based on split-flow lateral-transport thin (SPLITT) separation cells for rapid and continuous particle fractionation', *Separation Science and Technology*, 20: 749-68.
- ——. 1993. 'Field-flow fractionation: analysis of macromolecular, colloidal, and particulate materials', *Science*, 260: 1456-65.
- González-Cruz, Rafael D, Vera C Fonseca, and Eric M Darling. 2012. 'Cellular mechanical properties reflect the differentiation potential of adipose-derived mesenchymal stem cells', *Proceedings of the National Academy of Sciences*, 109: E1523-E29.
- Gordonov, S., M. K. Hwang, A. Wells, F. B. Gertler, D. A. Lauffenburger, and M. Bathe. 2016. 'Time series modeling of live-cell shape dynamics for image-based phenotypic profiling', *Integr Biol (Camb)*, 8: 73-90.
- Gossett, Daniel R, Henry TK Tse, Serena A Lee, Yong Ying, Anne G Lindgren, Otto O Yang, Jianyu Rao, Amander T Clark, and Dino Di Carlo. 2012. 'Hydrodynamic stretching of single cells for large population mechanical phenotyping', *Proceedings of the National Academy of Sciences*, 109: 7630-35.
- Guck, Jochen, Revathi Ananthakrishnan, Hamid Mahmood, Tess J Moon, C Casey Cunningham, and Josef Käs. 2001. 'The optical stretcher: a novel laser tool to micromanipulate cells', *Biophysical journal*, 81: 767-84.
- Gupta, Vivek K, and Ovijit Chaudhuri. 2022. 'Mechanical regulation of cell-cycle progression and division', *Trends in cell biology*, 32: 773-85.
- Guzniczak, E., O. Otto, G. Whyte, N. Willoughby, M. Jimenez, and H. Bridle. 2020. 'Deformability-induced lift force in spiral microchannels for cell separation', *Lab Chip*, 20: 614-25.
- Haandbæk, Niels, Sebastian C. Bürgel, Fabian Rudolf, Flavio Heer, and Andreas Hierlemann. 2016. 'Characterization of Single Yeast Cell Phenotypes Using Microfluidic Impedance Cytometry and Optical Imaging', ACS Sensors, 1: 1020-27.

- Hairer, G., G. S. Pärr, P. Svasek, A. Jachimowicz, and M. J. Vellekoop. 2008. 'Investigations of micrometer sample stream profiles in a three-dimensional hydrodynamic focusing device', *Sensors and Actuators B: Chemical*, 132: 518-24.
- Hairer, Gabriel, and Michael J Vellekoop. 2009. 'An integrated flow-cell for full sample stream control', *Microfluidics and Nanofluidics*, 7: 647-58.
- Han, Zhenzhen, Cheng Peng, Jia Yi, Dongxue Zhang, Xiaowei Xiang, Xinyan Peng, Bin Su, Baohong Liu, Yuhui Shen, and Liang Qiao. 2021. 'Highly efficient exosome purification from human plasma by tangential flow filtration based microfluidic chip', *Sensors and Actuators B: Chemical*, 333: 129563.
- Hansson, J., J. M. Karlsson, T. Haraldsson, W. van der Wijngaart, and A. Russom. 2011. "Inertial particle focusing in parallel microfluidic channels for high-throughput filtration." In 2011 16th International Solid-State Sensors, Actuators and Microsystems Conference, 1777-80.
- Hao, Yansheng, Shaokoon Cheng, Yo Tanaka, Yoichiroh Hosokawa, Yaxiaer Yalikun, and Ming Li. 2020. 'Mechanical properties of single cells: Measurement methods and applications', *Biotechnology Advances*, 45: 107648.
- Hattori, Akihiro, and Kenji Yasuda. 2010. 'Comprehensive study of microgel electrode for on-chip electrophoretic cell sorting', *Japanese journal of applied physics*, 49: 06GM04.
- Herbig, Maik, Alexander Mietke, Paul Müller, and Oliver Otto. 2018. 'Statistics for real-time deformability cytometry: Clustering, dimensionality reduction, and significance testing', *Biomicrofluidics*, 12: 042214.
- Hochmuth, Robert M. 2000. 'Micropipette aspiration of living cells', *Journal of biomechanics*, 33: 15-22.
- Hochstetter, Axel, Rohan Vernekar, Robert H Austin, Holger Becker, Jason P Beech, Dmitry A Fedosov, Gerhard Gompper, Sung-Cheol Kim, Joshua T Smith, and Gustavo Stolovitzky. 2020. 'Deterministic lateral displacement: Challenges and perspectives', *ACS nano*, 14: 10784-95.
- Hoffman, Brenton D, Gladys Massiera, Kathleen M Van Citters, and John C Crocker. 2006. 'The consensus mechanics of cultured mammalian cells', *Proceedings of the National Academy of Sciences*, 103: 10259-64.
- Holmes, D., D. Pettigrew, C. H. Reccius, J. D. Gwyer, C. van Berkel, J. Holloway, D. E. Davies, and H. Morgan. 2009. 'Leukocyte analysis and differentiation using high speed microfluidic single cell impedance cytometry', *Lab Chip*, 9: 2881-9.
- Hölzel, Ralph. 1999. 'Non-invasive determination of bacterial single cell properties by electrorotation', *Biochimica et Biophysica Acta (BBA)-Molecular Cell Research*, 1450: 53-60.
- Holzner, Gregor, Stavros Stavrakis, and Andrew DeMello. 2017. 'Elasto-inertial focusing of mammalian cells and bacteria using low molecular, low viscosity PEO solutions', *Analytical chemistry*, 89: 11653-63.
- Hong, Jhih-Lin, Kung-Chieh Lan, and Ling-Sheng Jang. 2012. 'Electrical characteristics analysis of various cancer cells using a microfluidic device based on single-cell impedance measurement', Sensors and Actuators B: Chemical, 173: 927-34.
- Honrado, C., P. Bisegna, N. S. Swami, and F. Caselli. 2021. 'Single-cell microfluidic impedance cytometry: from raw signals to cell phenotypes using data analytics', *Lab Chip*, 21: 22-54.
- Honrado, C., L. Ciuffreda, D. Spencer, L. Ranford-Cartwright, and H. Morgan. 2018. 'Dielectric characterization of Plasmodium falciparum-infected red blood cells using microfluidic impedance cytometry', *J R Soc Interface*, 15.

- Hou, Han Wei, Majid Ebrahimi Warkiani, Bee Luan Khoo, Zi Rui Li, Ross A Soo, Daniel Shao-Weng Tan, Wan-Teck Lim, Jongyoon Han, Ali Asgar S Bhagat, and Chwee Teck Lim. 2013. 'Isolation and retrieval of circulating tumor cells using centrifugal forces', *Scientific reports*, 3: 1259.
- Howell, P. B., Jr., J. P. Golden, L. R. Hilliard, J. S. Erickson, D. R. Mott, and F. S. Ligler. 2008. 'Two simple and rugged designs for creating microfluidic sheath flow', *Lab Chip*, 8: 1097-103.
- Huang, Lotien Richard, Edward C Cox, Robert H Austin, and James C Sturm. 2004. 'Continuous particle separation through deterministic lateral displacement', *Science*, 304: 987-90.
- Huang, R, TA Barber, MA Schmidt, RG Tompkins, M Toner, DW Bianchi, R Kapur, and WL Flejter. 2008. 'A microfluidics approach for the isolation of nucleated red blood cells (NRBCs) from the peripheral blood of pregnant women', *Prenatal Diagnosis: published in Affiliation with the International Society for prenatal Diagnosis*, 28: 892-99.
- Huang, Ying, Xiao-Bo Wang, R Holzel, FF Becker, and PRC Gascoyne. 1995. 'Electrorotational studies of the cytoplasmic dielectric properties of Friend murine erythroleukaemia cells', *Physics in Medicine & Biology*, 40: 1789.
- Huh, Dongeun, Joong Hwan Bahng, Yibo Ling, Hsien-Hung Wei, Oliver D Kripfgans, J Brian Fowlkes, James B Grotberg, and Shuichi Takayama. 2007. 'Gravity-driven microfluidic particle sorting device with hydrodynamic separation amplification', *Analytical chemistry*, 79: 1369-76.
- Hulett, Henry R, William A Bonner, Janet Barrett, and Leonard A Herzenberg. 1969. 'Cell sorting: automated separation of mammalian cells as a function of intracellular fluorescence', *Science*, 166: 747-49.
- Hurley, James. 1970. 'Sizing Particles with a Coulter Counter', Biophysical journal, 10: 74-79.
- Inglis, David W, John A Davis, Robert H Austin, and James C Sturm. 2006. 'Critical particle size for fractionation by deterministic lateral displacement', *Lab on a Chip*, 6: 655-58.
- Irimajiri, Akihiko, Tetsuya Hanai, and Akira Inouye. 1979. 'A dielectric theory of "multi-stratified shell" model with its application to a lymphoma cell', *Journal of theoretical biology*, 78: 251-69.
- Isozaki, A., H. Mikami, K. Hiramatsu, S. Sakuma, Y. Kasai, T. Iino, T. Yamano, A. Yasumoto, Y. Oguchi, N. Suzuki, Y. Shirasaki, T. Endo, T. Ito, K. Hiraki, M. Yamada, S. Matsusaka, T. Hayakawa, H. Fukuzawa, Y. Yatomi, F. Arai, D. Di Carlo, A. Nakagawa, Y. Hoshino, Y. Hosokawa, S. Uemura, T. Sugimura, Y. Ozeki, N. Nitta, and K. Goda. 2019. 'A practical guide to intelligent image-activated cell sorting', *Nat Protoc*, 14: 2370-415.
- Jaffe, A., and J. Voldman. 2018. 'Multi-frequency dielectrophoretic characterization of single cells', *Microsyst Nanoeng*, 4: 23.
- Jarmoshti, J., A. B. Siddique, A. Rane, S. Mirhosseini, S. J. Adair, T. W. Bauer, F. Caselli, and N. S. Swami. 2024. 'Neural Network-Enabled Multiparametric Impedance Signal Templating for High throughput Single-Cell Deformability Cytometry Under Viscoelastic Extensional Flows', Small: e2407212.
- Kang, Giseok, Young-jae Kim, Hong-sang Moon, Jeong-Woo Lee, Tag-Keun Yoo, Kwangsung Park, and Jong-Hyun Lee. 2013. 'Discrimination between the human prostate normal cell and cancer cell by using a novel electrical impedance spectroscopy controlling the cross-sectional area of a microfluidic channel', *Biomicrofluidics*, 7.
- Kang, Joon Ho, Teemu P Miettinen, Lynna Chen, Selim Olcum, Georgios Katsikis, Patrick S Doyle, and Scott R Manalis. 2019. 'Noninvasive monitoring of single-cell mechanics by acoustic scattering', *Nature methods*, 16: 263-69.
- Kang, Yoon-Tae, Il Doh, Jiyoung Byun, Hee Jin Chang, and Young-Ho Cho. 2017. 'Label-free rapid viable enrichment of circulating tumor cell by photosensitive polymer-based microfilter device', *Theranostics*, 7: 3179.

- Kawai, S., M. Suzuki, S. Arimoto, T. Korenaga, and T. Yasukawa. 2020. 'Determination of membrane capacitance and cytoplasm conductivity by simultaneous electrorotation', *Analyst*, 145: 4188-95.
- Keim, Kevin, Mohamed Z Rashed, Samuel C Kilchenmann, Aurélien Delattre, António F Gonçalves, Paul Éry, and Carlotta Guiducci. 2019. 'On chip technology for single cell arraying, electrorotation based analysis and selective release', *Electrophoresis*, 40: 1830-38.
- Ketelaar, Tijs, Harold JG Meijer, Marjolein Spiekerman, Rob Weide, and Francine Govers. 2012. 'Effects of latrunculin B on the actin cytoskeleton and hyphal growth in Phytophthora infestans', *Fungal Genetics and Biology*, 49: 1014-22.
- Klein, Ann-Kathrin, and Andreas Dietzel. 2021. 'A primer on microfluidics: from basic principles to microfabrication.' in, *Microfluidics in Biotechnology* (Springer).
- Knight, James B., Ashvin Vishwanath, James P. Brody, and Robert H. Austin. 1998. 'Hydrodynamic Focusing on a Silicon Chip: Mixing Nanoliters in Microseconds', *Physical Review Letters*, 80: 3863-66.
- Kobak, Dmitry, and Philipp Berens. 2019. 'The art of using t-SNE for single-cell transcriptomics', *Nature communications*, 10: 5416.
- Kollmannsberger, Philip, and Ben Fabry. 2011. 'Linear and nonlinear rheology of living cells', *Annual review of materials research*, 41: 75-97.
- Kong, Cong, Mengjia Hu, Kumuditha M Weerakoon-Ratnayake, Malgorzata A Witek, Kavya Dathathreya, Mateusz L Hupert, and Steven A Soper. 2020. 'Label-free counting of affinity-enriched circulating tumor cells (CTCs) using a thermoplastic micro-C oulter counter (μCC)', *Analyst*, 145: 1677-86.
- Kuntaegowdanahalli, Sathyakumar S, Ali Asgar S Bhagat, Girish Kumar, and Ian Papautsky. 2009. 'Inertial microfluidics for continuous particle separation in spiral microchannels', *Lab on a Chip*, 9: 2973-80.
- Lange, Janina R., Claus Metzner, Sebastian Richter, Werner Schneider, Monika Spermann, Thorsten Kolb, Graeme Whyte, and Ben Fabry. 2017. 'Unbiased High-Precision Cell Mechanical Measurements with Microconstrictions', *Biophysical journal*, 112: 1472-80.
- Lange, Janina R, Julian Steinwachs, Thorsten Kolb, Lena A Lautscham, Irina Harder, Graeme Whyte, and Ben Fabry. 2015. 'Microconstriction Arrays for High-Throughput Quantitative Measurements of Cell Mechanical Properties', *Biophysical journal*, 109: 26-34.
- Larsen, Ulrik D, Gert Blankenstein, and Jens Branebjerg. 1997. "Microchip Coulter particle counter." In *Proceedings of International Solid State Sensors and Actuators Conference (Transducers' 97)*, 1319-22. IEEE.
- Lavi, E. D., F. Crivellari, and Z. Gagnon. 2022. 'Dielectrophoretic detection of electrical property changes of stored human red blood cells', *Electrophoresis*, 43: 1297-308.
- Lee, S. S., Y. Yim, K. H. Ahn, and S. J. Lee. 2009. 'Extensional flow-based assessment of red blood cell deformability using hyperbolic converging microchannel', *Biomed Microdevices*, 11: 1021-7.
- Lekka, Malgorzata, Maria Fornal, Grażyna Pyka-Fościak, Kateryna Lebed, Barbara Wizner, Tomasz Grodzicki, and Jan Styczeń. 2005. 'Erythrocyte stiffness probed using atomic force microscope', *Biorheology*, 42: 307-17.
- Lewis, Claire E, and JO'D McGee. 1992. 'The macrophage'.
- Li, Huajun, Yining Wu, Xiaoda Wang, Chunying Zhu, Taotao Fu, and Youguang Ma. 2016. 'Magnetofluidic control of the breakup of ferrofluid droplets in a microfluidic Y-junction', Rsc Advances, 6: 778-85.
- Li, P., and Y. Ai. 2021. 'Label-Free Multivariate Biophysical Phenotyping-Activated Acoustic Sorting at the Single-Cell Level', *Anal Chem*, 93: 4108-17.

- Li, Peixian, Minhui Liang, Xiaoguang Lu, Joycelyn Jia Ming Chow, Chrishan JA Ramachandra, and Ye Ai. 2019. 'Sheathless acoustic fluorescence activated cell sorting (aFACS) with high cell viability', *Analytical chemistry*, 91: 15425-35.
- Li, Shan Shan, Chun Dong Xue, Yong Jiang Li, Xiao Ming Chen, Yan Zhao, and Kai Rong Qin. 2024. 'Microfluidic characterization of single cell biophysical properties and the applications in cancer diagnosis', *Electrophoresis*, 45: 1212-32.
- Li, Sixing, Xiaoyun Ding, Zhangming Mao, Yuchao Chen, Nitesh Nama, Feng Guo, Peng Li, Lin Wang, Craig E Cameron, and Tony Jun Huang. 2015. 'Standing surface acoustic wave (SSAW)-based cell washing', *Lab on a Chip*, 15: 331-38.
- Liang, M., D. Yang, Y. Zhou, P. Li, J. Zhong, and Y. Ai. 2021. 'Single-Cell Stretching in Viscoelastic Fluids with Electronically Triggered Imaging for Cellular Mechanical Phenotyping', *Anal Chem*, 93: 4567-75.
- Lin, J., D. Kim, H. T. Tse, P. Tseng, L. Peng, M. Dhar, S. Karumbayaram, and D. Di Carlo. 2017. 'High-throughput physical phenotyping of cell differentiation', *Microsyst Nanoeng*, 3: 17013.
- Liu, Yan, Ke Wang, Xiaohao Sun, Deyong Chen, Junbo Wang, and Jian Chen. 2020. 'Development of microfluidic platform capable of characterizing cytoplasmic viscosity, cytoplasmic conductivity and specific membrane capacitance of single cells', *Microfluidics and Nanofluidics*, 24: 1-11.
- Liu, Zongbin, Fei Huang, Jinghui Du, Weiliang Shu, Hongtao Feng, Xiaoping Xu, and Yan Chen. 2013. 'Rapid isolation of cancer cells using microfluidic deterministic lateral displacement structure', *Biomicrofluidics*, 7.
- Lu, Nan, Hui Min Tay, Chayakorn Petchakup, Linwei He, Lingyan Gong, Kay Khine Maw, Sheng Yuan Leong, Wan Wei Lok, Hong Boon Ong, and Ruya Guo. 2023. 'Label-free microfluidic cell sorting and detection for rapid blood analysis', *Lab on a Chip*.
- Luna, Elizabeth J, and Anne L Hitt. 1992. 'Cytoskeleton—plasma membrane interactions', *Science*, 258: 955-64.
- Malleo, Daniele, J Tanner Nevill, Luke P Lee, and Hywel Morgan. 2010. 'Continuous differential impedance spectroscopy of single cells', *Microfluidics and Nanofluidics*, 9: 191-98.
- Mansoorifar, A., A. Koklu, S. Ma, G. V. Raj, and A. Beskok. 2018. 'Electrical Impedance Measurements of Biological Cells in Response to External Stimuli', *Anal Chem*, 90: 4320-27.
- Mansoorifar, Amin, Arindam Ghosh, Ahmet C. Sabuncu, and Ali Beskok. 2017. 'Accuracy of the Maxwell-Wagner and the Bruggeman-Hanai mixture models for single cell dielectric spectroscopy', *IET Nanobiotechnology*, 11: 874-82.
- Maremonti, Maria Isabella, David Dannhauser, Valeria Panzetta, Paolo Antonio Netti, and Filippo Causa. 2022. 'Cell deformability heterogeneity recognition by unsupervised machine learning from in-flow motion parameters', *Lab on a Chip*, 22: 4871-81.
- Martel, J. M., and M. Toner. 2014. 'Inertial focusing in microfluidics', *Annu Rev Biomed Eng*, 16: 371-96.
- Matthews, K., E. S. Lamoureux, M. E. Myrand-Lapierre, S. P. Duffy, and H. Ma. 2022. 'Technologies for measuring red blood cell deformability', *Lab Chip*, 22: 1254-74.
- Mazutis, Linas, John Gilbert, W Lloyd Ung, David A Weitz, Andrew D Griffiths, and John A Heyman. 2013. 'Single-cell analysis and sorting using droplet-based microfluidics', *Nature protocols*, 8: 870-91.
- McGrath, J. S., C. Honrado, J. H. Moore, S. J. Adair, W. B. Varhue, A. Salahi, V. Farmehini, B. J. Goudreau, S. Nagdas, E. M. Blais, T. W. Bauer, and N. S. Swami. 2020. 'Electrophysiology-

- based stratification of pancreatic tumorigenicity by label-free single-cell impedance cytometry', *Anal Chim Acta*, 1101: 90-98.
- Meacham, J. M., K. Durvasula, F. L. Degertekin, and A. G. Fedorov. 2018. 'Enhanced intracellular delivery via coordinated acoustically driven shear mechanoporation and electrophoretic insertion', *Sci Rep*, 8: 3727.
- Mehendale, Ninad, Oshin Sharma, Shilpi Pandey, and Debjani Paul. 2018. 'Clogging-free continuous operation with whole blood in a radial pillar device (RAPID)', *Biomedical microdevices*, 20: 1-11.
- Mietke, A., O. Otto, S. Girardo, P. Rosendahl, A. Taubenberger, S. Golfier, E. Ulbricht, S. Aland, J. Guck, and E. Fischer-Friedrich. 2015a. 'Extracting Cell Stiffness from Real-Time Deformability Cytometry: Theory and Experiment', *Biophys J*, 109: 2023-36.
- Mietke, Alexander, Oliver Otto, Salvatore Girardo, Philipp Rosendahl, Anna Taubenberger, Stefan Golfier, Elke Ulbricht, Sebastian Aland, Jochen Guck, and Elisabeth Fischer-Friedrich. 2015b. 'Extracting Cell Stiffness from Real-Time Deformability Cytometry: Theory and Experiment', *Biophysical journal*, 109: 2023-36.
- Mills, JP, Lan Qie, Ming Dao, CT Lim, and S Suresh. 2004. 'Nonlinear elastic and viscoelastic deformation of the human red blood cell with optical tweezers', *Molecular & Cellular Biomechanics*, 1: 169.
- Mittelheisser, V., V. Gensbittel, L. Bonati, W. Li, L. Tang, and J. G. Goetz. 2024. 'Evidence and therapeutic implications of biomechanically regulated immunosurveillance in cancer and other diseases', *Nat Nanotechnol*, 19: 281-97.
- Moeendarbary, E., and A. R. Harris. 2014. 'Cell mechanics: principles, practices, and prospects', *Wiley Interdiscip Rev Syst Biol Med*, 6: 371-88.
- Mohd Yasin, Z. N., F. N. Mohd Idrus, C. H. Hoe, and G. B. Yvonne-Tee. 2022. 'Macrophage polarization in THP-1 cell line and primary monocytes: A systematic review', *Differentiation*, 128: 67-82.
- Morgan, Hywel, and Nicolas G Green. 2003. AC electrokinetics: colloids and nanoparticles (Research Studies Press).
- Nam, Jeonghun, Hyunjung Lim, Dookon Kim, and Sehyun Shin. 2011. 'Separation of platelets from whole blood using standing surface acoustic waves in a microchannel', *Lab on a Chip*, 11: 3361-64.
- Nawaz, A. A., M. Urbanska, M. Herbig, M. Notzel, M. Krater, P. Rosendahl, C. Herold, N. Toepfner, M. Kubankova, R. Goswami, S. Abuhattum, F. Reichel, P. Muller, A. Taubenberger, S. Girardo, A. Jacobi, and J. Guck. 2020. 'Intelligent image-based deformation-assisted cell sorting with molecular specificity', *Nat Methods*, 17: 595-99.
- Neher, Erwin, and Bert Sakmann. 1976. 'Single-channel currents recorded from membrane of denervated frog muscle fibres', *Nature*, 260: 799-802.
- Nematbakhsh, Yasaman, and Chwee Teck Lim. 2015. 'Cell biomechanics and its applications in human disease diagnosis', *Acta Mechanica Sinica*, 31: 268-73.
- Nitta, N., T. Sugimura, A. Isozaki, H. Mikami, K. Hiraki, S. Sakuma, T. Iino, F. Arai, T. Endo, Y. Fujiwaki, H. Fukuzawa, M. Hase, T. Hayakawa, K. Hiramatsu, Y. Hoshino, M. Inaba, T. Ito, H. Karakawa, Y. Kasai, K. Koizumi, S. Lee, C. Lei, M. Li, T. Maeno, S. Matsusaka, D. Murakami, A. Nakagawa, Y. Oguchi, M. Oikawa, T. Ota, K. Shiba, H. Shintaku, Y. Shirasaki, K. Suga, Y. Suzuki, N. Suzuki, Y. Tanaka, H. Tezuka, C. Toyokawa, Y. Yalikun, M. Yamada, M. Yamagishi, T. Yamano, A. Yasumoto, Y. Yatomi, M. Yazawa, D. Di Carlo, Y. Hosokawa, S. Uemura, Y. Ozeki, and K. Goda. 2018. 'Intelligent Image-Activated Cell Sorting', Cell, 175: 266-76 e13.

- Nyberg, K. D., K. H. Hu, S. H. Kleinman, D. B. Khismatullin, M. J. Butte, and A. C. Rowat. 2017. 'Quantitative Deformability Cytometry: Rapid, Calibrated Measurements of Cell Mechanical Properties', *Biophys J*, 113: 1574-84.
- Nyberg, Kendra D, Michael B Scott, Samuel L Bruce, Ajay B Gopinath, Dimitri Bikos, Thomas G Mason, Jin Woong Kim, Hong Sung Choi, and Amy C Rowat. 2016. 'The physical origins of transit time measurements for rapid, single cell mechanotyping', *Lab on a Chip*, 16: 3330-39.
- Oakey, John, Robert W Applegate Jr, Erik Arellano, Dino Di Carlo, Steven W Graves, and Mehmet Toner. 2010. 'Particle focusing in staged inertial microfluidic devices for flow cytometry', *Analytical chemistry*, 82: 3862-67.
- Ostermann, M., A. Sauter, Y. Xue, E. Birkeland, J. Schoelermann, B. Holst, and M. R. Cimpan. 2020. 'Label-free impedance flow cytometry for nanotoxicity screening', *Sci Rep*, 10: 142.
- Otto, O., P. Rosendahl, A. Mietke, S. Golfier, C. Herold, D. Klaue, S. Girardo, S. Pagliara, A. Ekpenyong, A. Jacobi, M. Wobus, N. Topfner, U. F. Keyser, J. Mansfeld, E. Fischer-Friedrich, and J. Guck. 2015. 'Real-time deformability cytometry: on-the-fly cell mechanical phenotyping', *Nat Methods*, 12: 199-202.
- Panciera, Tito, Luca Azzolin, Michelangelo Cordenonsi, and Stefano Piccolo. 2017. 'Mechanobiology of YAP and TAZ in physiology and disease', *Nature reviews Molecular cell biology*, 18: 758-70.
- Panwar, J., R. Utharala, L. Fennelly, D. Frenzel, and C. A. Merten. 2023. 'iSort enables automated complex microfluidic droplet sorting in an effort to democratize technology', *Cell Rep Methods*, 3: 100478.
- Pavillon, N., A. J. Hobro, S. Akira, and N. I. Smith. 2018. 'Noninvasive detection of macrophage activation with single-cell resolution through machine learning', *Proc Natl Acad Sci U S A*, 115: E2676-E85.
- Perry, Seth W, John P Norman, Justin Barbieri, Edward B Brown, and Harris A Gelbard. 2011. 'Mitochondrial membrane potential probes and the proton gradient: a practical usage guide', *Biotechniques*, 50: 98-115.
- Petchakup, C., H. Yang, L. Gong, L. He, H. M. Tay, R. Dalan, A. J. Chung, K. H. H. Li, and H. W. Hou. 2022. 'Microfluidic Impedance-Deformability Cytometry for Label-Free Single Neutrophil Mechanophenotyping', *Small*, 18: 2104822.
- Petchakup, Chayakorn, Paul Edward Hutchinson, Hui Min Tay, Sheng Yuan Leong, King Ho Holden Li, and Han Wei Hou. 2021. 'Label-free quantitative lymphocyte activation profiling using microfluidic impedance cytometry', *Sensors and Actuators B: Chemical*, 339.
- Petersson, Filip, Andreas Nilsson, Cecilia Holm, Henrik Jönsson, and Thomas Laurell. 2005. 'Continuous separation of lipid particles from erythrocytes by means of laminar flow and acoustic standing wave forces', *Lab on a Chip*, 5: 20-22.
- Piergiovanni, M., V. Galli, G. Holzner, S. Stavrakis, A. DeMello, and G. Dubini. 2020. 'Deformation of leukaemia cell lines in hyperbolic microchannels: investigating the role of shear and extensional components', *Lab Chip*, 20: 2539-48.
- Prieto, J. L., H. W. Su, H. W. Hou, M. P. Vera, B. D. Levy, R. M. Baron, J. Han, and J. Voldman. 2016. 'Monitoring sepsis using electrical cell profiling', *Lab Chip*, 16: 4333-40.
- Radmacher, Manfred. 2007. 'Studying the mechanics of cellular processes by atomic force microscopy', *Methods in cell biology*, 83: 347-72.
- Rajauria, S., C. Axline, C. Gottstein, and A. N. Cleland. 2015. 'High-speed discrimination and sorting of submicron particles using a microfluidic device', *Nano Lett*, 15: 469-75.
- Rapp, Bastian E. 2022. Microfluidics: modeling, mechanics and mathematics (Elsevier).

- Raub, CB, C Lee, and E Kartalov. 2015. 'Sequestration of bacteria from whole blood by optimized microfluidic cross-flow filtration for Rapid Antimicrobial Susceptibility Testing', *Sensors and Actuators B: Chemical*, 210: 120-23.
- Reale, R., A. Ninno, T. Nepi, P. Bisegna, and F. Caselli. 2022. 'Extensional-Flow Impedance Cytometer for Contactless and Optics-Free Erythrocyte Deformability Analysis', *IEEE Trans Biomed Eng*, 70: 565-72.
- Reinhart, WH, and A Singh. 1990. 'Erythrocyte aggregation: the roles of cell deformability and geometry', *European journal of clinical investigation*, 20: 458-62.
- Ren, X., P. Ghassemi, J. S. Strobl, and M. Agah. 2019. 'Biophysical phenotyping of cells via impedance spectroscopy in parallel cyclic deformability channels', *Biomicrofluidics*, 13: 044103.
- Righetto, M., C. Brandi, R. Reale, and F. Caselli. 2025. 'Integrating impedance cytometry with other microfluidic tools towards multifunctional single-cell analysis platforms', *Lab Chip*, 25: 1316-41.
- Roda, Barbara, Andrea Zattoni, Pierluigi Reschiglian, Myeong Hee Moon, Mara Mirasoli, Elisa Michelini, and Aldo Roda. 2009. 'Field-flow fractionation in bioanalysis: A review of recent trends', *Analytica chimica acta*, 635: 132-43.
- Rosenbluth, Michael J, Wilbur A Lam, and Daniel A Fletcher. 2008. 'Analyzing cell mechanics in hematologic diseases with microfluidic biophysical flow cytometry', *Lab on a Chip*, 8: 1062-70.
- Sakuma, S., Y. Kasai, T. Hayakawa, and F. Arai. 2017. 'On-chip cell sorting by high-speed local-flow control using dual membrane pumps', *Lab Chip*, 17: 2760-67.
- Salahi, A., C. Honrado, A. Rane, F. Caselli, and N. S. Swami. 2022. 'Modified Red Blood Cells as Multimodal Standards for Benchmarking Single-Cell Cytometry and Separation Based on Electrical Physiology', *Anal Chem*, 94: 2865-72.
- Salahi, A., A. Rane, L. Xiao, C. Honrado, X. Li, L. Jin, and N. S. Swami. 2022. 'Single-cell assessment of the modulation of macrophage activation by ex vivo intervertebral discs using impedance cytometry', *Biosens Bioelectron*, 210: 114346.
- Sarioglu, A Fatih, Nicola Aceto, Nikola Kojic, Maria C Donaldson, Mahnaz Zeinali, Bashar Hamza, Amanda Engstrom, Huili Zhu, Tilak K Sundaresan, and David T Miyamoto. 2015. 'A microfluidic device for label-free, physical capture of circulating tumor cell clusters', *Nature methods*, 12: 685-91.
- Schwende, Heike, Edith Fitzke, Petra Ambs, and Peter Dieter. 1996. 'Differences in the state of differentiation of THP-1 cells induced by phorbol ester and 1,25-dihydroxyvitamin D3', *Journal of Leukocyte Biology*, 59: 555-61.
- Seo, Kyung Won, Yang Jun Kang, and Sang Joon Lee. 2014. 'Lateral migration and focusing of microspheres in a microchannel flow of viscoelastic fluids', *Physics of Fluids*, 26.
- Serhatlioglu, M., M. Asghari, M. Tahsin Guler, and C. Elbuken. 2019. 'Impedance-based viscoelastic flow cytometry', *Electrophoresis*, 40: 906-13.
- Shan, Yuping, and Hongda Wang. 2015. 'The structure and function of cell membranes examined by atomic force microscopy and single-molecule force spectroscopy', *Chemical Society Reviews*, 44: 3617-38.
- Shen, Shaofei, Chang Tian, Tianbao Li, Juan Xu, Shu-Wei Chen, Qin Tu, Mao-Sen Yuan, Wenming Liu, and Jinyi Wang. 2017. 'Spiral microchannel with ordered micro-obstacles for continuous and highly-efficient particle separation', *Lab on a Chip*, 17: 3578-91.
- Shi, Dongyuan, Jinhong Guo, Liang Chen, Chuncheng Xia, Zhefeng Yu, Ye Ai, Chang Ming Li, Yuejun Kang, and Zhiming Wang. 2015. 'Differential microfluidic sensor on printed circuit board for biological cells analysis', *Electrophoresis*, 36: 1854-58.

- Shi, Wentao, Shunqiang Wang, Ahmad Maarouf, Christopher G Uhl, Ran He, Doruk Yunus, and Yaling Liu. 2017. 'Magnetic particles assisted capture and release of rare circulating tumor cells using wavy-herringbone structured microfluidic devices', *Lab on a Chip*, 17: 3291-99.
- Shoji, Kazuyasu, Kazumasa Ohashi, Kaori Sampei, Masato Oikawa, and Kensaku Mizuno. 2012. 'Cytochalasin D acts as an inhibitor of the actin–cofilin interaction', *Biochemical and biophysical research communications*, 424: 52-57.
- Sliogeryte, Kristina, Stephen D Thorpe, David A Lee, Lorenzo Botto, and Martin M Knight. 2014. 'Stem cell differentiation increases membrane-actin adhesion regulating cell blebability, migration and mechanics', *Scientific reports*, 4: 7307.
- Smith, Joshua T, Benjamin H Wunsch, Navneet Dogra, Mehmet E Ahsen, Kayla Lee, Kamlesh K Yadav, Rachel Weil, Michael A Pereira, Jyotica V Patel, and Elizabeth A Duch. 2018. 'Integrated nanoscale deterministic lateral displacement arrays for separation of extracellular vesicles from clinically-relevant volumes of biological samples', *Lab on a Chip*, 18: 3913-25.
- Soe, M. T. M., K. L. Spiller, and M. Noh. 2022. 'Dielectrophoretic characterization of macrophage phenotypes', *Electrophoresis*, 43: 2440-52.
- Sollich, Peter. 1998. 'Rheological constitutive equation for a model of soft glassy materials', *Physical Review E*, 58: 738.
- Soteriou, D., M. Kubankova, C. Schweitzer, R. Lopez-Posadas, R. Pradhan, O. M. Thoma, A. H. Gyorfi, A. E. Matei, M. Waldner, J. H. W. Distler, S. Scheuermann, J. Langejurgen, M. Eckstein, R. Schneider-Stock, R. Atreya, M. F. Neurath, A. Hartmann, and J. Guck. 2023. 'Rapid single-cell physical phenotyping of mechanically dissociated tissue biopsies', *Nat Biomed Eng*, 7: 1392-403.
- Spector, Ilan, Nava R Shochet, Dina Blasberger, and Yoel Kashman. 1989. 'Latrunculins—novel marine macrolides that disrupt microfilament organization and affect cell growth: I. Comparison with cytochalasin D', Cell motility and the cytoskeleton, 13: 127-44.
- Spencer, D. C., T. F. Paton, K. T. Mulroney, T. J. J. Inglis, J. M. Sutton, and H. Morgan. 2020. 'A fast impedance-based antimicrobial susceptibility test', *Nat Commun*, 11: 5328.
- Spencer, D., and H. Morgan. 2011. 'Positional dependence of particles in microfludic impedance cytometry', *Lab Chip*, 11: 1234-9.
- Spencer, D., and H. Morgan. 2020. 'High-Speed Single-Cell Dielectric Spectroscopy', *ACS Sens*, 5: 423-30.
- Starr, T., T. J. Bauler, P. Malik-Kale, and O. Steele-Mortimer. 2018. 'The phorbol 12-myristate-13-acetate differentiation protocol is critical to the interaction of THP-1 macrophages with Salmonella Typhimurium', *PLoS One*, 13: e0193601.
- Stevenson, Bruce R, and David A Begg. 1994. 'Concentration-dependent effects of cytochalasin D on tight junctions and actin filaments in MDCK epithelial cells', *Journal of cell science*, 107: 367-75.
- Sun, T., D. Holmes, S. Gawad, N. G. Green, and H. Morgan. 2007. 'High speed multi-frequency impedance analysis of single particles in a microfluidic cytometer using maximum length sequences', *Lab Chip*, 7: 1034-40.
- Sun, Tao, and Hywel Morgan. 2010. 'Single-cell microfluidic impedance cytometry: a review', *Microfluidics and Nanofluidics*, 8: 423-43.
- Sundararajan, Narayan, Michael S Pio, Luke P Lee, and Andrew A Berlin. 2004. 'Three-dimensional hydrodynamic focusing in polydimethylsiloxane (PDMS) microchannels', *Journal of Microelectromechanical systems*, 13: 559-67.

- Suresh, Subra. 2007. 'Biomechanics and biophysics of cancer cells', *Acta biomaterialia*, 3: 413-38.
- Tan, Q., G. A. Ferrier, B. K. Chen, C. Wang, and Y. Sun. 2012. 'Quantification of the specific membrane capacitance of single cells using a microfluidic device and impedance spectroscopy measurement', *Biomicrofluidics*, 6: 34112.
- Tang, Tao, Xun Liu, Yapeng Yuan, Ryota Kiya, Tianlong Zhang, Yang Yang, Shiro Suetsugu, Yoichi Yamazaki, Nobutoshi Ota, Koki Yamamoto, Hironari Kamikubo, Yo Tanaka, Ming Li, Yoichiroh Hosokawa, and Yaxiaer Yalikun. 2023. 'Machine learning-based impedance system for real-time recognition of antibiotic-susceptible bacteria with parallel cytometry', Sensors and Actuators B: Chemical, 374: 132698.
- Tewhey, Ryan, Jason B Warner, Masakazu Nakano, Brian Libby, Martina Medkova, Patricia H David, Steve K Kotsopoulos, Michael L Samuels, J Brian Hutchison, and Jonathan W Larson. 2009. 'Microdroplet-based PCR enrichment for large-scale targeted sequencing', *Nature biotechnology*, 27: 1025-31.
- Thomas, Rupert SW, Peter D Mitchell, Richard O C Oreffo, Hywel Morgan, and Nicolas G Green. 2019. 'Image based sorting and negative dielectrophoresis for high purity cell and particle separation', *Electrophoresis*, 40: 2718-27.
- Timoshenko, Stephen, and Sergius Woinowsky-Krieger. 1959. *Theory of plates and shells* (McGraw-hill New York).
- Torres Castro, Karina, Javad Jarmoshti, Li Xiao, Aditya Rane, Armita Salahi, Li Jin, Xudong Li, Federica Caselli, Carlos Honrado, and Nathan S. Swami. 2023. 'Multichannel Impedance Cytometry Downstream of Cell Separation by Deterministic Lateral Displacement to Quantify Macrophage Enrichment in Heterogeneous Samples', *Advanced Materials Technologies*, 8: 2201463.
- Tottori, Naotomo, and Takasi Nisisako. 2020. 'Particle/cell separation using sheath-free deterministic lateral displacement arrays with inertially focused single straight input', *Lab on a Chip*, 20: 1999-2008.
- Tse, Henry TK, Daniel R Gossett, Yo Sup Moon, Mahdokht Masaeli, Marie Sohsman, Yong Ying, Kimberly Mislick, Ryan P Adams, Jianyu Rao, and Dino Di Carlo. 2013. 'Quantitative diagnosis of malignant pleural effusions by single-cell mechanophenotyping', *Science translational medicine*, 5: 212ra163-212ra163.
- Urbanska, M., H. E. Munoz, J. Shaw Bagnall, O. Otto, S. R. Manalis, D. Di Carlo, and J. Guck. 2020. 'A comparison of microfluidic methods for high-throughput cell deformability measurements', *Nat Methods*, 17: 587-93.
- Velmanickam, Logeeshan, Vidura Jayasooriya, Madhava Sarma Vemuri, Umamaheswara Rao Tida, and Dharmakeerthi Nawarathna. 2022. 'Recent advances in dielectrophoresis toward biomarker detection: A summary of studies published between 2014 and 2021', *Electrophoresis*, 43: 212-31.
- Vykoukal, Jody, Daynene M Vykoukal, Susanne Freyberg, Eckhard U Alt, and Peter RC Gascoyne. 2008. 'Enrichment of putative stem cells from adipose tissue using dielectrophoretic field-flow fractionation', *Lab on a Chip*, 8: 1386-93.
- Wakatsuki, Tetsuro, Bill Schwab, Nathan C Thompson, and Elliot L Elson. 2001. 'Effects of cytochalasin D and latrunculin B on mechanical properties of cells', *Journal of cell science*, 114: 1025-36.
- Wan, Kai-Tak. 1999. 'Fracture mechanics of a shaft-loaded blister test–transition from a bending plate to a stretching membrane', *The Journal of Adhesion*, 70: 209-19.
- Wang, K., Y. Zhao, D. Chen, B. Fan, Y. Lu, L. Chen, R. Long, J. Wang, and J. Chen. 2017. 'Specific membrane capacitance, cytoplasm conductivity and instantaneous Young's modulus of single tumour cells', *Sci Data*, 4: 170015.

- Wang, L., L. A. Flanagan, E. Monuki, N. L. Jeon, and A. P. Lee. 2007. 'Dielectrophoresis switching with vertical sidewall electrodes for microfluidic flow cytometry', *Lab Chip*, 7: 1114-20.
- Wang, Xiao-Bo, Ying Huang, Peter RC Gascoyne, Frederick F Becker, Ralph Hölzel, and Ronald Pethig. 1994. 'Changes in Friend murine erythroleukaemia cell membranes during induced differentiation determined by electrorotation', *Biochimica et Biophysica Acta (BBA)-Biomembranes*, 1193: 330-44.
- Wang, Xiao-Bo, R Pethig, and Thomas B Jones. 1992. 'Relationship of dielectrophoretic and electrorotational behaviour exhibited by polarized particles', *Journal of Physics D: Applied Physics*, 25: 905.
- Wang, Xujing, Frederick F Becker, and Peter RC Gascoyne. 2002. 'Membrane dielectric changes indicate induced apoptosis in HL-60 cells more sensitively than surface phosphatidylserine expression or DNA fragmentation', *Biochimica et Biophysica Acta (BBA)-Biomembranes*, 1564: 412-20.
- Wang, Z., and S. O. Kelley. 2025. 'Microfluidic technologies for enhancing the potency, predictability and affordability of adoptive cell therapies', *Nat Biomed Eng*.
- Wilson, S., G. Gustafson, D. Lincoln, K. Murari, and C. Johansen. 2014. 'Performance evaluation of an overdriven LED for high-speed schlieren imaging', *Journal of Visualization*, 18: 35-45.
- Wood, Bayden R, Peter Caspers, Gerwin J Puppels, Shveta Pandiancherri, and Don McNaughton. 2007. 'Resonance Raman spectroscopy of red blood cells using near-infrared laser excitation', *Analytical and bioanalytical chemistry*, 387: 1691-703.
- Wu, Mengxi, Adem Ozcelik, Joseph Rufo, Zeyu Wang, Rui Fang, and Tony Jun Huang. 2019. 'Acoustofluidic separation of cells and particles', *Microsystems & Nanoengineering*, 5: 32.
- Wyatt Shields Iv, C., Catherine D. Reyes, and Gabriel P. López. 2015. 'Microfluidic cell sorting: a review of the advances in the separation of cells from debulking to rare cell isolation', *Lab on a Chip*, 15: 1230-49.
- Xavier, M., S. H. Holm, J. P. Beech, D. Spencer, J. O. Tegenfeldt, R. O. C. Oreffo, and H. Morgan. 2019. 'Label-free enrichment of primary human skeletal progenitor cells using deterministic lateral displacement', *Lab Chip*, 19: 513-23.
- Xavier, M., P. Rosendahl, M. Herbig, M. Krater, D. Spencer, M. Bornhauser, R. O. Oreffo, H. Morgan, J. Guck, and O. Otto. 2016. 'Mechanical phenotyping of primary human skeletal stem cells in heterogeneous populations by real-time deformability cytometry', *Integr Biol (Camb)*, 8: 616-23.
- Xu, Zhensong, Yi Zheng, Xian Wang, Nadine Shehata, Chen Wang, and Yu Sun. 2018. 'Stiffness increase of red blood cells during storage', *Microsystems & Nanoengineering*, 4.
- Yang, Jun, Ying Huang, Xujing Wang, Xiao-Bo Wang, Frederick F Becker, and Peter RC Gascoyne. 1999. 'Dielectric properties of human leukocyte subpopulations determined by electrorotation as a cell separation criterion', *Biophysical journal*, 76: 3307-14.
- Yang, Seungyoung, Jae Young Kim, Seong Jae Lee, Sung Sik Lee, and Ju Min Kim. 2011. 'Sheathless elasto-inertial particle focusing and continuous separation in a straight rectangular microchannel', *Lab on a Chip*, 11: 266-73.
- Yuan, D., Q. Zhao, S. Yan, S. Y. Tang, G. Alici, J. Zhang, and W. Li. 2018. 'Recent progress of particle migration in viscoelastic fluids', *Lab Chip*, 18: 551-67.
- Zak, Alexandra, Sara Violeta Merino-Cortés, Anaïs Sadoun, Farah Mustapha, Avin Babataheri, Stéphanie Dogniaux, Sophie Dupré-Crochet, Elodie Hudik, Hai-Tao He, and Abdul I Barakat. 2021. 'Rapid viscoelastic changes are a hallmark of early leukocyte activation', Biophysical journal, 120: 1692-704.

- Zeming, Kerwin Kwek, Thoriq Salafi, Chia-Hung Chen, and Yong Zhang. 2016. 'Asymmetrical deterministic lateral displacement gaps for dual functions of enhanced separation and throughput of red blood cells', *Scientific reports*, 6: 1-10.
- Zeng, Fangfa, Wen Yang, Jie Huang, Yuan Chen, and Yong Chen. 2013. 'Determination of the lowest concentrations of aldehyde fixatives for completely fixing various cellular structures by real-time imaging and quantification', *Histochemistry and cell biology*, 139: 735-49.
- Zhang, Gang, Mian Long, Zhe-Zhi Wu, and Wei-Qun Yu. 2002. 'Mechanical properties of hepatocellular carcinoma cells', *World journal of gastroenterology*, 8: 243.
- Zhao, Y., D. Chen, H. Li, Y. Luo, B. Deng, S. B. Huang, T. K. Chiu, M. H. Wu, R. Long, H. Hu, J. Wang, and J. Chen. 2013. 'A microfluidic system enabling continuous characterization of specific membrane capacitance and cytoplasm conductivity of single cells in suspension', *Biosens Bioelectron*, 43: 304-7.
- Zhao, Yang, Ke Wang, Deyong Chen, Beiyuan Fan, Ying Xu, Yifei Ye, Junbo Wang, Jian Chen, and Chengjun Huang. 2018. 'Development of microfluidic impedance cytometry enabling the quantification of specific membrane capacitance and cytoplasm conductivity from 100,000 single cells', *Biosensors and Bioelectronics*, 111: 138-43.
- Zheng, Y., E. Shojaei-Baghini, A. Azad, C. Wang, and Y. Sun. 2012. 'High-throughput biophysical measurement of human red blood cells', *Lab Chip*, 12: 2560-7.
- Zhong, J., D. Yang, Y. Zhou, M. Liang, and Y. Ai. 2021. 'Multi-frequency single cell electrical impedance measurement for label-free cell viability analysis', *Analyst*, 146: 1848-58.
- Zhong, Jianwei, Peixian Li, Minhui Liang, and Ye Ai. 2021. 'Label Free Cell Viability Assay and Enrichment of Cryopreserved Cells Using Microfluidic Cytometry and On Demand Sorting', *Advanced Materials Technologies*, 7.
- Zhou, Y., D. Yang, Y. Zhou, B. L. Khoo, J. Han, and Y. Ai. 2018. 'Characterizing Deformability and Electrical Impedance of Cancer Cells in a Microfluidic Device', *Anal Chem*, 90: 912-19.
- Zhou, ZL, XX Sun, J Ma, MH Tong, SKY To, AST Wong, and AHW Ngan. 2017. 'Actin cytoskeleton stiffness grades metastatic potential of ovarian carcinoma Hey A8 cells via nanoindentation mapping', *Journal of biomechanics*, 60: 219-26.
- Zhu, J., S. Pan, H. Chai, P. Zhao, Y. Feng, Z. Cheng, S. Zhang, and W. Wang. 2024. 'Microfluidic Impedance Cytometry Enabled One-Step Sample Preparation for Efficient Single-Cell Mass Spectrometry', *Small*: e2310700.
- Zhu, S., X. Zhang, Z. Zhou, Y. Han, N. Xiang, and Z. Ni. 2021. 'Microfluidic impedance cytometry for single-cell sensing: Review on electrode configurations', *Talanta*, 233: 122571.
- Zimmermann, D, A Zhou, M Kiesel, K Feldbauer, U Terpitz, W Haase, T Schneider-Hohendorf, E Bamberg, and VL Sukhorukov. 2008. 'Effects on capacitance by overexpression of membrane proteins', *Biochemical and biophysical research communications*, 369: 1022-26.